Flows, Instabilities, and Magnetism In Stars and Planets

Felix Sainsbury-Martinez

Submitted by Felix Sainsbury-Martinez to the University of Exeter as a thesis for the degree of Doctor of Philosophy in Physics, July, 2017.

I certify that all material in this thesis which is not my own work has been identified and that no material has previously been submitted and approved for the award of a degree by this or any other University.

Signed: .....

Felix Sainsbury-Martinez

Date: .....

Abstract

1st Supervisor: Matthew Browning 2nd Supervisor: David Sing

Flows, instabilities, and magnetism play significant roles in the internal and atmospheric dynamics of objects ranging from the smallest exoplanets to the largest stars. These phenomena are governed by the equations of magnetohydrodynamics (MHD), which link the flows and magnetic fields, and from which the operational parameters and growth rates of instabilities can be recovered. Here we present an overview of interesting phenomena (such as the internal dynamics of stellar and planetary objects, as well as instabilities which might operate within these environs), as well as computational techniques by which these phenomena might both be understood and analysed (through both 'simplifications' of the MHD equations and different numerical/computational approaches).

We first present an investigation into the Heat-Flux-Driven Buoyancy Instability (HBI) within stellar and planetary atmospheres, considering both the parameter space it might operate within as well as its non-linear effects during said operation. We find that whilst the HBI may be able to play a role in Solar, stellar and planetary atmospheres, it is likely to be quite limited in scope, only operating within small regions. However, its dramatic consequences for heat transport in the non-linearly evolved state, and the prospects that it may operate outside the narrow regimes that our analytical analysis suggested, suggest that it may merit further study.

This is followed with a discussion of a method by which the surface flows of exoplanets might be measured: The Rossiter-Mclaughlin Effect at Secondary Eclipse (RMse). We formulate the effect, showing that the formalism is identical to the traditional Rossiter-Mclaughlin effect, albeit in a different frame (a planet transiting a star becomes a star transiting a planet), and consider its observational implications: the effect should be observable for the brightest planet hosting stars using upcoming 40m-class telescopes (i.e.

E-ELT).

We finish with a series of 3D anelastic simulations of fully convective stars, designed to investigate how the internal flows are affected by varying stellar parameters, as well as a possible link between residual entropy and differential rotation contours, and a method by which this link can be used (via the thermal wind equation - TWE) to extrapolate the internal rotation. We find a clear transition between 'solar-like' and 'anti-solar' internal dynamics, characterised in the meridional circulation, differential rotation, residual entropy, and angular momentum flux profiles. Furthermore we find that, whilst the alignment between residual entropy and differential rotation contours is somewhat varied, the resultant extrapolation, via the TWE, produces a generally good fit to the differential rotation contours, suggesting a general robustness to the theory.

Contents

List of Figures

List of Tables

Acknowledgements

This thesis represents the culmination of four years of work, and there are many people without whom I would never have reached this stage.

I must of course start by thanking Matthew Browning, my invaluable guide to the world of (magneto)hydrodynamics and instabilities, without whom this work would never have existed. He has provided me with countless insight, many thought provoking questions, and has enabled me to explore the world of astrophysics. I would also like to thank David Sing for introducing me to the world of research, Nick Featherstone for both writing *Rayleigh* and providing invaluable optimisation advice, Richard Rollins for help in porting *Rayleigh* to the BlueGene/Q architecture, and of course all the academics within the Exeter astrophysics group for numerous, interesting, discussions.

I would also like to thank; Hannah Wakeford, for instigating movie night and forcing me out of my reclusive shell, Jon Rees, for many fascinating early morning discussions and book recommendations, Maria, Laura and Lucia, for both amazing advice, and as conference travel companions, the 'Astro Rainbow' gang (e.g. Tom W, Tom B, Ahmed, Freddy, Victor, Brendan, Jess, Sally, etc.) for their support and friendship throughout, and Emma Way, administrator extraordinaire, for guiding me though the labyrinth of university administration.

Of course I would also like to my family, both Human and Canine, for their support and understanding as I partook in my astrophysical adventures, sharing my joys and sorrows along the way.

Felix Sainsbury-Martinez

Exeter, U.K.

6th July 2017

Chapter 1

Introduction

"We apologize for the inconvenience."

— God's Final Message to His Creation, Douglas Adams

Flows, instabilities, and magnetism play significant roles in the internal and atmospheric dynamics of objects ranging from the smallest exoplanets to the largest stars. These phenomena are governed by the equations of magnetohydrodynamics (MHD), which link the flows and magnetic fields, and from which the operational parameters and growth rates of instabilities can be recovered. Since before the advent of modern computing, scientists have desired to solve these equations analytically (e.g. Maschke and Perrin 1984), and so model, and thus understand, magnetic flows and instabilities.

With the advent of modern high-performance computing, and massive data storage, it has now become possible to model fluids (and plasmas) whose dynamics are controlled by the MHD equations, with simulations extending from simple plasma in a box, to models of entire galaxies (e.g. Springel et al. 2005). This increase in computational technology has also come hand in hand with an increase in observational techniques and technology.

One of these new observational techniques is asteroseismology (and its solar analogue - helioseismology - Howard and Labonte 1980; Deubner and Gough 1984), which allows us to investigate the internal structure of a star via oscillation modes within the stellar interior. These oscillation modes can be detected as spikes in the power spectrum of a star's light curve, and can be used, for example, in the solar case to recover the internal rotation

profile (Gough 1985; Christensen-Dalsgaard et al. 1990).

More broadly, observational astrophysics is approaching a golden age, with a variety of both space-based (e.g. *Kepler* (Basri et al. 2005) and JWST (Gardner et al. 2006)), and ground-based (e.g. GMT (Johns et al. 2012), and E-ELT (Hook 2009)) telescopes either currently providing us, or on the cusp of providing us, with a wealth of stellar data, over long periods, and with high signal to noise ratios.

These observational and theoretical developments help set the stage for the work described here, which consists of an in-depth investigation into some of the flows, instabilities and magnetic fields that may form within stellar and planetary environments. In the rest of this chapter, we provide some context to our work, by briefly introducing some of the key theoretical and observational concepts that motivate it. We first outline the MHD equations and discuss instabilities that stem from them (section 1.1); next we discuss the internal dynamics of stars and the influence of magnetism therein (section 1.2). We give a brief overview of modern high performance computing and how it is changing the shape of astrophysical simulations (section 1.3), and we discuss a method by which the surface flows of a star or planet may be measured (section 1.4). We close by giving a brief overview of the remainder of this thesis (section 1.5).

1.1 A First Look at (M)HD Instabilities

In order to investigate the internal dynamics of stars and planets, we must understand the flows, instabilities, and magnetic field effects at play within. This can be achieved through the (M)HD equations, which govern the evolution of the system. We look at these equations, and various simplifications of them, in more depth in chapter 2. In some cases the solutions to these equations are steady; in many others they are time-dependent or chaotic. As in classical fluid mechanics, a key principle is that many flow fields that might on first inspection appear to be valid solutions to these equations are ultimately unstable – that is, perturbations to a 'base' state grow and may become dynamically important. These (M)HD instabilities will occupy us in one form or another for much of this thesis, so we begin here by providing a pedagogical outline of a particularly seminal thermal instability,

which serves to illustrate in a relatively simple way some of the dynamics and behaviours that might be expected in the more complex situations considered in this work.

We therefore start by considering Rayleigh-Bénard Convection (a type of buoyancy-driven convection - Rayleigh 1916; Berge and Dubois 1984), which was an early target of both experimental and theoretical analysis. In section 2.4 we briefly investigate this instability computationally, studying (for example) the flows and temperature profiles achieved in the nonlinear state (Figure 2.1); here we investigate it analytically, with a brief overview of the physics behind the instability. Although the instabilities and flows we investigate in the bulk of this thesis occur in different parameter regimes (and include somewhat different physics) than applicable in this simple problem, some of the concepts and results below are still relevant. In particular, this problem provides a particularly simple setting in which the Rayleigh number – a nondimensional number measuring buoyancy driving relative to dissipation – may be derived, and this number will figure prominently in some of our discussions later. Further, the nonlinear behaviour of Rayleigh-Bénard convection – in particular, its tendency to isotropise temperature within the convective domain – is in many ways similar to that realised in the more complex setups considered in chapter 5.

In its most basic form, Rayleigh-Bénard convection consists of a thin layer of fluid sandwiched between two plates perpendicular to the gravitational acceleration. The fluid is heated from below and cooled from above, leading to a temperature difference (ΔT) across the fluid. The temperature difference gives rise to density differences, as parcels of fluid near the top (bottom) boundary are cooled (warmed) and so contract (expand). This leads to a buoyancy force, which acts to reorganize the fluid such that the lighter fluid is near the top boundary (and the heavier is near the bottom). This reorganisation of hot/cold fluid can only occur when the temperature difference exceeds some critical value (ΔT_c). For small ΔT the fluid remains motionless: conduction (thermal diffusion) in the background state suffices to carry the heat, and small perturbations to this base state are suppressed by viscous and thermal diffusion. An example of the reorganising fluid motion that develops at higher ΔT can be seen in Figure 2.1. The instability criterion is typically defined in terms of a non-dimensional combination of fluid and system parameters, the Rayleigh Number (R_a), and the system is said to be unstable if this Rayleigh number exceeds a critical value: $R_a > R_{a_c}$.

To derive this Rayleigh number in a heuristic fashion, let us consider our fluid to be sandwiched between two horizontal plates separated by a distance h, and focus on a fluid parcel of volume d^3 located between these plates. If this parcel is displaced upwardly, it will have a buoyancy force acting upon it:

$$F_b = g\Delta\rho d^3, \tag{1.1}$$

where g is the gravitational acceleration and ρ is the density (with $\Delta\rho$ the density contrast between the parcel and its surroundings). If this density contrast is due solely to a contrast between the parcel's temperature (T) and its surroundings, we can rewrite it as:

$$\Delta\rho = \rho\alpha\Delta T, \tag{1.2}$$

in which α is the thermal expansion coefficient of the fluid. This buoyant motion will be opposed by a viscous force of the form

$$F_v = \mu d\frac{dz}{dt}, \tag{1.3}$$

where μ is the viscosity and z is the vertical spatial coordinate. (Here, we have assumed the usual form of the viscous force per unit volume $\propto \nu(\partial^2 w/\partial z^2)$, identifying the vertical velocity w with dz/dt, and assuming vertical gradients $d/dz \sim 1/d$.) In addition to this opposition by viscous forces, the parcel will also lose heat, via thermal conduction, to its surroundings at a rate that is dependent upon both the surface area of the parcel, and the parcel's thermal conductivity κ. We can derive this rate of heat loss via the steady state

heat diffusion equation:

$$\nabla^2 T = \frac{1}{\alpha}\frac{\partial T}{\partial t} \tag{1.4a}$$

$$\text{with: } \alpha = \frac{k}{mC_P} \text{ and } \nabla^2 T \approx \frac{-\Delta T^2}{d^2} \tag{1.4b}$$

$$\downarrow$$

$$\frac{dT}{dt} \propto \frac{-\kappa}{d^2} \tag{1.4c}$$

$$\downarrow$$

$$\Delta T = \Delta T_h e^{\frac{-\kappa t}{d^2}}. \tag{1.4d}$$

Using the above equation, and considering the viscous and buoyancy forces to be in balance (i.e. no acceleration), we can get a new expression for the velocity of the parcel

$$\frac{dz}{dt} = \dot{z} = \frac{g\rho\alpha d^2 \Delta T_h}{\mu} e^{\frac{-\kappa t}{d^2}}. \tag{1.5}$$

From this, we can now calculate how far the parcel can travel before it equilibrates with its surroundings:

$$\int_0^\infty \frac{dz}{dt} dt = \int_0^\infty \frac{g\rho\alpha d^2 \Delta T_h}{\mu} e^{\frac{-\kappa t}{d^2}} dt \tag{1.6a}$$

$$z_{max} = \frac{g\rho\alpha d^4 \Delta T_h}{\mu\kappa}. \tag{1.6b}$$

In order to convect heat, there must be movement between the plates on a timescale in which the fluid parcel retains its temperature difference, thus we require that:

$$z_{max} = \frac{g\rho\alpha d^4 \Delta T_h}{\mu\kappa} > h. \tag{1.7}$$

Now suppose the fluid parcel's size is some fraction $1/f$ of the separation between the plates, so $d = \frac{h}{f}$. Our requirement that the rise time be shorter than the thermal diffusion time then becomes:

$$\frac{g\rho\alpha h^3 \Delta T_h}{\mu\kappa} \equiv R_a > f^4. \tag{1.8}$$

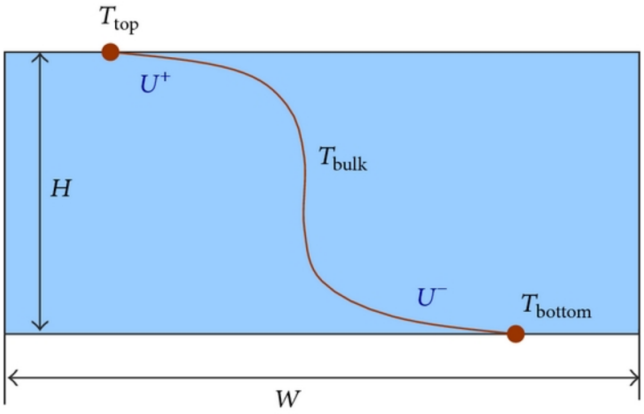

Figure 1.1: The non-linear temperature profile which develops during Rayleigh-Bénard convection. Note the sharp temperature gradient that forms in the boundary layers of the convecting fluid, accompanied by a nearly isothermal interior. Provided by *Commons*.

In this simple model, the right-hand-side defines the critical Rayleigh number Ra_c above which the flow can convect. If the parcel's dimensions are simply taken to be of order the plate separation, then $f = 1$ and the critical Rayleigh number is of order unity; smaller values of d give larger Ra_c. Quantitatively, this model is incorrect – a formal linear stability analysis (see, e.g., Chandrasekhar 1961) reveals that the critical Rayleigh number for convection in these circumstances varies between 658 and 1708 depending on boundary conditions. Still, it illustrates the general principle that the buoyant driving must exceed the stabilising influence of thermal and viscous diffusion for the fluid to convect.

Rayleigh-Bénard convection also possess a number of interesting non-linear effects. Most notably, at high Ra in the non-rotating regime the developed state tends to consist of a nearly isothermal interior, accompanied by strong thermal boundary layers that contain most of the imposed temperature contrast (Figure 1.1). (For rotating convection the situation is somewhat different, and in particular the interior may not become isothermal even at very high Ra; see, e.g., discussions in Stevenson 1979; Julien et al. 2012; Barker et al. 2014.) These interesting non-linear effects are something of a theme with (M)HD instabilities, with many instabilities only becoming astrophysically interesting due to their non-linear effects. For a more detailed investigation into Rayleigh-Bénard convection see any of the numerous reviews, for example Berge and Dubois (1984).

Rayleigh-Bénard convection is only the tip of the (M)HD instability iceberg, with many other interesting, and astrophysically significant, instabilities realised in various contexts.

In particular, the introduction of magnetism into a problem introduces qualitatively new behaviour, some of which we briefly outline here. In particular, we note below the existence of the magnetorotational instability (MRI), the magnetothermal instability (MTI), and the heat-flux-driven buoyancy instability (HBI).

The MRI is an MHD instability which may cause an accretion disk to become turbulent, leading to angular momentum transport in a variety of astrophysical contexts. It was first studied by Chandrasekhar (1960) and by Velikhov (1959), but its importance within accretion disks was demonstrated much later (Balbus and Hawley 1991, 1992; Hawley and Balbus 1991, 1992). Necessary conditions for the MRI to develop include the presence of a weak magnetic field and a disk that rotates differentially such that $\frac{d\Omega}{dr} < 0$. A brief qualitative explanation of the MRI is as follows:

In an ideal plasma, the action of a magnetic field is to link neighbouring fluid parcels together such that, if one is displaced, the magnetic tension will draw the parcels back together (essentially acting as a spring). However, let us now imagine a pair of fluid parcels in a differentially rotating disk, one slightly further inwards than the other. In this case, the inner parcel rotates - orbits - slightly faster than the outer parcel, creating an increasing displacement between the parcels. The magnetic tension opposes this displacement, creating a weak spring-like force between the parcels. Nominally, this spring-like force should bind the parcels together, however if it is sufficiently weak it will have the opposite effect: the inner parcel will rotate more rapidly as the spring torque drains its angular momentum transferring it to the outer fluid parcel, whose rotation will start to slow. As a result of this transfer of angular momentum, the inner (outer) fluid parcel will migrate inwardly (outwardly) to accommodate its new angular momentum. This increase in separation increases the tension between the parcels, increasing the flow of angular momentum between the parcels, and thus implying instability (since small displacements will be reinforced and grow with time). Note that if the magnetic field (tension) is too strong, it will instead damp the instability, and in some cases, lead to oscillations between fluid parcels. (Balbus 2003)

One of the key results of the MRI is linked to its non-linear effects. In particular, the MRI provides a physically plausible mechanism by which the large viscosities of accretion disks can be explained: the MRI leads to turbulence, and so to turbulent mixing, on the order of

that required to explain the observed viscosities in many contexts. See, for example, the work of Balbus and Hawley (1998) for more indepth review on the MRI and its non-linear effects.

Likewise, our interest in some of the other MHD instabilities described in this thesis was sparked by their possible nonlinear effects. For example, consider the HBI, which occurs in certain circumstances when heat transport is predominantly anisotropic (directed along magnetic field lines), in plasmas that would be stable to classical convection: this instability can restrict vertical heat transport under the correct conditions (e.g. in cooling flows - Quataert 2008). Our investigations into it and its sister instability, the MTI (in chapter 3) were partly motivated by noting that a similar restriction of vertical heat flow in the solar transition region, if realised, could help explain the long-standing problem of how the corona remains so hot (by restricting heat transport from the corona back to the inner atmosphere). We describe these instabilities further in chapter 3.

1.2 The Internal Dynamics of Stars

We now turn our investigation to stars, and specifically the motions and dynamical balances that prevail within them. The internal dynamics of a star are highly dependent upon its mass (i.e. its spectral class), with sufficiently low mass main-sequence stars possessing fully convective interiors, solar mass stars possessing a radiative core wrapped in a convective shell (i.e. the solar convective zone), and higher mass stars reversing this, with a convective core wrapped in a radiative shell (see Figure 1.2, and discussion in any standard text on stellar structure, e.g., Hansen and Kawaler (1994)). In the Sun, this transition from radiative to convective dynamics is marked by the tachocline (Spiegel and Zahn 1992), a region of strong shear related to the shift from solid body rotation in the core (radiative region) to differential rotation in the convective zone (SCZ). This can be clearly seen in the internal rotation profile (Figure 1.5) recovered using helioseismology, and discussed below.

In fact, the differential rotation of the solar surface has been known about, and in-

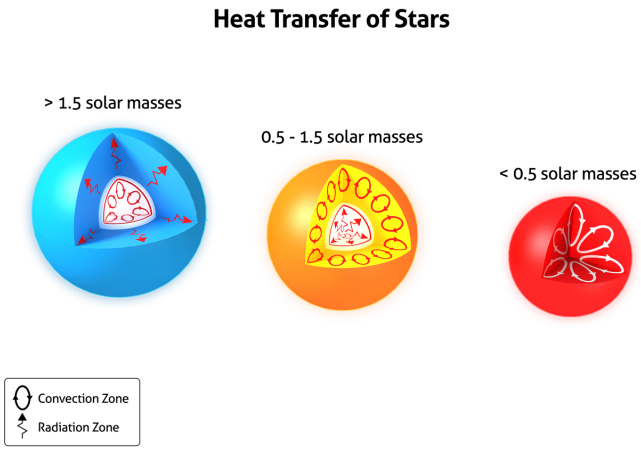

Figure 1.2: Diagrams showing how the internal structure of a star changes with decreasing mass. Note the shift from convective core and radiative envelope at high mass, to the revered case at approximately solar mass, to fully convective interiors at low mass. Provided by *Commons*.

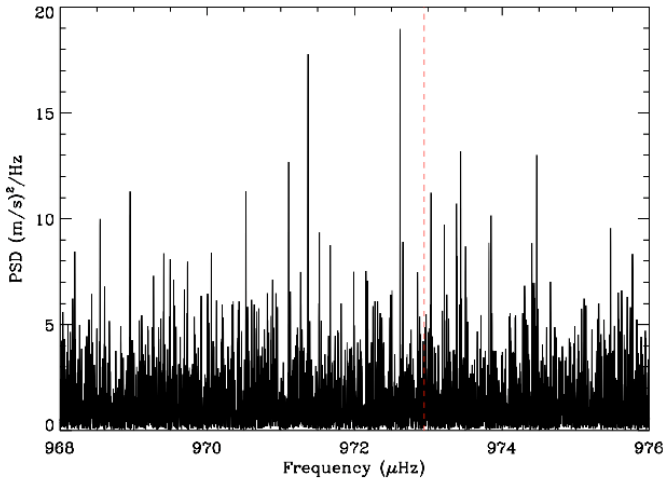

Figure 1.3: Example power spectrum density plots for solar data captured over 3620 days using the GOLF and GONG instruments. The dirac-delta like peaks represent oscillation modes from which the internal structure might be recovered. Reproduced from Salabert and García (2009).

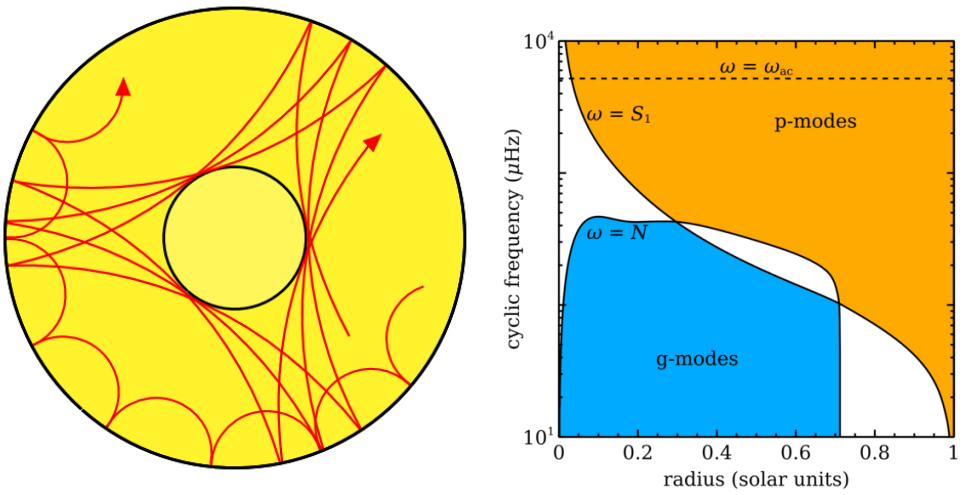

Figure 1.4: Diagrams showing the propagation of solar oscillation modes. Left: diagram showing how different oscillation modes have different sensitivities to the stellar structure (Provided by *Commons*). Right: A propagation diagram for a standard solar model (Christensen-Dalsgaard et al. 1996) showing where oscillations modes have either g-mode or p-mode characteristics. Between about 100 and 400μHz we find the overlap region, containing *mixed-mode* oscillations. Note how the different modes probe different regions of the Solar interior.

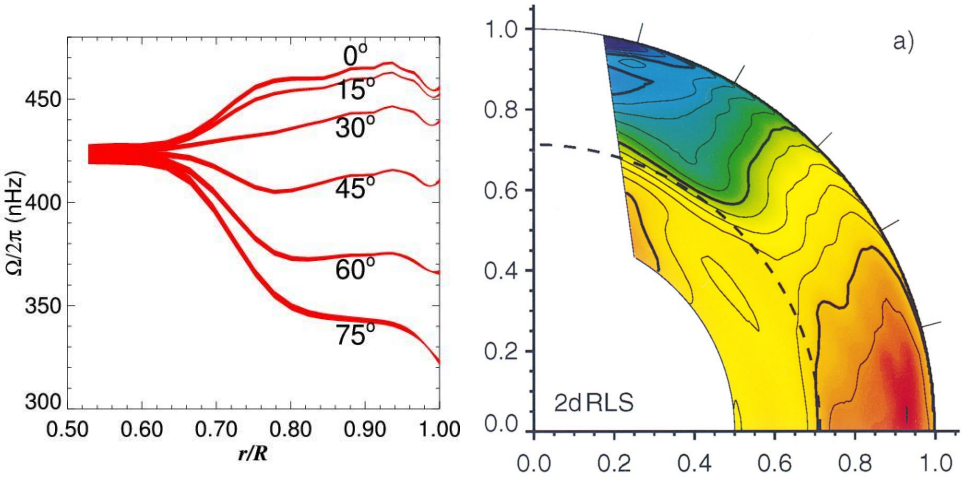

Figure 1.5: Left: internal rotation profile for the sun, recovered through a helioseismic inversion of solar data captured using GONG (Harvey et al. 1996). Note how the transition from the radiative core (solid body rotation) to the convective envelope (differential rotation) is confined to $0.7R_\odot$. Right: example differential rotation profile recovered using a helioseismic inversion by Schou et al. (1998). Again, this reveals then transition from solid-body to differential rotation, as well as evidence for the near-surface shear layer (Brandenburg 2007; Augustson et al. 2011).

vestigated, since long before the advent of helioseismology. Galilei (1613)'s seminal investigation into sunspots showed that their rotation rate depended upon their latitude (Sakurai 1980), i.e. that different parts of the solar surface were rotating at different rates. This result was later confirmed by, for example, Scheiner (1630), Carrington (1861) (who definitively measured the solar rotation period at various latitudes, and after whom the 'Carrington Rotation' frame is named), and Maunder and Maunder (1905).

It would not be until the advent of helioseismology (Howard and Labonte 1980) that the full extent of this differential rotation profile would be uncovered. Helioseismology is the study of the Solar interior via the propagation of seismic waves (particularly acoustic waves (p-modes), standing internal gravity waves (g-modes), and surface gravity waves (f-modes)), which are inferred from resonant frequencies within a stars light curve (see Figure 1.3 for an example spectra). The trick to extracting the interior structure from helioseismology is that different modes propagate through different regions of the Solar interior (see Figure 1.4 for a visual representation of this); the properties of the medium the modes traverse affects their structure (specifically, the frequency and travel time of a mode gives information about the local sound speed of the portion of the star it traverses). This information can be used to recover the internal (differential) rotation profile via a helioseismic inversion (Gough 1985; Christensen-Dalsgaard et al. 1996), with Figure 1.5 showing the results of this inversion for the Sun.

Note that, in the above analysis, we have not differentiated between local (propagating waves) and global-scale (standing-waves/eigenmodes) helioseimic techniques - for a more complete overview of the differences between the two methods see the review by Kosovichev (2011). Note also that the latter, while commonly called 'global' modes, are still spatially localised in radius: for example, higher-degree acoustic modes are trapped in the very outermost regions of the Solar convection zone, whereas modes with $\ell = 0$ penetrate the centre. This localisation in radius is essential for helioseismic inversion; see, Christensen-Dalsgaard (2002), page 1085 for discussion.

This process can also be applied to other stars (asteroseismology), where it can also be used to recover internal details, albeit at a decreased resolution due to the limited number of modes that can be observed without large data sets, and the comparatively poor frequency resolution of the measurements (e.g., Aerts et al. 2010). This has recently started to change,

thanks to the Kepler mission (Gilliland et al. 2010), which observed $\sim 10^5$ stars over a period of several years, and obtained asteroseismic diagnostics for a subset of these. Recently, for example, these measurements have revealed discrepancies between asteroseismically-determined ages of stars and those measured by other means (see Davies et al. 2015; van Saders et al. 2016), and have uncovered clear signatures of internal differential rotation in some evolved stars (Beck et al. 2012; Deheuvels et al. 2012). Still, it must be admitted that our knowledge of internal dynamics in stars other than the Sun is comparatively poor.

Given that stars are now known to differentially rotate, we now look at possible mechanisms to drive, and maintain, these flows. In essence, convective flows redistribute angular momentum, and this redistribution of angular momentum can drive differential rotation. In order to introduce some of the concepts that arise in our later discussion, we turn first to a brief discussion of another seminal result in classical fluid mechanics, called the Taylor-Proudman Theorem (Taylor 1917 and Proudman 1916). This states, loosely, that when a flow is sufficiently slow compared to the angular rotation (i.e. at low Rossby number), the fluid velocity will be uniform along any line parallel to the axis of rotation. This result can be seen experimentally as Taylor columns (Taylor 1917), and can be recovered theoretically by considering the below form of the Navier-Stokes momentum equation, for a slow, steady, and zero-viscosity flow within a cartesian plane:

$$\rho \left(\boldsymbol{u} \cdot \boldsymbol{\nabla} \right) \boldsymbol{u} = -2\rho \boldsymbol{\Omega} \times \boldsymbol{u} - \boldsymbol{\nabla} P, \tag{1.9}$$

in which $\boldsymbol{\Omega} = \Omega_0 \hat{\boldsymbol{z}}$ is the rotation vector, ρ is the density, and P is the pressure. If the flow is incompressible and the Rosby number is less than one (i.e. the Coriolis forces dominate), the left hand side term (the advective term) can be neglected. Thus, the fluid is approximately in geostrophic balance, with

$$2\rho \boldsymbol{\Omega} \times \boldsymbol{u} \approx -\boldsymbol{\nabla} P. \tag{1.10}$$

If we now take the curl of this equation, and assume that the angular velocity is divergence-

free ($\boldsymbol{\nabla} \cdot \boldsymbol{\Omega}$), we can recover the Taylor-Proudman theorem:

$$2\rho\nabla \times (\boldsymbol{\Omega} \times \boldsymbol{u}) = -\underbrace{\boldsymbol{\nabla} \times \boldsymbol{\nabla} P}_{0} \tag{1.11a}$$

$$\downarrow$$

$$(\boldsymbol{\Omega} \cdot \boldsymbol{\nabla})\, \boldsymbol{u} = 0. \tag{1.11b}$$

This result can be clarified if we expand the dot product:

$$\underbrace{\Omega_x}_{0} \frac{\partial \boldsymbol{u}}{\partial x} + \underbrace{\Omega_y}_{0} \frac{\partial \boldsymbol{u}}{\partial y} + \Omega_z \frac{\partial \boldsymbol{u}}{\partial z} = 0 \tag{1.12a}$$

$$\frac{\partial \boldsymbol{u}}{\partial z} = 0 \tag{1.12b}$$

i.e. all the velocity components are constant with respect to the vertical (z) - this typically implies a differential rotation profile that is aligned with the rotation axis. Of course in deriving this result, we have assumed that a variety of effects (including so-called 'baroclinic' effects, and stresses arising from the convection, magnetic fields, or viscous forces) are negligible; in stars many of these effects do play roles, and we expect that their internal differential rotation profile would exhibit at least some deviation from Taylor-Proudman rotation (either from these effects, or due to the star's magnetic field suppressing the shears/stresses associated with differential rotation, thus affecting the profile). Indeed, in the only example for which reliable inversion of the rotation profile is currently possible (the Sun - Figure 1.5), the angular velocity is more nearly constant on radial lines than it is on cylinders. This observational fact has motivated a great deal of theoretical interest, described more thoroughly in chapter 5.

We finish this section with a look at one mechanism by which the differential rotation profile might be changed: the inclusion of a magnetic field. Previous studies (e.g. Browning et al. 2004; Browning 2008) have found that the presence of a strong magnetic field often suppresses differential rotation: essentially, magnetic tension opposes the flows (i.e shears and stresses) that lead to the formation of a differential rotation profile. These

strong magnetic structures within stars are, in most cases, now thought to arise from the action of a magnetic dynamo: a process that converts kinetic energy to magnetic (Moffatt 1978). The presence of a magnetic dynamo within the Sun was first proposed by Larmor (1919a) (Larmor 1919b, 1919c), although it took a while to be accepted (with even Einstein proposing a alternate mechanism involving an asymmetry between proton and electron charge), with Elsasser (1956) eventually proposing a dynamo as the source of the Earth's magnetic field. An early and influential theoretical result that cast doubt on the possibility that dynamo action could build the observed fields in celestial objects was by Cowling (1933), who proved that no purely axisymmetric magnetic field vanishing at infinity could be maintained by dynamo action (a result now called "Cowling's theorem"). The key to dynamo action in stars, and in particular the key to circumventing Cowling's theorem, is convection, which (in the presence of rotation) provides some level of symmetry-breaking; without the associated fluid motions the magnetic field would eventually vanish thanks to ohmic decay (although, admittedly, this ohmic decay of a Solar-scale magnetic-field would still take of order 10^{10} yrs, comparable to the main sequence lifetime of the Sun - Charbonneau 2013. This result follows directly from calculating the Ohmic decay time, which is of order L^2/η, with η the magnetic diffusivity and L the length scale of the field, and adopting L of order the solar radius and η as appropriate for the Solar interior (e.g., Brun and Browning 2017)). The zonal flows of differential rotation (and possibly meridional flow) also play important roles, by stretching and advecting fields in concert with the convection. The magnetic dynamo is thus fundamentally linked to the (zonal) flows which form within a magnetic object (e.g. the Sun or the Earth). Unfortunately a full

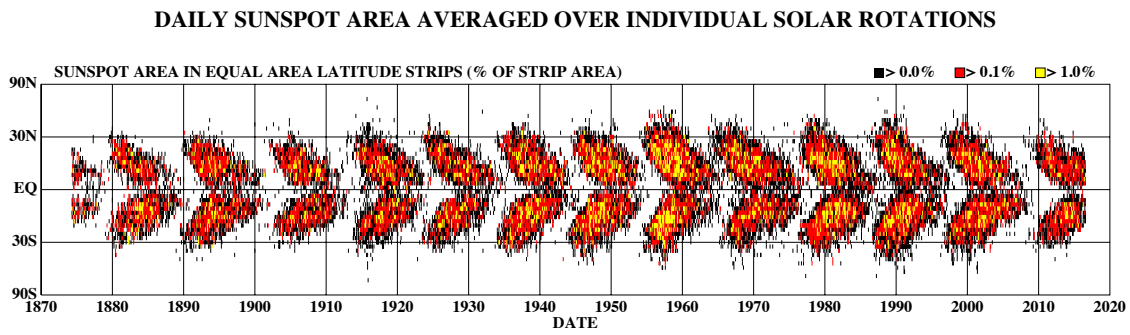

Figure 1.6: The Solar butterfly diagram, showing the change in latitude of sunspots with time. Note that this also provides evidence for the 22 year solar cycle, with spots migrating from high to low latitudes, as well as longer term effects (such as the Maunder Minimum - Eddy 1976). Figure created and provided by NASA (2017).

description of dynamo action is beyond the scope of this work, and as such we direct interested readers to an excellent review by Charbonneau (2010). Instead we close this section with an extremely brief look at some of the observational evidence for magnetic dynamos (and hence magnetic fields).

Starting with the Sun, one of the most obvious expressions of its magnetic field structure are sunspots - dark regions on the Sun's surface in which convection is inhibited by a strong magnetic field (more specifically, we see the eruption of a magnetic flux tube, resulting in a pair of sunspots of opposite polarity - see Borrero and Ichimoto 2011 for a more indepth review). These sunspots also provide an insight into the twenty-two year activity cycle (and hence magnetic dynamo) of the Sun, with each half of the cycle exhibiting a clear migration from high to low latitude flux emergence, as shown in the Solar butterfly diagram (Figure 1.6). These sunspots (pairs) change polarity each cycle (the Hale cycle - Hale et al. 1919), in unison with a change in the polarity of the Sun's magnetic dipole (Babcock 1961).

We must turn to alternate, more indirect, techniques to detect the magnetic dynamo of distant stars. Historically, these have largely been detected either by the photometric signatures induced by starspots, or by measuring the chromospheric or coronal heating and inferring that this arises partly from magnetic fields. The former class of measurements have a long history, dating back to the 17th century (see, e.g., review in Strassmeier 2009), but have lately been revolutionised thanks to the precision photometry provided by Kepler and COROT (see, e.g., Basri et al. 2011; McQuillan et al. 2012; McQuillan et al. 2014a; McQuillan et al. 2014b). The latter have also been employed for decades, as reviewed for example by Hall (2008). Broadly, these reveal that magnetic activity is widespread across the H-R diagram, and is typically linked to the presence of surface convection.

One technique for measuring stellar magnetic fields that has been widely used very recently is known as Zeeman-Doppler Imaging (ZDI - first proposed by Marsh and Horne 1988), which makes use of a magnetic field's ability to polarize the light emitted in spectral lines (the Zeeman effect - Zeeman 1897). This is then combined with the modulation by rotation (Doppler effect) to reconstruct the mean vectorial magnetic field at the stellar surface. Unfortunately the resolution of ZDI maps is limited (since these stars are, of course, very distant), and it only tells us about the global-scale, net, fields. In order to investigate

the finer details of the magnetic field structures of stellar objects, we must turn to models.

1.3 Advances in Computational Techniques

Since the heady days of 1971 and the release of Intel's 4004 microprocessor (a 4-bit processor clocked at a massive 740 kHz - Faggin et al. 1996), computing has come a long way, with modern processors reaching up to 5GHz clockspeeds with up to 18 cores on a single chip (and performances at least 5 orders of magnitude that of the 4004). With this increase in processing power comes an increase in our ability to accurately model the physics of astrophysical phenomena. This increase in computing performance has also been paired with an increase in the speed of interconnects (the connections which link computer hardware), and storage density. Interconnects have developed to the point that multiple computers can be linked together, over a specialised network (e.g. InfiniBand, which offers up a 50 Gbit/s transfer rate), and work on a single (distributed) problem – this is multi-processor parallelisation, which allows simulations which require hundreds of thousands of CPU hours to be completed in mere days. Digital storage density has also sky-rocketed over the last 40 years (approximately 58% growth per year), with current world storage reaching the same levels as that stored within human brains (Gillings et al. 2016), allowing for higher resolution simulations, which output more diagnostics, as well as the creation of large data sets exploring a varied parameter regime.

These developments in computational resources have also lead to developments in the computational techniques employed by astrophysicists, allowing for significantly more detailed, and in depth, studies of astrophysical fluids and phenomena. Examples of these techniques abound; fundamentally these represent different ways of harnessing modern computational resources to solve the underlying equations of fluid motion (with magnetism) with increasing fidelity. In some methods, smooth underlying dynamics are captured by a discrete set of point particles; examples include smooth particle hydrodynamics (SPH - (Gingold and Monaghan 1977; Lucy 1977)) codes (i.e. Gadget (Springel et al. 2001), sphNG (Bate et al. 1995), and Phantom (Price et al. 2017)), which are typically used on the largest scales (i.e. galaxy cluster, molecular clouds, and stellar disks). In some other codes,

the relevant variables are expanded in terms of appropriate basis functions (e.g., Fourier modes or spherical harmonics), with the resulting set of equations frequently transformed between real and "spectral" space in order to solve for both linear and nonlinear terms efficiently (i.e. the non-linear terms are solved in physical space and the linear terms are solved in spectral space, maximising the numerical performance - for more detail about this technique, see the discussion in chapter 2); examples include several pseudo-spectral codes (e.g., the Anelastic Spherical Harmonic code ASH (Clune et al. 1999; Browning et al. 2004) and a related code called Rayleigh (Featherstone and Hindman 2015)), which are used to efficiently model stellar objects. Still other codes discretise the dynamics on a grid, with derivatives replaced by difference equations between sets of neighbouring grid points; these finite-difference grid codes (e.g., ATHENA (Stone et al. 2008), or the PENCIL code (Brandenburg and Dobler 2002)) are widely used on smaller scales (such as plasma in a box), when more complicated physics is involved (such as anisotropic thermal conduction), or when the system is shock dominated. We employ examples of both the pseudo-spectral and finite-difference techniques in this thesis, as described below.

Thus, it has come to pass that simulations and models have become a primary tool in the astrophysicist's arsenal, allowing for investigations into environments and phenomena we cannot yet directly (or even indirectly) observe.

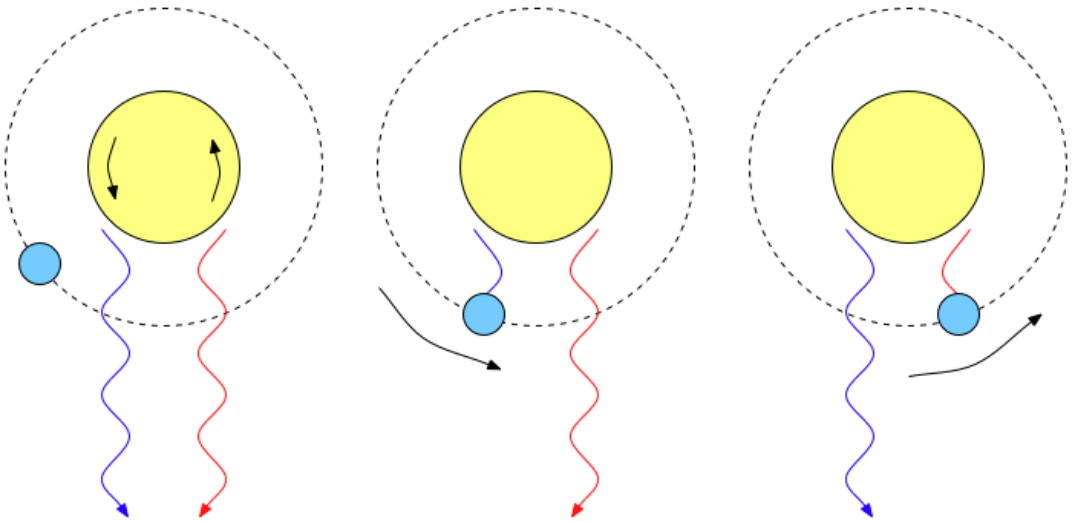

Figure 1.7: Schematic diagram showing the operation of the Rossiter-McLaughlin effect. Note how a transiting exoplanet obscures shifted flux, leading to a net shift in the observed flux. Provided by *Commons*.

1.4 Further Probes of the Dynamics of Stars and Planets

We have already noted that many stars possess a variety of internal flows – i.e. convection, differential rotation, or meridional circulations – and magnetism. Though not addressed to a large extent in this thesis, the same physics apply to many planets, where the combination of internal heating (e.g., by radioactive decay) and high opacity often leads to convection, which in turn may establish magnetic fields through dynamo action (see, e.g., review in Roberts and King 2013). The same core concepts that run through the rest of this thesis – instabilities, magnetism, and flows – thus figure prominently in the dynamics of planets as well.

Planets have the additional complication (relative to stars) that irradiation by a host star may drive near-surface flows; how these interact with the deeper-seated convection is not at all clear, but is the subject of much current theoretical and observational work (e.g. Burkert et al. 2005; Showman et al. 2008; Ricard et al. 2014). In both the stellar and planetary cases, ultimately we must turn to observations to constrain theoretical modelling of the complex flows that might be established. In this section we therefore briefly describe a method by which the near-surface flows might be explored observationally, and provide a sample of the types of flows that might be expected in irradiated planets.

We have already discussed one method by which the dynamics of *stars* might be measured: asteroseismology. However this has somewhat limited applicability to distant stars, requiring high signal-to-noise data taken over a sufficiently long period of time (in order to detect the oscillation modes). Furthermore, asteroseismology cannot tell us anything about the dynamics of exoplanets (which are of course difficult to directly observe). As such we must also turn to other techniques to probe the flows and dynamics of distant objects.

One such technique is the Rossiter-McLaughlin effect, which allows us to measure the surface rotation rate of a distant, transiting exoplanet hosting, star. The essential theory behind this technique is as follows: as a star rotates, half its surface becomes slightly blue-shifted (red-shifted) as it rotates towards (away) from the observer. Normally these shifts cancel each other out (although large star-spots can break this symmetry), but in

the presence of a transiting exoplanet this is no longer the case (Figure 1.7). As an exoplanet transits over the stellar surface, it obscures some of the shifted light, leading to a net observed shift (with an opposite sense to that obscured); this shift can then be used to calculate the rotation rate of the stellar surface (at the latitude of exoplanet transit). Even differential rotation might be recovered, either through the transit of multiple exoplanets at different latitudes, or via an exoplanet whose orbit (and hence transit) is oblique to the rotation plane. It is even possible to measure starspots on the stellar orbit: since these spots are noticeably cooler (and so dimmer) they contribute significantly less to the overall shift, thus when an exoplanet transits a star spots, the net detected shift will actually decrease since the planet is now occluding a dimmer part of the star.

But what about the transiting exoplanet itself? Much like its host star it rotates, and so it should be possible to use the same technique to measure its surface rotation rate (and hence surface flows). We explore this possibility in chapter 4, which examines the Rossiter-McLaughlin effect at secondary eclipse (RMse) as a possible probe of the dynamics in exoplanets.

As brief background and further motivation, we close this section with a quick look at the types of flows we might expect. From calculations performed using GCMs (Global Circulation Models - e.g. the Unified Model - Mayne et al. 2014), we might expect to see high velocity zonal flows at, or near, the planetary surface (e.g. Kataria et al. 2016). In addition to this, models have also suggested the presence of displaced hot spots on the surfaces of highly irradiated exoplanets (Mayne et al. 2017), which may be revealed as an enhancement in the observed shift as calculated by the RMse. An example of these GCM observations is shown in Figure 1.8.

It is through such alternative observational techniques that we hope to gain a greater understanding of the internal dynamics, and zonal flows, of extra-solar objects.

1.5 This Thesis

This thesis consists of a series of investigations into the flows, instabilities, and magnetic fields that may be established in certain stars and planets, examined here using both theo-

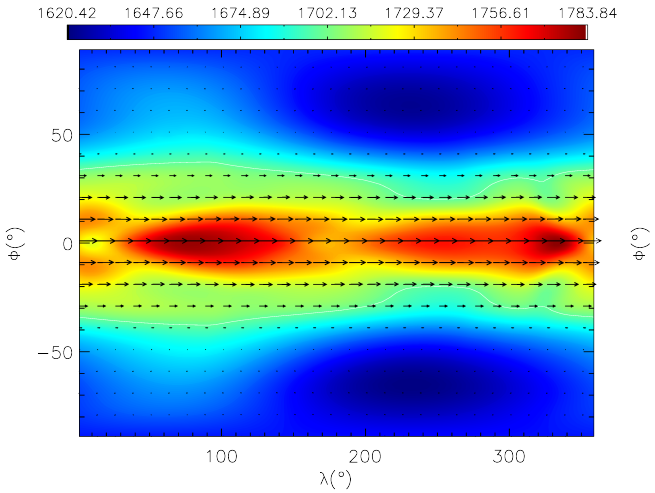

(a) Std Prim: 4.69×10^5 Pa, 10 000 days

Figure 1.8: Example temperature profile (map) and wind velocities (arrows) for a GCM model of a highly irradiated exoplanet by Mayne et al. (2017). Note the strong equatorial wind and the hot spot shifted slightly away from the point nearest the stellar surface (centre of plot).

retical and observational tools. In the remainder of this section (and chapter) we provide a brief overview of the three core projects that make up this thesis, and their placement within this work. Whilst the projects may appear disparate, they all represent investigations designed to probe (and explore) the dynamics of stars and (exo)planets.

In chapter 2 we provide some essential background for our work, by discussing the fundamental equations of MHD, along with two methods by which these equations might be reduced to a tractable form: Ideal and Anelastic MHD. This is followed by a discussion of a few methods by which these simplified MHD equations may be solved: the finite difference approximation to partial differential equations, the spectral expansion of variables in terms of spherical harmonics, and combinations of these techniques. We then look at computational approaches to modelling HD and MHD phenomena, including a look at a simple 2D model we developed for studying (Rayleigh-Bènard) convection. We also look at three 'production' codes used in the remainder of the thesis, giving a brief overview of the mechanisms behind them: ATHENA, a highly flexible, grid-based, finite-difference MHD code, and *Rayleigh* and ASH, which are anelastic, pseudo-spectral, codes designed to model global-scale stellar convection. We finish this chapter with a look at our data reduction and analysis pipelines for both the HBI simulations, and for simulations of con-

vective shells using *Rayleigh* and ASH.

In chapter 3 we consider the possibility that the Heat-Flux-Driven Buoyancy Instability (HBI), an instability which occurs in certain circumstances in the presence of anisotropic conductivity along magnetic field lines, might play a role in the dynamics of the Solar atmosphere, or in stellar/planetary atmospheres more generally. We were initially motivated to study the HBI both because of its instability criterion (an outwardly increasing temperature gradient, which is realised in the transition region of the Sun's atmosphere), and because of its possible non-linear effects. Specifically, in the context of the intracluster medium, the HBI has been demonstrated to restrict, or even cut off, vertical heat transport by thermal conduction; if this occurred in the Solar context as well, it could play a role in solving the coronal heating problem. We start with a discussion of the instability mechanism and a look at its linear growth rate before quantifying the conditions under which the HBI might develop. This leads to limits on both the magnetic field strengths, and perturbation length scales, that an atmosphere should satisfy in order to be HBI unstable. We then apply these limits to two exemplary cases; the solar transition region and corona, and the outer atmosphere of a highly irradiated exoplanet. The results of this analysis are then used to shape a series of 2.5D HBI simulations on both local and global length scales, and under different physical conditions (such as the inclusion of radiative loss - Appendix A).

In chapter 4 we turn to observational probes of dynamics, by presenting a novel approach for measuring the surface rotation rate of transiting exoplanets: the Rossiter-McLaughlin effect at secondary eclipse (*RMse*). Here we show how a simple series of coordinate transforms can be used to prove that the formalism of the effect is the same as for the original Rossiter-McLaughlin effect (at ingress and egress): essentially, we merely shift from the perspective of a planet transiting a star, to a star transiting a planet. A full derivation of the effect can be found in Appendix B. We then present results from a model (described in detail in Appendix C) of the *RMse* effect, including both typical radial-velocity anomalies and a discussion of the symmetries in the modelled results. Fi-

nally we discuss the effect from an observational perspective, and suggest that the new generation of 40m class telescopes might be able to detect the anomaly, and so directly measure the surface rotation rate of a transiting exoplanet. This may allow for detection of jets (since for example super-rotating winds might enhance the measurement several-fold). By using the techniques devised to detect exoplanet atmospheres, it may also be possible to probe the atmosphere at different radii (i.e. much like the observed size of an exoplanet, the *RMse* effect is expected to be wavelength dependent).

In chapter 5 we turn to the application of (M)HD on global scales with an investigation into the internal dynamics of fully convective stars using anelastic, spherical-shell, simulations calculated with both *Rayleigh* and ASH. In this chapter we investigate the zonal flows that develop within fully convective stars, including the transition from 'anti-solar' to 'solar' flow, as well as the balances that act to maintain said flows. We also briefly investigate a theory proposed by Balbus et al. (2009) (or Balbus (2009) in its original form) which suggests that a link exists between residual entropy and differential rotation contours, and that this link, combined with the thermal wind equation, might be used to recover the internal differential rotation profile of a star from surface data. As well as investigating these results using HD simulations, we also present some results for simulations including magnetism, in which the convective and zonal flows combine to build strong fields by dynamo action. In contrast to much prior work, we find a number of scenarios under which a significant internal shear (differential rotation profile - usually suppressed by the presence of a, strong, magnetic field) can be maintained.

Finally in chapter 6 we provide a series of concluding remarks and discuss possible (and already-in-progress) extensions to the work discussed in this thesis.

Chapter 2

Numerical Methods and Computational Tools

"Most good programmers do programming not because they expect to get paid or get adulation by the public, but because it is fun to program."

— Linus Torvalds

2.1 Introduction and Underlying Equations

This thesis deals with astrophysical phenomena on macroscopic scales: the internal motions of stars, or the flows that might occur in stellar and planetary atmospheres. These motions are often not amenable to direct measurement (as discussed in the previous chapter), so we have turned to theoretical modelling to explore some of the dynamics that must be occurring in these environments. This chapter describes some of the analytical and numerical tools used for these explorations.

Astrophysical phenomena on the scales explored in this thesis are generally well described using the equations of fluid dynamics, together with Maxwell's equations. Loosely, we might expect a fluid description to be appropriate in situations where the number of particles involved is large enough that the granularity of matter can be smoothed over (i.e. the dynamics exhibited by an individual particle are not important, rather it is the particle

motions as a whole that define how the system evolves: we treat the particles as a fluid), so that a continuum description is appropriate. In such an environment, the equations that describe fluids behaviour are the magnetohydrodynamic (MHD) equations, originally developed by Alfvén (1942). For a fully compressible fluid, these may be written as:

$$\boldsymbol{\nabla} \cdot \left(\rho \boldsymbol{v}\right) = -\frac{\partial \rho}{\partial t} \tag{2.1a}$$

$$\rho \left[\frac{D\boldsymbol{v}}{Dt} + 2\boldsymbol{\Omega}_0 \times \boldsymbol{v}\right] = -\boldsymbol{\nabla} P + \rho \boldsymbol{g} - \boldsymbol{\nabla} \cdot \mathcal{D} + \frac{1}{4\pi} \left(\boldsymbol{\nabla} \times \boldsymbol{B}\right) \times \boldsymbol{B} \tag{2.1b}$$

$$\rho T \frac{D0S}{Dt} = \boldsymbol{\nabla} \cdot \left[\kappa \rho T \boldsymbol{\nabla} S\right] + \frac{4\pi\eta}{c^2} \boldsymbol{j}^2 + 2\rho\nu \left[e_{ij} e_{ij} - \frac{1}{3} \left(\boldsymbol{\nabla} \cdot \boldsymbol{v}\right)^2\right] + Q \tag{2.1c}$$

$$\frac{\partial \boldsymbol{B}}{\partial t} = \boldsymbol{\nabla} \times \left(\boldsymbol{v} \times \boldsymbol{B}\right) - \boldsymbol{\nabla} \times \left(\eta \boldsymbol{\nabla} \times \boldsymbol{B}\right), \tag{2.1d}$$

with ρ as the density, $\boldsymbol{v}$ as the velocity vector, t as time, $\boldsymbol{\Omega}$ as the angular velocity, P as the pressure, g as the gravitational acceleration, $\boldsymbol{B}$ as the magnetic field vector, S as the entropy, κ as the thermal diffusivity, T as the temperature, η as the magnetic diffusivity, c as the speed of light, $\boldsymbol{j}$ as the current density, ν as the kinematic viscosity, Q as a heating function, e_{ij} as the strain rate tensor, $\mathcal{D}$ as the viscous stress tensor and $\frac{D}{Dt}$ as the Lagrangian derivative ($\frac{D}{Dt} = \frac{\partial}{\partial t} + \boldsymbol{v} \cdot \boldsymbol{\nabla}$). The first of these equations Equation 2.1a is the continuity equation, expressing the conservation of mass. Next is the momentum equation (Equation 2.1b), which essentially describes the force balance of the fluid: The fluid can be accelerated by pressure gradients, buoyancy forces, or lorentz forces. This is followed by an energy equation (Equation 2.1c), which expresses conservation of energy within our system. In the form written here, it allows for joule heating and viscous dissipation as well as some physical heating term, Q, which might represent nuclear fusion or radioactive decay. Finally, we have the induction equation (Equation 2.1d), which describes the stretching of field lines by advection and their decay due to ohmic resistivity. Note that in a partially collisional plasma, the decay is not purely ohmic and other terms (not discussed here) arise. A derivation of these equations can be found in Kulsrud (2005), and a discussion of small-scale kinetic effects may be found in Kunz et al. (2016)

In order to explore these equation fully, we must turn to different approaches and approximations which reduce the MHD equations to a tractable form (i.e. ideal MHD, anelastic

MHD), and frequently also to numerical solution.

In the sections below, we first discuss two approaches to numerical approximation of the underlying partial differential equations (section 2.2). This is followed (section 2.3) with details explaining two methods by which the MHD equations themselves may be simplified in certain circumstances. We then explore specific examples of computational astrophysics at work, starting with a simple 2D convection code (section 2.4) before moving onto the primary codes deployed in this thesis; ATHENA (section 2.5), and *Rayleigh* and ASH (section 2.6). In Appendix D we also present a brief overview of our diagnostic and analysis routine.

2.2 Approaches to the Numerical Solution

2.2.1 Finite-Difference Codes

In the finite difference approach, the continuous variables are approximated by their values at discrete points in a spatial grid. Values within the cells neighbouring a given location are used to approximate derivatives at that location (Glatzmaier 2013). Thus, using this method, the continuous PDEs can be replaced by a a set of algebraic expressions relating the values at all different grid point, which may then be solved by standard means, e.g. matrix manipulation. To illustrate this, consider the first-order, central, finite-difference approximation equations, for both first and second order derivatives:

$$\left(\frac{\partial f}{\partial z}\right)_k = \frac{f_{k+1} - f_{k-1}}{z_{k+1} - z_{k-1}} = \frac{f_{k+1} - f_{k-1}}{2\Delta z}, \tag{2.2a}$$

$$\left(\frac{\partial^2 f}{\partial z^2}\right)_k = \frac{f_{k+1} - 2f_k + f_{k-1}}{(\Delta z)^2}. \tag{2.2b}$$

These equations result from assuming that the function may be approximated by a Taylor expansion (presented here for clarity) of the standard form

$$f(x+h) = f(x) + \frac{f'(x)}{1!}h + \frac{f^2(x)}{2!}h^2 + \ldots + \frac{f^n(x)}{n!}h^n. \tag{2.3}$$

This can be used, for example, to derive an approximation of the first order derivative:

$$f(x+h) \approx f(x) + f'(x)h \tag{2.4a}$$

$$f'(x) \approx \frac{f(x+h) - f(x)}{h}. \tag{2.4b}$$

Note that forward and backward versions of the finite difference equations also exist. These versions only consider terms on one side of the central point, and have a number of different applications; for example, if forward differences are applied to a sequence, we recover the binomial transform of the sequence.

The finite-difference approach works for both linear and non-linear PDEs. Furthermore, thanks to the addition of variable grids, either through static mesh refinement (SMR - in which high resolution regions of the simulation domain are pre-defined) or adaptive mesh refinement (AMR - in which the grid cells representing complicated regions are automatically split[refined]), finite-difference codes are applicable to problems involving a large range of spatial scales, including sharp discontinuities. For a fuller account of the finite-difference approach, see, for example, (Ferziger and Peric 2002).

2.2.2 The Pseudo-Spectral Approach

Although the finite-difference approach is appropriate for many problems, its relatively slow convergence with increasing resolution has long restricted its use in certain environments (this can be linked to the scaling of both the accuracy and efficiency of the two approaches - a finite difference approach scales linearly, whilst a pseudo-spectral approach scales exponentially - i.e. the pseudo-spectral approach converges exponentially onto a solution - see, for example, Kidder and Finn 2000; Markakis and Barack 2014 for more details). A prominent example is turbulent flow, where many authors (e.g. Arakawa 1966; Gottlieb 1977; Canuto et al. 1988; Zang et al. 1989; Ferziger and Peric 2002) have turned to *spectral methods*, as described in this section, to better capture the dynamics (for a particular pool of computational resources) in these cases.

Further, when modelling spherical bodies in particular, the finite-difference ap-

proach (subsection 2.2.1) faces other difficulties. This is partially due to the poles of the system, which can lead to both discontinuities in the numerical solution (since they represent coordinate singularities), and severely limited timesteps under the CFL constraint (since uniform grids in θ and ϕ yield enhanced resolutions near the poles). In recent studies two approaches have been taken to solve these pole problems (e.g. Browning et al. 1989), either using specialised grids (e.g. geodesic grids) to avoid the singularities, or taking an entirely different approach to solving the equations (i.e. spectral approaches). Motivated by these challenges, we outline here the essentials of the spectral and pseudo-spectral methods.We start by looking at the purely spectral approach, which involves the expansion of variables in terms of orthogonal basis functions. For the spherical geometry we are interested in, this means an expansion in terms of spherical harmonics $Y_{lm}\left(\theta,\phi\right)$ - or more specifically, expansion in terms of the eigenfunctions of the horizontal Laplacian. This expansion results in a variable f taking the form:

$$f\left(r,\theta,\phi,t\right)=\mathcal{R}\left\{\sum_{l=0}^{l_{max}}\sum_{m=0}^{l}f_{l}^{m}\left(r,t\right)Y_{lm}\left(\theta,\phi\right)\right\} \tag{2.5}$$

in which $\mathcal{R}$ denotes that only the real part of the complex quantity is considered, and the sum over m goes from $0\rightarrow l$ due to the complex symmetry of the spherical harmonics (i.e. $Y_{l(-m)}\left(\theta,\phi\right)=(-1)^{m}Y_{lm}^{*}\left(\theta,\phi\right)$) and the spectral variable ($f_{l}^{m*}=(-1)^{m}f_{l}^{-m}$). As such, except for the case $m=0$, to account for this symmetry (and simplify the limits) we consider a slight redefinition of the variable function: $f_{l}^{m}\rightarrow 2f_{l}^{m}$ (see Boyd 1989 or Miesch 1998 for more a more detailed derivation of both the above expression, and other mathematics associated with the spectral approach).

The above equation can also be specified in an alternate, Real Value Only, form, swapping the order of the sums such that for each m, the full l sum is calculated (thus also changing the m values that the l sum is performed over). This is typically done in (pseudo)-spectral codes inorder to ease the distribution of l and m modes between different processes (i.e. inorder to ease parallelisation). This alternate form is as follows:

$$f\left(r,\theta,\phi,t\right)=\sum_{m=-m_{max}}^{m_{max}}\sum_{l=|m|}^{l_{max}(m)}f_{l}^{m}\left(r,t\right)Y_{lm}\left(\theta,\phi\right). \tag{2.6}$$

In both Equation 2.5 and Equation 2.6, the spherical harmonics are defined as

$$Y_{lm}\left(\theta,\phi\right)=\sqrt{\frac{2l+1}{4\pi}\frac{(l-m)!}{(l+m)!}}P_l^m\left(\cos\theta\right)e^{im\phi}, \tag{2.7}$$

where $P_l^m\left(\cos\theta\right)$ are the associated Legendre polynomials of order m. Note that the inner summation of the final version of Equation 2.6 is truncated in both Rayleigh and ASH using the **triangular truncation method;** $l_{max}\left(m\right)=l_{max}=m_{max}$, giving results which are both invariant to rotation, and have an equal resolution across the entire sphere (Boyd 1989). Furthermore triangular truncation allows aliasing errors that arise from quadratically non-linear terms to be eliminated, provided that the number of latitudinal and longitudinal grid points satisfy

$$N_\phi \geq 3l_{max}+1, \tag{2.8a}$$

$$N_\theta \geq \frac{3l_{max}+1}{2}. \tag{2.8b}$$

Note that the above limits, which also represent a form of triangular truncation, result from both the 3/2 *rule* (Orszag 1971) and the Gaussian Quadrature technique. For a more detailed analysis of the triangular truncation technique, as well as a full derivation of the above equations, see the appendix of Miesch (1998).

We also require a transform from physical space into spectral. If we consider the operation to occur over a set of predetermined collocation points $\left(\theta_i,\phi_j\right)$, i.e. our physical grid, the spherical harmonic transform is given by

$$f_l^m\left(r,t\right)=\sum_{i=1}^{N_\theta}\sum_{j=1}^{N_\phi}w_iw_jY_{lm}\left(\theta,\phi\right)f\left(r,\theta,\phi,t\right), \tag{2.9}$$

in which our collocation points are given by $\phi_j=\frac{2\pi j}{N_\phi}$ (Gaussian abscissae) in the ϕ direction and by the zeros of the Legendre polynomials of degree N_θ in the θ direction. The

weights, w_i, w_j, are given by

$$w_i = \frac{2}{\left(\sin^2(\theta_i) P'_{N_\theta}(\cos\theta_i)\right)^2} \tag{2.10a}$$

$$w_j = \frac{1}{N_\phi} \tag{2.10b}$$

where P' are the derivatives, w.r.t $\cos(\theta)$, of the associated Legendre polynomial of the first kind, $P_l(\cos(\theta))$ (see, for example, Miesch 1998, for a fuller derivation of these weights).

In the radial direction the variables are typically expanded in terms of Chebyshev polynomials T_n

$$T_n(x) = \cos(n)\arccos(x). \tag{2.11}$$

Then, by evaluating at discrete collocation points, $x_k = \cos\left(\frac{(k-1)\pi}{N_r-1}\right)$, and transforming to spectral space via the Gaussian quadrature technique (Miesch 1998), we arrive at an expression for the radial, Chebyshev, expansion

$$f_l^m(r_k, t) = \frac{2}{N_r - 1} \sum_{n=1}^{N_r} N_r \epsilon_k f_{ln}^m(t) T_{n-1}(x_k), \tag{2.12}$$

with the spectral coefficients f_{ln}^m (reverse spectral transform) given by:

$$f_{ln}^m = \sum_{k=1}^{N_r} N_r w_k T_{n-1}(x_k) f_l^m(x_k, t). \tag{2.13}$$

In the above equations, the weights w_k, are given by

$$w_k = \frac{\epsilon_k \pi}{N_r - 1} \tag{2.14}$$

and $\epsilon_k = 1$ for all k excluding $k = 1, N_r$, where $e_k = \frac{1}{2}$. One major advantage of this Chebyshev approach is that it gives us a higher resolution grid near the boundaries, i.e. in the areas that we might expect interesting effects, both physical and non-physical, to occur. On the other hand, numerical difficulties in one part of the domain tend to propagate quickly over the entire solution due to the global properties of the expansion (Note

that the spectral approach approximates variables as a global function, unlike the finite difference approach in which all calculations are local (i.e. nearest neighbours). As such any numerical difficulties tend to be affect not only by their nearest neighbour, but the entire simulation domain (typically by introducing anomalies into the spectral decomposition)). Hence, in certain circumstances it can be appropriate to employ a mixed approach in which the horizontal representation of the flow is spectral (or pseudo-spectral) but the vertical representation employs a finite-difference approximation. (Both the "production" pseudo-spectral codes employed in this work have this capability, as does our own "demonstration" code, as described below.)

Finally we come to the temporal evolution equation that our variable, $f_l^m(r,t)$ should obey. We express this evolution equation as the sum of the linear (L) and non-linear (N) terms that together make up our variable $f_l^m(r_k,t)$ (thus allowing us to use different, numerically optimal, methods to solve for each term in the evolution equation);

$$\frac{\partial}{\partial t} f_l^m(r_k,t) = L_{lmk}(t) + N_{lmk}(t). \tag{2.15}$$

The full forms of these linear (L) and non-linear (N) terms, as well as the method by which this evolution equation is solved, may be found in Clune et al. (1999), Brun et al. (2004), or Miesch (1998, 2001, 2003).

It is this split between linear and non-linear terms which takes us from the purely spectral approach to a pseudo-spectral approach. In spectral space, non-linear terms become convolution sums which are numerically expensive to evaluate. This cost can be reduced by three orders of magnitude (Falgarone and Passot 2003) if we instead compute the non-linear terms in physical space and use Fast-Fourier-Transforms (FFTs) for the shift between physical and spectral space (or in spherical geometry, using Legendre transforms). This is the Pseudo-Spectral approach: *solve the linear terms (L_{lmk}) in spectral space, and the non-linear terms (N_{lmk}) in physical space*. This reduction in cost is best illustrated if we consider a code performing n non-linear calculations: in spectral space, the time taken to perform these calculations will scale as n^2 whereas if we transform to linear space (using a fast-fourier transform which scales as $n \ln n$) and then perform the calculations (which now scales as n), the overall time taken is significantly reduced (i.e. setting $n = 10000$ gives a

speed up of approximately $\frac{n^2}{n \ln n + n}\ 10^3$), even if the FFTW transforms have to be performed multiple times per simulation step. This situation is reversed when performing linear calculations, with spectral codes converging on a solution exponentially and finite-difference converging linearly. The net result being that, for a mixture of non-linear and linear terms, a significant performance benefit can be maintained via a pseudo-spectral approach (over purely physical or spectral approaches).

2.3 Approximations of the MHD Equations

We now turn to the MHD equations, and investigate two methods by which they might be approximated. These are Ideal MHD and Anelastic MHD.

2.3.1 Ideal MHD

Ideal MHD consists of a series of simplifications, appropriate in highly conductive environments, which reduce the equations of MHD to a more tractable form. The primary assumption of ideal MHD is that the resistivity is negligible ($\eta = 0$), which itself implies that the magnetic field is tightly coupled to the flows (i.e., "frozen in"). Thus, the topology of a magnetic field in ideal MHD changes directly in response to the motion of the fluid: in particular, streamlines that diverge will cause a fieldline to be stretched, and so amplified. Another (conceptually distinct) approximation that is widely employed is the Boussinesq approximation, which ignores density differences except where they are prefaced by the acceleration due to gravity (g). This essentially suggests that differences in inertia are negligible, but gravity is sufficiently strong that a fluid's density, and hence weight, becomes relevant. Loosely, the Boussinesq approximation is expected to provide an adequate description of the dynamics when the depth of the layer under consideration is smaller than a density scale height (Hewitt et al. 1975). This is often not the case in stars, as described below, but holds true in local calculations and (for example) in planetary interiors.

The **ideal-MHD** equations, with the addition of thermal conduction, are shown below.

$$\frac{\partial \rho}{\partial t} + \boldsymbol{\nabla} \cdot (\rho \boldsymbol{v}) = 0 \tag{2.16a}$$

$$\rho \frac{D\boldsymbol{v}}{Dt} = \frac{(\boldsymbol{\nabla} \times \boldsymbol{B}) \times \boldsymbol{B}}{4\pi} - \boldsymbol{\nabla} P + \rho \boldsymbol{g} \tag{2.16b}$$

$$\frac{\partial \boldsymbol{B}}{\partial t} = \boldsymbol{\nabla} \times (\boldsymbol{v} \times \boldsymbol{B}) \tag{2.16c}$$

$$\frac{P}{\gamma - 1} \frac{D \ln P \rho^{-\gamma}}{Dt} = -\boldsymbol{\nabla} \cdot \boldsymbol{Q}. \tag{2.16d}$$

2.3.2 Anelastic Equations

The convection zones of stars are highly stratified. This stratification, which is not fully captured by calculations within the Boussinesq approximation (or by incompressible models) presents major computational challenges, which we describe here along with some of the methods used to alleviate them.

Let's start by assuming that we want to model the convection zone of the Sun. There is a large density contrast between the base of the convection zone, where the Sun is relatively dense ($\rho \approx 100 \rho_{\text{Surface}}$), and the near surface, where the atmosphere is rather diffuse ($r = 0.99 R_\odot$, ρ_{Surface}). These density variations play a key role in, for example, the asymmetry between convective upflows and downflows (Brummell et al. 1996), and may even be important in the dynamo process (Ossendrijver 2003). These density contrasts become even larger as we move towards M-dwarfs.

However, including this compressibility presents challenges of its own, specifically with the timestep required to run the simulation (and hence the resources required to reach an evolved state). In particular, the inclusion of compressibility introduces sound waves into the system. In order for the simulation to remain physically accurate and numerically stable, we would then need to capture these sound waves numerically. This would, in accord with the Courant-Freidrichs-Lewy (CFL) condition (Courant et al. 1928, 1967), limit, numerically stable, timesteps to approximately $\frac{L}{c_s}$ - where L is the size of the smallest grid cell, and c_s is the sound speed. Since convective velocities, in the interiors of stars and planets, are typically significantly slower than the sound speed, following the evolution of sound waves within the simulation would be incredibly inefficient. This is because

the time steps would be limited to a small fraction ($\frac{1}{M}$, where M is the convective Mach number) of the value needed to resolve the fluid motions alone. If the main effect of these acoustic waves is simply to establish a pressure field everywhere that enforces the constraint that the momentum density be solenoidal, this constraint can be imposed directly, rather than by explicitly resolving the sound waves at great computational expense – see, e.g.,Miesch and Toomre (2009) for discussion.

This leads us to to the Anelastic Approximation (Gough 1969; Gilman and Glatzmaier 1981), which allows us to capture the overall density stratification, but without the sound wave timestep limitations. It avoids the timestep limitation essentially by filtering out the restrictive acoustic modes; in an MHD context, it filters out fast magneto-acoustic modes, leaving both Alfven waves and the slow magneto-acoustic modes (Ogura and Phillips 1962; Lantz and Fan 1999). This filtering is achieved, essentially, by requiring that the time derivative of density in the continuity equation is zero. This implies that the momentum density must be divergence free (i.e. solenoidal). Note that the approximation is only valid when the fluid velocities are subsonic, which is generally true only when the radial entropy gradient, which itself drives the convective flows, is at most mildly superadiabatic.

If the above conditions are met, we find that the convection-induced variations in the thermodynamic quantities will be small relative to each variable's spherically-symmetric mean. This allows us to expand each variable as a sum of this mean, and small perturbations about the mean:

$$P\left(r,\theta,\phi,t\right) = \bar{P}\left(r,t\right) + P\left(r,\theta,\phi,t\right) \tag{2.17a}$$

$$\rho\left(r,\theta,\phi,t\right) = \bar{\rho}\left(r,t\right) + \rho\left(r,\theta,\phi,t\right) \tag{2.17b}$$

$$T\left(r,\theta,\phi,t\right) = \bar{T}\left(r,t\right) + T\left(r,\theta,\phi,t\right) \tag{2.17c}$$

$$S\left(r,\theta,\phi,t\right) = \bar{S}\left(r,t\right) + S\left(r,\theta,\phi,t\right), \tag{2.17d}$$

with mean density $\bar{\rho}$, pressure $\bar{P}$, temperature $\bar{T}$ and specific entropy $\bar{S}$; we denote the perturbations as ρ, P, T, and S. In the anelastic approximation, we assume that these perturbations are small thus enabling us to linearise the equations which describe the evolution of these thermodynamic quantities. However, the equations for both the veloc-

ity and the magnetic field remain fully non-linear.

We now introduce an example of the MHD equations solved by an anelastic code, focusing on the method followed by both Rayleigh and ASH. These codes solve the conservation equations for momentum and energy in a rotating spherical shell, together with the induction equation for the magnetic field:

$$\rho\left[\frac{D\boldsymbol{v}}{Dt}+2\boldsymbol{\Omega}_0\times\boldsymbol{v}\right]=-\boldsymbol{\nabla}P+\rho\boldsymbol{g}-\boldsymbol{\nabla}\cdot\mathcal{D}+\frac{1}{4\pi}\left(\boldsymbol{\nabla}\times\boldsymbol{B}\right)\times\boldsymbol{B} \tag{2.18a}$$

$$\bar{\rho}\bar{T}\frac{DS}{Dt}=\boldsymbol{\nabla}\cdot\left[\kappa\bar{\rho}\bar{T}\boldsymbol{\nabla}S\right]+\frac{4\pi\eta}{c^2}\boldsymbol{j}^2+2\bar{\rho}\nu\left[e_{ij}e_{ij}-\frac{1}{3}\left(\boldsymbol{\nabla}\cdot\boldsymbol{v}\right)^2\right]+Q \tag{2.18b}$$

$$\frac{\partial\boldsymbol{B}}{\partial t}=\boldsymbol{\nabla}\times\left(\boldsymbol{v}\times\boldsymbol{B}\right)-\boldsymbol{\nabla}\times\left(\eta\boldsymbol{\nabla}\times\boldsymbol{B}\right), \tag{2.18c}$$

where $\boldsymbol{v}=\left(v_r,v_\theta,v_\phi\right)$ is the velocity vector in a frame of reference rotating at constant angular velocity Ω_0, $\boldsymbol{B}=\left(B_r,B_\theta,B_\phi\right)$ is the magnetic field vector, $\boldsymbol{j}=c/4\pi\left(\nabla\times\boldsymbol{B}\right)$ is the current density, $\boldsymbol{g}$ is the acceleration due to gravity, κ is the effective thermal diffusivity, ν as the effective kinematic viscosity, η is the effective magnetic diffusivity, Q is a heating function which depends upon the code considered (section 2.6), e_{ij} is the strain rate tensor, and $\mathcal{D}$ is the viscous stress tensor, defined by

$$\mathcal{D}_{ij}=-2\bar{\rho}\nu\left[e_{ij}-\frac{1}{3}\left(\boldsymbol{\nabla}\cdot\boldsymbol{v}\right)\delta_{ij}\right], \tag{2.19}$$

with δ_{ij} the Kronecker delta. To close this set of equations, we require that the thermodynamic fluctuations satisfy the linear relations

$$\frac{\rho}{\bar{\rho}}=\frac{P}{\bar{P}}-\frac{T}{\bar{T}}=\frac{P}{\gamma\bar{P}}-\frac{S}{c_p}, \tag{2.20}$$

under the assumption that the ideal gas law takes the form

$$P=\mathcal{R}\rho T, \tag{2.21}$$

in which $\mathcal{R}$ is the gas constant. Finally, we require that both the momentum flux, and the magnetic field, be divergence free:

$$\boldsymbol{\nabla} \cdot \left(\bar{\rho}\boldsymbol{v}\right) = 0 \tag{2.22a}$$

$$\boldsymbol{\nabla} \cdot \boldsymbol{B} = 0. \tag{2.22b}$$

In order to satisfy (enforce) the above requirements, we express the momentum flux, and the magnetic field, in terms of poloidal and toroidal streamfunctions (W, Z), and magnetic potentials (C, A), which are defined such that;

$$\bar{\rho}\boldsymbol{v} = \nabla \times \nabla \times (W\hat{r}) + \nabla \times (Z\hat{r}), \tag{2.23}$$

$$\boldsymbol{B} = \nabla \times \nabla \times (C\hat{r}) + \nabla \times (A\hat{r}), \tag{2.24}$$

where $\hat{r}$ is the radial unit vector. Not only does this decomposition (mathematically) enforce the conditions expressed in Equation 2.22, it also aids in linking the simulation domain to the boundary conditions: the boundary conditions can be imposed in W, Z, C, A which, for example, makes the application of potential field boundary conditions much easier - just set a suitable condition for C and A with no need to solve a poisson equation (Jones et al. 2011). Finally it is worth noting that, unlike a standard $B = \boldsymbol{\nabla} \times A$ decomposition, and because the magnetic flux is divergence free, this toroidal/poloidal fully specifies the magnetic field (Jones 2011).

We finish this section with a potential warning: In some situations, such as the radiative envelopes of more massive stars (i.e. A-, B-, and O-type stars) these anelastic MHD equations may not fully conserve energy, instead conserving a "stratification weighted pseudo-energy" (Brown et al. 2012). These equations can also fail to fully capture the dynamics of gravity waves in sub-adiabatically stratified atmospheres. Whilst this may present problems in anelastic models of radiative zones and other sub-adiabatic atmospheres, it should not be an issue for our models of fully-convective stars (with their adiabatic, polytropic, reference states - subsection 5.3.1).

2.3.3 Large-Eddy Formalism

The range of spatial scales within a star is vast (ranging from less than a centimetre in scale to almost gigameter size), and no simulation will be able to model all these simultaneously. In Rayleigh and ASH (as in many other codes) we choose to focus on, and thus resolve, the largest scales of flows and magnetic fields, which we expect to play a dominant role in the generation of the zonal flows, and overall energy balances. As such, our simulations fall within the large-eddy formalism, and we employ sub-grid-scale (SGS) descriptions of the unresolved turbulent motions. In Rayleigh and ASH, these SGS motions manifest simply as enhancements to the thermal diffusivity (κ), the kinematic viscosity (ν) and the magnetic diffusivity (η), which are thus effective eddy viscosities and diffusivities. As a result, our eddy diffusivities and viscosities are significantly enhanced compared to Solar values. For example, in the upper SCZ, the molecular viscosity is typically on the order of $\nu \simeq 1\text{cms}^{-1}$ (Miesch 2005b) whereas the simulations shown in chapter 5 have eddy viscosities on the order of $\nu = 10^{11}\text{cms}^{-1}$. Similarly, the thermal diffusivity in the upper SCZ is also much smaller ($\kappa \approx 10^5$ - Miesch (2005b)) than the values we consider in our simulations ($\kappa \approx 10^{12}$). Whilst these differences in physical verses eddy viscosities and diffusivities might be expected to lead to significant changes to the dynamics observed in our simulations, in subsection 5.5.1 we discuss how this may not be the case (with our simulations reaching a 'freefall' state in which the convective driving is diffusivity/viscosity independent).

This is one of the simplest approaches to SGS motions; we are assuming that the small scale motions are essentially unaffected by the larger, resolved motions. Furthermore, in Rayleigh and ASH, we typically hold these viscosities and diffusivities constant in space and time, thus assuming that the effects of unresolved motions are the same throughout the simulation domain. Whilst this parametrisation has become popular in recent studies (e.g. Featherstone and Miesch 2015; O'Mara et al. 2016), previous studies have also varied the eddy transport coefficients with depth (e.g. Browning et al. 2006; Browning 2008), suggesting that SGS motions may play a larger role near the surface. A description of more complex SGS treatments (as employed recently in, for example, Nelson et al. 2013) is beyond the scope of this work, but several such treatments are also implemented in ASH.

2.4 A Simple Model of 2D Convection

As part of our initial investigation into the internal operation of grid codes, and as a pedagogically useful example of the work that will be the focus of much of this thesis, we created a simple two dimensional convection code, following the process outlined in Glatzmaier (2013) (to which we refer readers for a full description of the numerical model). Specifically, we wrote a 2D code, in a mixture of different programming languages (more specifically we used both Fortran90 and Python2 programming languages, along the f2py interface to cross-couple a code containing source written in both languages - specifically fortran code for computationally expensive functions and a python wrapper as both an interface, and as a method of visualising the results), which was designed to solve a non-dimensional, Boussinesq, version of the MHD equations (Equation 2.25) in such a way as to model Rayleigh-Bénard convection. The equations being solved are as follows

$$\nabla \cdot \boldsymbol{v} = 0 \tag{2.25a}$$

$$\frac{\partial \boldsymbol{v}}{\partial t} = -(\boldsymbol{v} \cdot \nabla)\,\boldsymbol{v} - \nabla P + R_a P_r T \hat{\boldsymbol{z}} + P_r \nabla^2 \boldsymbol{v} \tag{2.25b}$$

$$\frac{\partial T}{\partial t} = -(\boldsymbol{v} \cdot \nabla)\,T + \nabla^2 T, \tag{2.25c}$$

where:

$$R_a = \frac{g_0 \alpha \Delta T L^3}{\nu \kappa}, \tag{2.26a}$$

$$P_r = \frac{\nu}{\kappa}. \tag{2.26b}$$

The code uses a mixture of spectral decomposition (for the horizontal direction) and finite difference (for the vertical).

For illustrative purposes we now present a brief sampling of the results acquired using this code, starting with a multi-celled Rayleigh-Bénard convection model, shown in Figure 2.1. That figure displays the steady state temperature map, and velocity streams for Rayleigh-Bénard convection in which only the first and eighth temperature modes have been initialised (initialising only the first mode results in a single celled structure, to recover the multi-celled structure shown in Figure 2.1, an additional even mode must by ini-

tilised (e.g. the 8th mode). Note that because this dual-cell structure is symmetric about the mid-point, any remaining odd modes become vanishingly small - Glatzmaier 2013.). This ultimately leads to a two cell structure with hot buoyant upflows near the horizontal boundaries, and a central, cold, heavy downflow. This impression is reinforced by the streamfunction (Ψ), which shows two circulation cells, one acting in a clockwise direction (positive ψ - solid lines) and one anticlockwise (negative ψ - dashed lines). These convection/circulation cells are also clearly present in the velocity profile, with rapid motions corresponding to the upflows and downflows. The resolution of both this simulation, and the simulation described below, was 50 spectral modes in the horizontal direction and 100 grid cells (for finite-difference calculations) in the vertical direction. The spectral modes were then analysed at 100 collocation points (essentially grid cells) to generate the final (100 by 100) figures.

Our second example focuses on the modification of physics within a simulation, specifically running a simulation with different physics in different spatial domains (a technique which will play a significant role in our simulations of the Heat-flux-driven Buoyancy Instability). Figure 2.2 also shows temperature and velocity profiles in a simulation in which Rayleigh-Bénard convection is allowed to operate in the lower half of the simulation domain, whilst only thermal diffusion is allowed to operate in the upper half. This is achieved by suppressing ψ and ω in the upper region – i.e. setting $\psi = I_n$, $\omega = 0$, where I_n is the identity matrix of degree n and omega is the vorticity. Once again, we see convective cells forming which alternate between clockwise and anticlockwise flow. Like the above case, we only initialised the first and eighth modes in the convective region, and yet here we find that four convective cells form compared to the two in the previous case. This can be linked to the change in the aspect ratio of the convectively unstable region affecting which modes are unstable, and thus changing the convective cell pattern which forms (i.e. for the $m = 1$ mode, the most unstable mode number (which defines the number of convective cells) is given by $n_{crit} = INT\left(\frac{a}{\sqrt{2}}\right)$). As for the purely diffusive region, we see a clean interface with the convective region, and that the effects of the convective region are rapidly diffused as we move towards the upper boundary.

However, despite the functionality of the above code, it is not suitable for our investigations into instabilities and interiors. While this is partially due to limitations in the physics

solved (ideal MHD), it is also related to performance. The code is single threaded (i.e. it only deals with one operation at a time); this is fine for a testbed but completely unsuitable for global-scale work. Thus we turn to more mature codes, which make use of parallelisation to distribute the workload over many threads (processors). In the codes considered below, the message passing interface (MPI) is used to split the domain into discrete sub-domains, with each thread dealing with its own sub-domain. This allows for a massive performance boost.

Overall, this simple, 'toybox', model of convection provided the author with a good basis to understand, and eventually modify, the more complex models used during the remainder of the work.

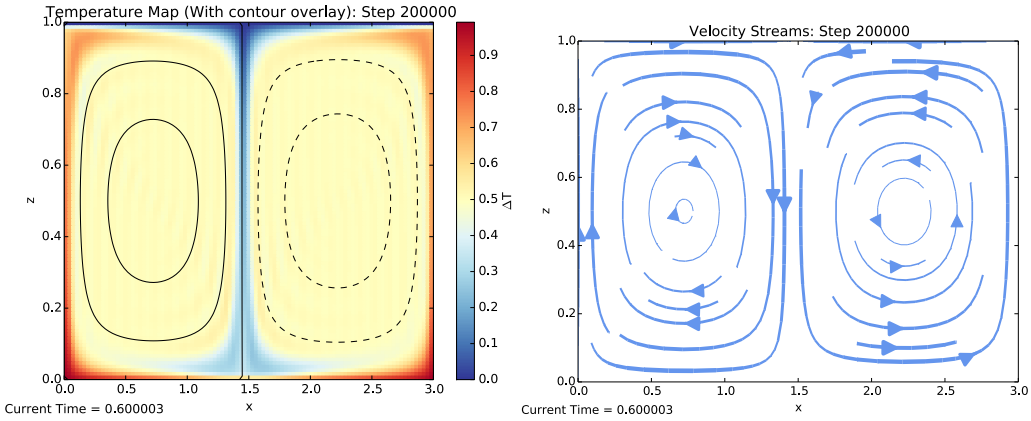

Figure 2.1: Steady state temperature map, with streamfunction contours, (left), and velocity streams (right) for a 'toybox' Rayleigh-Bénard convection model. In this simulation, the first and eighth temperature modes where initialised, and the initial non-dimensional parameters were $R_a = 10^6$ and $P_r = 0.5$. For the temperature profile, red corresponds to hot buoyant upflows whilst blue corresponds to cold heavy downflows. Solid contours of the streamfunction represent positive ψ (i.e., clockwise flow), whilst dashed contours represent negative ψ (i.e., anticlockwise flow).

2.5 Compressible, Finite-Difference, MHD with Athena

In order to model the heat-flux-driven buoyancy instability (HBI - see chapter 3 for more details and results), we use ATHENA, a grid-based, finite-difference, MHD code which has a large array of functionality, ranging from compressible 1D hydrodynamics to 3D relativistic MHD with self gravity.

In our configuration, ATHENA solves the equations of Ideal MHD (Equation 2.16), with

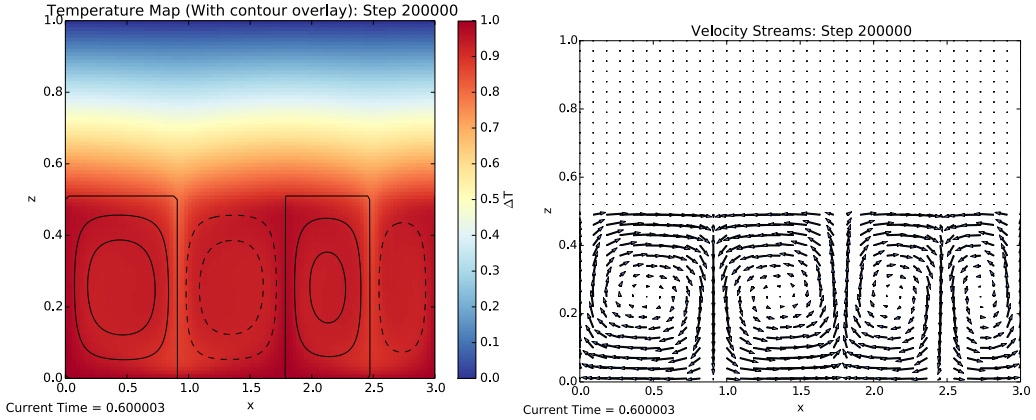

Figure 2.2: Steady state temperature map, with streamfunction contours, (left), and velocity streams (right) for a modified, and restricted, Rayleigh-Bénard convection model. In this simulation, convection has been purposefully limited to the lower half of the simulation domain, with the upper half of the domain dominated by thermal diffusion. In the convective region, as in Figure 2.1, we find that strong circulations form, alternating between clockwise and anticlockwise convective cells. As for the thermal diffusion region, we find that variations inherited from the convective region are rapidly diffused as we move towards the top boundary.

the addition of mixed mode thermal conduction:

$$\boldsymbol{Q} = -\chi_0 \boldsymbol{\nabla} T - \chi_{||} \hat{\boldsymbol{b}} (\hat{\boldsymbol{b}} \cdot \boldsymbol{\nabla}) T, \tag{2.27}$$

in which χ_0 is the isotropic thermal conductivity, and $\chi_{||}$ is the anisotropic thermal conductivity. But what exactly is the difference between these types of conductivity? Essentially, Isotropic thermal conduction is directionally independent, it only 'cares' about the temperature gradient (as can be seen in Equation 2.27). On the other hand, Anisotropic thermal conduction is directional, not only must a temperature gradient exist, there must also be a mechanism driving conduction in that direction. Here we consider anisotropic thermal conduction by electrons: In a low collisionality plasma threaded by a magnetic field strong enough that the mean free path of an electron is much longer than the electrons gyroradius (as seen in Figure 2.3), electron motion will be primarily along magnetic field lines - i.e. directional (anisotropic) transport of heat. This can be seen in the second term in Equation 2.27, which reveals that the level of anisotropic thermal conduction depends upon the alignment (dot product) of the temperature gradient and the magnetic field.

Additionally we make good use of ATHENA's parallelisation routines, in which it decomposes the problem into multiple MPI processes, each of which deals with a small

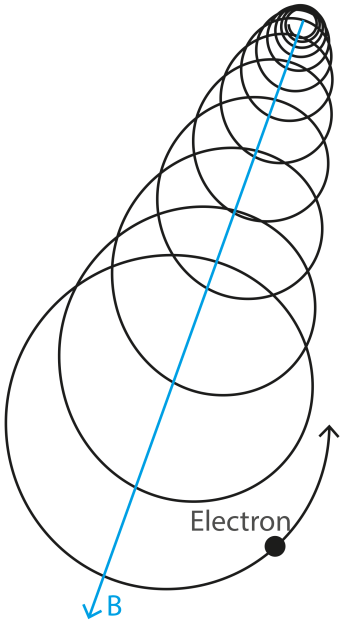

Figure 2.3: The motion of an electron in a low collisionality plasma subject to a magnetic field strong enough that the electron mean free path is much greater than the electron gyroradius. In such a scenario, the electrons motion will be directed along magnetic field lines, leading to directional thermal conduction (by said electrons). This is anisotropic thermal conduction, and it is essential for the operation of the Heat-Flux-Driven Buoyancy Instability.

subsection of the grid, with narrow ghost zones representing both the current status of neighbouring subsections, and the only regions which have to travel between processes (thus significantly reducing MPI overhead).

A full description of the internal operations of ATHENA is beyond the scope of this work. Instead, we direct interested readers to ATHENA's method paper, Stone et al. (2008), and here note only a series of modifications we made to ATHENA for the simulations described in chapter 3. Specifically we made, and describe here, modifications to the thermal conduction subroutine; we also describe the inclusion of a new output format, and the addition of new, vertical, boundary conditions.

Starting with the thermal conduction subroutine, we modify it such that the simulation domain is split into three distinct regions. The top and bottom regions are restricted to purely isotropic conduction (buffer regions), whilst the central region is allowed to contain a mix of both isotropic and anisotropic thermal conduction. The presence of anisotropic conductivity is essential for the instabilities described in chapter 3. The exact location of the split, as well as the levels of isotropic and anisotropic conduction in each region, are user defined. By default, the buffers act as a purely isotropic region surrounding a purely anisotropic HBI region, allowing the instability to develop and grow without being affected by the top and bottom boundary conditions. The modifications to the code were wrapped within c-preprocessor statements, such that ATHENA could be built with either

default conduction or our modified conduction, based upon compile time flags.

We now move onto ATHENA's data output format. By default, ATHENA can output a full grid of variables (more specifically the primitive variables and the energies) in only three formats, an ASCII table, a raw binary dump, or in the legacy VTK format. Initially we made use of the tabular output, however this was quickly found to be both slow and storage space intensive. As such, we decided to create a new output for ATHENA, in the style of the tabular output, but stored in a structured, and portable, binary file. This was achieved via netCDF, a portable, binary, file format, as well as the addition of a new output generator to our ATHENA problem file. This led to a significant speed-up in our analysis, as well as a non-trivial reduction in the storage space required by each simulation.

Finally we come to the boundary conditions. None of the default boundary conditions included with ATHENA are suitable for use as either the top or bottom boundary of our HBI simulations. As such we define custom top and bottom boundaries, based upon those used by Avara et al. (2013). These boundaries are momentum reflective, in order to conserve mass, have the magnetic field vector set identically to that of the last active cell in each column, thus conserving the total vertical magnetic flux (i.e. ensuring that no convergence or divergence of magnetic flux occurs at the boundaries), and have their temperature held constant at their initial value throughout the simulation. Additionally, in order to preserve hydrostatic equilibrium, we recalculate the density using an exponential extrapolation from the start of each boundary region.

2.6 Anelastic, Pseudo-Spectral, Models of Global Stellar Interiors

2.6.1 Rayleigh and ASH

In this section, we wrap up some loose threads left by the above discussion and introduce some details regarding the operation of the 'production' codes, *Rayleigh* and ASH, used to compute anelastic global-scale models of stellar convection in chapter 5. Both codes have been used extensively for prior numerical investigations into stellar convection, and are described extensively elsewhere (e.g., Clune et al. 1999; Browning et al. 2004; Featherstone and Hindman 2015). Here, we mention only a few salient points that are important for understanding the operation of these codes, and which are not covered by our discussion above. In subsubsection 2.6.1.1 we give a brief overview of the parallelisation of Rayleigh and its transforms between physical and spectral space. Following this, in subsubsection 2.6.1.2 and subsubsection 2.6.1.3 we discuss the implementation of internal heating in Rayleigh and ASH respectively, finishing in subsubsection 2.6.1.4 with a discussion of points salient to both profiles.

2.6.1.1 Parallelisation in Rayleigh

Rayleigh was designed from the ground up to be both efficient in its use of inter-process communication, and massively parallelisable ($> 10^5$ cores). We now discuss a few of the techniques Rayleigh uses to parallelise and optimize the distribution and calculation of the anelastic MHD problem, including the transition between physical, hybrid, and spectral space.

Rayleigh distributes work by assigning each rank (a group of processes working on the same set of m-modes) a set of m-modes for which the calculation should be performed; due to the triangular truncation, each m-value has a different number of l-modes, thus requires a different amount of computation time to complete. At initialisation, Rayleigh tries to balance this load, assigning m-modes in such a way that each rank has an approximately equal number of l-modes (effectively limiting the number of ranks to $N_{max} = \frac{l_{max}+1}{2}$).

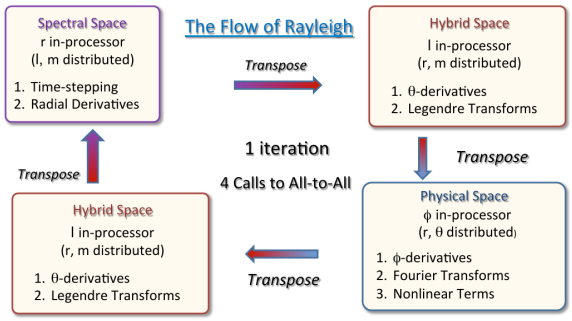

Figure 2.4: Distribution of work between spectral, hybrid and physical space in Rayleigh, including calculations and transforms performed at each stage. Figure courtesy of our collaborator, Nick Featherstone.

Within each rank the l-modes are then evenly distributed to individual processes. Once the simulation is running, Rayleigh then times each process, and redistributes work accordingly such that each process, and rank, finishes at approximately the same time. This distribution of work also occurs in hybrid and physical space, with combinations of either m-modes and r-values, or θ-values and r-values being distributed.

Each of these processes is not an island: due to the global nature of the spectral method, they need to know what is happening in the rest of the simulation domain. Rayleigh solves this problem by requiring that each process creates a single buffer containing all the fields of data and then transposes this buffer (a key step in the spectral↔physical conversion). An MPI All-to-All call is then used, sending this buffer to every other process (and hence receiving buffers from every other process). Figure 2.4 shows how Rayleigh moves through physical, hybrid, and spectral space, with each transition requiring an All-to-All MPI call. Thus, for each timestep Rayleigh uses four All-to-All calls, a significantly smaller number than predecessor codes (e.g. ASH requires 8 All-to-All calls each timestep). As a final note, during the operation outlined above, and in Figure 2.4 a number of transposes and transforms were used. In order to maximise the efficiency of these transforms, Rayleigh has been written to take advantage of compiler optimised mathematical operations (and hence specialised CPU data paths), either through the Math-Kernal-Library (MKL - Intel Compilers), or the Engineering and Scientific Subroutine Library (ESSL - IBM), for an order of magnitude performance increase compared to free and open source compilers.

2.6.1.2 Internal Heating in Rayleigh

In Rayleigh, Q (see Equation 2.18b) represents an internal deposition of energy, which drops to zero at the upper boundary, and is designed to ensure that one luminosity of heat flux flows through the upper boundary. The functional form of Q depends only upon the background pressure profile such that

$$Q\left(r,\theta,\phi\right) = \alpha\left(\bar{P}\left(r\right) - \bar{P}\left(r_o\right)\right). \tag{2.28}$$

in which the normalisation constant α is chosen such that

$$L_\star = 4\pi\int_{r_i}^{r_o} Q\left(r\right) r^2 dr, \tag{2.29}$$

with $L_\star$ as the stellar luminosity. This is then used to set the thermal energy flux $F\left(r\right)$ that convection and conduction must transport across a spherical surface of radius r:

$$F\left(r\right) = \frac{1}{r^2}\int_{r_i}^{r_o} Q\left(x\right) x^2 dx. \tag{2.30}$$

This functional form of Q means that the internal heating profile is highly dependent upon the number of density scale heights $\left(N_\rho\right)$ simulated, with the heating becoming increasingly focused near the lower boundary condition as N_ρ increases.

2.6.1.3 Internal Heating in ASH

In ASH, Q (see Equation 2.18b) can be split into two components, a temperature dependent radiative heating term

$$Q_{\text{rad}} = \nabla\cdot\left[\kappa_r\bar{\rho}c_p\nabla\left(\bar{T}+T\right)\right]. \tag{2.31}$$

where κ_r is typically taken from a 1D stellar model, and a volume heating term, which represents energy generation by nuclear burning within the convective core and also scales with temperature

$$Q_{\text{vol}} = \bar{\rho}\epsilon\left(\rho,T\right). \tag{2.32}$$

2.6.1.4 Internal Heating in Rayleigh and ASH: Key Notes

- Since the timescales spanned by any practical MHD simulation are tiny compared to the Kelvin-Helmholtz timescale of the star, the heating profile in both codes is essentially fixed in time.

- Whilst the exact functional forms of the heating profiles are interesting, and must be considered when setting up a model using the associated code, they are just different, built in, approaches to modelling a realistic stellar heating profile. Further to this, when considering more complicated atmospheres, both codes/approaches allow for the use of an, arbitrary, user defined heating profile.

- For a more detailed discussion the internal heating profile in Rayleigh, including a comparison with models of the Solar heating profile, see section 3 in Featherstone and Hindman (2015).

- As for the heating function in ASH, this is similar to the profiles used in 1D stellar models (i.e. Chabrier 2003). For more details, see the ASH reference papers (i.e. Clune et al. 1999; Miesch et al. 2000; Miesch 2005a).

Chapter 3

The Heat-Flux-Driven Buoyancy Instability - Theory, Applicability and Models

"You know what they say, General. If at first you don't succeed, try, try, try, try, try again."

— Col. O'Neill, Stargate SG1

Declaration: This work was conducted in collaboration with Matthew Browning. In this chapter we apply techniques from prior studies into the HBI (specifically prior perturbation analyses of the instability) to new environs, specifically the atmospheres of stellar and planetary objects, exploring a series of magnetic field strength and perturbation wavelength limitations that these environs must satisfy for the possibility of HBI growth to exist. We also explore the instability numerically, extending the local scale simulations of Avara et al. (2013) though a combination of new physics (i.e. slowed thermal conduction, radiative loss) and shifting length scales (i.e. both local and global scale calculations).

3.1 Introduction

An atmosphere is subject to the classic convective instability if its entropy gradient decreases outwardly (Schwarzschild 1906). However, for a low-collisionality plasma threaded by a weak magnetic field, MHD instabilities exist that can change this requirement so that stability is now dependent upon the temperature gradient and the properties of an ambient magnetic field. In particular, the presence of anisotropic thermal conduction along magnetic field lines can induce unusual behaviour. This effect was first demonstrated by the MagnetoThermal Instability (MTI – Balbus (2000)), which can occur when the temperature profile is outwardly decreasing ($\boldsymbol{g}\cdot\nabla T > 0$) and a horizontal magnetic field component is present; another is the Heat-Flux-Driven Buoyancy Instability (HBI – Quataert (2008)), which can occur when the temperature profile is outwardly increasing ($\boldsymbol{g}\cdot\nabla T < 0$) and a vertical magnetic field component is present (with an associated background heat flux). Previous investigations of the HBI have focused upon its application to the intra-cluster medium (ICM) of galaxy clusters (e.g. Avara et al. (2013), Balbus and Reynolds (2010), Kunz et al. (2012), Parrish and Quataert (2007), and Parrish et al. (2012)), since these regions possess the temperature and magnetic field profile required for the HBI to operate and grow.

However there exist other regions that also possess temperature profiles that upon first inspection appear to be vulnerable to the HBI. Examples of these regions include the transition region and corona of stars, like the Sun, or the outer atmospheres of highly irradiated exoplanets. In both cases heat transport is generally thought to be mediated partly by conduction along magnetic field lines. To date, the HBI has not been investigated in these regions – partly because their relatively strong magnetic fields lead to plasma betas that are lower than early studies considered to be viable for the HBI (Kunz et al. 2012). However, recent work (Avara et al. 2013) has shown that the HBI may operate at lower plasma betas, though its non-linear evolution in these cases differs somewhat from what was observed in the original weak field cases (Parrish and Quataert 2007).

If the HBI were to operate in the solar transition region, this could have profound implications for the thermal structure of the Sun's upper atmosphere. One of the enduring mysteries of solar physics is why the solar corona is millions of Kelvin hotter than the solar

surface. The mechanisms by which the corona is heated remain a topic of much debate (e.g. Aschwanden et al. 2007), but its temperature also depends upon the rate at which heat is transported down through the transition region. This transport is thought to be primarily by thermal conduction (Aschwanden 2005) (Note: This conduction is referred to as Thermal Conduction in the solar community (see, for example, Aschwanden 2005), in other communities (such as the accretion disk community), it is often explicitly stated to be Coulomb Conduction, that is conduction by electrons). One of the non-linear effects of the HBI highlighted by previous studies, e.g. Avara et al. (2013), is its tendency to greatly reduce the rate of vertical heat conduction, essentially by reorientation of the magnetic field lines. If this were to occur in the solar transition region, it could alleviate conductive heat loses from the corona, and so help explain why this region is so hot. Similar considerations may apply in the outer atmospheres of highly irradiated exoplanets, where, again, conductive heat losses form an important part of the energy balance. Motivated by these considerations, this chapter investigates in detail whether the HBI, or related instabilities, may operate in portions of the atmospheres of stars or planets. In order to investigate the viability of the HBI within these regions, we make use of atmospheric models (P-T profiles) to examine whether regions of the atmosphere are suitable for sustainable HBI growth. We also study aspects of these instabilities via non-linear simulations. In particular, we have constructed two dimensional simulations of the HBI using ATHENA (a grid-based MHD code), which includes the key physics and geometry required to understand the effects that the HBI may have in these environments, on both local and global scales.

In section 3.2 we describe the HBI and the MTI in somewhat more detail. In section 3.3, we calculate growth rates for the HBI in scenarios both containing (subsection 3.3.2) and lacking (subsection 3.3.1) radiative loss. Next, in section 3.4 we use these calculations to explore the conditions that an atmosphere's pressure-temperature profile and magnetic field intensity must satisfy, both including and excluding radiative loss, in order for the HBI to develop and grow. Then in section 3.5 we apply these limits to example Solar and planetary atmospheres, in order the assess the viability of the HBI in these environs. We then use what we learn from these limits to shape a series of 2.5D HBI simulations (whose setup is detailed in section 3.6), investigating the effect on both local (section 3.7)

and global (section 3.8) scales, and with different physics (such as radiative loss). Finally, in section 3.9, we summarise our work and comment briefly on its implications for the structure of stellar and planetary atmospheres.

3.2 Buoyancy Instabilities

Ordinarily, when considering the convective stability of an atmosphere, the requirement for an instability to form is an upwardly decreasing entropy gradient (the Schwarzschild stability criterion (Schwarzschild 1906)). However, an interesting change occurs if we consider a thermally stratified, low-collisionality, plasma in the presence of a weak magnetic field, whose primary effect is to channel heat along its field lines (i.e. to enforce anisotropic heat transport) (Balbus 2000). More specifically, we consider a low-collisionality plasma in which:

1. The collisional mean free path of electrons is much larger than both the electron and ion Larmor (cyclotron) radius. (Balbus 2000)

2. The dominant mode of energy transport, for any perturbations, is thermal conduction that, thanks to the first requirement, is primarily anisotropic.

In this case, it is now a combination of the temperature gradient and the magnetic field orientation that characterises if an atmosphere is convectively unstable, and how this instability will grow. Under these conditions, two instabilities are known to form; the MagnetoThermal Instability (MTI) and the Heat-flux-driven Buoyancy Instability (HBI).

3.2.1 The MagnetoThermal Instability

For the MTI, an atmosphere can be unstable if the temperature *increases* in the direction of gravity, and a *horizontal* magnetic field component is present, along which thermal conduction is channelled (i.e. anisotropic thermal conduction) – (Balbus 2000). Under these conditions the operation of the instability can be illustrated by considering a pair of fluid parcels, one upwardly displaced and one downwardly. As the parcels separate, they draw

the magnetic field lines with them, causing the field to become partially aligned with the background temperature gradient – thus thermally connecting the parcels. Heat flux now flows between the parcels; because the upwardly displaced parcel is magnetically and thermally connected to lower, and hotter, regions of the atmosphere than its surroundings, it will tend to be hotter and less dense than those surroundings. It will, therefore, experience a buoyancy force and continue to rise. This, in turn, will further realign the field, and so further increase the heat flux, leading to a runaway buoyancy instability. Figure 3.1 shows a series of snapshots of the magnetic field lines, and temperature profile, for a simulation of plasma subject to the MTI, and is provided as a visual aid for how the instability operates.

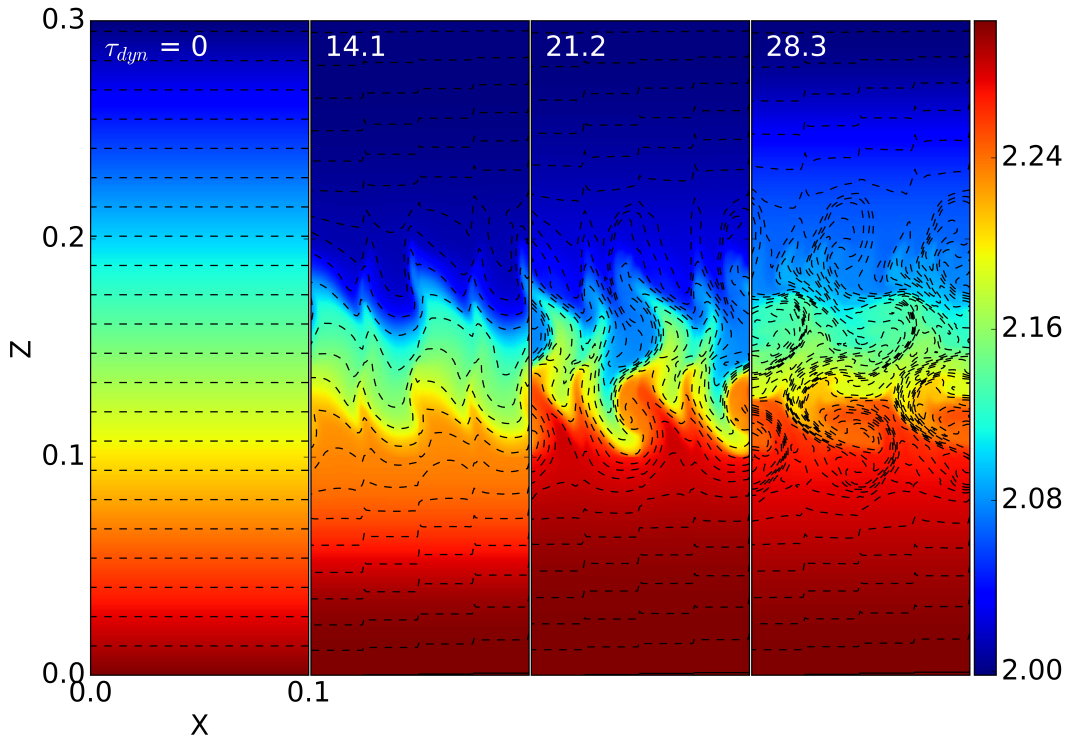

Figure 3.1: Snapshots of the temperature profile and magnetic field lines in a MTI simulation. Note how it reorientates a primarily horizontal field to the vertical via buoyant motions. Based upon a 2D simulation of the MTI using ATHENA.

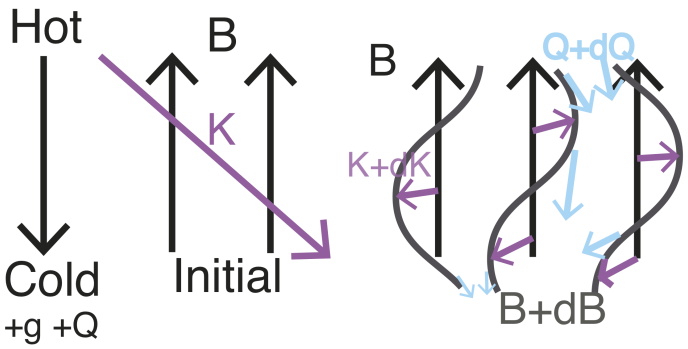

Figure 3.2: An x-z plane schematic of the Heat-Flux-Driven Buoyancy Instability. The plasma initially contains a vertical magnetic field with a matching vertical background heat flux ($dT/dz > 0$). A perturbation then modifies the field as shown on the far right diagram. The heat flux, which is forced to follow the perturbed magnetic field lines, converges and diverges, thus leading to local heating and cooling of the plasma. This then causes a downwardly displaced fluid parcel to lose energy, resulting in it sinking further into the atmosphere (and vice-versa for an upwardly displaced parcel).

3.2.2 The Heat-Flux-Driven Buoyancy Instability

For the HBI, an atmosphere can be unstable if the temperature *decreases* in the direction of gravity and a background heat flux is present. It requires the presence of a *vertical* magnetic field along which the background heat flux is channelled (Quataert 2008). When this criterion is satisfied, the presence of magnetic field line perturbations with non-vanishing perpendicular and parallel wave vectors can lead to the formation of regions of heat flux convergence or divergence, corresponding to local plasma heating or cooling. As a direct result of this, when a fluid parcel is displaced downwardly, it is conductively cooled via the background heat flux, thus causing it to lose energy and so to sink further in the atmosphere. Similarly, an upwardly displaced fluid parcel gains energy from the background heat flux, and so buoyantly rises. This is illustrated schematically in Figure 3.2.

3.3 Analytic Description of the HBI

In this section (section 3.3) we provide the reader with relevant background to aid in their understanding of the HBI, and to elucidate the source of the growth rate calculations provided below. Note that whilst the derivations presented in this section are not original, the formalism considered here represents a combination of multiple studies.

3.3.1 HBI Without Radiative Cooling

Following the method of Quataert (2008) with modifications based upon the analysis of Balbus and Reynolds (2010), we present an analysis of the HBI using the standard equations of MHD, but with a term added to the entropy equation to represent anisotropic thermal conduction along magnetic field lines. We show this analysis here because both the assumptions made during the analysis, and the resulting growth rates, play an important role in the work we perform below. The mass, momentum, magnetic flux, and entropy equations are then

$$\frac{\partial \rho}{\partial t} + \nabla \cdot (\rho \boldsymbol{v}) = 0 \tag{3.1a}$$

$$\rho \frac{D\boldsymbol{v}}{Dt} = \frac{(\nabla \times \boldsymbol{B}) \times \boldsymbol{B}}{4\pi} - \nabla P + \rho \boldsymbol{g} \tag{3.1b}$$

$$\frac{\partial \boldsymbol{B}}{\partial t} = \nabla \times (\boldsymbol{v} \times \boldsymbol{B}) \tag{3.1c}$$

$$\rho T \frac{\partial s}{\partial t} = \frac{P}{\gamma - 1} \frac{D \ln P \rho^{-\gamma}}{Dt} = -\nabla \cdot \boldsymbol{Q} = \nabla \cdot [\chi \hat{\boldsymbol{b}} (\hat{\boldsymbol{b}} \cdot \nabla) T], \tag{3.1d}$$

where ρ is the mass density, $\boldsymbol{v}$ is the plasma velocity, $\boldsymbol{B} = B_x \hat{\boldsymbol{x}} + B_z \hat{\boldsymbol{z}}$ is the magnetic field, $\boldsymbol{g} = -g\hat{\boldsymbol{z}}$ is a uniform, vertical, gravitational acceleration, P is the pressure, T is the temperature, $\hat{\boldsymbol{b}} = \boldsymbol{B}/B$ is the magnetic field unit vector, $D/Dt = \partial/\partial t + \boldsymbol{v} \cdot \nabla$ is the Lagrangian derivative, and χ is the thermal conductivity due to electrons. Additionally, we also define a diffusion coefficient $\kappa = \chi T/P$, dimensionless magnetic field strength components $b_x = B_x/B$ and $b_z = B_z/B$, and the wavevector perpendicular to the local gravitational field $k_\perp^2 = k_x^2 + k_y^2$.

Next we need to consider the properties of the background plasma. Firstly, since the instability requires the magnetic field to be very weak, force balancing implies that the atmosphere is initially in hydrostatic equilibrium $\frac{dP}{dz} = -\rho g$, and, secondly, because $\hat{\boldsymbol{b}} \cdot \nabla \boldsymbol{T} \neq 0$, there is a background heat flux given by

$$\boldsymbol{Q} = -\chi (b_x b_z \hat{\boldsymbol{x}} + b_z^2 \hat{\boldsymbol{z}}) \frac{dT}{dz}, \tag{3.2}$$

so that in order for the initial equilibrium to be a steady state ($\nabla \cdot \boldsymbol{Q} = 0$), the temperature must vary linearly with height.

Next we carry out a Wentzel-Kramers-Brillouin (WKB) perturbation analysis on the background plasma state. To do this, all the dynamical variables are assumed to vary as $\exp(-i\omega t + i\boldsymbol{k}\cdot\boldsymbol{x})$ and the WKB approximation requires $kH \gg 1$ (Balbus 2001), where H is the scale height of the system. Working in the Boussinesq Approximation (Boussinesq 1903), the linearly perturbed versions of the MHD Equations (3.1) become

$$\boldsymbol{k}\cdot\delta\boldsymbol{v} = 0 \tag{3.3a}$$

$$-i\omega\delta\boldsymbol{v} = \frac{\delta\rho}{\rho^2}\boldsymbol{\nabla}P - i\boldsymbol{k}\frac{\delta P}{\rho} + \frac{i(\boldsymbol{B}\cdot\boldsymbol{k})\delta\boldsymbol{B}}{4\pi\rho} - \frac{i\boldsymbol{k}(\boldsymbol{B}\cdot\delta\boldsymbol{B})}{4\pi\rho} \tag{3.3b}$$

$$\omega\delta\boldsymbol{B} = -(\boldsymbol{B}\cdot\boldsymbol{k})\delta\boldsymbol{v} \tag{3.3c}$$

$$\frac{\gamma}{\gamma-1}i\omega P\frac{\delta\rho}{\rho} + \rho T(\delta\boldsymbol{v}\cdot\boldsymbol{\nabla}s) = -i\boldsymbol{k}\cdot\delta\boldsymbol{Q}, \tag{3.3d}$$

with a perturbed heat flux

$$\delta\boldsymbol{Q} = -\chi\delta\hat{\boldsymbol{b}}(\hat{\boldsymbol{b}}\cdot\boldsymbol{\nabla}T) - \chi\hat{\boldsymbol{b}}(\delta\hat{\boldsymbol{b}}\cdot\boldsymbol{\nabla}T) - i\chi\hat{\boldsymbol{b}}(\hat{\boldsymbol{b}}\cdot\boldsymbol{k})\delta T, \tag{3.4}$$

where $\delta\hat{\boldsymbol{b}} = \delta(\boldsymbol{B}/B) = \delta\boldsymbol{B}/B - \hat{\boldsymbol{b}}(\delta B/B)$.

After extensive algebraic manipulation, Equations 3.3 can be combined to yield the following dispersion relation

$$0 = \omega\tilde{\omega}^2 + i\omega_{\rm cond}\tilde{\omega}^2 - N^2\omega\frac{k_\perp^2}{k^2} - i\omega_{\rm cond}g\left(\frac{d\ln T}{dz}\right)\frac{\mathcal{K}}{k^2}, \tag{3.5}$$

with

$$N^2 = \frac{-g}{\gamma}\frac{\ln P\rho^{-\gamma}}{dz} = g\left[\frac{1}{\gamma}\frac{d\ln P}{dz} - \frac{d\ln\rho}{dz}\right] \tag{3.6a}$$

$$\mathcal{K} = (1-2b_z^2)k_\perp^2 + 2b_xb_zk_xk_z \tag{3.6b}$$

$$\tilde{\omega}^2 = \omega^2 - (\boldsymbol{k}\cdot\boldsymbol{v}_{\rm A})^2 \tag{3.6c}$$

$$\omega_{\rm cond} = \frac{\gamma-1}{\gamma}\kappa(\hat{\boldsymbol{b}}\cdot\boldsymbol{k})^2, \tag{3.6d}$$

where N is the Brunt-Väisälä frequency, $v_{\rm A} = B/\sqrt{4\pi\rho}$ is the Alfvén speed, $\omega_a = \boldsymbol{k}\cdot\boldsymbol{v}_{\rm A}$ is the Alfvén frequency and $\omega_{\rm cond}$ is the characteristic conduction frequency.

Finally we can form an expression for the growth rate of the instability by considering

the dispersion relation under the assumption that the characteristic frequencies can be ordered such that $\omega_{\rm cond} \gg \omega_{\rm dyn} \sim \sqrt{g/H} \gg \omega_{\rm a}$, which can be achieved for a sufficiently weak magnetic field operating on sufficiently small scales (these conditions are expanded upon in section 3.4). The dispersion relation thus reduces to

$$\omega^2 \simeq g \frac{d \ln T}{dz} \frac{\mathcal{K}}{k^2}. \tag{3.7}$$

In the presence of a purely vertical magnetic field ($b_z = 1, b_x = 0$) and a background heat flux (3.2) (without a background heat flux, $dT/dz > 0$ is stable, as shown by Balbus (2001)), the dispersion relation further reduces to

$$\omega^2 \simeq -g \frac{d \ln T}{dz} \frac{k_\perp^2}{k^2}. \tag{3.8}$$

This is unstable if $\omega^2 < 0$, occurring when $dT/dz > 0$ (i.e. an outwardly increasing temperature profile), and is maximised for perturbations which are perpendicular to the background magnetic field.

3.3.2 HBI with Radiative Cooling

We next present an analysis of the HBI with the effects of radiative loss included. This analysis is a reproduction of the work of Balbus and Reynolds (2010), and is included here to aid the readers understanding (and to provide some key results which will form part of our own analysis). This approach to the analysis of the HBI differs from the work of Quataert (2008) in a number of ways:

1 The addition of a radiative energy loss per unit volume term $\left(\rho\mathcal{L}\right)$ into the MHD entropy equation (Equation 3.1d) such that it becomes,

$$\frac{P}{\gamma - 1} \frac{D \ln P\rho^{-\gamma}}{Dt} = -\left[\boldsymbol{\nabla} \cdot \boldsymbol{Q} + \rho\mathcal{L}\right]. \tag{3.9}$$

2 The growth rate is redefined as $\sigma = i\omega$.

3 The initial equilibrium heat flux no longer satisfies $\nabla \cdot Q = 0$, instead there is a thermal

balance between conductive heating and radiative losses,

$$-\nabla \cdot Q \equiv \frac{d^2\left(b_z^2 \chi\right) T}{dz^2} = \rho \mathcal{L} \tag{3.10}$$

Using this new MHD equation, and by once again performing a WKB analysis, the dispersion relation now becomes

$$\sigma^3 + a_1\sigma^2 + a_2\sigma + a_3 = 0, \tag{3.11}$$

where

$$a_1 = \left(\frac{\gamma - 1}{\gamma}\right) T \left[\frac{1}{P}\frac{\partial\left(\rho\mathcal{L}\right)}{\partial T}\right]_P + C \tag{3.12a}$$

$$a_2 = \frac{k_\perp^2}{k^2}N^2 + \omega_a^2 \tag{3.12b}$$

$$a_3 = C\mathcal{K}\frac{g}{k^2}\frac{d\ln T}{dz} + \omega_a^2 a_1 \tag{3.12c}$$

$$C = \left(\frac{\gamma - 1}{\gamma}\right)\kappa\left(\boldsymbol{k}\cdot\boldsymbol{b}\right)^2. \tag{3.12d}$$

There are stable solutions to this dispersion relationship if $a_1 a_2 > a_3 > 0$ and $a_1 > 0$.
If we consider the stability condition, $a_3 > 0$, we essentially recover the stability criterion from Quataert (2008) (see subsection 3.3.1):

$$C\mathcal{K}\frac{g}{k^2}\frac{d\ln T}{dz} + \left(\boldsymbol{k}\cdot\boldsymbol{v_A}\right)a_1 > 0. \tag{3.13}$$

If we now consider the condition $a_1 a_2 > a_3 > 0$, two different growth rates are possible, depending upon the values of a_1, a_2 and a_3:

- If a_2 is large and positive (i.e. if either N^2 or ω_a^2 are dominant), the unstable roots to the dispersion relation are approximately

$$\sigma = \pm i\sqrt{a_2} + \frac{a_3 - a_1 a_2}{2a_2}. \tag{3.14}$$

- If a_1 and a_3 are both the same sign and the dominant terms, then the unstable roots

to the dispersion relation are approximately

$$\sigma = \pm i \sqrt{\frac{a_3}{a_1}} + \frac{a_3 - a_1 a_2}{2a_1^2}. \tag{3.15}$$

In both of these cases, it is the combination of $a_3 - a_1 a_2 < 0$ that determines the stability of the modes:

$$a_1 \frac{k_\perp^2}{k^2} N^2 - C\mathcal{K} \frac{g}{k^2} \frac{d \ln T}{dz} > 0. \tag{3.16}$$

These equations can then be used, in combination with both a cooling function $\mathcal{L}$ and an appropriate pressure-temperature profile, to calculate both the scenarios under-which the radiative HBI can operate, and then the growth rate when those conditions are met.

3.4 Limits for HBI growth

On their own, the presence of an outwardly increasing temperature profile and a vertical magnetic field profile are not sufficient to ensure that the HBI is applicable. There are a number of other conditions that may limit the temperatures, pressures and magnetic field intensities at which the HBI is able to operate. In this section, we present our investigation/analysis into these limits.

Note that, in principle, the stability boundaries of the dispersion relations could be solved for (and in Appendix E we explore this possibility and compare the results to the analysis below). However, here we take a more heuristic approach, considering a simpler set of limits that allows for a broader understanding of HBI applicability.

3.4.1 Magnetic Field Limits

First, we consider limits on the magnetic field range for which the HBI is likely to operate. As detailed at the start of subsection 3.2.2, the HBI requires the electron mean free path

to be much greater than the electron gyroradius.

To start, the mean free path for electrons is given by

$$\lambda_{\mathrm{MFP}} = \frac{1}{n\sigma}, \tag{3.17}$$

in which σ is the electron collision cross-section

$$\sigma = \pi b_0^2 = \frac{\pi q_e^4}{4\pi^2 \epsilon_0^2 m_e^2 v_e^4}, \tag{3.18}$$

where q_e is the electron charge, ϵ_0 is the permittivity of free space, m_e is the mass of an electron, and v_e is the velocity of an electron.

Then, the electron gyroradius is given by

$$r_g = \frac{m_e v_\perp}{|q_e| B}, \tag{3.19}$$

where B is the magnetic field strength, and $v_\perp$ is the electron velocity perpendicular to the magnetic field.

Thus for an ideal gas ($P = nk_BT$), and assuming that the electron motion is purely thermal (in 3D (for the MFP): $\frac{1}{2}mv_e^2 = \frac{3}{2}k_BT$ and in 1D (for the gyroradius): $\frac{1}{2}mv_\perp^2 = \frac{1}{2}k_BT$) , this condition reduces to

$$\lambda_{\mathrm{MFP}} > r_g \tag{3.20a}$$

$$\Downarrow$$

$$\frac{4\pi^2 \epsilon_0^2 m_e^2 v_e^4}{n\pi q_e^4} > \frac{m_e v_\perp}{q_e B} \tag{3.20b}$$

$$\Downarrow$$

$$B > \frac{\sqrt{m_e} q_e^3}{36\pi\epsilon_0^2} \frac{n^{5/2}}{P^{3/2}} \tag{3.20c}$$

$$\Downarrow$$

$$B > \left(4.41 \times 10^{-52}\right) \frac{n^{5/2}}{P^{3/2}}, \tag{3.20d}$$

where n is the electron number density and B is the magnetic field strength in Tesla. This is a lower limit on the magnetic field strength required to ensure sustainable HBI growth.

(Note, in this subsection (subsection 3.4.1), and more specifically in Equation 3.20d (and its associated calculations), we employ SI units in order to simplify the presentation of our results; in the remainder of this thesis, all dimensional quantities are in CGS units.)

Defining an upper limit on the magnetic field strength for the HBI is more complicated, mainly due to the number of different ways that a strong magnetic field can suppress the HBI. For now, we focus on two plausible upper limits.

A firm upper limit on the magnetic field strength comes from the requirement that the magnetic pressure is less than the gas pressure, which is equivalent to requiring that the plasma beta $\left(\beta = \frac{P}{P_{\text{mag}}}\right)$ must be greater than one. Thus

$$P_{\text{mag}} = \frac{B^2}{2\mu_0} < P \tag{3.21a}$$

$$B < \sqrt{2\mu_0}\sqrt{P}. \tag{3.21b}$$

This limit can then be combined with the MFP requirement to give a magnetic field restriction that must always be met for the HBI to operate and grow:

$$\frac{\sqrt{m_e}q_e^3}{36\pi\epsilon_0^2}\frac{n^{5/2}}{P^{3/2}} < B < \sqrt{2\mu_0}\sqrt{P}. \tag{3.22}$$

A second, more restrictive, upper limit on the magnetic field strength can be formulated by requiring that the effects of magnetic tension be negligible. Note that this limit is highly dependent upon the wavelength of the unstable modes.

We assume that magnetic tension is negligible if

$$kH = \frac{2\pi H}{\lambda} < \sqrt{\beta}. \tag{3.23}$$

For a fuller derivation of the above equation (Equation 3.23), see subsubsection 3.4.1.1 at the end of this subsection.

Now, if we consider an unstable mode with $\lambda \approx H$ (i.e. global scale perturbations), Equation 3.23 can be reduced to a new upper limit on the plasma beta, and thus a second,

tighter, maximum allowed magnetic field strength

$$\beta > 4\pi^2 \tag{3.24a}$$

$$B < \sqrt{\frac{2\mu_0}{4\pi^2}}\sqrt{P}. \tag{3.24b}$$

We then use this to obtain an allowed magnetic field range that is more stringent than that set by Equation 3.22, which is highly dependent upon the scale of the system, and which should ideally be met for the atmosphere to conform to our WKB analysis

$$\frac{\sqrt{m_e}q_e^3}{36\pi\epsilon_0^2}\frac{n^{5/2}}{P^{3/2}} < B < \sqrt{\frac{2\mu_0}{4\pi^2}}\sqrt{P}. \tag{3.25}$$

Overall, Equation 3.22 and Equation 3.25, provide a reasonable, heuristic, range on the sort of magnetic field strengths an atmosphere should posses to be vulnerable to HBI growth.

3.4.1.1 Magnetic Tension: A Derivation

Here, we provide a full derivation of the magnetic tension wavelength limit expressed in Equation 3.23.

We start with Equation 3.6c, which expresses a modified growth rate combining both the instabilities growth rate, and the effects of magnetic tension. In order for the effects of magnetic tension (and Alfvén waves) to be negligible, we require that ω be the dominant term:

$$\omega^2 \geq (\boldsymbol{k}\cdot\boldsymbol{v}_\mathrm{A})^2 \tag{3.26a}$$

$$\omega^2 \geq k^2 v_A^2. \tag{3.26b}$$

Next, we substitute both the Alfvén speed (expressed in terms of the thermal velocity, $v_{th} = \left(\frac{P}{\rho}\right)^{\frac{1}{2}}$, and the plasma beta β: $v_A^2 = \frac{B^2}{4\pi\rho} = \frac{v_{th}^2}{\beta}$), and the maximal growth rate, Equation 3.8, into the above equation:

$$k^2\frac{v_{th}^2}{\beta} \leq g\frac{d\ln T}{dz}. \tag{3.27}$$

Then we substitute in for the scale-height, H, using the following relationship:

$$\frac{v_{th}}{H} = \sqrt{\frac{g}{H}} = \omega_{\rm dyn} \tag{3.28a}$$

$$\downarrow$$

$$v_{th}^2 = Hg, \tag{3.28b}$$

giving:

$$k^2 H \leq \beta \frac{d\ln T}{dz}. \tag{3.29}$$

Finally, we use the force balance equation:

$$\frac{d\ln P}{dz} = -\frac{g}{vth} = -\frac{1}{H} \tag{3.30}$$

and a fiducial cool-core temperature profile:

$$\frac{d\ln T}{d\ln P} = \frac{d\ln T}{dz}\frac{dz}{d\ln P} = -1 \tag{3.31}$$

to simplify our equation for the magnetic tension limit:

$$k^2 H \leq \beta \underbrace{\frac{d\ln T}{dz}\frac{dz}{d\ln P}}_{-1}\underbrace{\frac{d\ln P}{dz}}_{-\frac{1}{H}} \tag{3.32a}$$

$$\downarrow$$

$$k^2 H^2 \leq \beta \tag{3.32b}$$

$$\downarrow$$

$$kH \leq \sqrt{\beta}. \tag{3.32c}$$

Thus we have recovered Equation 3.23.

3.4.2 Conductive vs. dynamical times

The fastest growing modes for the HBI typically have very short wavelengths since it is at these scales that thermal conduction has the largest effect (Quataert 2008). In particular,

rapid HBI growth is limited to modes which experience rapid conduction, that is modes whose conduction time is shorter than the local growth time for the instability; for the fastest growing modes the growth time is of order the dynamical time, implying ($t_c < t_{\rm dyn}$).

Following Quataert (2008), we can approximate the conduction time, t_c over a length L as

$$t_c \sim \frac{L^2}{\kappa_c} \approx \frac{L^2}{\frac{\chi T}{P}} \approx \frac{L^2 n k_B}{\chi}, \tag{3.33}$$

where n is the number of molecules per unit volume, k_B is the Boltzmann Constant, and χ is the thermal conductivity. Then using the Spitzer Thermal Conductivity (Spitzer 1962), $\chi = 6 \times 10^{-7} T^{5/2}$erg cm^{-1} s^{-1} K^{-1}, this becomes

$$t_c \approx \frac{L^2 n k_B}{(6 \times 10^{-7}) T^{5/2}}. \tag{3.34}$$

Using our previous definition of $\omega_{\rm dyn}$, from section 3.3, we can express the dynamical (growth) time as

$$t_{\rm dyn} = \frac{2\pi}{\omega_{\rm dyn}} = 2\pi \sqrt{\frac{H}{g}}. \tag{3.35}$$

To find the maximum wavelength (length scale) for which the conduction time is shorter than the dynamical time, we set $t_c = t_{\rm dyn}$ and $L = \lambda_{\rm max}$:

$$\frac{\lambda_{\rm max}^2 n k_B}{(6 \times 10^{-7}) T^{5/2}} = 2\pi \sqrt{\frac{H}{g}} \tag{3.36a}$$

$$\Downarrow$$

$$\lambda_{\rm max} = \sqrt{\frac{(3.77 \times 10^{-6})\, T^{5/2} \sqrt{H}}{n k_B \sqrt{g}}}, \tag{3.36b}$$

where the scale height H is defined as:

$$H = \frac{v_{\rm thermal}^2}{g} \approx \frac{k_B T}{\mu m_p g}. \tag{3.37}$$

Thus:

$$\lambda_{\rm max} \approx \sqrt{\frac{(3.77 \times 10^{-6})\, T^3}{n \sqrt{\mu m_p k_B} g}} \tag{3.38}$$

However there is also a minimum wavelength, below which the effects of magnetic tension become too important to ignore and the HBI breaks down due to magnetic stabilisation (e.g. Kunz et al. 2012). To prevent this, we require

$$\lambda > \frac{2\pi H}{\sqrt{\beta}}. \tag{3.39}$$

Thus we get a range of wavelengths that are not stabilised by magnetic tension and for which $t_c < t_{\rm dyn}$:

$$\frac{2\pi H}{\sqrt{\beta}} < \lambda < \sqrt{\frac{(3.77\times10^{-6})\,T^3}{n\sqrt{\mu m_p k_B}\,g}}. \tag{3.40}$$

3.4.3 Radiative vs. conductive times

In order for the HBI to operate effectively, it is natural to assume that thermal conduction must be a major contributor to energy transport. Radiative cooling could compete with this transport, and if rapid enough, could eliminate the temperature contrasts which lead to buoyant motions and hence to the HBI. Thus, in the presence of radiative cooling, we get our second set of limits on the length scales (wavelengths) at which the HBI is able to operate

$$t_c < t_{\rm rad}, \tag{3.41}$$

i.e. we require the conduction time to be shorter than the radiative cooling time $t_{\rm rad}$. Following Aschwanden et al. (2007), we define the radiative cooling time as

$$t_{\rm rad} = \frac{E_{\rm thermal}}{\frac{dE}{dt}} \approx \frac{3k_B T}{n_e \Lambda(T)}, \tag{3.42}$$

where $\Lambda(T)$ is the radiative loss function with units of ergs cm^3 s^{-1}. For full details of the radiative loss function we use in our later calculations, see Appendix A. Broadly, this radiative loss function is intended to represent the complex cooling function of the upper solar atmosphere.

Following the same method as subsection 3.4.2, we set $t_c = t_{\rm rad}$ and $L = \lambda_{max}$, then using

Equation 3.34 we get the maximum wavelength for which Equation 3.41 holds true

$$\frac{\lambda_{max}^2 n k_B}{(6\times10^{-7})T^{5/2}} = \frac{3k_B T}{n_e \Lambda(T)} \tag{3.43a}$$

$$\Downarrow$$

$$\lambda_{\max} = \sqrt{\frac{(18\times10^{-7})\,T^{7/2}}{n_e^2 \Lambda(T)}}. \tag{3.43b}$$

Combining this with the minimum wavelength due to the effects of magnetic tension (Equation 3.39), gives us a range of valid wavelengths for the radiative HBI

$$\frac{2\pi H}{\sqrt{\beta}} < \lambda < \sqrt{\frac{(18\times10^{-7})\,T^{7/2}}{n_e^2 \Lambda(T)}}. \tag{3.44}$$

Clearly, to have thermal conduction be faster than radiative cooling *and* to have $t_c < t_{dyn}$, we require that the wavelength be shorter than the smallest limit imposed by either Equations 3.36b or 3.43b.

3.5 Magnetic Field Strengths, Length Scales, and Growth Rates in Solar and Planetary Atmospheres

As discussed in the previous sections, the growth of the HBI depends upon the temperature and pressure profiles within a region. To investigate the possibility that the HBI may operate within the solar atmosphere, or the atmospheres of highly irradiated exoplanets, we must therefore turn to **temperature-pressure profiles** for these regions. For the solar case, we consider the Avrett and Loeser (2008) average quiet Sun model – a semiempirical, one-dimensional, time-independent model with the temperature distribution adjusted to obtain optimal agreement with observed intensities and line profiles, whilst also maintaining an energy balance within the transition region – which gives T, P and ρ at different heights above the photosphere. For the planetary case, we consider the Moses et al. (2011) day-side average model of HD209458b – based upon the general circulation models (GCMs) of Showman et al. (2009) with an assumed Solar abundance – which gives only gives T and P, thus requiring us to calculate relative heights by assuming

both hydrostatic equilibrium and an ideal gas. Both T-P profiles are shown in Figure 3.3.

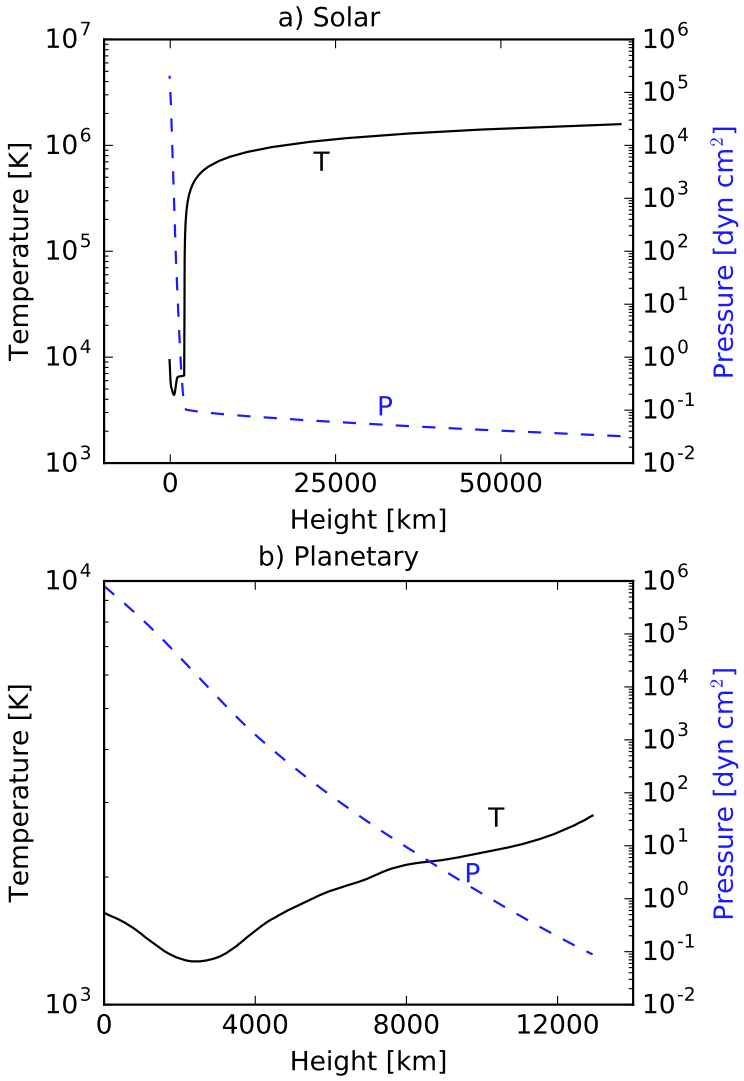

Figure 3.3: Pressure-Temperature-Density profile for both the Solar and planetary cases. The Solar case makes use of the Avrett and Loeser (2008) 'C7' average quiet Sun model in which the zero point of height is the top of the photosphere. The planetary case makes use of the Moses et al. (2011) day-side average model of HD209458b (which itself is based upon the GCMs of Showman et al. (2009)), in which the heights are all relative to the bottom of the profile.

3.5.1 Allowed Magnetic Field Intensities for HBI Growth

We can use these ***P-T* profiles** to calculate the range of allowed magnetic field intensities for which the HBI is able to grow, as constrained by our magnetic field requirments: the perturbations are not stabilised by magnetic tension, the gas pressure exceeds the mag-

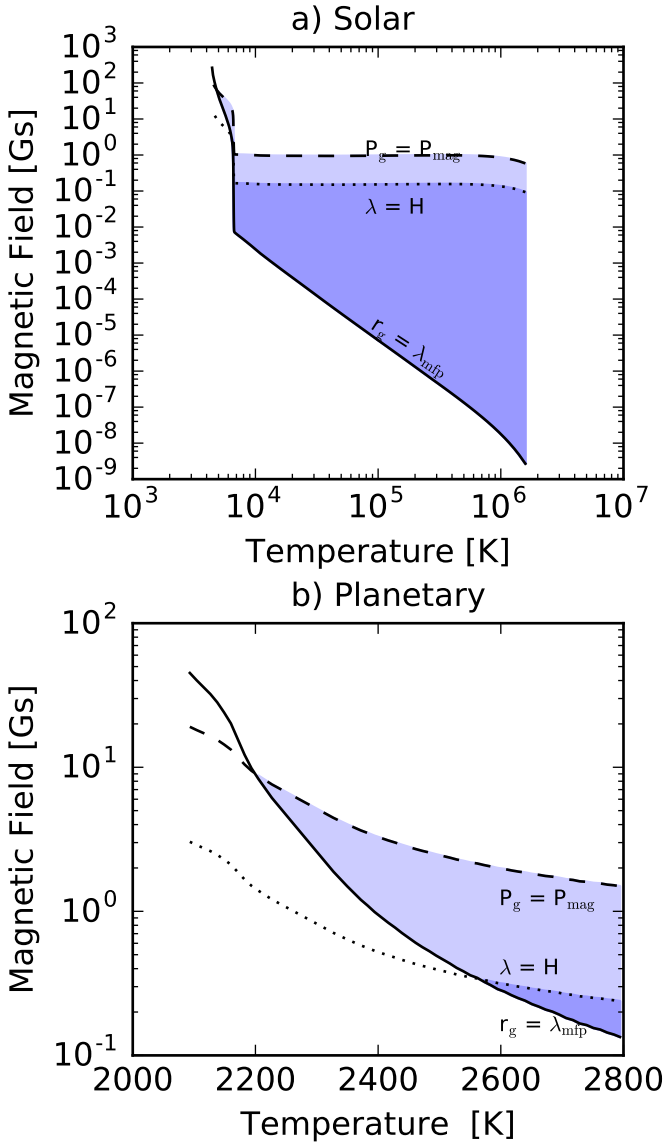

Figure 3.4: The range of magnetic field strengths at which the HBI could, in principle, grow, plotted against temperature, for both the Solar and planetary cases. The allowed magnetic field-temperature space is shown by the shaded regions, with the darker shading indicating the more stringent condition that both the gas pressure exceeds the magnetic pressure ($P_g \geq P_{mag}$), and that the effects of magnetic tension are negligible on at least some scales with $\lambda < H$. The lower magnetic field strength limit comes from the requirement that the electron mean free path be greater than the electron gyroradius, i.e. anisotropic thermal conduction. Note that the results shown in the above figure are based upon the analysis, and formulae, presented in subsection 3.4.1.

netic pressure, and the electron mean free path is greater than the electron gyroradius (i.e. anisotropic conduction). The results of these calculations are shown in Figure 3.4.

For the Solar case (Figure 3.4a), there exists a broad range of magnetic field intensities over which the HBI is potentially viable in both the upper transition region and the corona, even when we take into account the more stringent conduction of negligible magnetic tension on the global scale (and even on local scales). However, the maximum allowed field strengths within the corona are quite weak (less than 1 G). This is weaker than the average field within these regions (i.e., the corona is on average in a low-beta state), suggesting that the HBI is unlikely to operate except perhaps in regions of unusually weak magnetism (e.g., coronal holes (Wiegelmann et al. 2014), near magnetic null points (Longcope 2005)). On the basis of this criterion alone, the regions somewhat below the corona (i.e., in the transition region and chromosphere) might seem more susceptible to the instability: although the range of allowed field strengths there is quite narrow, it includes fields of 10-100 G, roughly in line with what is observed in these regions of the Solar atmosphere (see, Gary (2001) and Wiegelmann et al. (2014) etc. for more details). However, we will see in subsection 3.5.2 that other factors likely prevent the instability from acting there.

The planetary case (Figure 3.4b) is also not clear cut. There exists a range of field strengths for which the HBI might be thought viable (with $r_g < \lambda_{\mathrm{MFP}}$, $P_{\mathrm{gas}} > P_{\mathrm{mag}}$), and this range includes fields of the same order of magnitude (1-10 G) as expected for hot Jupiters (e.g. Christensen et al. (2009)). However, including the effects of magnetic stabilisation significantly reduces the range of allowed field strengths; further, the only modes that are plausibly unstable have wavelengths comparable to the scale height, suggesting that a local analysis will be insufficient.

3.5.2 Allowed Length Scales for HBI Growth

Next, we use both the ***P-T* profiles**, and our extended Rosner radiative loss function (Table A.1), to calculate the range of allowed wavelengths for HBI growth, for models both with (subsection 3.4.3) and without (subsection 3.4.2) radiative cooling. The results of these sample calculations for both the Solar and planetary cases are shown in Figure 3.5.

That figure illustrates the wavelengths for which we might expect HBI growth, requiring both that magnetic tension be negligible and thermal conduction be rapid. The black lines represent the time-scale ordering restrictions whilst the coloured lines represent the (β dependent) wavelengths below which the effects of magnetic tension stabilises the HBI. Wavelengths which fall below the coloured lines are stabilised by magnetic tension; on wavelengths that are below the black lines conduction is rapid relative to radiative cooling and/or the local dynamical time. Hence, domains defined by a black line lying above a coloured line represent regions in which the HBI might in principle grow, for the indicated wavelengths and plasma betas.

Turning first to the solar case (Figure 3.5a), we see that short wavelengths are stabilised at most temperatures, through the effects of magnetic tension; meanwhile on long wavelengths, conduction is typically slow relative to either cooling or the local dynamical time. However, some particularly long wavelength HBI modes would be unstable in the upper transition region and corona, if such regions have sufficiently low values of the plasma beta. Note that these unstable modes would have wavelengths on the order of the local scale height, calling into question our local WKB analysis; later we will investigate the HBI on these global scales via 2.5D HBI simulations. Finally, note that in the corona, it is the requirement for $t_c < t_{\rm dyn}$ that provides the upper wavelength limit, regardless of the presence of radiative cooling.

Our analysis of the planetary case (Figure 3.5b) likewise suggests that the HBI is unlikely to operate at plausible plasma betas. Even at higher plasma betas, all modes are either stabilised by magnetic tension or do not obey the time-scale ordering we initially required ($t_c < t_{\rm dyn}$ and $t_c < t_{\rm rad}$). Although the HBI can be shown to continue to operate when the dynamical time-scale is shorter than the conduction time, (see subsection 3.7.3), the instability is probably easily disrupted in this regime; HBI growth then requires many dynamical times to develop, suggesting competing effects may play a dominant role.

3.5.3 HBI Growth Rates

Finally we come to the application of the **dispersion relation**, specifically we make use of our previously defined temperature-pressure profiles to caluclate the dynamical growth

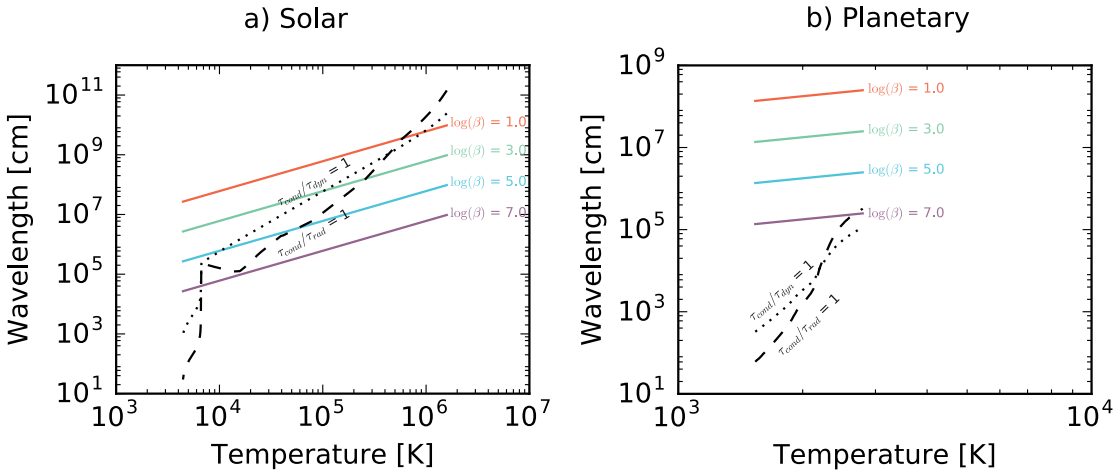

Figure 3.5: The allowed wavelength ranges for the HBI to operate, in both cases calculated using the T-P profiles found in Figure 3.3. The maximum wavelengths are shown in black, and are calculated by requiring either rapid conduction or that thermal conduction dominates over radiative loss. The minimum wavelengths are shown in colour for different plasma betas; any wavelengths below these lines will be stabilised by magnetic tension. Thus, for the HBI to operate at a particular plasma beta, the unstable modes (wavelengths) must fall below the black lines and above the corresponding coloured line.

rates of the HBI. We limit this calculation to the solar case, due to the strict requirement that $\omega_{\text{cond}} \gg \omega_{\text{dyn}}$ in the current analysis. In addition to this, we modify the non-radiative growth rate calculation formula (shown in Equation 3.8), in order to allow for the possibility that the Alfvén frequency will be not be much less than the dynamical frequency (section 3.3)

$$\tilde{\omega}^2 \simeq g \frac{d \ln T}{dz} \frac{\mathcal{K}}{k^2} \tag{3.45a}$$

$$\sigma^2 = -\left(\tilde{\omega}^2 + (\boldsymbol{k} \cdot \boldsymbol{v}_a)^2\right), \tag{3.45b}$$

where σ is our final growth rate and is comparable to the radiative growth-rate. The results of the non-radiative dynamical growth rate calculation using the Solar P-T-ρ are shown in Figure 3.6 for four different plasma betas.

Comparing the dynamical growth rates with the Solar P-T-ρ profile, it becomes clear that the growth rate is acting as expected in that it is maximised when the rate of change of temperature with height is a maximum, i.e. in the solar transition region. Additionally, the almost zero growth rates at $\beta = 10$ confirm that the HBI cannot quickly grow at low-betas ('strong' magnetic fields), even though these modes are linearly unstable. As a consequence of this very slow growth rate at low betas, the instability is likely to be sensitive

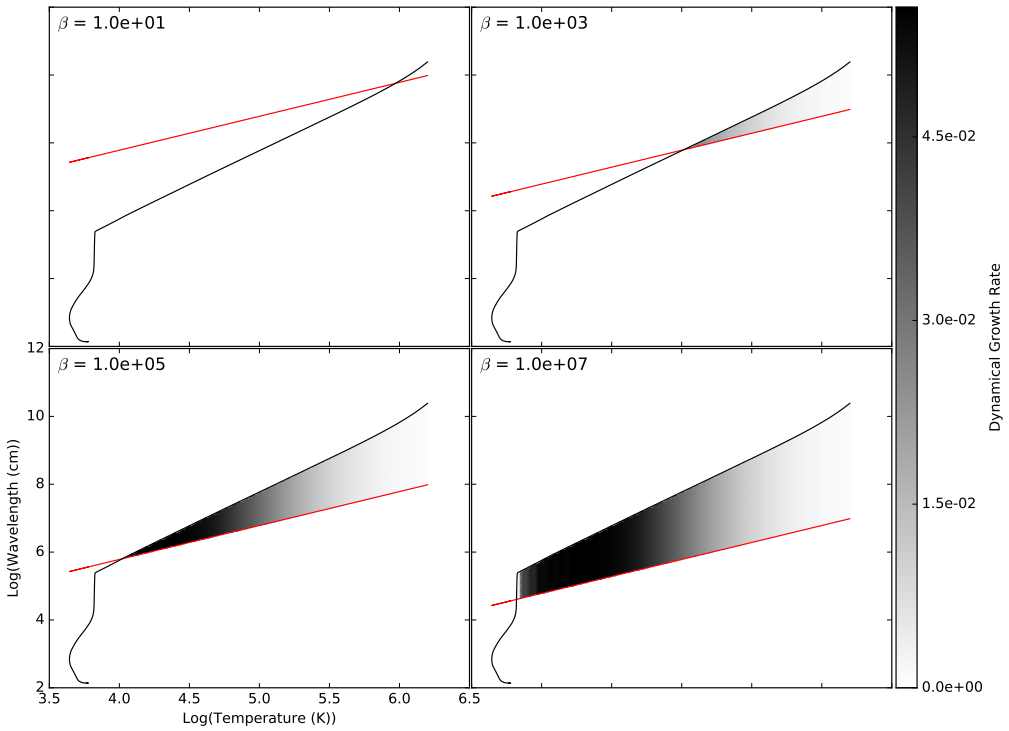

Figure 3.6: Magnitude of non-radiative dynamical growth rates (Equation 3.45 - itself a solution to the dispersion relation) for the Avrett and Loeser (2008) Solar P-T-ρ profile (Figure 3.3) at different plasma betas and with equal amplitude parallel and perpendicular perturbations. The black line corresponds to the wavelength at which $t_c = t_{\rm dyn}$ (Equation 3.36b) whilst the red lines represent the (β dependent) wavelengths below which magnetic tension stabilises the HBI (Equation 3.39).

to external influences, with any external motions/perturbations, acting on times on the order of of the dynamical time, able to destroy the magnetic field profile required for HBI development before the instability can grow.

When radiative loss is included in the growth rate calculation (Figure 3.7), the growth rates now split into two components: an imaginary component (Figure 3.7a), representing the true HBI growth rate (i.e. equivalent to dynamical growth rate in Figure 3.6), and an additional real component (Figure 3.7b) which represents exponential decay due to the presence of radiative cooling. Note that, whilst we find a significantly smaller region in which the HBI can operate when we include the effects of radiative loss, the maximal growth rates we find are approximately the same as those found in the purely dynamical (non-radiative) case.

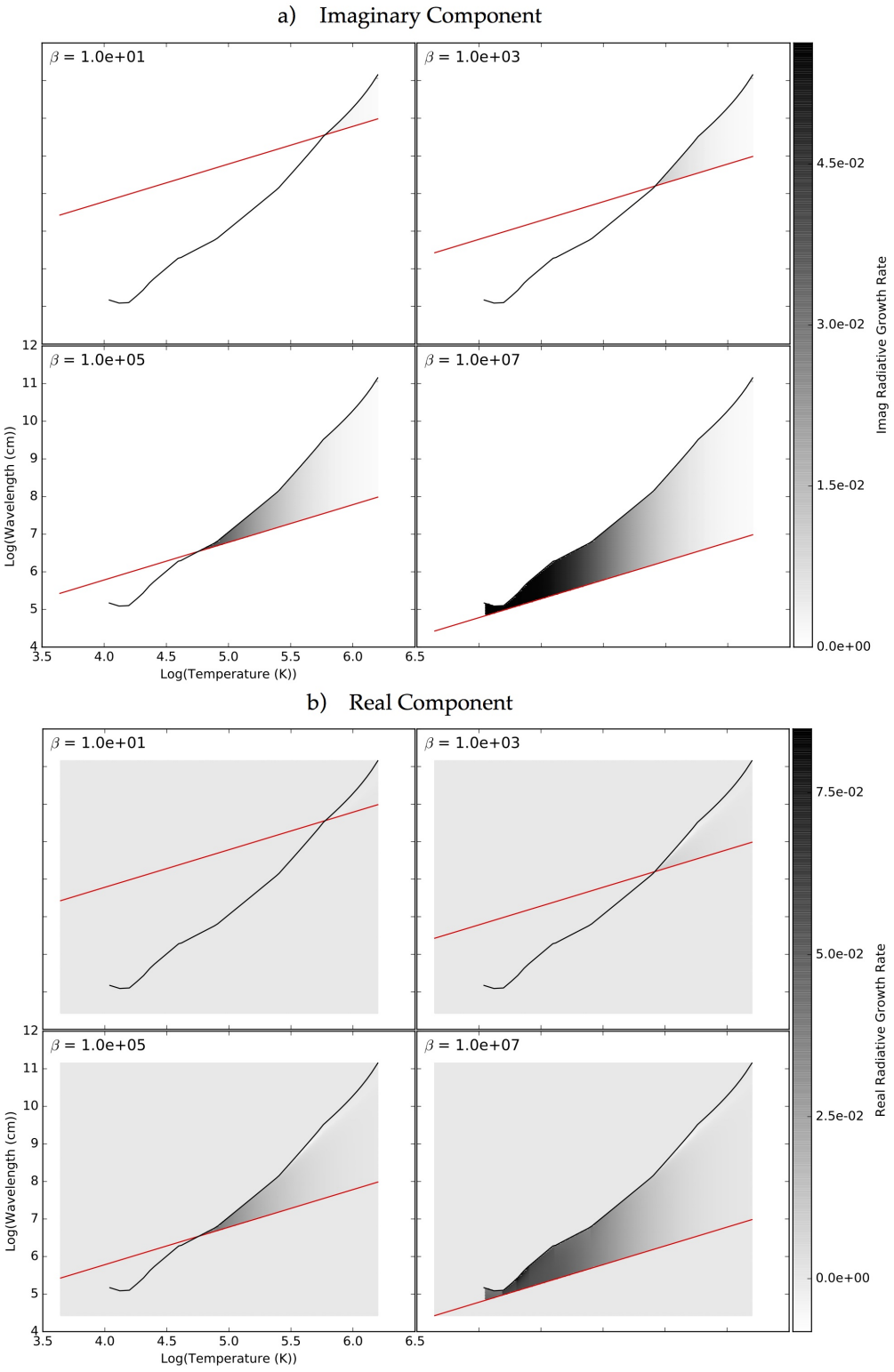

Figure 3.7: Maximums of the real (b) and imaginary (a) components of the radiative HBI growth rates (Equation 3.14 and Equation 3.15 - representing real and imagninary solutions to the dispersion relation) for the Avrett and Loeser (2008) Solar P-T-ρ profile (Figure 3.3) at different plasma betas and with equal amplitude parallel and perpendicular perturbations. The black line corresponds to the wavelength at which $t_c = t_{\text{rad}}$ (Equation 3.36b) whilst the red lines represent the (β dependent) wavelengths below which magnetic tension stabilises the HBI (Equation 3.39).

3.6 Simulating the HBI

We have seen from the above analysis that many competing effects influence the growth of the HBI and related instabilities: radiative cooling, magnetic tension and rapid dynamical processes all may play roles. Furthermore, we have found that in many cases the only unstable modes have wavelengths that are long, on the order of the local scale height, suggesting that a linear, local analysis may not be sufficient. Motivated by these considerations, we turn in this section to 2.5D simulations of plasmas in which the HBI may operate.

3.6.1 Numerical Setup

We use ATHENA, a grid-based MHD code, with the addition of isotropic/anisotropic thermal conduction, to simulate plasmas which may be subject to the HBI. A brief introduction to this code (including the equations solved: Ideal MHD with anisotropic thermal conduction - Equation 2.16 and Equation 2.27), and the changes we made to it for HBI modelling, may be found in section 2.5, and we direct interested readers to Stone et al. (2008) for a complete description of ATHENA's internal workings.

The HBI requires an atmosphere with a positive temperature gradient (Equation 3.2), which we have selected to be in initial hydrostatic equilibrium. Thus, like Avara et al. (2013), we set up an initial configuration with temperature, density and pressure profiles of the form

$$T(z) = T_0 \left(1 + \frac{z}{H_T}\right) \tag{3.46a}$$

$$\rho(z) = \rho_0 \left(1 + \frac{z}{H_T}\right)^{-2} \tag{3.46b}$$

$$P(z) = P_0 \left(1 + \frac{z}{H_T}\right)^{-1}, \tag{3.46c}$$

where $H_T = (d \ln T/dz)^{-1}$ is the characteristic scale height of the atmosphere.
To this we then add a purely vertical magnetic field that has a fixed amplitude

$$\boldsymbol{B} = B_0 \hat{z}, \tag{3.47}$$

and a downward, constant, gravitational acceleration

$$\boldsymbol{g}(z) = -g_0 \hat{z}. \tag{3.48}$$

Finally we apply a single-mode velocity perturbation to the central, anisotropic, region of the form

$$\delta v = \delta v_0 \left(\sin\left(\frac{n\pi x}{L_x}\right) \hat{x} + \sin\left(\frac{n\pi z}{L_{z\_\text{central}}}\right) \hat{z} \right), \tag{3.49}$$

where n is the mode number of the perturbation, L_x is the width of the simulation domain and L_{z_central} is the height of the central anisotropic region.
Note: As detailed in section 2.5, we also have made some modest adjustments to the internal workings of ATHENA in order to conduct these simulations. First we added momentum reflective, fixed temperature vertical boundary conditions. Secondly, we modified ATHENA's conduction subroutine such that only the central third of the simulation contains anisotropic thermal conduction - with the remaining top and bottom regions acting as isotropic buffers.

3.6.2 Radiative Loss in HBI Simulations

Our analytical analysis suggests that radiative losses may present a major hurdle in the growth/development of the HBI. In this section, we therefore introduce radiative cooling into our HBI simulations, to assess how this modifies the growth rate and non-linear characteristics of the instability. The addition of radiative loss to our 2.5D HBI simulations poses some difficulties; our simulations are non-dimensional, making it difficult to translate a physical radiative loss function (such as the Rosner radiative loss function (Appendix A)) into the required unit system.
Instead, we investigate the effects of radiative cooling on the HBI in a simplified way by

varying the ratio of the conductive and radiative time-scales

$$\frac{t_c}{t_{rad}} = \frac{\frac{\lambda^2}{\kappa_c}}{\frac{3T}{n_e \Lambda(T^\star)}} = \frac{\lambda^2}{\kappa_c}\frac{n^2\Lambda(T^\star)}{3P} \tag{3.50a}$$

$$\Lambda(T^\star) = \frac{t_c}{t_{rad}}\frac{3P\kappa_c}{n^2\lambda^2}, \tag{3.50b}$$

where $T^\star$ is a modified temperature, defined such that $P = nT^\star$, and $\Lambda(T^\star)$ is our modified (and parameter driven) radiative loss profile. Note that, on its own, this modified radiative loss function is not non-dimensional - it is the combination of our non-dimensional simulation parameters (i.e. section 3.7) and this function that leads to a non-dimensional radiative loss function, controlled by the ratio of the conductive and radiative timescales ($\frac{t_c}{t_{rad}}$).

3.6.3 Diagnostics: Vertical Heat Flux

In cases in which the HBI develops, most of the vertical heat transport is accomplished by anisotropic thermal conduction along the field lines. We therefore assess the vertical heat flux (VHF), as formulated by Avara et al. (2013), within the system

$$\text{VHF} = -\int_S Q \cdot dS, = -\int_S \chi \hat{b}\left(\hat{b}\cdot\nabla\right)T \cdot dS, \tag{3.51}$$

where Q is the anisotropic thermal conduction, as presented in Equation 2.27, and S is a surface that cuts horizontally though the simulation domain. The VHF not only provides a useful measure of how the HBI affects thermal conduction, but can also be used to differentiate between simulations with different plasma betas, as demonstrated explicitly below.

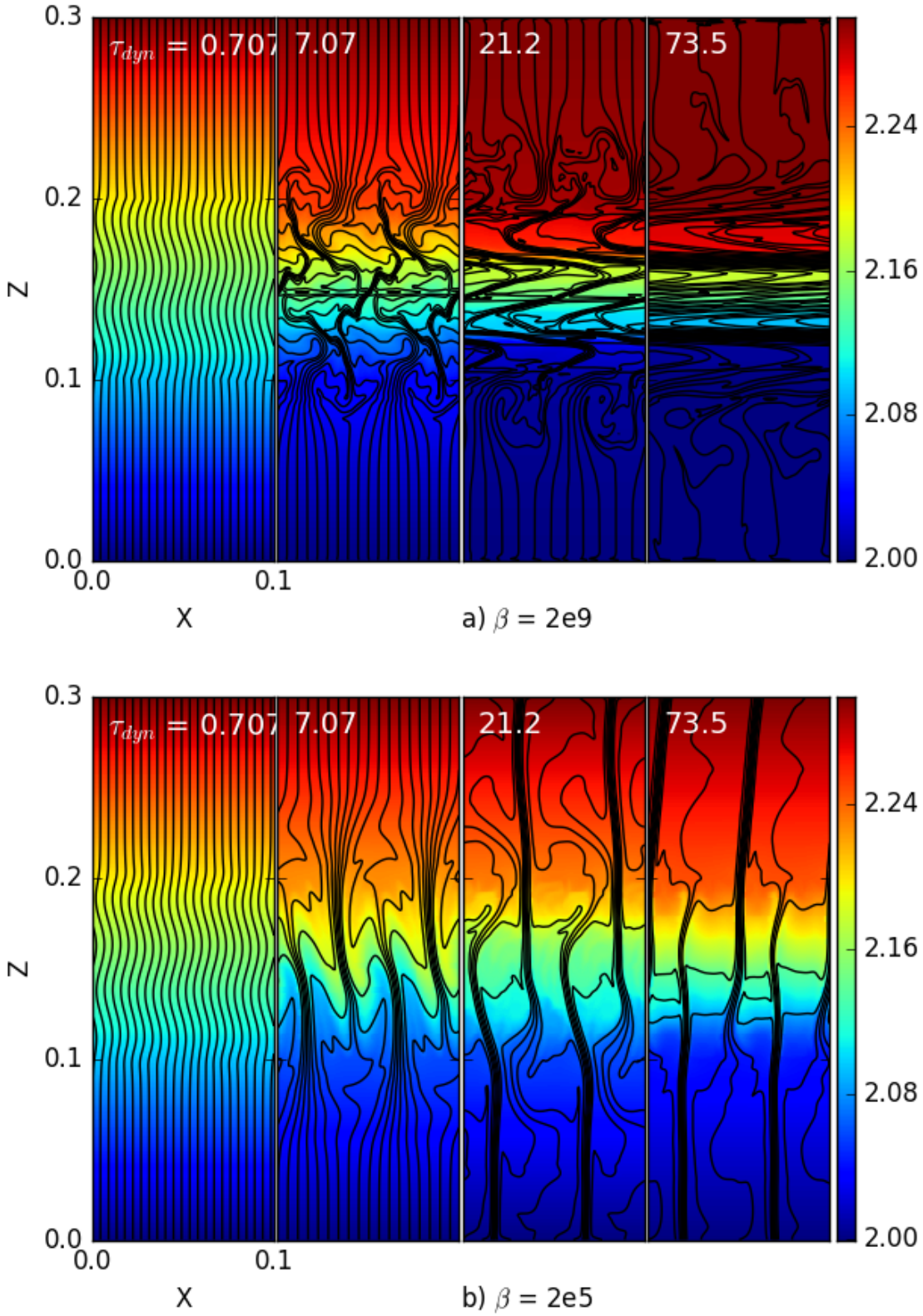

Figure 3.8: Temperature profile and magnetic field lines at four different times in both high and mid beta local simulations akin to those of Avara et al. (2013). It is important to note how an increase in magnetic field, i.e. a decrease in the plasma beta, changes the final field profile from insulating field layers at high betas, to thermal conduction along magnetic filaments at mid beta (with insulating regions between the filaments).

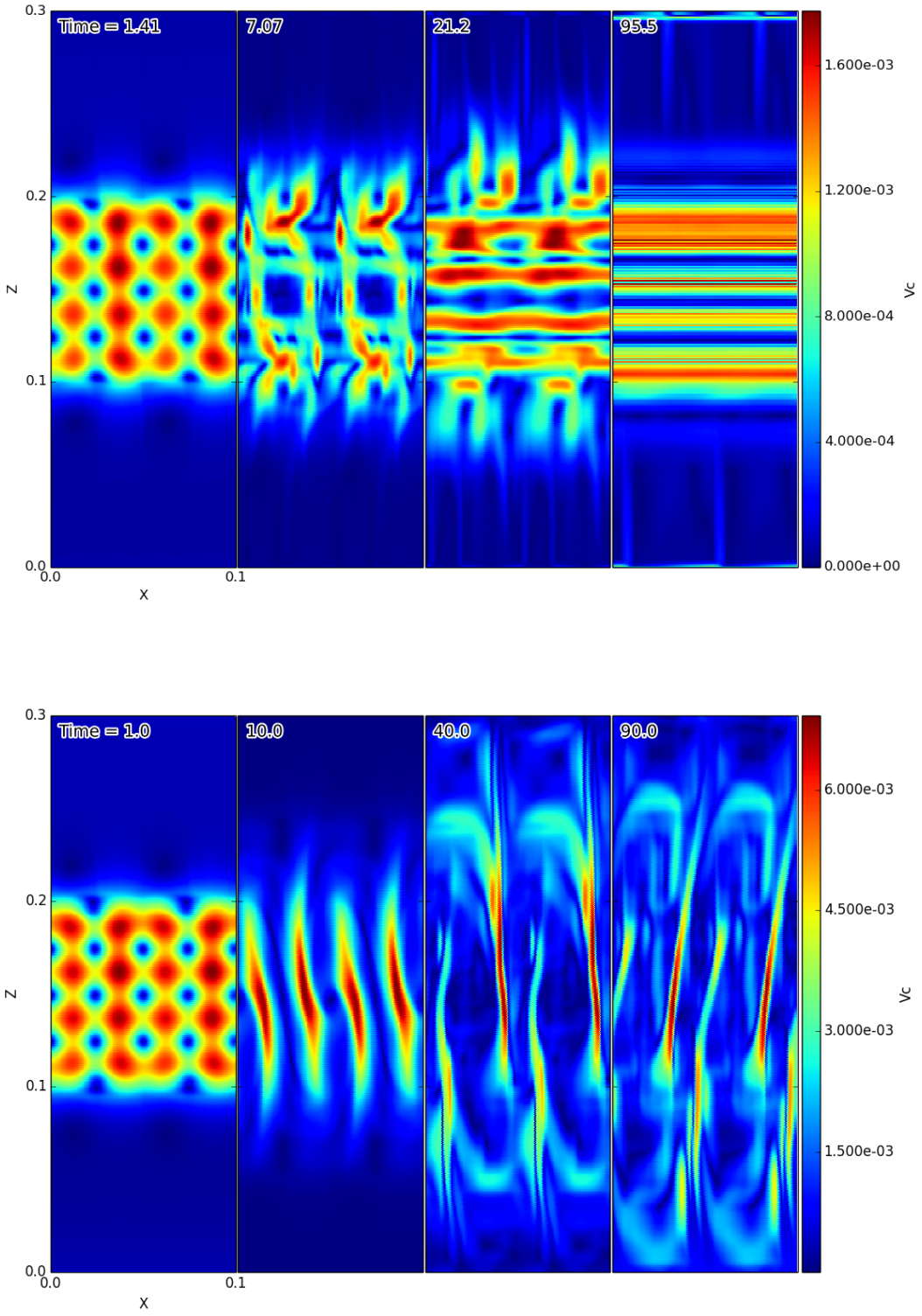

Figure 3.9: Velocity maps at four different times in both high and mid beta local simulations. In both cases we find that velocity motions are channelled along magnetic field lines, resulting in strong horizontal flows at high beta, and vertical velocity motions along magnetic filaments at mid beta.

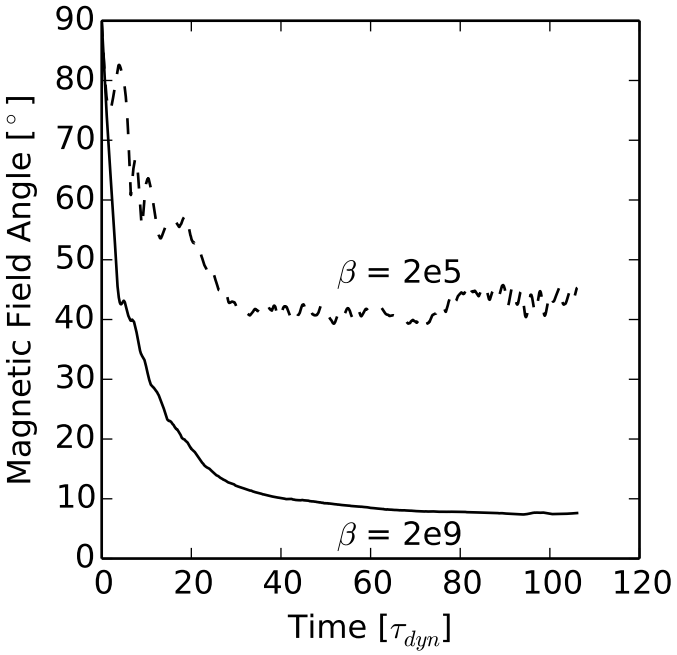

Figure 3.10: Average magnetic field angle in the central anisotropic region, measured against the horizontal, for both our high $(\beta = 2e9)$, and mid $(\beta = 2e5)$ plasma beta, local scale, simulations.

3.7 The HBI on Local Scales

3.7.1 Non-Radiative HBI with Rapid Thermal Conduction

We initially conducted simulations of an HBI unstable plasma on a local scale, without the effects of radiative loss, and considering cases in which thermal conduction is rapid relative to other effects. This situation has previously been analysed using numerical simulations by, for example, Avara et al. (2013), so the results in this section also serve as a consistency check and validation that we could correctly simulate the HBI with ATHENA. In these models, we set $T_0 = 2\rho_0 = P_0 = 2\mu = 2g_0 = 2$ giving a characteristic scale height $H_T = 2$ and a sound speed $c_s \equiv \sqrt{\frac{\gamma P}{\rho}} \approx 1.3$. Additionally we set $\gamma = 5/3$, $\delta v_0 = 0.002$, $n = 4$, $\kappa = 0.01$ and considered four different plasma betas $\beta = 2 \times 10^{(9,\,7,\,5,\,3)}$.

Finally we set the simulation to have a domain size of 0.1×0.3, split vertically into three regions, with a central, anisotropic, region size of 0.1×0.1. At this domain size, we choose a resolution of 128×384 in order to balance the quality of results with the CPU time required.

An analysis of our local HBI results is best started by considering the evolution of the

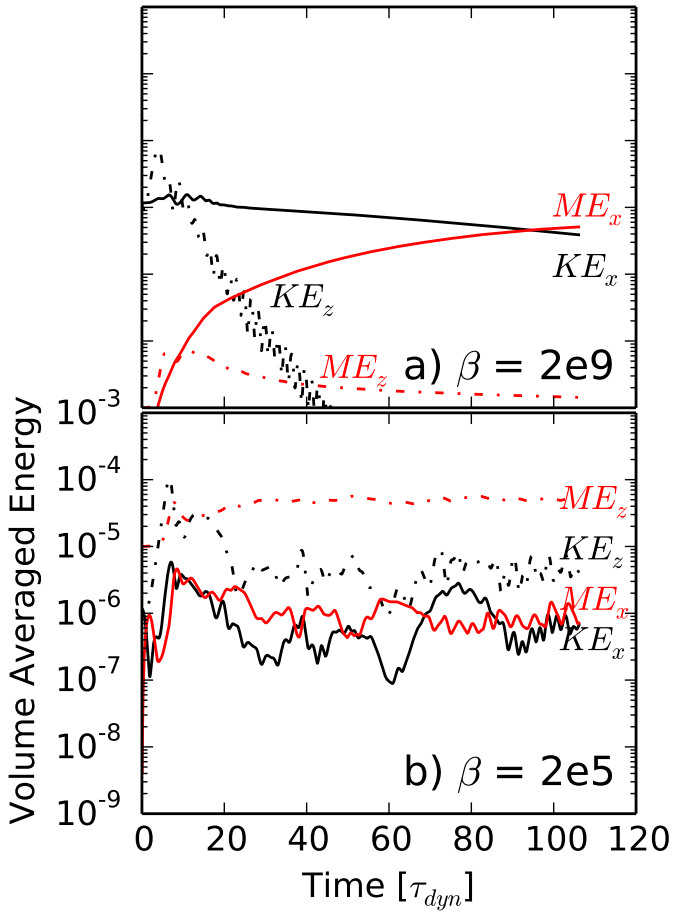

Figure 3.11: Evolution of the, volume-averaged, kinetic and magnetic energy components over the central, anisotropic, region of both our high $(\beta = 2e9)$ and mid $(\beta = 2e5)$ plasma beta, local scale, simulations.

background temperature profile, velocity profile, and magnetic field structure with time and at varied plasma betas. These are sampled for a few cases in Figure 3.8 and Figure 3.9. At high beta, $\beta = 2e9$, the HBI acts to reorientate the magnetic field towards an almost purely horizontal (closed) magnetic field configuration; this is visible in Figure 3.8a, which shows the temperature profile and magnetic field lines as a function of time, in a high beta simulation. Similarly, examining the velocity field in the same simulation, Figure 3.9a, reveals a related non-linear effect of the HBI, namely the development of velocity motions which trace the magnetic field structure. This results in, at high beta, the formation of strong horizontal velocities. The rearrangement of the magnetic fields lines is more quantitatively addressed by Figure 3.10, which shows how the magnetic field orientation evolves from a nearly vertical initial condition, to nearly horizontal in the non-linearly

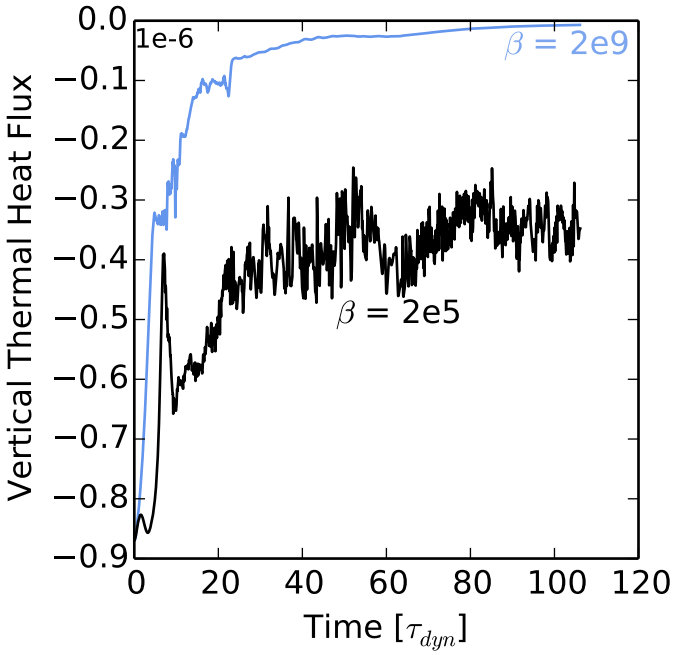

Figure 3.12: Horizontally averaged vertical thermal heat flux (arbitrarily scaled) passing through a horizontal surface situated on the central, i.e. middle, layer of both our high $(\beta = 2e9)$ and mid $(\beta = 2e5)$ plasma beta, local scale, simulations.

evolved state.

Further assessment of the dynamics of the non-linear state is provided by Figure 3.11a, which examines the volume-averaged kinetic and magnetic energy components. Here we see that at early times the evolution of the system is dominated by kinetic energy (specifically horizontal kinetic energy since vertical motions are rapidly suppressed); at later times strong horizontal motions, with an associated kinetic energy, have developed, whilst the vertical motions have been damped. The horizontal magnetic energy has also grown by nearly three orders of magnitude.

This reorientation of the field lines has a profound effect on the vertical heat transport within the system. This is assessed in Figure 3.12, which shows the horizontally averaged vertical conductive heat flux, as a function of time, within the simulation. Initially a strong downwards heat flux is present, but in the non-linearly evolved state this has been reduced to only 1/125th of its original value, in keeping with the horizontal reorientation of the field lines. Thus the non-linear action of the HBI at high betas is to create insulating layers of magnetic field structure within the plasma, thermally isolating the hot upper atmosphere from the cooler region below.

As we move to a lower beta, $\beta = 2e5$, (Figure 3.8b), the ability of the HBI to reorientate

the magnetic field is significantly reduced resulting in the presence of persistent magnetic filaments. These filaments are visible in both the magnetic field lines, Figure 3.8b, and the velocity profile Figure 3.9a. They represent small regions which have, though the grouping of magnetic field lines (and thus the local enhancement [decrease] in the magnetic field strength [plasma beta]), become locally stable to the HBI; as such, they retain their vertical structure and act as conduits of vertical conductive heat transport, preventing the complete restriction of the VHF, as seen in Figure 3.12. Considering the energy evolution of the system, Figure 3.11b, it is likewise clear that the system differs significantly from its high beta counterpart, specifically with the continued dominance of vertical energy components over horizontal. This again reflects the prominent role of the magnetic filaments, along which most vertical motions are focused.

Finally, we conducted simulations at even lower plasma betas, namely $\beta = 2e3$ (i.e. a plasma beta 100 times smaller than the lowest considered in our above simulations). In the parameter space explored here, the HBI fails to operate at that beta, with no magnetic field evolution or temperature profile changes. This is in accord with the linear stability analysis presented in section 3.4, which would predict that the beta must be significantly higher for field growth (i.e Equation 3.23 suggests that, for $\lambda \approx 0.1H$, $\beta < 400\pi^2 \approx 4000$ will be stable.).

3.7.2 Radiative Loss

We now turn to an investigation of the evolution of the local-scale HBI when radiative cooling is enabled. To do this, we used the method outlined in subsection 3.6.2; we start with lower levels of radiative loss, such that thermal conduction is still the dominant mode of heat transport, and then move towards higher levels, until radiative loss clearly dominates over thermal conduction.

Figure 3.13a shows the temperature profile and magnetic field lines for a local-scale, high beta, simulation with the radiative loss function set such that $\frac{t_c}{t_{\text{rad}}} = 0.1$ throughout the simulation domain. First, if we compare the magnetic field structure with a reference local simulation (Figure 3.8a), we find that low levels of radiative loss have only had a

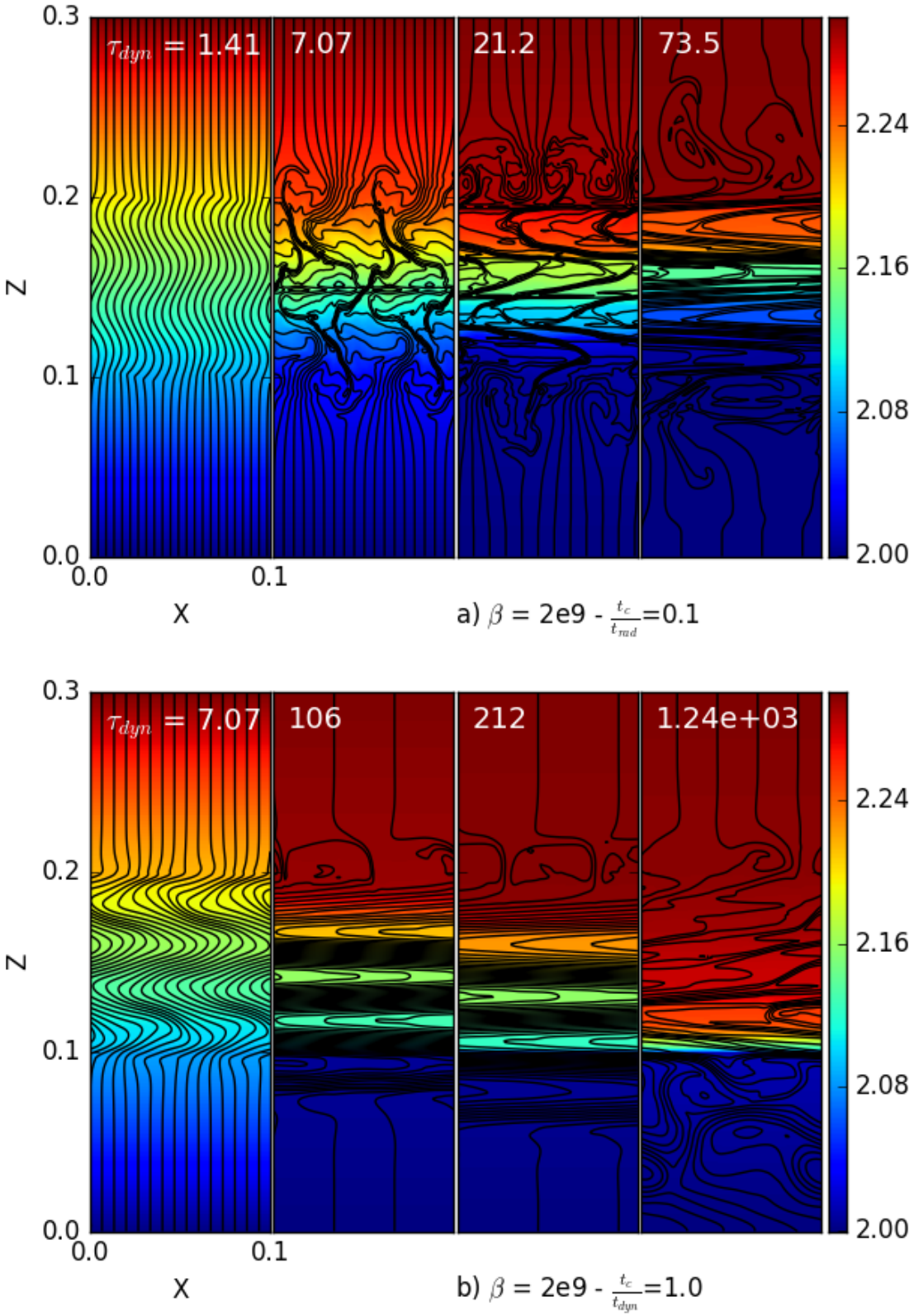

Figure 3.13: Temperature profile and magnetic field lines for example HBI simulations with either a) radiative cooling or b) slow thermal conduction. Note that the slow thermal conduction simulation was allowed to run for a significantly longer time than normal, partially due to the slow growth of the instability in this limit.

minor effect on the magnetic field structure, causing slight variations that do not significantly affect the overall structure/evolution of the HBI. On the other hand, the temperature profile shows clear signs of the effects of radiative cooling, with the (thermally isolated) temperature strata that form in the central anisotropic region exhibiting noticeably lower temperatures than the equivalent strata in the reference local run and also showing a slow decrease in temperature as the simulation progresses, both of which are signs of radiative cooling locally removing energy from the system. Note that, for the fixed temperature boundary conditions employed here, the overall thermal energy in the system is not necessarily conserved, and indeed here decreases as the HBI prevents conductive heating from compensating for the radiative losses.

Whilst the above simulation shows that a low level of radiative loss does not significantly affect the overall evolution of the HBI, this does not remain the case as we move to higher levels of radiative cooling. Figure 3.14a investigates the temperature structure and magnetic field lines in a case in which $t_c = t_{\text{rad}}$; the HBI field structure initially forms, reorientating the magnetic field lines towards the horizontal and thereby restricting heat transport from the warm upper atmospheric region. At the same time, the radiative losses from the central anisotropic region cause this region to continue to cool, leading to a increased temperature gradient at $z = 0.2$. This leads to an enhanced, localised, HBI growth rate, further thermally isolating the central region and leading to the temperature profile found in Figure 3.14a. At even higher levels of radiative loss, i.e. $\frac{t_c}{t_{\text{rad}}} = 10.0$ (Figure 3.14b), the non-linearly established temperature gradient is even sharper. Here the HBI reorientation of the magnetic field lines towards the horizontal is confined to a very narrow region near $z = 0.2$; elsewhere the field structure is more chaotic.

Overall, we have confirmed that a low level of radiative cooling, such that anisotropic thermal conduction is still the dominant mode of heat transport, does not significantly hinder the evolution of the HBI. Indeed, cases in which radiative cooling is rapid compared to thermal conduction still show localised HBI growth and field reorientation. However the non-linearly established state differs appreciably from the non-radiative case: the HBI is ultimately confined to a narrow region with very sharp temperature gradients, whilst elsewhere the temperature becomes homogenised. This HBI active region essentially represents a small sub-domain in which thermal conduction is rapid, due to the short length

scale involved, and HBI growth is fast, due to the enhanced temperature gradient.

3.7.3 Slow Thermal Conduction

We now investigate the effect of a slowed thermal conduction, achieved via a decreasing anisotropic thermal diffusion coefficient (κ_c), on a local-scale simulation. Our reference local run had a κ_c such that $\frac{t_c}{t_{\rm dyn}} = 0.11$. Figure 3.13b shows the temperature map and magnetic field profiles in a simulation with increased κ_c such that $t_c = t_{\rm dyn}$. This simulation (and several companion ones which are not shown) was conducted in order to investigate the importance of the time-scale ordering, $t_c < t_{\rm dyn}$ (i.e. rapid conduction). The first conclusion apparent from Figure 3.13b is that the HBI takes significantly longer to develop/evolve when compared to our standard, local-scale, simulation (Figure 3.8a). For example, within $7t_{\rm dyn}$ the reference calculations has already developed significant HBI induced structure, whereas this calculation, at the same time, still carries signatures of the initial state. This is in keeping with the slower rate of conductive heat transport increasing the time required for HBI structures to both form, and evolve. This impression is reinforced by simulations we conducted with further decreased κ_c, i.e. $\frac{t_c}{t_{\rm dyn}} = 5.0$ and $\frac{t_c}{t_{\rm dyn}} = 50.0$; in these calculations (not shown) we found that HBI growth was even more seriously retarded.

We must caution that over the extended intervals required to study the HBI in this regime, the simulations exhibit some unphysical behaviour. In particular, at the resolutions employed here, the simulations are unable to maintain perfect hydrostatic balance over the very large number of dynamical times over which the HBI grows when conduction is slow. This is a numerical limitation of the current generation of solvers implemented in finite-difference codes such as ATHENA (and only very recently have techniques become available that somewhat mitigate this problem) - the only way we have found to somewhat mitigate this departure from HSE is through a significantly increased resolution, with a stable run predicted to require up to a million CPU hours to evolve (something we do not have access to). As a result, our slow thermal conduction simulations eventually develop a 'sag'. This causes the atmosphere to collapse, drawing the HBI structure with it, and eventually leading to unexpected field structures as the HBI perturbed field passes out-

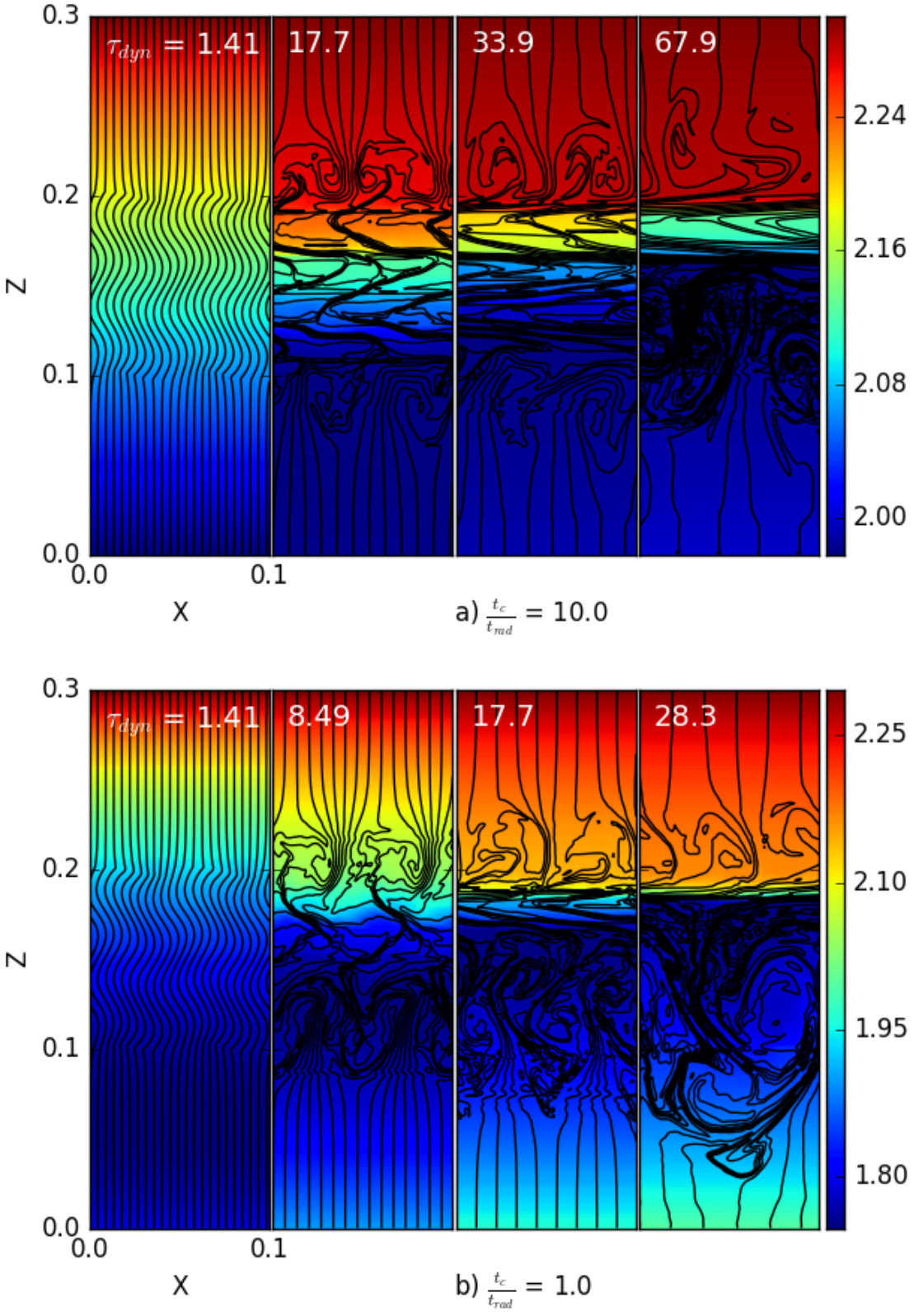

Figure 3.14: Temperature profile and magnetic field lines for example HBI simulations with either a) $\frac{t_c}{t_{\rm rad}} = 1.0$ or b) $\frac{t_c}{t_{\rm rad}} = 10.0$. Here we show the effects of strong radiative loss: it collapses the temperature gradient, and disrupts the formation of the HBI.

side of the anisotropic domain (see the final pane of Figure 3.13b).

Whilst this effect ('sag') cannot be expected to be present in physical systems, the slowing of HBI development is likely more robust. In physical systems, such as the transition region of the Sun, this will increase the time-scale over which other physical effects, such as bulk fluid flows, might disrupt HBI development. Our simulations thus provide support for the view that the HBI is most effective (and likely to have any significant impact) when $t_c < t_{\text{dyn}}$.

3.7.4 Anisotropic and Isotropic Conduction

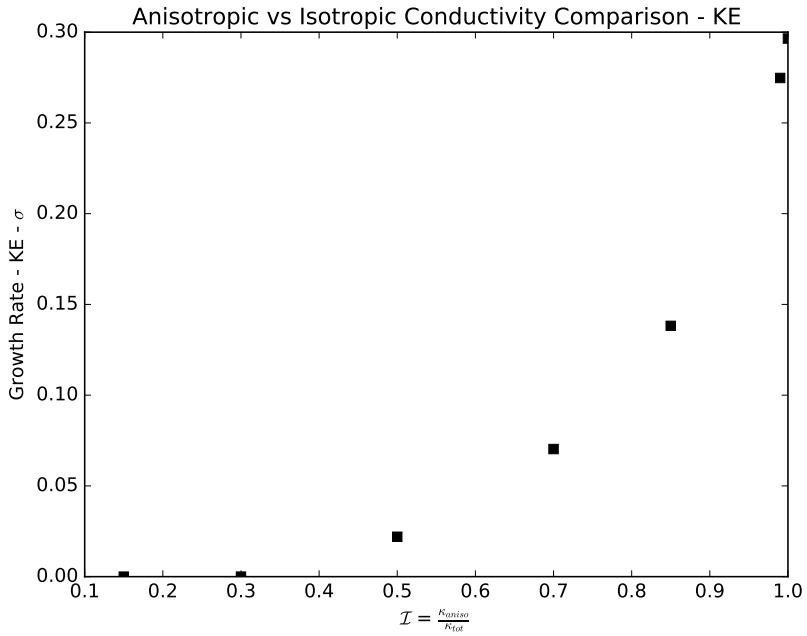

Figure 3.15: The $\mathcal{I}$ factor ($\mathcal{I} = \frac{\kappa_{aniso}}{\kappa_{total}}$), showing how increasing levels ($\mathcal{I} \to 0$) of isotropic thermal conduction within our HBI unstable region slows the growth of the instability. Whilst this is for local-scale simulations, we find almost identical results on the global scale.

Finally, we investigate the effect of introducing isotropic thermal conduction to our HBI unstable central region. We use the parameter $\mathcal{I} = \frac{\kappa_{aniso}}{\kappa_{total}}$ to quantify the level of isotropic conduction, with a high $\mathcal{I}$ ($\mathcal{I} \to 1$) indicating primarily anisotropic conduction, whilst a low $\mathcal{I}$ ($\mathcal{I} \to 0$) indicates primarily isotropic thermal conduction. Then, for each simulation we calculate the kinetic energy growth rate ($\sigma_{\text{KE}} = \max\left[i = 0, 1, ...N_{\text{steps}}\right] \frac{\log\left(\frac{\text{KE}_i}{\text{KE}_0}\right)}{t_i - t_0}$), and compare this to $\mathcal{I}$. The results of this calculation are shown in Figure 3.15, which shows how the growth rate changes as the level of isotropic conduction is reduced. The

growth rates shown here were calculated for a series of simulations via the average kinetic energy growth rate within the anisotropic domain. For low levels of isotropic conduction, we only find a slight reduction in the HBI growth rate. However, as we move towards equal levels of anisotropic and isotropic conduction ($\mathcal{I} = 0.5$), we find that the growth rate has been reduced by almost an order of magnitude, with higher levels of isotropic conduction essentially suppressing the instability altogether. These results do not offer any real surprise; as earlier stated (subsection 3.2.2), the development of the HBI relies upon a primarily anisotropic thermal conduction, with any isotropic conduction bypassing this mechanism and thus allowing fluid parcels to equilibrate with their surroundings after displacement. Note that we find almost exactly the same results for our global scale simulations (section 3.8).

3.8 The HBI on Global Scales

3.8.1 Non-Radiative HBI

We now extend our local-scale simulations to encompass a larger vertical domain size, on the order of the scale height. This was motivated by the findings of subsection 3.5.2, which suggest that any HBI-unstable modes in stellar and planetary atmospheres (which are at relatively low plasma betas) are likely to have wavelengths comparable to the atmospheric scale height.

To do this, we used the same initial parameters as the local simulations, but increased the domain size to $2.0 \times 6.0 \equiv H_T \times 3H_T$, thus giving a central, anisotropic, region size of $2.0 \times 2.0 \equiv H_T \times H_T$. This required a corresponding increase in simulation resolution to 512×1536 in order to allow magnetic field lines to properly group and form magnetic filaments at lower plasma betas. We must note that, due to the way the simulations were set up, the plasma beta is actually a factor of 2 lower than in the equivalent local calculations; the value reported in the figures is the plasma beta at the bottom boundary.

If we compare the evolution of our global-scale simulations (Figure 3.16, showing the temperature and magnetic field profiles, and Figure 3.17, showing the velocity profiles) to our standard local-scale simulations, some differences are immediately clear.These include a

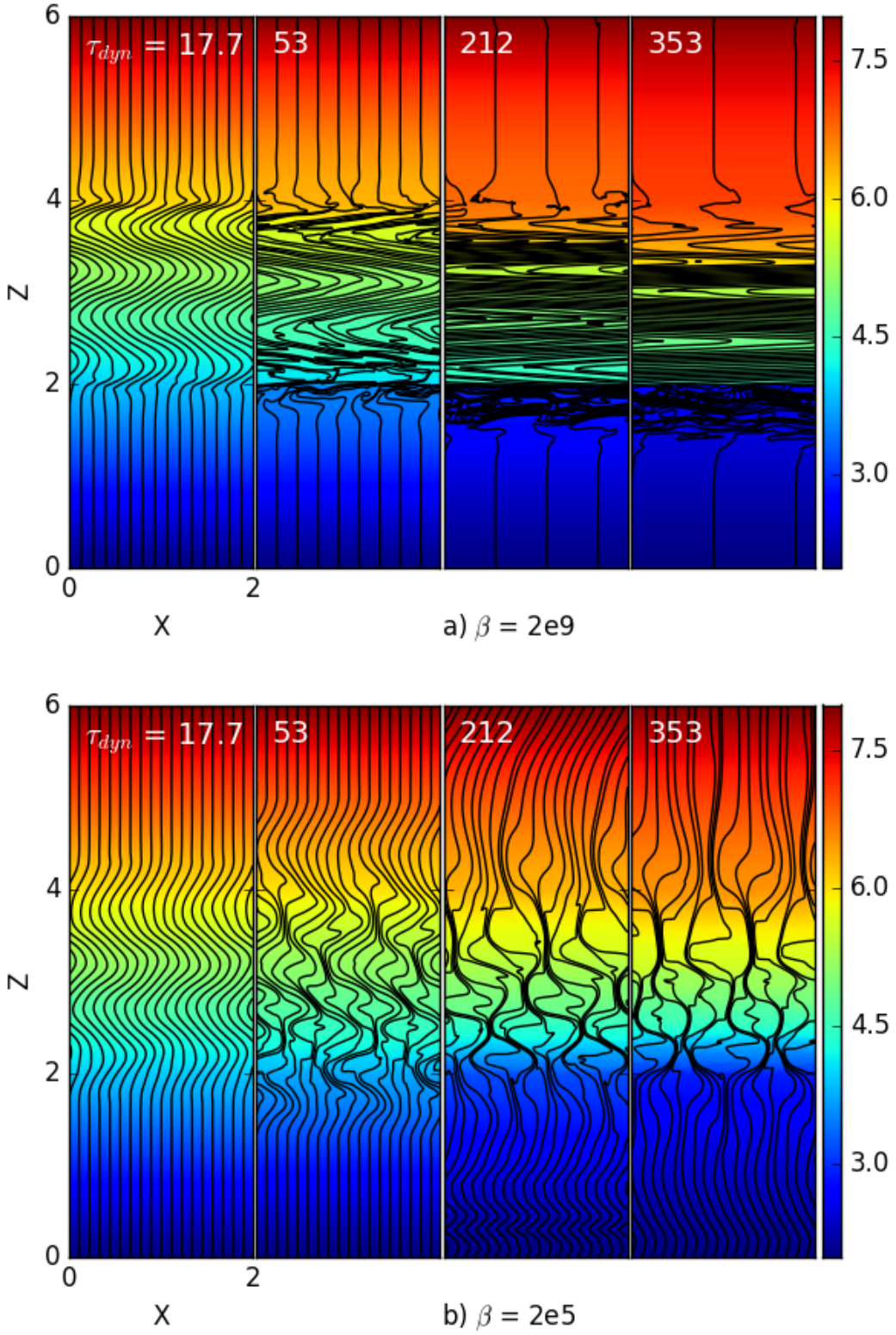

Figure 3.16: Temperature profile and magnetic field lines at four different times for our $\beta = 2e9$ and $\beta = 2e5$ global HBI simulations. For the high beta simulation, it is clear that the magnetic field profile, when compared to its local counterpart (Figure 3.8a), appears to sag as the simulation progresses. Much like our slow thermal conduction case, this is most-likely related to the increase in conduction time as the scale of the perturbations increases, and hence the long time-frame required to simulate the global HBI. ATHENA then struggles to maintain a hydrostatic balance over many dynamical times.

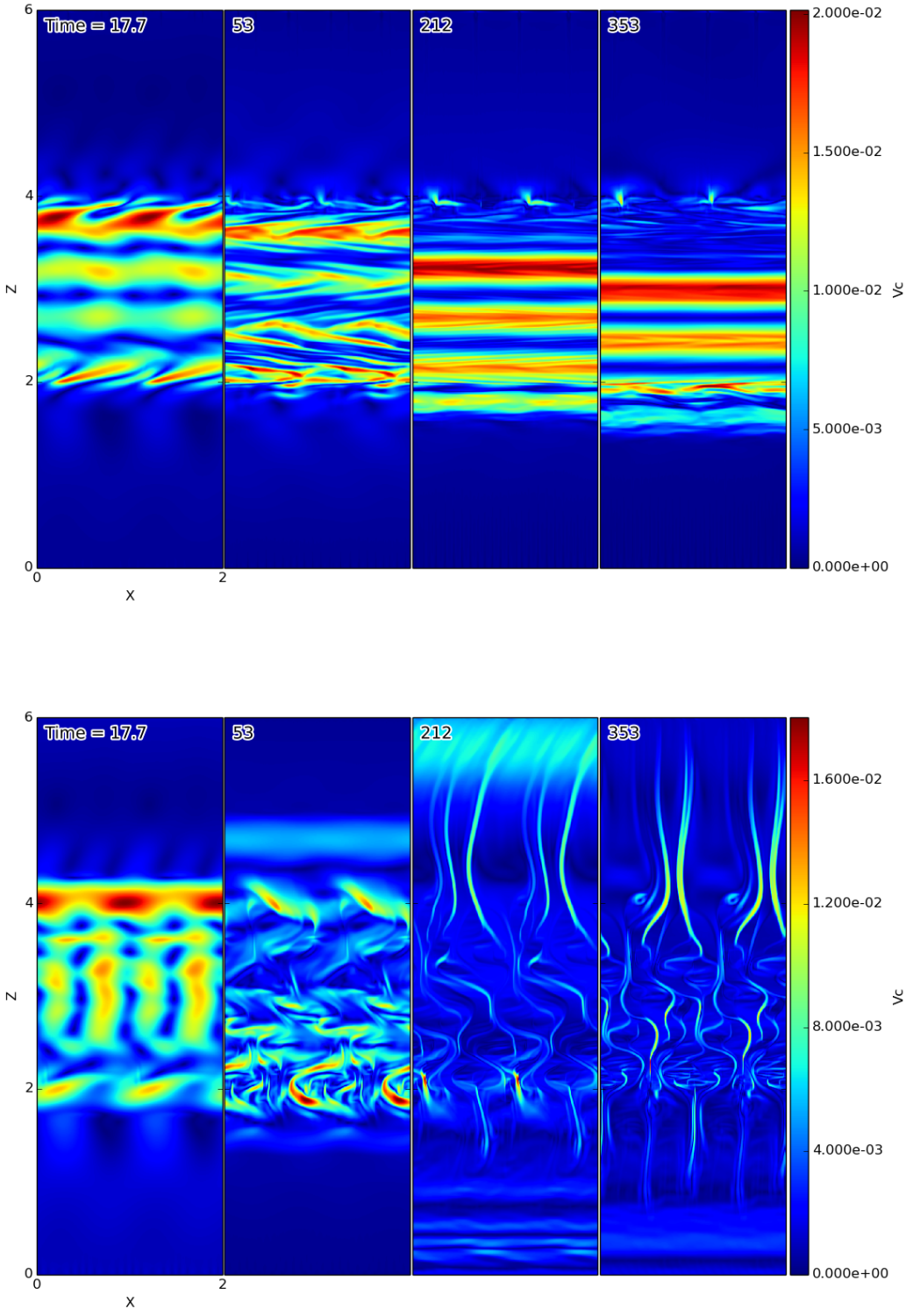

Figure 3.17: Velocity maps for, global-scale, HBI simulations with either high $(\beta = 2e9)$ or mid $(\beta = 2e5)$ plasma beta. In both cases we find that velocity motions are channelled along magnetic field lines, resulting in strong horizontal flows at high beta (which follow the magnetic field structure), and vertical velocity motions along magnetic filaments at mid beta.

markedly different magnetic field structure, most obvious for magnetic filaments, a significantly slower development of the HBI structure, and again a slight (unphysical) 'sag' of the magnetic field profile. However, the non-linear behaviour remains comparable to that realised in our local simulations section 3.7, with strong velocity motions tracing magnetic field structures.

The difference in the magnetic field profile is most obvious if we consider the lower beta run (whose field and temperature profile is shown in Figure 3.16b) which exhibits two different types of magnetic filaments: longer, weak, filaments that form within the isotropic buffer regions, and shorter, stronger, filaments that dominate the central anisotropic region. These shorter filaments are on a similar length-scale to the filaments realised in the local-scale calculations (but of course due to the increased domain size here, they appear smaller). Unlike in the local calculations, the filaments realised in the isotropic region do not clearly extend over the complete domain in the magnetic field line renderings; however, inspection of the velocity maps (Figure 3.17b) reveals that some filamentary structure does persist nearly to the upper boundary. Note that the velocity structures are not symmetric about the midplane. This may partially reflect the variation in plasma beta over the extended domains: near the top boundary, beta is four times lower than at the bottom, so magnetic fields are more able to resist dragging by fluid motions there.

By increasing the domain size of the simulations, we have effectively increased the length scale over which conduction must transport heat (the central anisotropic region is a factor twenty larger than in the local calculations), and so have dramatically increased the timescale over which this conduction operates. Hence $\frac{t_c}{t_{\rm dyn}} \approx 11.3$ in these calculations, whereas $\frac{t_c}{t_{\rm dyn}} \approx 0.1$ in the equivalent local run. Much as in local calculations with slower thermal conduction (subsection 3.7.3), this slows the growth of the HBI considerably, requiring us to evolve the simulation for many dynamical times in order to assess the non-linear evolution. This behaviour is sampled in Figure 3.16a, which shows the temperature map and magnetic field profile, and Figure 3.17a, which shows the velocity map. As in the slow-conduction local cases (subsection 3.7.3), the atmosphere also eventually begins to 'sag' vertically, which again is linked to the simulation's inability to maintain perfect hydrostatic balance over hundreds of dynamical times.

Overall, these simulations confirm that the HBI can operate (in the parameter regimes

probed here) on scales comparable to the scale height of the system. This development, however, is slow, in accord with the leisurely transport of heat by conduction over these long length scales, and hence may be prone to disruption by events that operate on the dynamical time. Here the disruption is artificial, however in a stellar atmosphere, such as the Sun, many different competing processes operate (Aschwanden 2005; Charbonneau 2013). In essence, the artificial disruption serves to illustrate an important point: On global lengthscales, HBI development is slow and thus prone to external disruption (both physical and unphysical). As a result of this, global HBI development is likely to be limited to quiescent atmospheres.

3.8.2 Radiative Loss

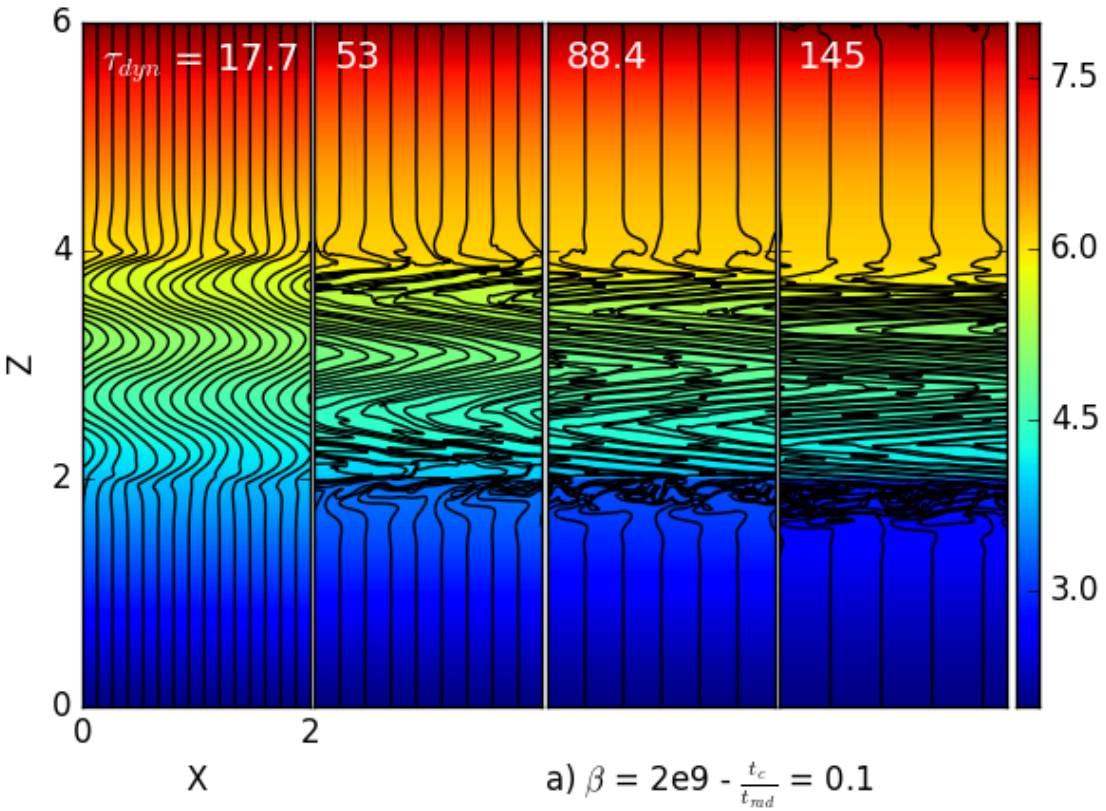

Figure 3.18: Temperature profile and magnetic field lines for a global-scale HBI simulation with $\frac{t_c}{t_{\rm rad}} = 0.1$. Here we show that, like on local-scales, low levels of radiative loss do not have a significant impact on the HBI structure/evolution.

We also investigated the effects of radiative cooling on our global-scale simulations, following the method outlined in subsection 3.6.2. Figure 3.18 shows the temperature profile and magnetic field lines for a global-scale simulation, with $\beta = 2e9$ and $\frac{t_c}{t_{\rm rad}} = 0.1$.

Much as in our local-scale results (subsection 3.7.2), we find that low levels of radiative loss do not have a significant effect on the evolution of the HBI. Compared with our standard global-scale case (Figure 3.16a)), we find almost no difference in the HBI profile which forms, only a slight cooling of the temperature bands that form between the magnetic field 'layers', in accord with the radiative cooling. As we move to higher levels of radiative cooling (not shown here), we once again find that the HBI structure either collapses or fails to form in the first place, as radiative cooling destroys the temperature profile that the instability relies upon. Furthermore, it is possible that, in the rapid radiative loss regime, other instabilities, such as the classical Field (1965) thermal instability (which is reliant upon a strong radiative loss function), might operate, further reducing both the likelihood and potential impact of the HBI.

3.9 Concluding Remarks

In this chapter we have investigated whether the Heat-Flux-Driven Buoyancy Instability (HBI) might plausibly occur in the atmospheres of stars and exoplanets, and have explored some of the consequences of this instability using non-linear simulations. We were motivated to study this instability partly because of its non-linear behaviour: namely its tendency to reorient a pre-existing vertical field towards the horizontal, thereby inhibiting vertical heat conduction from hot regions down towards cooler ones. If this were to occur in the Sun, it would have major implications for the energy balance of the solar transition region and corona.

Our linear stability analysis (section 3.4) revealed only limited regions in parameter space where the HBI might play a role: throughout much of these atmospheres, either magnetic tension or slow conduction conspire to suppress the instability or greatly slow it. Although broad regions of these atmospheres have the property that conduction is anisotropic, magnetic tension typically suppresses the HBI on small length scales; meanwhile on larger length scales, conduction is often simply too slow relative to other effects. Nonetheless, our analysis has suggested that the HBI might conceivably operate within very weak-field regions of the solar atmosphere. In the transition region and chromo-

sphere, the temperature increases outwards and thermal conduction dominates over radiative loss; the average plasma beta is too low for the HBI to persist there, but some localised regions may have much higher betas, and it is possible that the instability could act locally there. It is unclear, however, whether these regions are commonplace enough to play any dynamical role. Different models of the outer solar atmosphere (such as Gary and Alexander (1999) and Gary (2001)) give estimated field strengths that vary by orders of magnitude, with only some of them implying plasma betas for which the HBI may be viable. Furthermore, the values of temperature, pressure, and magnetic field strength in a 1-D model are necessarily averages over surfaces at a given height; as such there may exist regions in which the field is much weaker (e.g., coronal holes (Wiegelmann et al. 2014), or near magnetic null points (Longcope 2005)). Indeed, it has long been realised that the local plasma properties of the solar upper atmosphere vary significantly with position (e.g. Ayres 2002). However, it must be noted that the regions we have explored here lie, in some models, above the 'magnetic canopy', i.e. the region in which the tightly grouped magnetic fields from magnetic flux tubes spread out; this may imply that the entire region is permeated by a strong enough magnetic field to suppress HBI growth on local scales. Ultimately what is needed is a detailed comparison with high-precision observations of the dynamic Solar atmosphere, which we reserve for future work.

We have not yet investigated the prospects for HBI growth in other stellar atmospheres in any detail. Most stars are magnetic at some level, and the structure of their upper atmospheres is thought to vary enormously (e.g. Ayres and Linsky 1975; Dominguez et al. 1999; Baraffe et al. 2015)). It is possible that the atmospheres of some of these objects may prove to be more suitable for HBI development. Unfortunately, no universally accepted model of these regions, which would provide us with quantitative assessment of the P-T profiles in stars across the H-R diagram, currently exists. We therefore defer a detailed investigation into the HBI in other stars.

Similarly, the applicability of the HBI to the atmospheres of highly irradiated exoplanets is also not straightforward to analyse, mostly due to the vast array of P-T-ρ-B profiles proposed for these objects. In addition to the case we considered here, we also investigated a small number of other exoplanet atmospheres, finding allowed wavelength ranges and magnetic field strengths on the order of those presented here. Overall, it appears un-

likely that the HBI can act quickly enough (on scales that are not suppressed by magnetic tension) to play a significant role in these atmospheres.

We have also investigated the non-linear behaviour of the HBI, should it occur in any of these environs. As noted above, we were particularly interested in the ability of the HBI to reorientate the field structure in such a way as to restrict the vertical heat transport by anisotropic thermal conduction (see Figure 3.12). Our non-linear simulations with ATHENA revealed that this reorientation of the field lines occurs rapidly at high beta, even in the presence of modest levels of radiative cooling, and (in this regime) can almost completely inhibit vertical heat transport; when the field strengths are higher, however, the field is concentrated into narrow filaments along which conduction continues, leading to more modest reductions in the vertical heat transport. Similar behaviour has been noted previous in the context of the ICM (e.g. Avara et al. 2013). By carrying out a series of simulations in which the conductive time varied enormously, we also showed that the HBI continues to operate even when conduction is "slow" relative to the dynamical time; however, the slow growth of the instability in this limit may hamper its ability to compete with other phenomena in any real atmosphere. We also showed that the instability continues to operate effectively on global scales (i.e., over domains with sizes comparable to the local scale height), albeit slowly, in accord with the large spatial scales over which conduction then operates. Overall, our simulations broadly confirm the estimates of our linear stability analysis, though they also offer the tantalising prospect that the HBI could act in some regimes (namely on global scales, with radiative losses, and with relatively slow conduction) that our analytical analysis would have suggested are stable.

We thus conclude on a mixed note: the HBI may play a role in Solar, stellar and planetary atmospheres, but it is likely to be quite limited in scope. If it occurs at all, it is probably limited to small portions of the atmosphere; it is therefore unlikely to have the same significance or broad applicability as it does in the ICM, for example. However, its dramatic consequences for heat transport in the non-linearly evolved state, and the prospects that it may operate outside the narrow regimes that our analytical analysis suggested, suggest that it merits further study. We discuss a few prospects for future work in chapter 6.

Chapter 4

The Rossiter-McLaughlin effect at secondary eclipse

"And now for something completely different."

— Monty Python

Declaration: This chapter, and its associated appendices (a full derivation of the effect in Appendix B and a brief exploitation of the model in Appendix C), represent the final output of a joint project between Nikolay Nikolov and myself. The original idea, and the observational application are the purview of Nikolay, whilst I was responsible for both the formalism of the effect, and the resultant model. The original text was a joint effort, with each author focusing upon their area of expertise. Below is a rewritten, and expanded (for accessibility) version of the resultant publication: Nikolov and Sainsbury-Martinez (2015).

4.1 Introduction

Knowledge of planetary rotation rates, surface flows/winds, and axial tilts is critical for understanding the habitability of an exoplanet: not only do they determine how the atmosphere mixes, they are also inexorably linked to the determination of the seasonal climate (Williams and Kasting 1997; Cowan et al. 2012), and are relevant to the study of the planet

formation and evolution history (Agnor et al. 1999). However, to date, the measurement of these quantities has proved to be quite elusive, with no current methodology able to probe both the rotation rate (or wind) and the axial tilt of an exoplanet (Snellen et al. 2014 did successfully retrieve the rotation rate of β Pic b - a young, fast rotator - using rotational broadening of spectral lines, but this technique is unable to recover the axial tilt). Here, we explore a new technique: The Rossiter-McLaughlin effect at secondary eclipse (*RMse*) - a modification of the traditional Rossiter-McLaughlin effect designed to work on exoplanets themselves rather than their host stars. In this introduction we will explore some of the key concepts required to understand the *RMse* (including exactly what it measures), the (primary/original) Rossiter-McLaughlin effect, and of course the *RMse* itself.

As mentioned above, an understanding of the rotation rate and axial tilts is critical to understanding the evolution history, and hence habitability, of an exoplanet, but what are these quantities? By definition the planetary rotation rate and the axial tilt (e.g. obliquity) are respectively the time it takes for a complete revolution of the planet (i.e. the planets 'day') and the angle between the planetary spin angular momentum axis and the planet's orbital angular momentum vector (or put another way, the normal of the planetary orbit). The axial tilt of a planet can be used to define its obliquity: planets with an obliquity of $< 90°$ are said to exhibit prograde rotation, whilst planets with an obliquity of $> 90°$ exhibit retrograde rotation. To understand these obliquities, we now turn to the Solar system and planet formation theory. In the Solar system, planetary spins and obliquities are well-constrained, spanning a wide range of rotational rates and axial titles (Cox and Pilachowski 2000), and are considered to reflect the unique formation and evolutionary history of each planet (Laskar and Robutel 1993). Planets accumulate rotational angular momentum from the relative motions of the material accreted during their formation. The stochastic nature of this planetary accretion from planetesimals (and other disk material) allows for a random component to the net spin angular momentum. Prograde angular momentum (i.e. spin) could be accumulated by a planet on a circular orbit within a uniform surface density disk of small planetesimals (and dust): The planet clears a gap and thus accretes a larger fraction of material from the edges of its accretion zone - this accretion of material will lead to an angular momentum transfer that will impart a prograde rotational

sense onto the forming planet (essentially the planet forms in a prograde disk, accretes matter with a prograde angular momentum sense, and thus itself picks up a prograde rotation to match) - Sing (2017 - private communication). Retrograde spins are considered to originate from giant impacts during the early stages of planet formation, resulting in a massive change in the rotational angular momentum vector (i.e. switching the planet from prograde to retrograde rotation). As a result of this, constraints on the planet spins are of high scientific interest, because deviations of the axes of rotation may have been caused by impacts of large bodies during their early history, and these impacts may have a significant effect on the composition (and hence habitability) of the planetary atmosphere. Even the axes of rotation of the gaseous planets may have been affected by impacts on their rocky cores before these planets accumulated their large atmospheres of hydrogen and helium. Note that such gaseous atmospheres are considered to be accreted hydrodynamically, in flows quite different from those which govern the dynamics of planetesimals and lead to prograde rotation (i.e. the rotation of giant planets is likely to have been decided before they accrete their gaseous atmospheres).

Collisions are not the only way that a planet might lose/change its obliquity. For planets with short orbits ($\lesssim 10$ days), tidal dissipation theory (as applied to exoplanets orbiting their host stars) provides a mechanism by which the obliquity might be eroded, typically on time scales of < 1 Gyr (i.e. on timescales comparable to the current age of the planets). This erosion will suppress seasonal variations and eventually tidally lock the planet (a planet is tidally locked when its rotation period and orbital period are synchronised such that the same surface always faces the star), both of which may have consequences for the habitability of the exoplanet - (Heller et al. 2011a; Heller et al. 2011b; Li and Winn 2016).

Observational methods have also been proposed to probe both the rotation rates and obliquities of exoplanets from either oblateness measurements or variability due to surface inhomogeneities during a (primary) transit e.g. Hui and Seager 2002; Seager and Hui 2002; Barnes and Fortney 2003; Pallé et al. 2008; Kawahara and Fujii 2010; Fujii and Kawahara 2012, but these techniques require very high precisions (in excess of ~ 0.1 μmag). Thus we must turn to a new technique to measure these fundamental properties - the Rossiter-McLaughlin effect at secondary eclipse.

Before we introduce the *RMse*, we must discuss its precursor, the Rossiter-McLaughlin effect (first introduced by Rossiter 1924 and McLaughlin 1924). This technique allows us to measure the surface rotation rate of a distant, transiting exoplanet hosting, star. The essential theory is as follows: as a star rotates, half its surface becomes slightly blue-shifted (red-shifted) as it rotates towards (away) from the observer. Normally these shifts cancel each other out, but in the presence of a transiting exoplanet this is no longer the case (Figure 1.7). As an exoplanet transits over the stellar surface, it obscures some of the shifted light, leading to a net observed shift (with an opposite sense to that obscured); this shift can then be used to calculate both the rotation rate of the stellar surface (at the latitude of exoplanet transit) and the obliquity of the star, typically by matching the RM radial velocity anomaly (shift) to a model of the effect (such as Ohta et al. 2005) - see, for example, Winn et al. (2005) for more details.

A similar effect can be expected to take place for a rotating planet at secondary eclipse (i.e. when the planet is eclipsed by the host star). Much like the star in the (primary) Rossiter-Mclauglin effect, the surface of the planet will become slightly blue-shifted (red-shifted) as it rotates towards (away) from the observer. Normally this effect cancels out, however during secondary eclipse the surface of the star will occlude regions of the planetary surface, leading to a net radial velocity shift. This shift will be time dependent, leading to a radial velocity anomaly during ingress and egress (and zero radial velocity during the total (secondary) eclipse) that is dependent upon the rotation rate, the axial tilt, and the planets spin-orbit alignment (i.e. the angle between the planets spin-vector and the normal of the orbital plane). Thus if we can measure the anomaly, we might recover these important parameters.

But how can we measure/detect the *RMse*? Ground-based high-dispersion spectroscopy ($R \geq 20,000$) in the near-infrared has recently become successful in characterising the atmospheres of hot Jupiters (Snellen et al. 2010; Brogi et al. 2012; Birkby et al. 2013; Brogi et al. 2014; Schwarz et al. 2015). At high spectral resolution molecular absorption bands are resolved into individual lines allowing their robust identification by line matching with model templates/atmospheres (after the removal of any contamination). Thus we can now measure accurate radial velocities of transiting exoplanets.

This technique works as follows: As the planet orbits its star, the radial component of the planet orbital velocity changes by tens of km s^{-1}, enabling a discrimination of the resultant Doppler shifted planet spectrum from the steady telluric contamination (i.e. the contamination of the spectrum by the Earth's atmosphere). This separation can be enhanced via comparisons with (cross-correlations against) model spectra (which themselves can be obtained by creating a model hot-Jupiter atmosphere containing both the expected atmospheric components that contribute to the spectral lines, and a suitable temperature-pressure profile for the planet under consideration - for more information on this modelling, see, for example, Seager and Sasselov 2000 or Venot et al. 2012). One the Doppler-shifted lines have been identified, their Doppler shifts can be calculated and we are able to extract the time-dependent planetary radial-velocity curve, including the *RMse* induced anomaly, and thus attempt to extract the rotation rate and axial tilt/spin-orbit alignment.

The rest of this chapter is organised as follows. In section 4.2 we derive the planetary radial velocity anomaly due to the *RMse* effect. To derive this, we follow the methodology of Ohta et al. (2005), who found an analytic solution for the Rossiter-McLaughlin effect at primary eclipse, and show that their solution can equivalently be applied to the problem discussed here. Next, section 4.3 details the amplitude and shape of the *RMse* effect and discusses potential targets. Then in section 4.4 we discuss the potential applications of the *RMse* in light of both available and future instrumentation. Finally, section 4.5 is devoted to our conclusions.

4.2 Formalism of the Effect

We will now quantitatively formulate an expression for the radial velocity anomaly caused by the *RMse* effect for a two body problem consisting of a central star of mass m_s orbited by a planet of mass m_p. Figure 4.1 shows a schematic illustration of the top-down-view of the planet-star system, including the key angles required to derive the planets (and stars) radial velocity curve. In such a system, the radial velocity of the planet, as a function of

time, is as follows:

$$v_{\mathrm{rad},p} \approx \frac{m_s}{m_s + m_p} na \sin i \left[\sin\left(M + \overline{\omega}\right) + e \sin\left(2M + \overline{\omega}\right)\right]. \tag{4.1}$$

where $n = \frac{2\pi}{\mathrm{P_{orb}}}$ is the mean motion, $\mathrm{P_{orb}}$ is the orbital period, a is the semi-major axis of the orbit (see Figure 4.1), e is the eccentricity of the orbit, M is the mean anomaly, and $\bar{\omega}$ is the angle of the line of sight (both M and $\bar{\omega}$ are more fully defined in Figure 4.1). A fuller derivation of this equation can be found in both Murray and Dermott (1999) and Ohta et al. (2005), and in Appendix C we explore the use of this equation when modelling a planets radial velocity curve (as part of an investigation into the *RMse*).

We now look at what happens to the planets radial velocity around, and during, a secondary eclipse (i.e. when part of the rotating planetary surface is occluded). Essentially, like the Rossiter-McLaughlin effect for stars, an asymmetry in the planetary absorption/emission line profiles occurs, resulting in a anomaly in the radial velocity profile of the planet.

Here, we hope to show that the formalism of this anomaly is similar (if not almost identical) to the formalism for the primary Rossiter-McLaughlin effect: just changed to be from the perspective of a planet transiting a star to a star 'transiting' a planet. As such, we explore the (primary) Rossiter-McLaughlin effect formalism of Ohta et al. (2005), just from our altered perspective. For a full proof of the below derivation, see Appendix B.

Following Ohta et al. (2005), we initially set the coordinate system such that it is centred on the star, and its y-axis aligns/coincides with the observers line of sight (Figure 4.2a). In such a coordinate system, the planets position is described by the coordinates $\left(x_p, z_p\right)$, which correspond to the orbital plane position $\left(x_p\right)$ and the impact parameter (z_p - the observed 'vertical' distance between the centre of the star and the centre of the planet at mid-transit/eclipse). Whilst this coordinate system is well suited to calculating the planetary motion, and hence the radial velocity profile of the planet, it is not optimal for calculating the *RMse* anomaly.

As such, we transform to a new coordinate system (x', z') which is both: centred on the planet, and rotated such that both the z' axis is parallel to the sky-projected rotation axis

of the planet (i.e. parallel to Ω_p - see Figure 4.2b) and the real rotation axis lies within the $y' - z'$ plane (y' is once again aligned with the observers line of sight). In such a system, we also define both λ_p, which is the angle between the sky-projected rotation axis and the normal of the planetary orbit ($\hat{n_p}$), and I_p which is the angle between the planetary spin-axis and the y'-axis (i.e. I_p defines the sky-projection of the planetary rotation axis). In this coordinate system, and ignoring any effects of either differential rotation of the planetary surface or motions associated with atmospheric dynamics, a point on the rotating surface of the planet with coordinates (x', z') will move with a velocity

$$v_p = \Omega_p x' \sin I_p. \tag{4.2}$$

This motion will result in an associated Doppler shift of any radiation emitted from said point, taking the form

$$\left(\frac{\Delta\nu}{\nu}\right)_{\text{obs}} = \frac{\Omega_p x' \sin I_p}{c}, \tag{4.3}$$

with respect to an observer situated along the line of sight (the y'-axis).

Using this, and once again following the work of Ohta et al. (2005), we can now derive an expression for the total radial velocity anomaly due to the *RMse*, albeit in terms of surface integrals (Equation 4.9).

We start by considering a specific, absorption or emission, line whose intensity at the point (x', z') on the projected planetary surface is given by $I_\nu(x', z') = I(x', z')\, H(\nu)$, where $H(\nu)$ is the emission/absorption line profile. The observed flux can then be computed by integrating the **Doppler-shifted** intensity at each point over the entire, projected, planetary surface:

$$F_\nu = \iint \left(1 + \frac{\Delta\nu}{\nu}\right)^3 I(x', z')\, H(\nu - \Delta\nu)\, D^{-2} dx' dz', \tag{4.4}$$

where D is the distance between the planet and the observer. Note that the factor of $\left(1 + \frac{\Delta\nu}{\nu}\right)^3$ appears due to the Lorentz invariance of $\frac{I_\nu}{\nu^3}$. If we now focus our analysis onto a single emission line centred at $\nu = \nu_0$, the line profile $H(\nu)$ satisfies the following con-

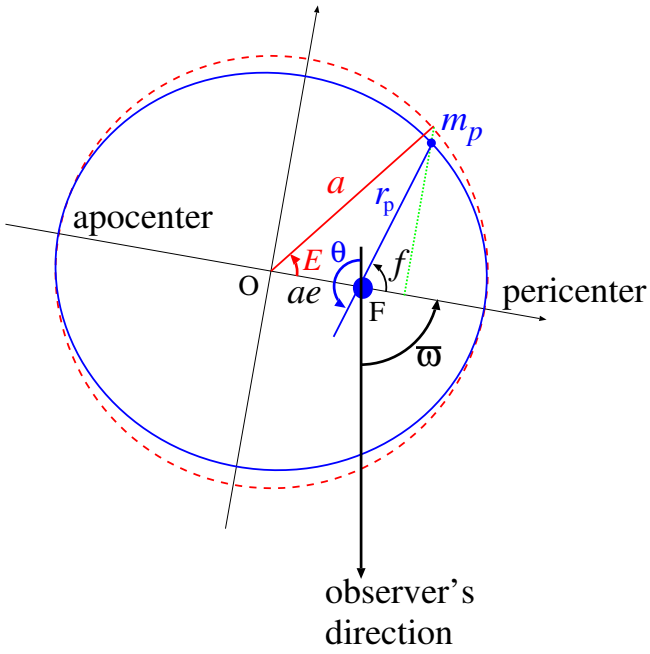

Figure 4.1: Schematic top down view of the planetary orbit. The star is located at point F, whilst the barycentre (common centre of mass) may be found at point O. As for the angles, the important ones are as follows: f is the true anomaly (the angular coordinate of the planet, as measured from the pericentre), E is the eccentric anomaly (the angular coordinate of the planet, centred on the barycentre, and projected onto a circle), $\bar{\omega}$ is the angle of the line of sight (essentially the angle between the observers line of sight and the pericentre), and M is the mean anomaly (the angular position, measured from pericentre, the planet would have if it moved in a circular orbit, with constant speed, and the same orbital period as its true eccentric orbit). Reproduced from Ohta et al. (2005).

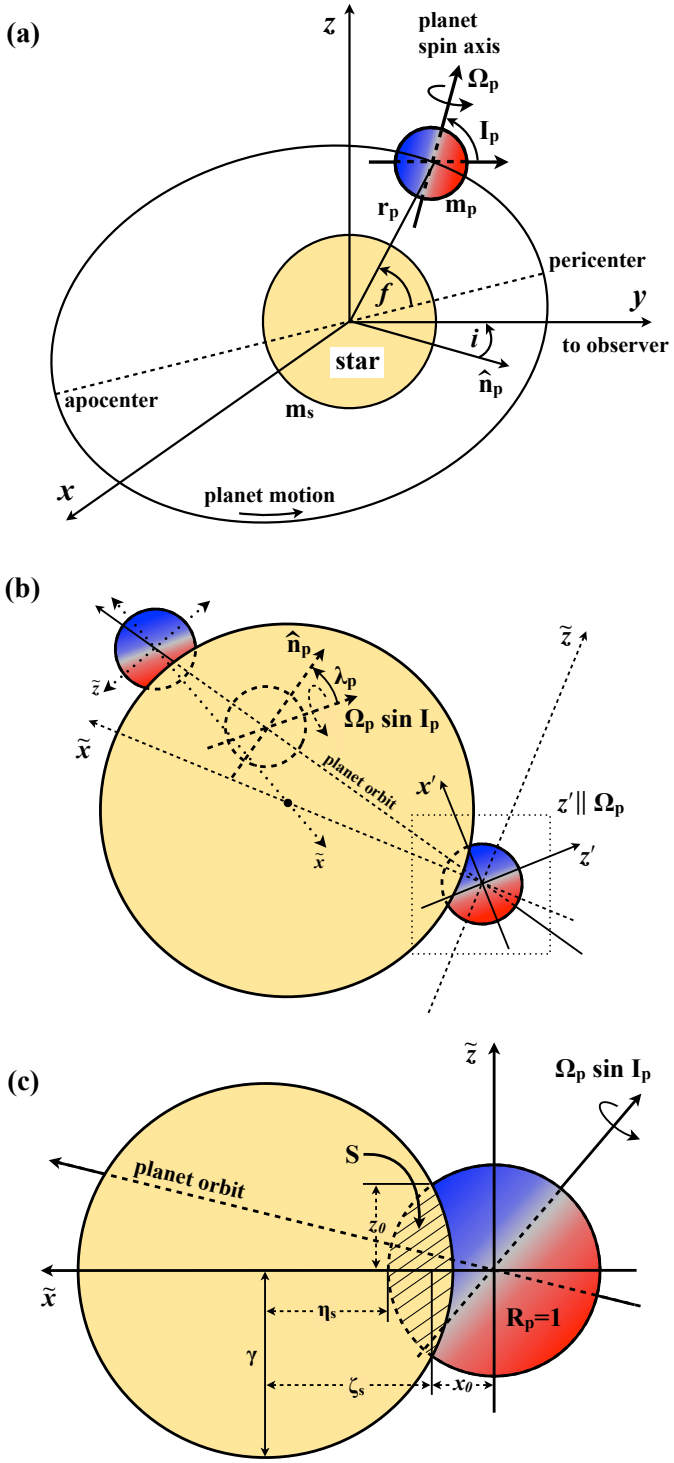

Figure 4.2: (a): Schematic illustration of the planetary orbit plane, spin axis, and the observer's line of sight; (b): Planet secondary eclipse ingress and egress phases and rotation axis; (c): A zoom of the planet and star configuration at ingress in the new coordinates.

ditions:

$$\int H(\nu)\, d\nu = 1 \tag{4.5a}$$

$$\int \nu H(\nu)\, d\nu = \nu_0. \tag{4.5b}$$

Furthermore, since $H(\nu)$ is supposed to be sharply peaked only around ν_0 (i.e. not significantly broadened), we have approximately

$$\int f(\nu) H(\nu)\, d\nu \approx f(\nu_0) \tag{4.6}$$

for an arbitrary smooth function $f(\nu)$.

Taking into account all of the above, we can now calculate the time-dependent shift of the line-profile weighted mean position $\bar{\nu}$ (mean Doppler-shift) due to the observed asymmetric occultation of the planetary surface during ingress and egress at secondary eclipse (i.e. the mean anomaly due to the *RMse*). Thus, using Equation 4.4 and the properties described in Equation 4.5 and Equation 4.6, we obtain (Ohta et al. 2005):

$$\bar{\nu} \equiv \frac{\int \nu F_\nu d\nu}{\int F_\nu d\nu} = \nu_0 \left[\frac{\iint \left(1 + \frac{\Delta\nu}{\nu_0}\right)^3 \left(\frac{\Delta\nu}{\nu_0}\right) I(x', z' dx' dz')}{\iint \left(1 + \frac{\Delta\nu}{\nu_0}\right)^3 I(x', z')\, dx' dz'} \right]. \tag{4.7}$$

Furthermore, since the amplitude of the *RMse* induced radial velocity shift should be small, it is safe to expand $\bar{\nu}$ up to the leading order in $\frac{\Delta\nu}{\nu}$ and then substitute in for Equation 4.3:

$$\begin{aligned} \bar{\nu} &= \nu_0 \left[1 + \frac{\iint \left(\frac{\Delta\nu}{\nu_0}\right) I(x', z')\, dx' dz'}{\iint I(x', z')\, dx' dz'} + O\left(\frac{\Delta\nu^2}{\nu_0^2}\right) \right] \\ &\approx \nu_0 \left[1 + \frac{\Omega_p \sin I_p}{c} \frac{\iint x' I(x', z')\, dx' dz'}{\iint I(x', z')\, dx' dz'} \right]. \end{aligned} \tag{4.8a}$$

Thus, the observed radial velocity anomaly due to the *RMse* can be expressed as:

$$\Delta v_p = -\Omega_p \sin I_p \frac{\iint x' I(x', z') dx' dz'}{\iint I(x', z') dx' dz'}. \tag{4.9}$$

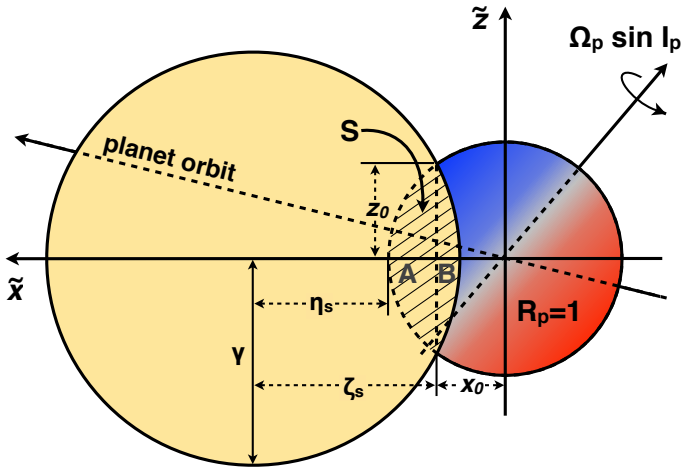

Figure 4.3: Schematic illustration of the planetary ingress at secondary eclipse, showing the overlap region (S) and how it is divided into two segments (A and B). This division greatly simplifies the integrals, allowing us to treat the overall integral as two circle segments with clearly defined limits based upon the points at which the stellar and planetary disks intersect $(x_0, \pm z_0)$.

In order to model the *RMse* we now need to evaluate the above integrals, which we do assuming a uniform model of the (unocculted) planets surface intensity profile $I(x', z')$:

$$I(x', z') = \begin{cases} I_o & \underbrace{x'^2 + z'^2 \leq R_p^2}_{\text{Planet Surface}} \oplus \underbrace{(x' - x'_s)^2 + (z' - z'_s)^2 \geq R_s^2}_{\text{Not The Stars Surface}} \\ 0 & \text{otherwise.} \end{cases} \tag{4.10}$$

where (x'_s, z'_s) is the location of the star at any given time, R_p is the radius of the planet and R_s is the radius of the host star. Note that we have limited the applicability of the *RMse* anomaly to both the ingress and egress of the secondary eclipse - at all other times the planet will either be fully visible or fully occluded. This condition can also be expressed by requiring that the following condition be satisfied: $R_s - R_p < (x'^2_s + z'^2_s)^{1/2} < R_s + R_p$.

Further to this limitation, and in order to simplify the computational task of solving the integrals, we introduce a new coordinate system that rotates in a time-dependent manner such that the stellar centre is always located along the new $\tilde{x}$-axis (see Figure 4.2b and Figure 4.3). This greatly simplifies the integral by making the occluded area both symmetric about the new $\tilde{x}$-axis, and the sum of two segments of a circle (regions A and B in Figure 4.3). This coordinate system, and its transformation from the (x', z') coordinate

system, is defined by the transform:

$$\begin{pmatrix}\tilde{x}\\ \tilde{z}\end{pmatrix} = \frac{1}{R_p\sqrt{x_s'^2 + z_s'^2}}\begin{pmatrix}x_s' & z_s'\\ -z_s' & x_s'\end{pmatrix}\begin{pmatrix}x'\\ z'\end{pmatrix}. \tag{4.11}$$

In this new coordinate system $(\tilde{x}, \tilde{z})$, the position of the star is given by:

$$\begin{pmatrix}\tilde{x}_s\\ \tilde{z}_s\end{pmatrix} = \begin{pmatrix}1+\eta_s\\ 0\end{pmatrix}, \tag{4.12}$$

where η is:

$$\eta_s = \sqrt{\frac{x_s'^2 + z_s'^2}{R_p^2}} - 1. \tag{4.13}$$

We can now also transform our planetary surface intensity profile to the new coordinate system:

$$I(\tilde{x}, \tilde{z}) = \begin{cases} I_0, & \tilde{x}^2 + \tilde{z}^2 \leq 1 \text{ and } (\tilde{x} - 1 - \eta_s)^2 + \tilde{z}^2 \geq \gamma^2, \\ 0 & \text{otherwise,} \end{cases} \tag{4.14}$$

where $\gamma = R_s/R_p$ is the ratio of the stellar and planetary radii, and $R_p = 1$ (i.e. we normalise to the planets radius).

Finally, we can also transform the moments of intensity (the integrals in Equation 4.9) to our new, time-dependent coordinate system:

$$\iint x' I(x', z')\,\mathrm{d}x'\,\mathrm{d}z' = -\frac{R_p^2}{1+\eta_s}\iint_S (x_s'\tilde{x} - z_s'\tilde{z}) I(\tilde{x}, \tilde{z})\,\mathrm{d}\tilde{x}\,\mathrm{d}\tilde{z}, \tag{4.15a}$$

$$\iint I(x', z')\,\mathrm{d}x'\,\mathrm{d}z' = R_p^2\left[\pi I_0 - \iint_S I(\tilde{x}, \tilde{z})\,\mathrm{d}\tilde{x}\,\mathrm{d}\tilde{z}\right]. \tag{4.15b}$$

The range of the integrals is denoted with S and is defined as the star-planet overlapping region (shaded area) in Figure 4.2c (which is the sum of A and B in Figure 4.3):

$$\iint_S \mathrm{d}\tilde{x}\,\mathrm{d}\tilde{z} = \underbrace{\int_{x_0}^{1}\mathrm{d}\tilde{x}\int_{-\sqrt{1-\tilde{x}^2}}^{\sqrt{1-\tilde{x}^2}}\mathrm{d}\tilde{z}}_{A} + \underbrace{\int_{\tilde{x}_s-\gamma}^{x_0}\mathrm{d}\tilde{x}\int_{-\sqrt{\gamma^2-(\tilde{x}-\tilde{x}_s)^2}}^{\sqrt{\gamma^2-(\tilde{x}-\tilde{x}_s)^2}}\mathrm{d}\tilde{z}}_{B}, \tag{4.16}$$

where $(x_0, \pm z_0)$ are the points at which the planetary and stellar circles intersect:

$$x_0 = 1 - \frac{\gamma^2 - \eta_s^2}{2(1+\eta_s)}, \tag{4.17a}$$

$$z_0 = \sqrt{1 - x_0^2} = \frac{\sqrt{(\gamma^2 - \eta_s^2)[(\eta_s + 2)^2 - \gamma^2]}}{2(1+\eta_s)}. \tag{4.17b}$$

Taking all of this into account, we are now ready to analytically integrate the moments of intensity (Equation 4.15) and thus find the radial velocity anomaly associated with the *RMse*. The moments of intensity, after integration, take the following forms:

$$\iint_S I(\tilde{x}, \tilde{z}) \mathrm{d}\tilde{x}\, \mathrm{d}\tilde{z} = I_0 \left[\sin^{-1} z_0 - (1+\eta_s) z_0 + \gamma^2 \cos^{-1} \zeta/\gamma \right], \tag{4.18a}$$

$$\iint_S (\tilde{x} x_s' - \tilde{z} z_s') I(\tilde{x}, \tilde{z}) \mathrm{d}\tilde{x}\, \mathrm{d}\tilde{z} = I_0 x_s' (1+\eta_s) \left[- z_0 \zeta + \gamma^2 \cos^{-1} \zeta/\gamma \right], \tag{4.18b}$$

where we have introduced ζ to simply the final expressions:

$$\zeta = 1 + \eta_s - x_0 = \frac{2\eta_s + \gamma^2 + \eta_s^2}{2(1+\eta_s)}. \tag{4.19}$$

Substituting these integrals into Equation 4.9 gives us our final expression for the radial velocity anomaly (during ingress or egress), due to the *RMse*, as a function of the stars position (x_s'):

$$\Delta v_p = \Omega_p x_s' \sin I_p \frac{-z_0 \zeta + \gamma^2 \cos^{-1}(\zeta/\gamma)}{\pi - \sin^{-1} z_0 + (1+\eta_s) z_0 - \gamma^2 \cos^{-1}(\zeta/\gamma)}. \tag{4.20}$$

This final expression is equivalent to the expression derived in Ohta et al. (2005), just from the point of view of a planet being occluded by a star. We can now use this to explore the shape, and amplitude, of the *RMse* radial velocity anomaly for a number of different planet-star configurations and spin-orbital alignments.

4.3 *RMse* effect amplitude and shape

We now use Equation 4.20 to explore the shape and amplitude of the *RMse* effect - specifically focusing on what happens as both the impact parameter ($b = \frac{a}{R_*} \cos i$, where i is the

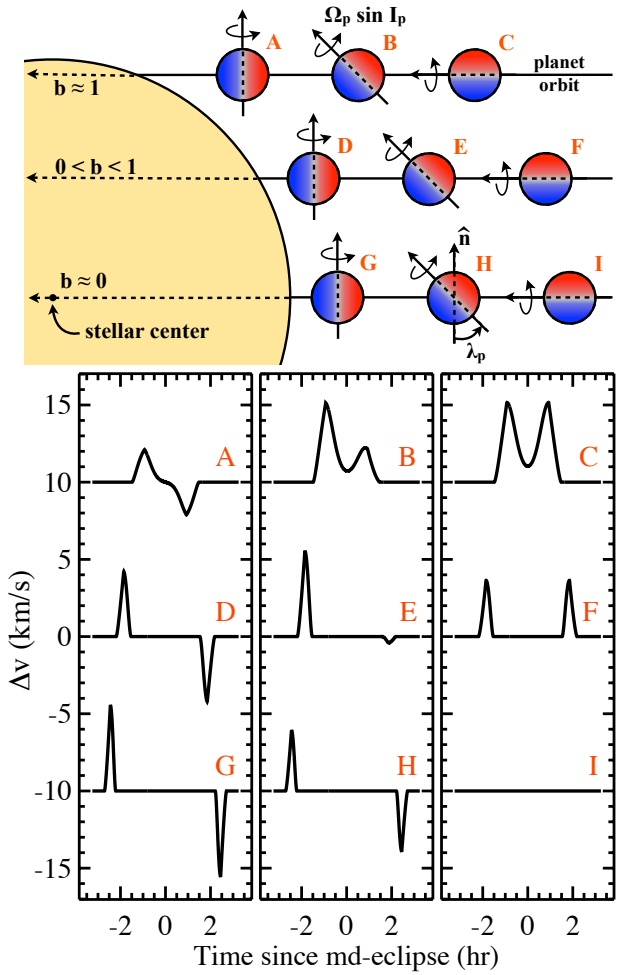

Figure 4.4: Illustration of planet radial velocity curve anomaly due to *RMse* effect for nine (representative) prograde spin-orbital alignments, assuming a Jupiter-like hot-Jupiter. The curves are plotted with a constant 10 km s^{-1} offset for clarity. Cases A to I correspond to the top planet-star configurations. The curves flip and invert as λ_p increases to 360° and when b < 0.

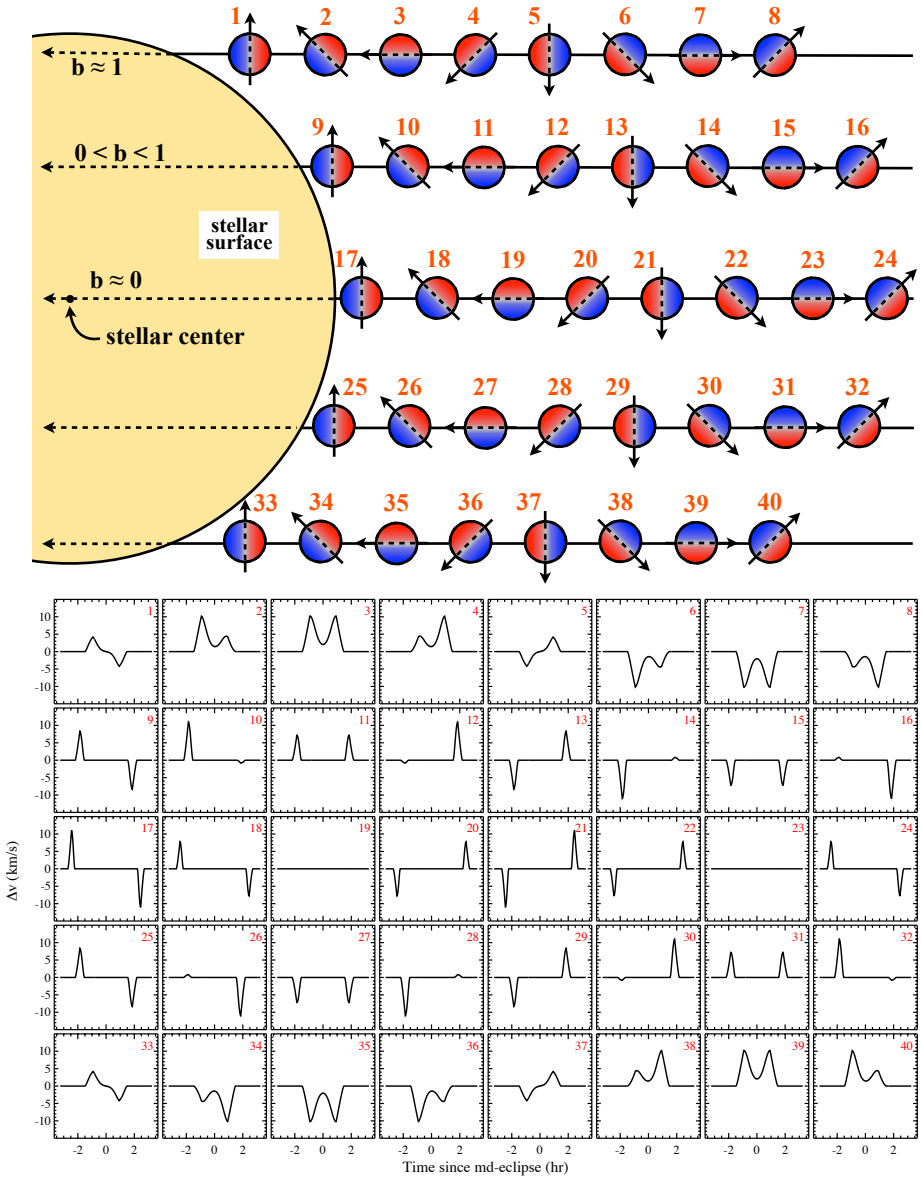

Figure 4.5: Illustration of planet radial velocity curve anomaly due to *RMse* effect for a complete set of forty different spin-orbital alignments, assuming a β Pic b like hot-Jupiter. Cases 1 to 40 correspond to the planet-star configurations shown in the top panel. The curves flip and invert as λ_p increases to 360° and when b < 0, creating a series of symmetries, which allows us to reduce the system to nine representative cases (Figure 4.4)

.

orbital inclination) and the spin-orbital alignment (λ_p - the angle between the normal of the orbital plane and the spin axis of the planet) are changed. Figure 4.4 shows the *RMse* induced radial velocity anomalies for nine representative cases with prograde ($\lambda_p \leq 90$ - i.e. the planet rotation and orbital motion are in the same direction) planetary rotation. These representative cases cover the full range of typical *RMse* results, with other scenarios (such as retrograde ($\lambda_p \geq 90$) rotation) having results symmetric to these nine - this is illustrated in Figure 4.5, which explores a full set of forty planet-star configurations, and in which the symmetries can be observed.

4.3.1 Parameters for an *RMse* Investigation

The *RMse* computations in Figure 4.4 assume a Jupiter-like planet, with an observed ($v \sin I_p$) equatorial rotational velocity of 12.6 km s^{-1}, on a 20 day orbit around a Sun-like star. Note that this orbital period is significantly longer than that of a typical hot-Jupiter: typical hot-Jupiters have an orbital period on the order of a few days, and as such orbit very closely to their host stars. This short orbital period presents us with a couple of problems; firstly a planet which orbits very closely to its host star will present difficulties when trying to measure its radial velocity profile (and so detect the *RMse*), and secondly, it has been observed that close-in exoplanets are typically tidally locked: that is that the rotation period and orbital period are synchronised such that the same surface always faces the star. This can be seen if we look at the time (τ_{syn}) it takes for the tidal effects of the star on the planet to spin-down the planets rotation such that it becomes synchronised with the orbital period:

$$\tau_{syn} \approx Q_p \left(\frac{R_p^3}{G M_p} \right) (\omega - \omega_s) \left(\frac{M_p}{M_*} \right)^2 \left(\frac{a_p}{R_p} \right)^6 , \tag{4.21}$$

where Q_p is the planets tidal dissipation factor (essentially a measure of how resistant a planet is to tidal factors: e.g. how quickly the energies associated with tidal forces/deformations are dissipated), R_p is the radius of the planet, M_p is the mass of the planet, ω is the rotational angular velocity of the planet, ω_s is the synchronised rotational angular velocity (i.e. the orbital angular velocity), M_* is the mass of the host star, and a_p is the semi-major-axis of the planetary orbit (Goldreich and Soter 1966; Guillot et al. 1996). If we assume that

$Q_p \sim 10^5$ (Correia and Laskar 2010), and that the orbital periods are of the order of about 4 – 20 days, we find a synchronisation time τ_{syn} of between $\sim 10^6$ (4 day orbit) and 10^9 (20 day orbit) years - i.e. ages on the order of the currently observed transiting hot-Jupiters (and hot-Jupiter hosting stars). Thus, by the time we observe them, short orbit (close in) exoplanets are typically tidally locked due to tidal forces.

As for our choice of the value of $v \sin I_p$, this is driven by the correlation between the equatorial rotational velocities and masses of solar system planets, which suggests that more massive planets typically rotate faster (Hughes 2003). This is reinforced by measurements of the rotational velocity of β Pic b ($v \sin I_p \sim 25$ km s−1), whose position of the spin velocity-mass relation is in line with solar system results (Snellen et al. 2014), and which we use for our expanded set of results (Figure 4.5). Thus our value of 12.6 km s^{-1} represents a decent exemplary rotation rate for a typical Jupiter-like hot-Jupiter.

4.3.2 Analysis of an *RMse* Investigation

We now look at Figure 4.4 and Figure 4.5 in more detail. The maximum amplitude of the *RMse* effect occurs for central eclipses ($b = 0$) with $\lambda_p = 0°$ or 180° (i.e. when the rotation axis is either aligned or anti-aligned with the normal of the orbital plane). In the case of a Jupiter-like hot-Jupiter (Figure 4.4), this corresponds to an amplitude of around ±6 km s^{-1}, whereas for the β Pic b like case (Figure 4.5), we find an *RMse* effect on the order of about ±11 km s^{-1}. However, the minimum *RMse* effect also occurs for central eclipses ($b = 0$), this time with $\lambda_p = 90°$ or 270° (i.e. when the rotation axis is perpendicular to the normal of the orbital plane): here the effect has zero amplitude as equal amounts of red and blue-shifted surfaces are occluded at all times. Turning to the full set of cases, Figure 4.5, we find that, for the most part, if you know the impact parameter of the exoplanet (which you can recover via other observational techniques, such as measurements of the primary transit), there exists little to no degeneracy between λ_p and $v \sin I_p$ - a measurement of the *RMse* should allow you to pin down both because of the unique signature of the radial

velocity anomaly curve. To be more specific, its the shape of the radial velocity anomaly curve, the ratio of the peaks in the anomaly curve, and the amplitude of the peaks taken together that can be used to identify a unique solution. This can seen in Figure 4.6, where a fitting procedure operating on mock data recovers both λ_p and $v \sin I_p$ to within their (observational) uncertainties. However, this is not the case for $b = 0$: for $b = 0$, λ_p is fully degenerate with $v \sin I_p$ and no unique solution exists for the *RMse* anomaly.

As such, if you can observe the anomaly, and except in the unusual case of $b = 0$, the *RMse* provides a mechanism by which both the surface rotation rate and the spin-orbit alignment might be recovered.

4.4 An observational perspective for *RMse*

In order to investigate the observational possibilities of the *RMse* effect we must turn to mock observational data, which we generate for two telescopes, one 8m class and one 40m class, each of which is equipped with a near-infrared, high spectral resolution (i.e. R $\sim 100,000$) spectrometer (i.e. a spectrometer of the same class as that installed on the E-VLT - CRIRES). We assume that the orbit of the planet is highly constrained, and with enough precision to be subtracted prior to the search for the *RMse* radial velocity anomaly. Further to this, we calibrate our simulation by adopting a base precision of $\sim 5\,\mathrm{km\,s^{-1}}$, the same as was achieved by Birkby et al. (2013) at 3.2 μm for water detection in the day side atmosphere of HD 189733b.

This precision is then scaled by the square root of the number of collected spectra (i.e. 48 in Birkby et al. 2013), the ratio of the employed spectral coverage (assuming a hypothetical high-resolution spectrometer with a wavelength coverage of 400 nm), and the square root of the ratio of the target planet-to-star-flux-ratio and HD 189733b's planet-to-star-flux-ratio (i.e. 1.3×10^{-3} - based on data from Birkby et al. 2013). This final factor plays a critical role in our mock data calculations as it accounts for the strength of the planetary signal, which is determined by the planet-to-star flux contrast ratio. This contrast ratio decreases from $\sim 10^{-3}$ to $\sim 10^{-6}$ as the planetary orbital period is increased from ~ 0.5 day to 20 days (i.e. long orbit planets are less irradiated, thus dimmer, and so harder to detect). Finally,

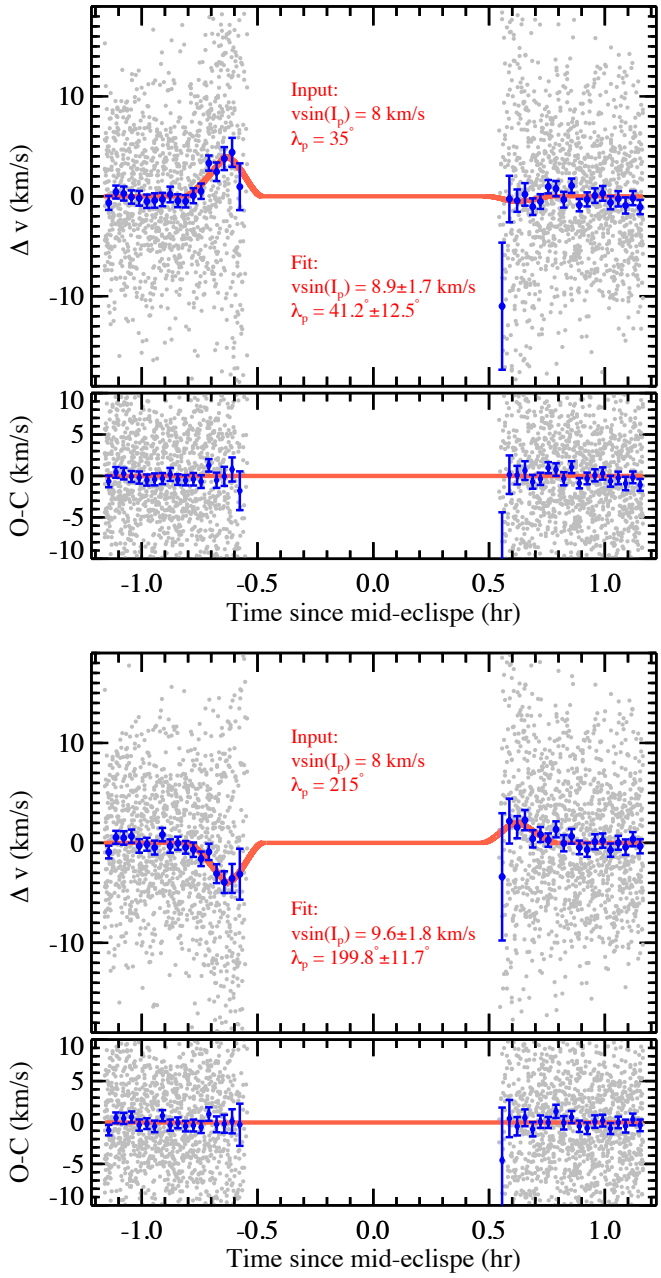

Figure 4.6: Mock data (grey dots) illustrating the *RMse* effect, best-fit radial velocity curve (red lines - upper panels), and radial velocity residuals (lower panels). Top and bottom figures illustrate the cases of a WASP-19 system, assuming tidally synchronised prograde and a retrograde rotating planet, respectively. The blue symbols indicate the radial velocity curves binned into 2 min intervals.

we also include factors which account for the sampling rate (with respect to the telescope diameter), the brightness of the host star, and the change in the planetary flux during secondary eclipse (which we achieve by factoring the radial velocity uncertainties with the square-root of the flux of a secondary eclipse Mandel and Agol (2002) model with a unity out-of-eclipse baseline and zero in-eclipse flux - i.e. by factoring by the fractional flux of the planet).

Figure 4.6 shows mock observational data generated for an 'idealised' system/detector: a 40 m-class telescope, a hypothetical planet hosting star of brightness K = 5.5 mag (i.e. similar to the currently brightest transiting hot-Jupiter hosting star HD 189733), and a hypothetical, tidally locked, planet with the physical properties of WASP-19 b (i.e. large, giving a strong rotational signal even when synchronised, with a very short orbit, leading to a high planet-star contrast making it's signal easier to detect). We assumed either a prograde (top panels - $\lambda_p = 35°$) or a retrograde (bottom panels - $\lambda_p = 215°$) rotation with $v \sin I_p = 8\,\mathrm{km\,s^{-1}}$.
For these two (idealised) systems, we then performed an *RMse* fit to the mock data utilising a Levenberg-Marquardt least-squares minimization to optimize the fit, and estimate both $\lambda_p / v \sin(I_p)$ and their associated uncertainties (Markwardt 2009). We find the planetary *RMse* to be well-detected (i.e. with at least a $\sim 5\sigma$ confidence) when combining **nine** secondary eclipses (i.e nine orbits). At this signal level, the Levenberg-Marquardt fit returns values of λ_p and $v \sin(I_p)$ that match the input system data well (i.e. agree within the uncertainties).

We next explored the potential of an 40 m-class telescope to detect the *RMse* effect in the *current* brightest transiting exoplanet system HD 189733 b. Assuming a synchronised planet rotation (i.e. *RMse* amplitude of $\sim 1\,\mathrm{km\,s^{-1}}$) and $\lambda_p > 0°$ we find that around **fifty** secondary eclipses (orbits) need to be co-added to detect the spin/alignment of HD 189733 b. Again, λ_p and $v \sin(I_p)$ are well constrained.

Finally, we investigated the potential of a much smaller 8 m-class telescope to detect the *RMse* effect in our idealised system (i.e. K=5.5 host star with a WASP-19b-like planet and synchronised rotation). We find that around **fifty** secondary eclipses (orbits) will have

to be co-added in order to detect the *RMse* effect at a $\sim 3\sigma$ confidence. Once again, λ_p and $v \sin(I_p)$ are also well constrained.

4.5 Discussion and Conclusions

In this chapter, we have introduced a new method by which a transiting exoplanets rotation rate and spin-orbit alignment (axial tilt) might be measured: the Rossiter-McLaughlin effect at secondary eclipse (*RMse*). We have investigated both the formalism and observational implications of the effect, exploring how the *RMse* relates to the (primary) Rossiter-McLaughlin effect, and the observational equipment/techniques required to both quantify and leverage the effect.

In section 4.2 we have shown that the formalism of the effect, observable only at ingress/egress, is the same as for the (primary) Rossiter-McLaughlin effect, with just the coordinate system shifted from the perspective of a star being transited by a planet, to a planet transited by a star (for a full, mathematical, proof of this, see Appendix B). We achieve this by considering a relatively simple model of the (primary) Rossiter-McLaughlin effect as formulated by Ohta et al. (2005). Whilst more accurate, and mathematically complicated, models exist (such as the RM effect models of Hirano et al. 2011), the formalism of Ohta et al. 2005 provides a conservative estimate of the radial velocity amplitude, and is precise enough to illustrate the *RMse* effect and its mathematical/physical links to the (primary) Rossiter-McLaughlin effect.

As part of this relatively simple model, our analysis of the *RMse* assumes a rather idealised target exoplanet: the planet is rigidly rotating (i.e no differential rotation), exhibits no limb darkening, and is uninfluenced by any atmospheric dynamics. Whilst the inclusion of differential rotation or limb darkening would require us to reformulate our expression for the *RMse* (by changing the surface intensity profile - Equation 4.10 - a possibility we leave open for future work), we can investigate the inclusion of atmospheric dynamics in a more qualitative manner.

This qualitative investigation is possible because the radial velocity anomaly associated with the *RMse* is expected to be degenerate with respect to rotation, atmospheric dynamics, and winds (i.e. atmospheric dynamics can either enhance or suppress the *RMse* anomaly associated with planetary rotation). In exoplanets, atmospheric dynamics are expected to become increasingly important as we move to shorter orbital periods (i.e. towards the more easily detected planets). This can be linked to the increased levels of solar irradiation that short orbit planets experience (Kataria et al. 2015). Typically, in hot-Jupiters, these increased atmospheric dynamics take the form of a super-rotating equatorial jet (with wind speeds on the order of the rotation speed) - an example of these equatorial jets can be seen in Figure 1.8 (for more details, see, e.g. Showman et al. 2008; Showman et al. 2009; Mayne et al. 2014; Mayne et al. 2017). Therefore it is expected that the observed radial velocity curves of many short-orbit (close-in) exoplanets may differ significantly from that assumed in this work, with super-rotating jets significantly enhancing the observed radial velocity signals. Whilst these atmospheric jets do pose a problem when trying to measure the rotation rate of short-orbit exoplanets, its not as bad as it first appears. Since short-orbit exoplanets are expectedly to 'rapidly' synchronise their rotation rate (i.e. become tidally locked), and inorder for the *RMse* effect to occur the planet must transit (thus giving us access to the orbital period), we can remove the rotation from any measured *RMse* anomalies, leaving us with just the contribution of the atmospheric jet (thus allowing us to characterise the jets). Furthermore, when wide coverage, high dispersion, spectroscopy capable of providing per-point precisions on the order of $\sim 1\,\mathrm{m\,s}^1$ becomes available (hopefully with the commissioning of upcoming 40m class telescopes), it may be possible to probe the probe atmospheric dynamics with altitude, using the same physics used to characterise the atmospheres of transiting planets (essentially a transiting exoplants appears to change size, with wavelength, as different elements, with varied masses and hence scale-heights, absorb/emit at different wavelengths - for more information see, for example, Charbonneau et al. 2002; Burrows 2014; Sing et al. 2016). We leave both this possibility, and the possibility of using a reformulated, longitudinally-varying, *RMse* formalism (which may provide a powerful tool to investigate both equatorial jets and offset-hot-spots that have been long observed in GCM models of hot-Jupiters) for future work.

Planetary variations are not the only thing that might affect the measured/detected *RMse* anomaly. It is also possible that, in certain circumstances, stellar activity or stellar pulsations (i.e. stellar variability) may produce a radial velocity anomaly that mimics those induced by the orbital motion, or rotation, of an exoplanet. This may lead to the misinterpretation of radial velocity variations, especially when those variations have periods less than or equal to the stellar rotation period (Lagrange et al. 2010). One source of stellar variability that operates on these timescales is starspots (regions of the photosphere that appear dark due to a strong magnetic flux-tube locally suppressing convection): these regions typically have lifetimes on the order of a few stellar rotation periods, and, since they are associated with the stellar surface, rotate into and out of view. As a result of this, starspots can induce both distortions in the stellar spectral line profiles that may lead to residual radial velocities that mimic an exoplanets radial velocity curve, or changes in the observed stellar intensity that mimic an exoplanet transit (Roettenbacher et al. 2013). Not even co-added observations obtained over multiple nights are safe from this effect, with starspots able to significantly affect the fit to the co-added data.

Fortunately the *RMse* effect should be fairly immune to the effects of starspots. To start with, a typical *RMse* observation would last for ~ 0.8 h on each of the ingress and egress phases of a WASP-19b-like secondary-eclipse (see Figure 4.6). This time interval is significantly shorter than the rotation periods of the typical planet hosting stars (which range from around 10 to 40 days - Paz-Chinchón et al. 2015), and so also significantly shorter than the period that starspot contamination is expected to operate on. In addition to this, starspots are expected to produce sine-wave-like radial velocity variations (i.e. markedly different from the *RMse* anomaly) with amplitudes of upto a few hundred $\mathrm{m\,s^{-1}}$ in the optical (and significantly reduced at near infrared, where where the contrast between the photosphere and cool star spots (e.g. $\Delta T \sim 550$K) is significantly reduced). Thus, if present, any residual stellar signal caused by starspots would be significantly smaller than the expected 1-2 $\mathrm{km\,s^{-1}}$ amplitude of the *RMse* anomaly for the closest orbiting synchronized planets. This contamination becomes even smaller than that for non-synchronised planets on longer than 20 day orbits. Only in the case of a highly evolved,

tidally-locked, planet (i.e. a typical hot Jupiters) with an orbital period of between ~ 4 and ~ 20 days could the starspot induced residual significantly affect radial velocity observations when co-added. However, such planets are expected to have *RMse* anomalies much smaller than $1\,\mathrm{km\,s^{-1}}$ and would therefore be difficult targets by definition. Thus, with current, and near future, observational techniques, any planet that has a detectable *RMse* effect should be resilient to the effects of starspots (and hence stellar activity/variability) on its associated radial velocity anomaly.

Above, we have alluded to the *RMse* anomaly, but what form does it take? In section 4.3 we explored the *RMse* induced radial velocity anomaly, finding it to be an almost unique signature of a planets (projected) rotation-rate and spin-orbit alignment, allowing for the accurate recovery of both quantities (which we explore in section 4.4). We say almost because these two quantities become degenerate for cases in which the planetary orbit passes through the centre of the stellar disk (i.e. when the impact parameter b is zero): no unique solution exists for both the rotation rate and the spin-orbit alignment. We also explored typical amplitudes for the *RMse* effect in a number of different scenarios, finding radial velocity anomalies on the order of a few $\mathrm{km\,s^{-1}}$ for both a Jupiter-like hot-Jupiter ($6\,\mathrm{km\,s^{-1}}$ amplitude), and a β Pic b like planet ($11\,\mathrm{km\,s^{-1}}$). However, in both the cases considered above, we assumed a non-synchronised planet (i.e. not tidally locked): exoplanets with short-orbits typically have their rotation 'spun-down' by tidal effects. Thus these tidally locked planets typically rotate slowly, resulting in a smaller (and more difficult to detect) *RMse* anomaly. Yet, as we discuss below (and in section 4.4), they also our most likely candidates for *RMse* observations due to their enhanced detectability (high contrast ratio). Examples of these tidally locked planets (and their maximal *RMse* amplitude) include WASP-103 b ($\sim 3.7\,\mathrm{km\,s^{-1}}$), WASP-12 b ($\sim 3.4\,\mathrm{km\,s^{-1}}$), and WASP-19 b ($\sim 3\,\mathrm{km\,s^{-1}}$).

As shown in section 4.3, the strongest *RMse* signal is expected for planets exhibiting non-synchronized rotation, i.e. planets on longer than 20 day orbits, with a typical $v \sin I_p$ $12.5\,\mathrm{km\,s^{-1}}$ or more. However, such planets exhibit lower temperatures (i.e. $<$ 700 K), compared to the typical, short-orbit, hot-Jupiters giving a small planet-to-star flux

contrasts (i.e. $\sim 10^{-6}$ or lower at $\sim 3\,\mu$m). This makes the detection of the planetary radial velocity signature, and hence the *RMse* anomaly, an extremely challenging, if not impossible, task, even when using one of the upcoming 40 m class telescopes to observe a long-orbit hot-Jupiter around a star brighter than any known exoplanet host (i.e. K $\sim$ 6). As such, we must turn to either tidally locked, short-orbit, exoplanets with low-amplitude *RMse* anomalies or look at more unusual cases.

One such unusual case could be young planets which have not yet become synchronised. Observations using high-dispersion, near-infrared spectroscopy have currently constrained the rotational rate of the only one such case (β Pic b) from rotationally broadened absorption lines (Snellen et al. 2014). An important opportunity could exist if the orbital orientation of this planet allows for transits and secondary eclipses, because the large brightness of the host star (i. e. K $\sim$ 3.5 mag) and the fast spin of the planet (i. e. $v \sin I_p \sim 27\,\mathrm{km\,s^{-1}}$) would produce a strong and detectable *RMse* anomaly.

Another interesting opportunity could be offered by transiting brown dwarfs with orbital periods larger than 10-20 days. Such systems introduce high flux contrasts between the star and the brown dwarf in the near-infrared which, in the case of a bright host star (i. e. K $\sim$ 5 mag), could provide an opportunity to probe the spins and latitudinal radial velocity maps of these objects.

These are just some examples of possible targets for the *RMse* effect. In the near future, the Next Generation of Transit Surveys (NGTS), the Transiting Survey Satellite (TESS) and the Planetary Transits and Oscillations of stars (PLATO) projects are expected to significantly expand the sample of known exoplanets hosted by bright stars (i.e. brighter than K $\sim$ 9.5 mag) and hence to provide more targets suitable for the detection of the *RMse* radial velocity anomaly.

To conclude the conclusion, we have shown that the formalism of the effect, observable only at ingress/egress, is the same as in the (primary) Rossiter-McLaughlin effect, with just the coordinate system shifted from the perspective of a star being transited by a planet, to a planet transited by a star (and fully derived this - Appendix B). We then used this analytical description to create a model of the effect, investigating typical *RMse* anomalies for both Jupiter-like and β Pic b-like hot-Jupiters orbiting Sun-like stars. We

found anomalies on the 10km/s scale, as well as degeneracies and symmetries between different scenarios. We also investigated the observational implications of the effect, finding that the anomaly is most easily detected for large (and preferably unsynchronised) short-orbit exoplanets hosted by bright stars when using the upcoming 40m-class telescopes (e.g. the E-ELT). Further to this, detections by smaller telescopes (e.g. 8m) are only possible in optimal scenarios (i.e. bright star with a large, short-orbit, planet). The *RMse* effect provides a powerful observational probe, one we hope will become prominent during future studies with the upcoming 40m class of telescopes.

Chapter 5

Anelastic Models of Fully-Convective Stars: Differential Rotation, Meridional Circulation, and Residual Entropy

> *"Perfection. That's what it's about. It's those moments. When you can feel the perfection of creation. The beauty of physics, you know, the wonder of mathematics. The elation of action and reaction, and that is the kind of perfection that I want to be connected to."*
>
> *— Sam Anders, Battlestar Galactica*

Declaration: This work was conducted in collaboration with Matthew Browning, who provided that initial idea and has assisted in formation on our analytical techniques. We have also benefited from useful conversations with Nick Featherstone and Mark Miesch, who will be co-authors on the final manuscript (in prep). The vast majority of the work and analysis presented in this chapter is the work of the author.

5.1 Introduction

Fully convective stars are among the most common in the night sky, and in recent years have become major targets in the search for habitable exoplanets, thanks both to the location of their habitable zones and their sheer abundance (Kroupa 2002; Seager 2013; Burke et al. 2014; Barnes et al. 2015). Despite this, our understanding of the internals of these vitally important stars is still limited: broadly, we expect these may differ appreciably from what is realised in more massive stars like our Sun, which possess both a convective envelope and a radiative (stable) layer below (see e.g. Durney et al. 1993). In recent years, a number of numerical studies have investigated these stars, via the careful application of 3D convective simulations, with varying degrees of complexity (e.g. Dobler et al. 2006; Browning 2008; Yadav et al. 2015). These prior simulations have revealed, for example, that fully convective stars drive persistent differential rotation in some regimes; that the flows act effectively as magnetic dynamos; and that the dynamo-generated magnetism can have some impact on the flows. But many theoretical aspects that have attracted significant attention in the *Solar* dynamics community in recent years has not yet been explored in these lower-mass objects. In particular, no prior work has systematically addressed the *meridional* flows that might be established in these objects, and how these are linked to the zonal flow of differential rotation, even though these meridional flows play a crucial role in many mean-field models of the dynamo process (e.g., Jouve and Brun 2007; Dikpati and Charbonneau 1999). Here, we explore these issues using a series of 3D simulations of convective flows in a global, spherical geometry using the anelastic MHD approximation. Our simulations, conducted primarily using the open-source code *Rayleigh*, allow us to constrain how differential rotation and meridional circulation vary as stellar parameters (like rotation rate or luminosity) are varied, and how these may be influenced by magnetism. The simulation set up employed here is more idealised than that considered in some prior models (e.g., Browning 2008); by a systematic exploration of parameter space, we provide a crude "mapping" between the more easily-reproducible models employed here and the more intricate situations considered in some prior work. Finally, we take this opportunity to investigate how a theory proposed by Balbus (2009), linking isorotation and residual entropy contours in sun-like stars, translates to the fully convective regime.

In this section, we briefly review prior work on the internal dynamics of stars like the Sun, and contrast this with what has been found for fully convective objects. We also provide a brief introduction to the theory of Balbus (2009), which also partly motivates the work described here, before outlining the plan of this chapter.

5.1.1 The Internal Dynamics of Sun-Like Stars

The quest to understand how our nearest star the Sun produces and transports energy dates back to ancient times (e.g., Guthrie (1979)). In the modern era, these have been probed extensively using both observations and theoretical modelling. Observationally, particularly crucial insights have come from either surface measurements of convective flows and of magnetism, for example by the space-based instruments on the SOHO mission (Domingo et al. 1995) or the Solar Dynamics Observatory (Pesnell et al. 2012; Lemen et al. 2012; Woods et al. 2012; Schou et al. 2012), and via helioseismic inversions arising from those measurements. These provide, among other constraints, a reliable measure of the time-averaged zonal velocity profile $\Omega(r, \theta)$ throughout most of the solar convection zone (SCZ, see Thompson et al. 2003; Howe 2009, for more details), but currently do not reveal details of the meridional circulation (Howard and Labonte 1980; Gough 1985; Christensen-Dalsgaard et al. 1996). As for models, a number of different approaches have been employed, ranging from mean field models (which parametrise the small-scale convective momentum and energy transport in order to solve for mean flows and fields – e.g. Rempel 2006a) to non-linear spherical shell simulations (see Gilman 1976; 1977; 1978; 1979; 1980, for examples of pioneering studies in this area), which allow for a more complete view of the internal dynamics.

A more detailed overview of these observational and theoretical findings is contained in the Introduction to this thesis; here we briefly review only a few salient aspects that inform our work here. Crucially, helioseismology has revealed the surface differential rotation pattern of the Sun – with a fast equator and a slower pole – largely persists through the bulk of the convection zone, but transitions rapidly to nearly solid-body rotation in a narrow region at the base of that zone (Spiegel and Zahn 1992). That region of shear, called the tachocline, was not anticipated but is now widely thought to play a central role

in the generation of global magnetism in the Sun (Rempel 2005; Ossendrijver 2003). In the convection zone, the angular velocity is more nearly constant on radial lines than on cylinders, in some tension with the Taylor-Proudman constraint discussed in section 1.2 (see discussion in Miesch et al. 2006a). The meridional flow is more difficult to probe. Near the surface, there is a persistent poleward flow with an amplitude of about 15-20 ms^{-1} (Duvall 1979; Gizon et al. 2003), and (by mass conservation) there must be a return (equatorward) flow at some depth. Different studies have reached somewhat different conclusions about the nature of this sub-surface flow, using different helioseismic inversion techniques (Zhao et al. 2013; Jackiewicz et al. 2015); broadly, it appears that the circulation profile may be rather complex, consisting of multiple cells in radius (and possibly in latitude), in sharp contrast to the single-celled flows often assumed in mean-field dynamo models (Krause and Raedler 1980; van Ballegooijen et al. 2000; Blackman and Field 2002; Brandenburg et al. 2009). In stars other than the Sun, observational constraints are even scarcer: whilst asteroseismic data are readily available (e.g. Gilliland et al. 2010; Lund et al. 2017), they are not sufficiently precise to investigate the zonal flows in most stars (though see Stello et al. (2016) for an example of asteroseismic inversion for an evolved star). As such, in order to probe the internal dynamics of these stars, we must turn to theoretical models. Numerical models of Solar-like convection zones are summarised in great detail elsewhere (Miesch 2005a; Miesch and Toomre 2008; Brun et al. 2015); here we note only a few key aspects. Since the seminal work by Gilman and collaborators in the 1970s, it has been clear that convection, subject to moderate rotational constraints, can establish differential rotation that bears some resemblance to what is observed at the Solar surface – namely, with a fast equator and slow pole. Gilman found that the sense of this differential rotation changed as a control parameter related to rotation rate (the convective Rossby number, defined by $R_{oc} = \sqrt{\frac{R_a}{T_a P_r}} = \frac{v}{2L\Omega \sin\phi}$ - where v is the convective velocity, L is the length scale over which convection operates, Ω is the convective cells angular velocity, and ϕ is the convecting cells latitude.) was varied: the slowest rotators tended to establish "anti-solar" rotation profiles (a slow equator and a fast pole) while more rapid rotators exhibited more solar-like surface flows. With the advent of helioseismology, however, it became clear that some aspects of the internal flows were not being captured by the models, which (when subjected to rotational constraints that produce a solar-like surface flow) tended also to possess angu-

lar velocities nearly constant on cylinders within the convection zone, in accord with the Taylor-Proudman theorem. Later work has shown explicitly, for example, that this tendency towards cylindrical rotation profiles can be broken by the presence of even modest variation in temperature (or entropy) at the base of the convection zone, whether imposed as a boundary condition by the subadiabatic layer or generated self-consistently by the convection (e.g. Rempel 2006b, 2006a; Miesch et al. 2006b). Other simulations have extended the basic approach pioneered by Gilman and Glatzmaier to study envelopes of convection under a variety of rotational constraints, confirming the basic picture outlined here (e.g., Brun et al. 2004; Browning et al. 2004; Gastine et al. 2014b; Fan and Fang 2014). Recently, attention has also focused on links between the differential rotation and the meridional flow; in particular, Miesch and Hindman (2011) have argued that, in the Sun, these two are intimately linked via the mechanism of *gyroscopic pumping*, described in subsection 5.2.2 below, and Featherstone and Miesch (2015) have explored this concept using simulations of Solar-like convection zones. They showed that, in the parameter space accessible by their simulations, the meridional flow was linked to convergences and divergences in the Reynolds stresses arising from the fluctuating convective flow field. Later work (e.g. Passos et al. 2017) has examined, for example, how these meridional circulations might vary with time in response to changing magnetic fields.

5.1.2 Fully Convective Stars

Most stars are smaller than the Sun (e.g., Chabrier 2003), and those of less than about a third of a solar mass are convective throughout their interiors. Comparatively few studies have investigated the internal dynamics of these fully-convective M-Stars. Example of studies into the simulation of fully convective stars include; Dobler et al. (2006), who conducted a series 3D finite-difference simulations, finding both 'anti-solar' differential rotation and the formation of dynamo action, and both Browning (2008) and Yadav et al. (2015), who investigated both the dynamo action itself and the mechanisms which act to maintain said dynamo action. Broadly, they find smaller scale, intermittent, flows near the surface, with weaker, large-scale, flows in the deep interior; the convective flows act

as a magnetic dynamo, enhancing a small seed field and sustaining it against ohmic dissipation. This field then largely follows the same scaling as the convection (i.e., small-scale and strong near the surface, weak and larger-scale in the deep interior); in many cases it also possesses a significant, long-lasting, axisymmetric magnetic field component. Both Browning (2008) and Yadav et al. (2015) also find differential rotation profiles that, in MHD cases, are almost entirely suppressed by Maxwell stresses associated with the magnetic dynamo.

These studies have however left many effects unexplored, such as the transition from 'solar' to 'anti-solar' differential rotation, or the maintenance of the zonal flows. With this work we aim partly to fill these gaps, providing a series of easily reproducible simulations covering a wide gamut of possible M-star configurations.

5.1.3 Simplifying Interiors: A Link Between Differential Rotation and Residual Entropy?

In many rotating fluids, pressure gradients and Coriolis forces are tightly linked. If these two terms dominate in the momentum equation, the fluid is said to be in *geostrophic balance*; if in addition the vertical stratification is hydrostatic, and provided certain other criteria are satisfied (see, e.g., discussion in Vallis 2006), the fluid may be in *thermal wind balance*. A practical consequence of this state is that (in a Cartesian layer, for example) *horizontal* temperature gradients are linked to *vertical* gradients in the horizontal "wind"; in a spherical geometry, this amounts to a relationship between latitudinal variations in entropy and deviations of the angular velocity profile away from a Taylor-Proudman state (see discussion in the introduction, and below). It has been suggested by many authors that much of the solar convection zone, for example, might be approximately in thermal wind balance (e.g. Miesch et al. 2006b; Brun et al. 2010).

If, in addition to this, there is a functional relationship between isentropic (constant/fixed entropy) and isorotational (constant/fixed differential rotation rate) contours, as suggested by Balbus (2009), then a remarkable simplification of the thermal wind equation (TWE) results. In particular, the isorotation contours are then given by solution to a

characteristic equation (given below), subject to boundary conditions. This would imply that the internal differential rotation profile, and hence the internal entropy profile, could be extrapolated from surface rotation measurements. This approach led to model differential rotation profiles that fit remarkably well with helioseismology data for the Sun.
Further, Balbus et al. (2009) suggest a gauge freedom exists for the entropy profile, splitting the total entropy into convective (purely radial) and residual components in such a way that the final result of Balbus (2009) holds true. They also, thanks to data from Miesch et al. (2006b), visually confirmed that, for simulations of the SCZ, residual entropy and isorotation contours show general agreement. This led to a series of papers suggesting methods by which the theory could be extended to work in the boundaries of the SCZ, i.e. the near surface shear layer and the tachocline, (Balbus and Latter 2010; Balbus et al. 2012; Balbus and Schaan 2012; Caleo et al. 2015) and also the suggestion that this theory could be extended to fully convective stars (Balbus and Weiss 2010). More recently, the theory has also been applied to even more exotic environments; see, e.g., Rossi (2017) for an application to "quasi-stars."
Balbus and Weiss (2010) present a series of purely theoretical models for isorotation contours of fully convective stars; to date this has not been followed up with either observational data or data from fully-convective M-star simulations. If the tight link between isorotation and isoentropy contours were to exist, it would have immense value, not only for our understanding of the physics of M-stars, but for stellar convection zones more generally.

5.1.4 This Work

In order to gain a better understanding of the zonal flows within M-stars, the dynamical balances which maintain them, and a possible link between residual entropy and differential rotation, we turn here to 3D anelastic models of fully convective stars. In subsection 5.2.1 we explore the theoretical background, describing the possible link between residual entropy and differential rotation via the TWE in more detail. Then, in section 5.3 we introduce our 3D simulations, focusing on *Rayleigh*'s set-up which was used for the majority of the results herein. This is followed, in section 5.4, by a discussion of some of

the key diagnostics used to understand the zonal flows and their maintenance. In section 5.5, we show the results of our hydrodynamic (HD) simulations, investigating the shift from 'solar' to 'anti-solar' differential rotation (and zonal flows), and analysing the balances at play, which act to maintain said flows. We also investigate the link between residual entropy and differential rotation, including a comparison of our simulation's differential rotation profile to that extrapolated, using TWB, from purely surface data. This is followed by section 5.6, in which we introduce magnetic fields into our simulations and comment briefly on both the levels of magnetism that are sustained and the impact these have on the zonal flows. Finally, in section 5.7, we summarise our work and comment briefly on its implications for our understanding of M-star dynamics.

5.2 Theoretical Background

5.2.1 Thermal Wind Balance and Residual Entropy

We begin here by introducing the notion of thermal wind balance in more detail, and commenting on some of its possible consequences in stellar convection zones. To begin, consider the vorticity equation in a rotating spherical shell (derived by taking the curl of the momentum equation given in chapter 2), averaging the zonal component over both longitude and time. Assuming a statistically steady state, this yields the force balance in

the meridional plane (Brun et al. 2011):

$$
\begin{aligned}
2\Omega_0 \frac{\partial \langle v_\phi \rangle}{\partial z} &= \underbrace{-\left\langle (\boldsymbol{\omega}\cdot\boldsymbol{\nabla})v_\phi - \frac{\omega_\phi v_r}{r} - \frac{\omega_\phi v_\theta \cot\theta}{r} \right\rangle}_{\text{Stretching}} \\
&+ \underbrace{\left\langle (\mathbf{v}\cdot\boldsymbol{\nabla})\omega_\phi + \frac{v_\phi \omega_r}{r} + \frac{v_\phi \omega_\theta \cot\theta}{r} \right\rangle}_{\text{Advection}} \\
&- \underbrace{\left\langle \omega_\phi v_r \right\rangle \frac{d\ln\bar{\rho}}{dr}}_{\text{Compressibility}} + \underbrace{\frac{1}{r}\left[\frac{\partial}{\partial r}\left(r\langle \mathcal{A}_\theta\rangle\right) - \frac{\partial}{\partial\theta}\langle \mathcal{A}_r\rangle\right]}_{\text{Viscous stresses}} \\
&+ \underbrace{\frac{g}{rc_p}\frac{\partial\langle\sigma\rangle}{\partial\theta}}_{\text{Baroclinicity}} + \underbrace{\frac{1}{r\bar{\rho}c_p}\frac{d\bar{\sigma}}{dr}\frac{\partial\langle P\rangle}{\partial\theta}}_{\text{Non-adiabatic stratification}}
\end{aligned}
\tag{5.1}
$$

where $\frac{\partial}{\partial z} = \cos\theta\frac{\partial}{\partial r} - \frac{\sin\theta}{r}\frac{\partial}{\partial\theta}$ and

$$
\langle \mathcal{A}_r \rangle = \frac{1}{\bar{\rho}}\left\langle \left[\frac{1}{r^2}\frac{\partial(r^2\mathcal{D}_{rr})}{\partial r} + \frac{1}{r\sin\theta}\frac{\partial(\sin\theta\mathcal{D}_{\theta r})}{\partial\theta} - \frac{\mathcal{D}_{\theta\theta}+\mathcal{D}_{\phi\phi}}{r}\right]\right\rangle, \tag{5.2}
$$

$$
\langle \mathcal{A}_\theta \rangle = \frac{1}{\bar{\rho}}\left\langle \left[\frac{1}{r^2}\frac{\partial(r^2\mathcal{D}_{r\theta})}{\partial r} + \frac{1}{r\sin\theta}\frac{\partial(\sin\theta\mathcal{D}_{\theta\theta})}{\partial\theta}\right] + \frac{1}{\bar{\rho}}\left[\frac{\mathcal{D}_{\theta r} - cot\theta\mathcal{D}_{\phi\phi}}{r}\right]\right\rangle, \tag{5.3}
$$

where $\mathcal{D}$ is the viscous stress tensor. In Equation 5.1 we have labelled the terms on the RHS: 'Stretching' describes the stretching and tilting of the vorticity due to velocity gradients; 'Advection' describes the advection of vorticity by the flow; 'Compressibility' describes the change in vorticity due to compression effects; 'Viscous stresses' account for the viscous diffusion of vorticity; 'Baroclinicity' is the dominant baroclinic term when the stratification is nearly adiabatic (arising when surfaces of constant pressure and density do not coincide), and finally the non-adiabatic stratification term represents the baroclinic forcing linked with a finite radial entropy profile.

If we then assume that the convection zone is nearly adiabatic and hydrostatic, that the Rossby number is small, and that viscous stresses are dynamically unimportant, we can recover the 'classical' thermal wind equation (TWE - Kitchatinov and Ruediger (1995), Thompson et al. (2003), and Balbus (2009)):

$$
\frac{\partial\langle v_\phi\rangle}{\partial z} = \frac{g}{2\Omega_0 r c_p}\frac{\partial\langle\sigma\rangle}{\partial\theta}. \tag{5.4}
$$

This has been explored in many different contexts by, for example, Balbus (2009), Brun et al. (2011), Passos et al. (2016), and Passos et al. (2017).

We now present a method by which isentropic and isorotation contours may be linked, via the thermal wind equation (Equation 5.6). This method was developed by Balbus et al. (2009) [BBLW] and here, as a aid to the readers understanding, we detail their formalism. In order to develop this theory we work in both cylindrical (R, ϕ, z) and spherical coordinates (r, θ, ϕ). Additionally, we consider the angular velocity, Ω, the Pressure, P, and the density, ρ to be azimuthally averaged (i.e. independent of ϕ). As part of this, we define a dimensionless entropy function,

$$\sigma \equiv \ln\left(P\rho^{-\gamma}\right), \tag{5.5}$$

where γ is the adiabatic index. With this, we also consider a slightly rearranged form of the thermal wind equation;

$$R\frac{\partial\Omega^2}{\partial z} = \frac{g}{\gamma r}\frac{\partial\sigma}{\partial\theta}, \tag{5.6}$$

which implies that σ's only contribution is in the form of a θ gradient. Note that we have assumed that the r gradient of σ is much smaller than the θ gradient - i.e. $\frac{\partial\sigma}{\partial r}$ vanishes - an assumption that is typically made for the SCZ, and which is backed up by our analysis of the force balance in the meridional plane (subsection 5.5.5) for our simulations. This analysis reveals that the primary balance in the meridional plane is between deviations from Taylor-Proudman and baroclinic effects (associated with the θ gradient of sigma), as required for the thermal wind approximation to be applicable. This implies a gauge freedom in which σ can be split into a primarily radial component σ_r and a residual entropy component σ',

$$\sigma(r, \theta) = \sigma' + \sigma_r(r). \tag{5.7}$$

Note that σ_r is the minimal adverse radial entropy profile required to drive, and maintain, ongoing convection (Balbus et al. 2012). BBLW argue for this split into radial and residual components (with resulting gauge freedom) as follows: within a convective cell, the mixing of entropy leads to the elimination of any residual entropy gradient, so that each

convective cell maintains a constant, but different, σ'. They then argue that the presence of shear favours the tendency for long-lived, coherent, convective structures to lie within constant Ω surfaces. Thus it can be suggested that constant σ' and Ω surfaces tend to coincide, and we consider a residual entropy of following form: $\sigma' = f\left(\Omega^2\right)$.

If this argument holds true, the thermal wind equation may be written, in purely spherical coordinates, as

$$\frac{\partial \Omega^2}{\partial r} - \left(\frac{g f'}{\gamma r^2 \sin\theta \cos\theta} + \frac{\tan\theta}{r}\right)\frac{\partial \Omega^2}{\partial \theta} = 0, \tag{5.8}$$

where $f' = \mathrm{d}f/\mathrm{d}\Omega^2$.

If we now denote, using the subscript '0' a fiducial starting point of the characteristic, at which we can specify Ω, the solution to Equation 5.8 is that Ω^2 is constant along characteristic contours of the form (BBLW):

$$R^2 = r^2 \sin^2(\theta) = r_0^2 \sin_0^2(\theta_0) - B\left(\frac{1}{r} - \frac{1}{r_0}\right) \tag{5.9}$$

with

$$B = -\frac{2G\,\mathrm{M}_\odot f'}{\gamma}, \tag{5.10}$$

for a gravitational acceleration $\left(g(r)\right)$ profile that varies as GM_i/r^2. Using this formulation, and reasonably simple parametrisations of f', previous studies (BBLW) into this relation in the solar convection zone (SCZ) have shown good agreement between the predicted characteristic contours and both simulations (using data from Miesch et al. 2006b), and observational data (e.g. Balbus et al. 2012; Balbus and Schaan 2012). For our TWB extrapolations, we use a slightly rearranged formalism

$$\cos^2(\theta) = 1 - \frac{r^2}{r_0^2}\sin^2(\theta) + \left(\frac{B}{r_0^3}\right)\left(1 - \frac{r_0}{r}\right) \tag{5.11a}$$

$$\text{Where } \frac{B}{r_0^3} \sim 0 \rightarrow 1 \qquad \text{(Balbus 2009)}, \tag{5.11b}$$

along with a fit to the surface rotation profile

$$\Omega = a + b\cos^2(\theta) + c\cos^4(\theta). \tag{5.12}$$

An example of the result of this fit is shown in Figure 5.13.

We (the authors) also specify an alignment factor,

$$\mathcal{A} = \cos\left(\phi\right) = \frac{|\nabla\Omega \cdot \nabla\sigma'|}{|\nabla\Omega| \times |\nabla\sigma'|}, \tag{5.13}$$

in which we vectorise the differential rotation and residual entropy profiles by taking their gradient, and then use these quantities to measure the alignment.

5.2.2 Gyroscopic Pumping

The thermal wind equation as described above (Equation 5.8) does not contain explicit information about the meridional circulation; i.e., it is "degenerate" with respect to the meridional flow. Likewise, any cylindrically-invariant zonal flow can be added to a solution of the TWE to give another solution. There are various ways of breaking this degeneracy: one, explored extensively in the context of mean-field models, is via the meridional components of the Reynolds stress (e.g., Ruediger 1982). Another is the concept of *gyroscopic pumping*, long explored in the meteorology and atmospheric community (Plumb and McEwan 1978; McIntyre 2001) and lately applied to the astrophysical context by Miesch and Hindman (2011), Featherstone and Miesch (2015), and Passos et al. (2017). We briefly outline the nature of gyroscopic pumping here, while deferring a fuller description to these references.

The essential action of gyroscopic pumping is best illustrated by considering the zonal force balance in a steady state, which in the absence of Lorentz forces and viscous effects reduces to (Miesch and Hindman 2011)

$$\bar{\rho}\left\langle v_m \right\rangle \cdot \nabla\mathcal{L} = \mathcal{F} \approx -\nabla \cdot \boldsymbol{F}_{\mathrm{RS}} \tag{5.14}$$

where $\mathcal{L} = R^2\Omega$ is the specific angular momentum, R is the cylindrical radius ($R = r\sin\theta$), and $\mathcal{F}$ is the net axial torque:

$$\mathcal{F} = -\boldsymbol{\nabla}\cdot\left[\bar{\rho}R\left\langle \boldsymbol{v}'_m v'_\phi\right\rangle - \bar{\rho}\nu R^2\boldsymbol{\nabla}\Omega\right] \tag{5.15a}$$

$$= -\boldsymbol{\nabla}\cdot\left[\boldsymbol{F}_{\mathrm{RS}} + \boldsymbol{F}_{\mathrm{VD}}\right]. \tag{5.15b}$$

In Equation 5.14, we expect the Reynolds Stress component ($\boldsymbol{F}_{\mathrm{RS}}$) to dominate over viscous diffusion ($\boldsymbol{F}_{\mathrm{VD}}$) in stars; in simulations this dominance must be checked by direct calculation. We can now use this equation to describe gyroscopic pumping; since $\boldsymbol{\nabla}\mathcal{L}$ is orientated away from the rotation axis, we can expect a *convergence* of angular momentum flux ($\mathcal{F} > 0$) to induce a meridional flow $\langle \boldsymbol{v}_m\rangle$ directed *away* from the rotation axis. Conversely, a *divergence* of angular momentum flux ($\mathcal{F} < 0$) will lead to a meridional flow $\langle \boldsymbol{v}_m\rangle$ directed *towards* from the rotation axis. That is, in a steady state the meridional circulation must respond to convergences or divergences of angular momentum flux (provided by the Reynolds stresses or by other means) by advecting said angular momentum.

Furthermore, it is possible to link the cylindrical mass flux streamfunction (Ψ), the net axial torque ($\mathcal{F}$), and the components of the meridional circulation ($\left\langle\bar{\rho}v_R\right\rangle$ and $\left\langle\bar{\rho}v_z\right\rangle$):

$$\Psi(R,z) = \frac{1}{2R\Omega_0}\int_{z_b}^{z}\mathcal{F}(R,z')\,dz' \tag{5.16a}$$

$$\left\langle\bar{\rho}v_R\right\rangle = \frac{\partial\Psi}{\partial z} \tag{5.16b}$$

$$\left\langle\bar{\rho}v_z\right\rangle = -\frac{1}{R}\frac{\partial(R\Psi)}{\partial z} \tag{5.16c}$$

where $z_b = \sqrt{r_o^2 - R^2}$ (Miesch and Hindman 2011).

Finally, following the method of Featherstone and Miesch (2015), we define a convective angular momentum transport potential χ, which is related to $\boldsymbol{F}_{\mathrm{RS}}$ via a Helmholtz decomposition (which is valid for any arbitrary two-dimensional [axisymmetric] vector):

$$\boldsymbol{F}_{\mathrm{RS}} = \boldsymbol{\nabla}\boldsymbol{\chi} + \boldsymbol{\nabla}\times\Lambda\hat{\boldsymbol{\phi}}. \tag{5.17}$$

Thus, when we take the divergence of the Reynolds Stress, only the first component remains to contribute to the meridional circulation. This transport potential can be found

by solving a Poisson equation:

$$\nabla^2 \chi = \boldsymbol{\nabla} \cdot \boldsymbol{F}_{\mathrm{RS}}. \tag{5.18}$$

An example of the results of this analysis can be found in subsection 5.5.4.

5.3 Simulations of Fully Convective Stars

In order to understand the internal dynamics of fully convective M-stars, and to investigate the link between residual entropy and differential rotation contours, we performed a series of calculations using both *Rayleigh* and ASH. The majority of our calculations are highly idealised simulations performed using *Rayleigh*, with ASH simulations used as a bridge to previous works (e.g. Browning 2008). Both codes solve the 3D MHD anelastic equations of motion for a rotating spherical geometry using a semi-implicit, pseudo-spectral, approach. A full description of the anelastic, pseudo-spectral approach, including the equations solved (the anelastic MHD equations: Equation 2.18), may be found in chapter 2. In this section, we detail the exact numerical set-up of these calculations.

5.3.1 Rayleigh Numerical Setup

The majority of our simulations were performed using *Rayleigh* and a polytropic background state, as formulated in the anelastic benchmark suite of Jones et al. (2011). Whilst highly idealised, the simulations are straightforward for the community to reproduce, requiring only access to the open-source code and supercomputer time. The base parameters for our *Rayleigh* simulations are shown in Table 5.1; all simulations stem from these parameters, changing any one or more of the diffusivities, the luminosity, or the rotation rate, as required.

Note: As discussed in subsection 2.3.3, the viscosities and diffusivities considered in our simulations are eddy viscosities and diffusivities, which encompass both kinematic and thermal effects, and sub-grid-scale motions (i.e. unresolved, turbulent, motions). As a result, our eddy diffusivities and viscosities are significantly enhanced compared to Solar values. For example, in the upper SCZ, the molecular viscosity is typically on the order

of $\nu \simeq 1\text{cms}^{-1}$ (Miesch 2005b) whereas here, our simulations have eddy viscosities on the order of $\nu = 10^{11}\text{cms}^{-1}$. Similarly, the thermal diffusivity in the upper SCZ is also much smaller ($\kappa \approx 10^5$ - Miesch (2005b)) than the values we consider in our simulations ($\kappa \approx 10^{12}$). Whilst this might initially be expected to have a significant affect on our simulation results, in subsection 5.5.1 we postulate that our simulations have reached a free-fall regime, with the resultant convective driving being independent of the imposed diffusivity.

In order to formulate our polytropic background, we consider a thick convective shell

Param	Value
M_i	4.345×10^{31}
ρ_i	75.543
c_p	3.5×10^8
n	1.5
N_p	4.0
r_i	5.0×10^9
r_o	1.96×10^{10}
Ω_0	2.6×10^{-6}
L_0	3.846×10^{33}
κ_0	1.2×10^{12}
ν_0	4×10^{11}
η_0	2×10^{11}

Table 5.1: Input parameters for our idealised set of *Rayleigh* simulations.

which surrounds an interior mass M_i, and a gravitational acceleration $\left(g\left(r\right)\right)$ profile that varies as GM_i/r^2. Note that the anelastic equations solved here neglect centrifugal force terms, on the grounds that for the rotation rates considered here these are small compared to the overall gravitational force. However, it must be acknowledged that the centrifugal terms may in general be of the same order as terms (like the latitudinal entropy gradient) that play a significant dynamical role. This issue has not been seriously investigated in any prior work on this topic, mainly owing to the numerical difficulties involved in correctly capturing small centrifugal distortions around the spherically symmetric base state; we defer a detailed investigation into the possible effects of centrifugal terms to later work.

The anelastic equations thus allow for an adiabatically stratified, polytropic, atmosphere defined by

$$\rho_0 = \rho_i \left(\frac{\zeta}{\zeta_i}\right)^n, \quad T_0 = T_i \left(\frac{\zeta}{\zeta_i}\right), \quad P_0 = P_i \left(\frac{\zeta}{\zeta_i}\right)^{n+1}, \tag{5.19}$$

where the subscript i refers to quantities measured at the inner boundary of the shell, and n is the polytropic index. ζ defines the radial variation of the reference state

$$\zeta = c_0 + \frac{c_1 H}{r} \tag{5.20}$$

where $H = r_o - r_i$ is the thickness of the convective shell, and the constants c_0 and c_1 are given by

$$c_0 = \frac{2\zeta_o - \beta - 1}{1 - \beta}, \quad c_1 = \frac{(1+\beta)(1-\zeta_o)}{(1-\beta)^2} \tag{5.21}$$

$$\zeta_o = \frac{\beta + 1}{\beta \exp \frac{N_\rho}{n} + 1}, \quad \zeta_i = \frac{1 + \beta - \zeta_o}{\beta}. \tag{5.22}$$

In the above equations, $\beta = r_i/r_o$ is the aspect ratio of the convective shell, and N_ρ is the number of density scale heights.

At the boundaries of our convective shell, we adopt stress-free and impenetrable boundary conditions such that

$$v_r\left(r = r_i, r_o\right) = \left.\frac{\partial\left(\frac{v_\theta}{r}\right)}{\partial r}\right|_{r=r_i,r_o} = \left.\frac{\partial\left(\frac{v_\phi}{r}\right)}{\partial r}\right|_{r=r_i,r_o} = 0. \tag{5.23}$$

Next we match the magnetic profile to an external potential field at the top boundary

$$\boldsymbol{B} = \nabla\Phi \rightarrow \Delta\Phi = 0\Big|_{r=r_o} \tag{5.24}$$

and to a perfect conductor (i.e. purely tangential field) at the bottom boundary. Note that matching the magnetic field to an external potential field at the top boundary is only one possibility: Alternatives include matching the field to an external radial magnetic field (e.g. Brun et al. 2005), or, like the bottom boundary, matching to a perfect conductor. We choose to match our field to an external potential field because it is the closest match to the real, external, magnetic field of a star that we can achieve without significant computa-

tion of non-convecting regions. This result is best shown by potential-field source-surface (PFSS - first developed by Schatten et al. 1969 and Newkirk and Altschuler 1970) models of the solar coronal magnetic field which can be used to, accurately, recover the coronal field from observations of the magnetic structure at the solar surface (e.g. Riley et al. 2006; Mackay and Yeates 2012; Schrijver et al. 2013). This technique has also been shown to work for cooler stars by, for example, Rosén et al. (2015).

Furthermore, we require that the radial entropy gradient vanishes at the lower boundary, and that the entropy perturbations vanish at the upper boundary,

$$\left.\frac{\partial S}{\partial r}\right|_{r=r_i} = 0, \quad S(r_o) = 0. \tag{5.25}$$

As a consequence of the above, there is no diffusive entropy flux across the lower boundary, and at the upper boundary, all heat must exit the system via thermal conduction. This, along with our internal heating profile (subsubsection 2.6.1.2), means that the equilibrated entropy gradient is purely dependent upon the background state, the thermal diffusivity, and the systems luminosity, and so the time-averaged value of the entropy gradient must equilibrate to

$$\left.\frac{\partial S}{\partial r}\right|_{r=r_o} = \frac{L_\star}{4\pi r_o^2 \kappa \rho\left(r_o\right) T\left(r_o\right)}. \tag{5.26}$$

Finally, following the formalism of Featherstone and Hindman (2015), we define a flux Rayleigh number in terms of the imposed heat flux, the averaged background state, and the diffusivity:

$$\mathrm{Ra}_F = \frac{\tilde{g}\tilde{F}H^4}{c_p \tilde{\rho}\tilde{T}\nu\kappa^2}. \tag{5.27}$$

in which the tilde denotes either a shell average or the volume average, depending upon the context.

5.3.2 ASH Numerical Setup

We also performed a small number of simulations using ASH, which we set up in a similar manner to the models of Browning (2008). They are designed to bridge the gap between our more idealised *Rayleigh* simulations and ASH's more traditional set up, which essen-

Param	Value
c_p	3.23×10^8
r_i	2.0×10^9
r_o	1.96×10^{10}
Ω_0	2.6×10^{-6}
L_0	4.08×10^{31}
κ_0	4.0×10^{11}
ν_0	1.0×10^{11}
η_0	1.252×10^{10}

Table 5.2: Input parameters for our 'bridge' set of ASH simulations.

tially adopts a 1-D stellar model as the initial background state. These also served as an initial check on our *Rayleigh* results. We direct readers to Browning (2008) for a more complete description of ASH; here, we provide only a brief overview, contrasting these simulations with their more idealised cousins.

Compared to our *Rayleigh* simulations, these simulations use a more physical initial background state, namely a 1D stellar model (I. Baraffe, private communication; Chabrier et al. 2000). This background state is not strictly adiabatic (since it has a, small, finite entropy gradient leaving it only close to being adiabatic), and this leads to a number of small differences in the numerical approach. The main parameters for our simulations are given in Table 5.2; much like the above *Rayleigh* cases, we performed simulations with differing diffusivities, luminosities, and rotation rates. As for the boundary conditions, we again adopt stress-free, impenetrable, boundaries (Equation 5.23), matching the magnetic profile to an external potential field (Equation 5.24). However, for comparison with Browning (2008) and related works, we consider a different set of restrictions on the entropy profile, setting a constant entropy gradient at both the top and bottom boundaries

$$\left.\frac{\partial S}{\partial r}\right|_{r=r_i,r_o} = \text{Const} = 1 \times 10^{-8}. \tag{5.28}$$

This has a series of practical consequences for the resulting flows and thermodynamic variables; in particular, it allows for latitudinal entropy contrasts near the top of the domain, which our standard boundary conditions suppress.

5.4 Diagnostics

As part of our investigation into the internal dynamics of fully convective stars, and the balances which maintain the zonal flows, we make use of a number of different diagnostics. Here, for clarity of presentation, we define and describe these diagnostics in detail.

5.4.1 Heat Transport

Convection in our simulations ultimately arises because a heat flux, in excess of that which can be transported by conduction (or radiative diffusion) in a subadiabatic stratification, must be carried through the system. Hence, one method by which we can understand the internal dynamics of our fully convective stars is via their energy flux balances. Expressions for these arise from consideration of the total energy equation (see, e.g. Nordlund et al. 2009). This can then be expressed in conservative form, defining a series of "transport" terms; these are the enthalpy flux

$$F_e = \bar{\rho} c_p \langle v_r T \rangle \,, \tag{5.29}$$

the kinetic energy flux

$$F_{KE} = \frac{1}{2} \bar{\rho} \left\langle v_r |\boldsymbol{v}|^2 \right\rangle , \tag{5.30}$$

the conductive flux

$$F_c = \kappa \bar{\rho} \bar{T} \left\langle \frac{\partial S}{\partial r} \right\rangle . \tag{5.31}$$

the radiative flux

$$F_r = -\kappa_r \bar{\rho} c_p \left\langle \frac{\partial \bar{T}}{\partial r} \right\rangle , \tag{5.32}$$

and the viscous flux

$$F_v = -\langle \boldsymbol{v} \cdot \mathcal{D} \rangle \,. \tag{5.33}$$

In simulations with Rayleigh, there is no explicit radiative diffusion as above; rather, the equivalent amount of heating or cooling associated with this is prescribed by the heating/cooling function Q, as described in subsubsection 2.6.1.2. We also frequently omit

explicit discussion of the viscous flux, as it is typically small compared to the other terms (see, for example, Featherstone and Hindman 2015, who find an almost completely negligible viscous flux for high Rayleigh-number simulations of the SCZ). (Note, however, that in the context of radiative zones with high shear, even a small viscous flux may be important in considerations of the Goldreich-Schubert-Fricke instability Goldreich and Schubert 1967; Fricke 1969; see, e.g., Caleo et al. 2016 for more detailed discussion.)

At each radius, the sum of fluxes must be equal to the net flux $F(r)$, whether established by the internal heating Q (subsubsection 2.6.1.2) or as imposed by the boundary conditions. All the simulations reported here were run until a statistically steady state in the heat transport was achieved (so that the energy conducted out at the top boundary is equal to the energy imposed at the bottom plus that generated within the domain).

5.4.2 Overall Energetics

Another method by which we can investigate the balances at play within our simulated stars is to decompose the kinetic and magnetic energies into physically meaningful components. This can, for example, allow us to investigate how the presence of a magnetic field affects the differential rotation.

In particular, we decompose the kinetic energy (KE) into three components; a convective kinetic energy (CKE), a meridional circulation kinetic energy ($MCKE$), and a differential rotation kinetic energy ($DRKE$)

$$CKE = \frac{1}{2}\bar{\rho}\left[(v_r - \langle v_r \rangle)^2 + (v_\theta - \langle v_\theta \rangle)^2 + \left(v_\phi - \left\langle v_\phi \right\rangle\right)^2\right], \tag{5.34}$$

$$MCKE = \frac{1}{2}\bar{\rho}\left[\langle v_r \rangle^2 + \langle v_\theta \rangle^2\right], \tag{5.35}$$

$$DRKE = \frac{1}{2}\bar{\rho}\left[\left\langle v_\phi \right\rangle^2\right]. \tag{5.36}$$

As for the magnetic energy (ME), we find it convenient to decompose this into an azimuthal mean (the shell-averaged toroidal mean magnetic energy - TME) and fluctuations about this mean (FME)

$$TME = \frac{1}{8\pi}\left\langle B_\phi \right\rangle^2, \tag{5.37}$$

$$FME = \frac{1}{8\pi}\left[(B_r - \langle B_r\rangle)^2 + (B_\theta - \langle B_\theta\rangle)^2 + \left(B_\phi - \left\langle B_\phi\right\rangle\right)^2\right]. \tag{5.38}$$

The above quantities can then be used as a rough measure of the size of typical magnetic field structures: if the field is mostly on small scales only a marginal signal will survive the azimuthal averaging.

5.4.3 Angular Momentum Transport

The simulations described here all begin in a state of uniform (solid-body) rotation. Any differential rotation in the equilibrated state is the result of competing angular momentum redistribution processes: Reynolds stresses, meridional circulation, viscous diffusion, and both torques and Maxwell stresses associated with any magnetic field. It is the combination of these processes which yields the differential rotations profiles we wish to analyse. In order to understand, and quantify, the angular momentum transport, we follow the formulation of Browning (2008) (which itself is based upon Elliott et al. (2000) and Brun et al. (2004)), and turn to the zonal component of the momentum equation, averaged in both time and longitude:

$$\frac{1}{r^2}\frac{\partial\left(r^2\mathcal{F}_r\right)}{\partial r} + \frac{1}{r\sin\theta}\frac{\partial\left(\sin\theta\mathcal{F}_\theta\right)}{\partial\theta} = 0, \tag{5.39}$$

where

$$\mathcal{F}_r = \bar{\rho} r\sin\theta\left[-\nu r\frac{\partial}{\partial r}\left(\frac{\hat{v}_\phi}{r}\right) + \widehat{v_r' v_\phi'} + \hat{v}_r(\hat{v}_\phi + \Omega r\sin\theta)\right. \tag{5.40}$$

$$\left. - \frac{1}{4\pi\bar{\rho}}\widehat{B_r' B_\phi'} - \frac{1}{4\pi\bar{\rho}}\hat{B}_r\hat{B}_\phi\right] \tag{5.41}$$

and

$$\mathcal{F}_\theta = \bar{\rho} r\sin\theta\left[-\nu\frac{\sin\theta}{r}\frac{\partial}{\partial\theta}\left(\frac{\hat{v}_\phi}{\sin\theta}\right) + \widehat{v_\theta' v_\phi'} + \hat{v}_\theta(\hat{v}_\phi + \Omega r\sin\theta)\right. \tag{5.42}$$

$$\left. - \frac{1}{4\pi\bar{\rho}}\widehat{B_\theta' B_\phi'} - \frac{1}{4\pi\bar{\rho}}\hat{B}_\theta\hat{B}_\phi\right] \tag{5.43}$$

are the mean radial and latitudinal angular momentum fluxes, respectively. The terms on the right hand side of the above equations are, in order, the contributions from; viscous

diffusion, Reynolds stresses, meridional circulations, Maxwell stresses, and large-scale magnetic torques. The Reynolds stresses can be associated with correlations of the fluctuating velocity components $\left(v_r', v_\theta', v_\phi'\right)$ that arise when convective structures possess organised tilts. Similarly, Maxwell stresses are correlations of the fluctuating magnetic field components corresponding to the tilt and twist of magnetic structures.

To more easily analyse the various components of both $\mathcal{F}_r$ and $\mathcal{F}_\theta$, we integrate both radially and colatitudinally in order to find the net fluxes through both shells at each radius, and cones at each latitude:

$$I_r(r) = \int_0^\pi \mathcal{F}_r(r,\theta)\, r^2 \sin\theta d\theta, \tag{5.44}$$

$$I_\theta(\theta) = \int_{r_{\text{bot}}}^{r_{\text{top}}} \mathcal{F}_\theta(r,\theta)\, r \sin\theta dr. \tag{5.45}$$

Results of this analysis can be found in subsection 5.5.3.

Table 5.3

Luminosity	Rotation Rate	Diffusivity	Pr	Ek	Ro	Raf
0.5	0.25	1.0	$0.3\dot{3}$	0.0029	0.62	172656
0.5	0.5	1.0	$0.3\dot{3}$	0.0014	0.32	172656
0.5	1.0	0.5	$0.3\dot{3}$	0.00036	0.18	1381252
0.5	1.0	1.0	$0.3\dot{3}$	0.00072	0.15	207187
0.5	2.0	1.0	$0.3\dot{3}$	0.00036	0.041	172656
0.5	4.0	1.0	$0.3\dot{3}$	0.00018	0.0041	172656
1.0	0.25	0.5	$0.3\dot{3}$	0.0014	0.61	2762505
1.0	0.25	1.0	$0.3\dot{3}$	0.0029	0.71	345313
1.0	0.25	1.5	$0.3\dot{3}$	0.0043	0.70	102315
1.0	0.25	2.0	$0.3\dot{3}$	0.0058	0.70	43164
1.0	0.25	3.0	$0.3\dot{3}$	0.0087	0.78	12789
1.0	0.25	4.0	$0.3\dot{3}$	0.0115	0.61	5395
1.0	0.25	5.0	$0.3\dot{3}$	0.0144	0.55	2762
1.0	0.5	0.5	$0.3\dot{3}$	0.00072	0.44	2762505
1.0	0.5	1.0	$0.3\dot{3}$	0.0014	0.43	345313
1.0	0.5	2.0	$0.3\dot{3}$	0.0029	0.42	43164

Table 5.3 – *Continued from previous page*

Luminosity	Rotation Rate	Diffusivity	Pr	Ek	Ro	Raf
1.0	0.75	1.0	$0.3\dot{3}$	0.00096	0.32	345313
1.0	0.9	1.0	$0.3\dot{3}$	0.00080	0.43	345313
1.0	1.0	0.5	$0.3\dot{3}$	0.00036	0.21	2762505
1.0	1.0	0.9	$0.3\dot{3}$	0.00065	0.40	473680
1.0	1.0	1.0	$0.3\dot{3}$	0.00072	0.38	345313
1.0	1.0	1.1	$0.3\dot{3}$	0.00079	0.38	259438
1.0	1.0	2.0	$0.3\dot{3}$	0.0014	0.15	43164
1.0	1.1	1.0	$0.3\dot{3}$	0.00066	0.36	345313
1.0	1.5	1.0	$0.3\dot{3}$	0.00048	0.14	345313
1.0	2.0	0.5	$0.3\dot{3}$	0.00018	0.14	2762505
1.0	2.0	1.0	$0.3\dot{3}$	0.00036	0.091	345313
1.0	2.0	2.0	$0.3\dot{3}$	0.00072	0.040	43164
1.0	4.0	0.5	$0.3\dot{3}$	9.0×10^{-5}	0.052	2762505
1.0	4.0	1.0	$0.3\dot{3}$	0.00018	0.019	345313
1.0	4.0	2.0	$0.3\dot{3}$	0.00036	0.0041	43164
2.0	0.25	1.0	$0.3\dot{3}$	0.0029	0.90	690626
2.0	0.5	1.0	$0.3\dot{3}$	0.0014	0.50	690626
2.0	1.0	1.0	$0.3\dot{3}$	0.00072	0.42	690626
2.0	2.0	1.0	$0.3\dot{3}$	0.00036	0.13	690626
2.0	4.0	1.0	$0.3\dot{3}$	0.00018	0.058	690626

Table 5.3: Dimensional and Non-Dimensional parameters for HD simulations.

5.5 Hydrodynamic Simulations: Results and Analysis

The exact parameter set-up for our hydrodynamic simulations can be found in subsection 5.3.1 and all HD simulations have been run until their internal energy fluxes equilibrated.

Table 5.3 shows a complete listing of the HD simulations performed, along with their dimensional and non-dimensional parameters. The results shown here are examples of the

structures seen across the parameter space, and have been chosen to highlight the transition from 'anti-solar' to 'solar' differential rotation and meridional circulation, and the mechanisms which generate the zonal flows.

5.5.1 Overview of convective flows and energetics

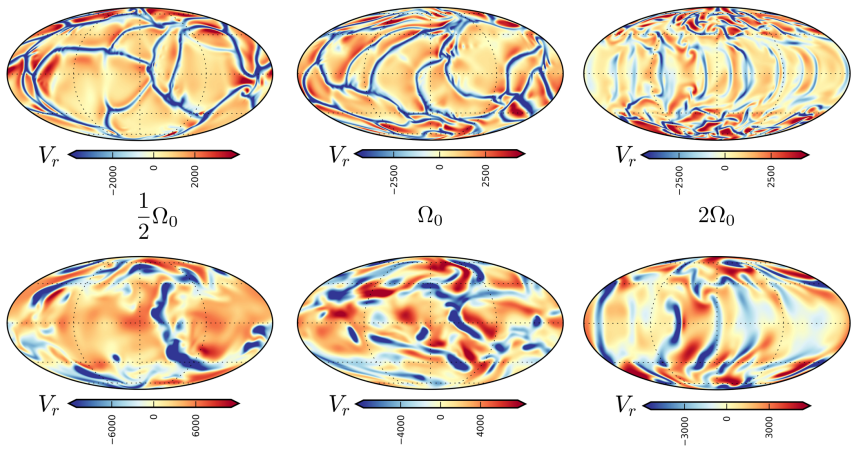

Figure 5.1: Near surface ($R = 0.97R_0$) and deep ($R = 0.63R_0$) radial velocity components for 3 simulations showing how a increasing rotation rate has a significant effect on the convective profile, changing the convective structure from large-scale 'solar-like' cells to a 'banana-cell' like structure near the equator.

We start by investigating the convective structures that form within our simulations, along with some of the fundamental energy balances associated with them.

The convective flows observed in our simulations show structure on varying spatial scales, and, as in many prior simulations of rotating, stratified convection (e.g., Browning et al. 2004; Miesch et al. 2008; Featherstone and Miesch 2015; Augustson et al. 2015; Passos et al. 2016), are highly dependent upon the rotation rate of the star. Figure 5.1 shows an instantaneous view of both the near surface and deep convective flows, as presented by the radial velocity v_r, for three simulations. Upflows are rendered in reddish tones and downflows are blue. At 'slow' rotation rates (left), we find large scale convective cells that exhibit a clear asymmetry between compact and strong downflows, and broader and weaker upflows, with some structures extending deep within the convective shell. This asymmetry between strong, compact downflows and broader, weaker upflows persists as we increase the rotation rate to our 'base' value (centre). However, the convective cells become both smaller and stronger, and significantly smaller convective cells form near the pole. Finally as we move into the rapid rotation regime (right), we find that the convection

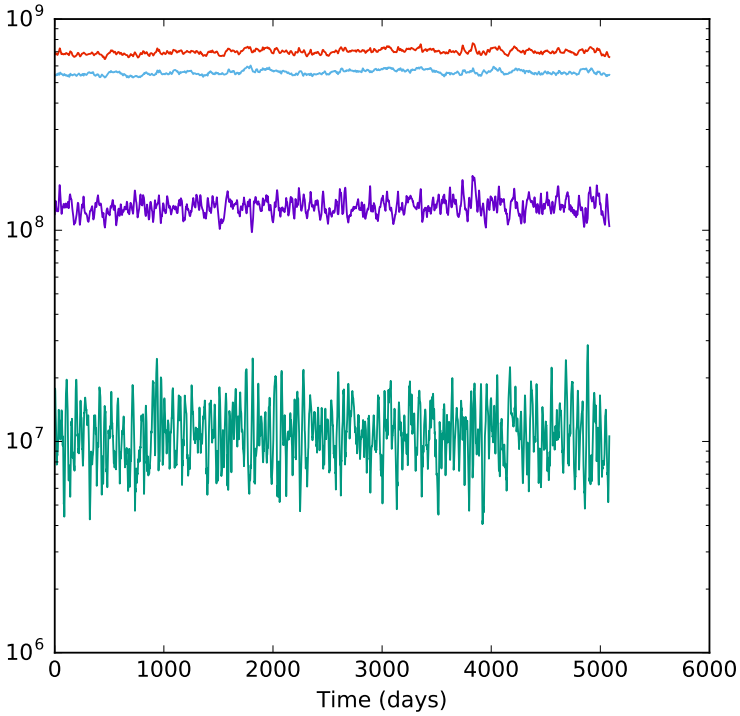

Figure 5.2: The kinetic energy evolution for our reference, 'base', HD case after evolving to near equilibrium. Convective KE is shown in purple, meridional circulation KE is shown in green, differential rotation KE is shown in blue, and the total KE is shown in red. Here, like a significant fraction of our simulations, we find that differential rotation is the main contributor to the KE.

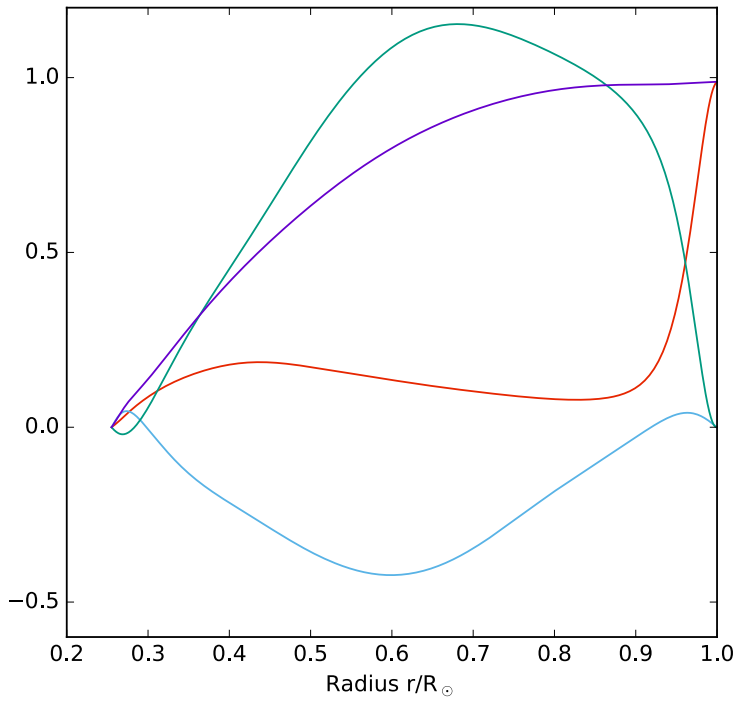

Figure 5.3: The radial energy fluxes (luminosity profiles) for the same case as Figure 5.2. Here, conductive flux is shown in red, KE flux is shown in blue, enthalpy flux is shown in green, and the total energy flux is shown in purple. For most of our cases we find a fairly similar overall energy flux, but with significant variations in the relative contributions of KE, conduction, and enthalpy.

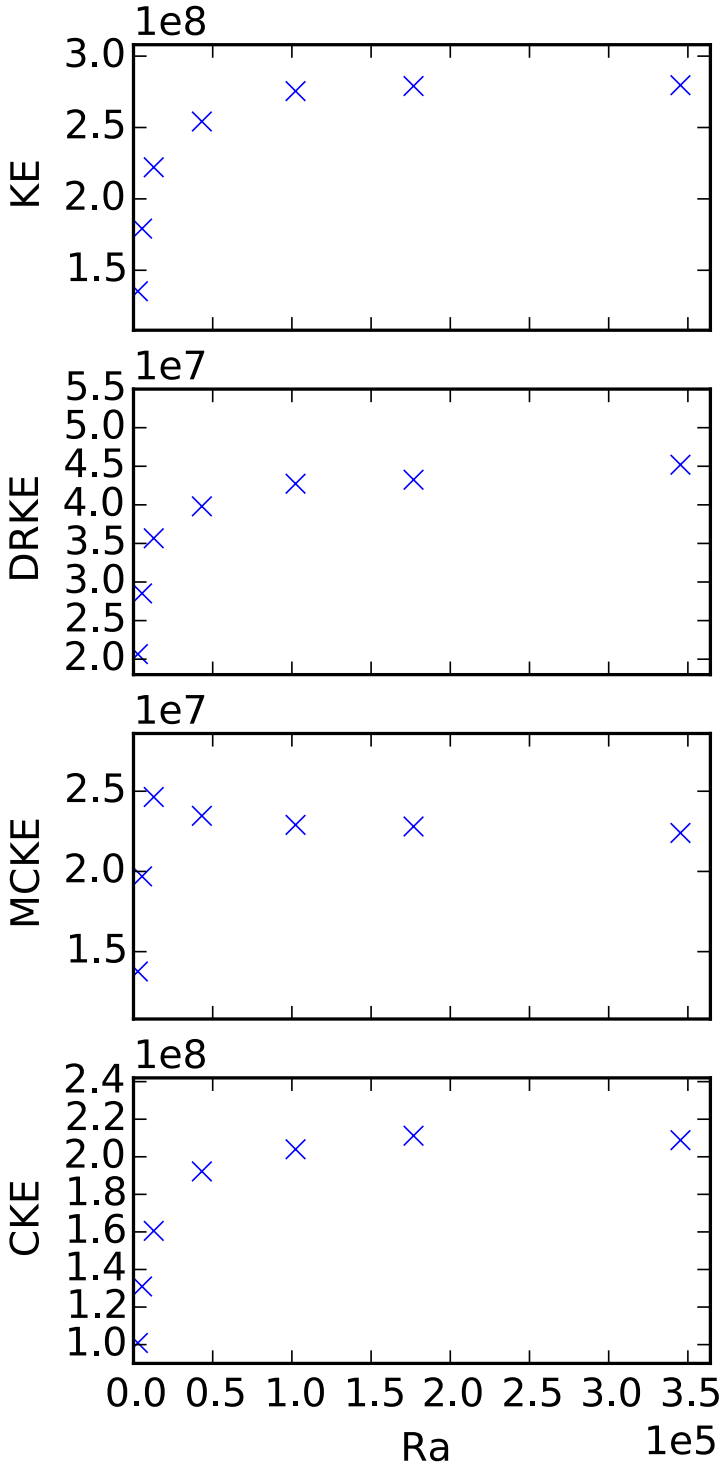

Figure 5.4: Equilibrium kinetic energy, and its constituent components (differential rotation (DRKE), meridional circulation (MCKE), and convection (CKE)), for a series of 'anti-solar' simulations at $\frac{1}{4}\Omega_0$, and with varying Rayleigh numbers (achieved by adjusted the diffusivities κ/ν). In all of the above plots, we see clear evidence that the KE, and the KE components, saturates as we move towards high R_a.

tends to align in rolls that are largely aligned with the rotation axis. These are reminiscent of the most unstable modes for the linear onset of convection in a rotating spherical shell, as analysed in Busse (1978) or Busse and Cuong (1977) in the limit of rapid rotation. Such modes are commonly called 'banana cells,' though the term has no precise meaning; ultimately the motions here are influenced also by stratification and by the overall geometry, but they share with these linearly-preferred modes the tendency to propagate in a prograde sense and to exhibit some degree of cylindrical alignment in the equatorial region, in accord with the Taylor-Proudman constraint. (For discussions of the physical mechanisms for prograde propagation, see Busse 1970, Busse 1973, and Gilman 1975.) Since the poles are not so rotationally influenced, we still find that a more isotropic network of downflow cells is able to form there.

Overall, the convective flow fields in our simulations are similar to those realised in previous studies of both M-stars and "solar-like" convection, despite the relatively idealised nature of our simulations. For example, sampling only one rotation rate in deep simulations of a fully convective star, Browning (2008) found behaviour similar to our "solar-like" case, with convection strongly shaped by rotation into patterns reminiscent of the "banana cells" long found in models of convection near onset (e.g., Busse 1970; Gilman 1972; Busse 1978). Likewise, the strong asymmetry between upflows and downflows appears to be a generic feature of highly stratified convection (e.g., Brummell et al. 2002; Nordlund et al. 2009); this asymmetry is absent in Boussinesq convection, which has a perfect up-down symmetry about the midplane of the domain.

Associated with these flows is a substantial kinetic energy, which we find it instructive to decompose in the manner described in subsection 5.4.2. This decomposition is assessed for an example simulation in Figure 5.2, which displays the volume-averaged kinetic energy density (KE) and its components the differential rotation kinetic energy (DKRE), meridional circulation kinetic energy (MCKE), and the convective kinetic energy (CKE).

We find that in this regime the kinetic energy is dominated by the contribution from differential rotation, with convective kinetic energy playing a much smaller supporting role, and a meridional circulation component so weak that it is essentially insignificant. Note

that, whilst the exact nature of the equilibrium kinetic balance is highly dependent upon the form of flows that develop (i.e. 'anti-solar' vs. 'solar'), it is fairly typical of our simulations in that one contribution dominates.

These flows arise ultimately from the need to carry energy outwards, so we turn next to an analysis of the radial energy transport in the same simulation. Figure 5.3 shows the component energy fluxes described in subsection 5.4.1, sampled as a function of radius and averaged over spherical surfaces and time. The profile we show here is again fairly typical of our simulations, with an outward enthalpy flux, an inward kinetic energy flux, and conductive flux which transports the total luminosity (energy flux) through the upper boundary. Of course, as with the KE, the exact energy balance formed, and the relative contributions depend upon the flows/structures that develop at a given rotation rate and luminosity. A general feature of this analysis is the fact the enthalpy flux is generally larger than the imposed (total) flux; the excess is compensated for by the inward-directed kinetic energy flux. This inward-directed kinetic energy flux is in turn a consequence of the asymmetry between upflows and downflows in these highly stratified systems. Similarly, the conductive flux in our simulations is generally small in the bulk of the domain, but grows to carry all the flux out the upper boundary (as it must, since the convective velocity is required to go to zero there). We have not displayed the viscous flux, as its contribution is negligible in this case.

Whilst individual equilibrium states are interesting, many detailed properties of the flow field are affected by the parameters of the simulation; hence, we turn next to an analysis of how these equilibrium states are affected by changes in these parameters. In order to investigate this, we look at the equilibrium kinetic energies for a series of simulations with identical initial conditions, apart from the Rayleigh number, which we control via the diffusivity. Specifically, we adjusted the (eddy) thermal diffusivity, κ, and the (eddy) kinematic viscosity, ν, whilst maintaining a constant Prandtl number, $\mathrm{Pr} = \frac{\nu}{\kappa} = \frac{1}{3}$. The results of this analysis, for a series of 'anti-solar' simulations at $\frac{1}{4}\Omega_0$ are shown in Figure 5.4. Here, we see that as we move towards higher R_a (lower diffusivity), the kinetic energy, and

its constituent components, start to equilibrate at a value independent of R_a. For almost all the initial conditions (i.e. both 'solar' and 'anti-solar') we considered, like Figure 5.4, we found that this occurred at about twice our standard diffusivities ($R_a \approx 1 \times 10^5$), a diffusivity that does not require a particularly high resolution to simulate. This suggests that our simulations may be approaching an asymptotic regime in which certain aspects of the flow field (like the bulk kinetic energies sampled here) are relatively insensitive to the numerical dissipation parameters adopted. This in turn implies that in the particular configuration adopted here, further decreases in the diffusivities might lead to qualitatively similar results, offering some hope that the dynamics sampled here may be representative of those realised in actual stars. A similar "plateau" in the saturated kinetic energy has been found for non-rotating convection in simulations by Featherstone and Hindman (2015), who interpreted the results as arising from the simulations reaching a state of 'turbulent free-fall' (e.g. Spiegel 1971). In essence, they suggest that the upper boundary layer possesses an energy deficit with respect to the adiabatic interior, this deficit then translates to an overdensity within the boundary. As a direct result of this, the potential energy, and thus the kinetic energy associated with convection, becomes independent of the thermal diffusivity. This, diffusivity independent, scaling has been previously observed in both high R_a laboratory set-ups (e.g. Ahlers et al. 2009), and in Boussinesq studies performed within a spherical geometry with symmetric, fixed temperature, boundary conditions (e.g. Gastine et al. 2015).

5.5.2 Overview of zonal flows

The convective flows in our simulations transport not just heat but also angular momentum; this results in substantial differential rotation in the evolved calculations despite our uniformly-rotating initial conditions. The differential rotation is intimately linked to meridional circulations and to the thermal properties of the convection zone, as described in subsection 5.5.1, so we turn now to an analysis of these quantities in a sample of our calculations. An example is provided by Figure 5.5, which shows the azimuthally averaged residual entropy, differential rotation and meridional circulation profiles for three simulations that span the transition from 'anti-solar' to 'solar' dynamics, via an increasing

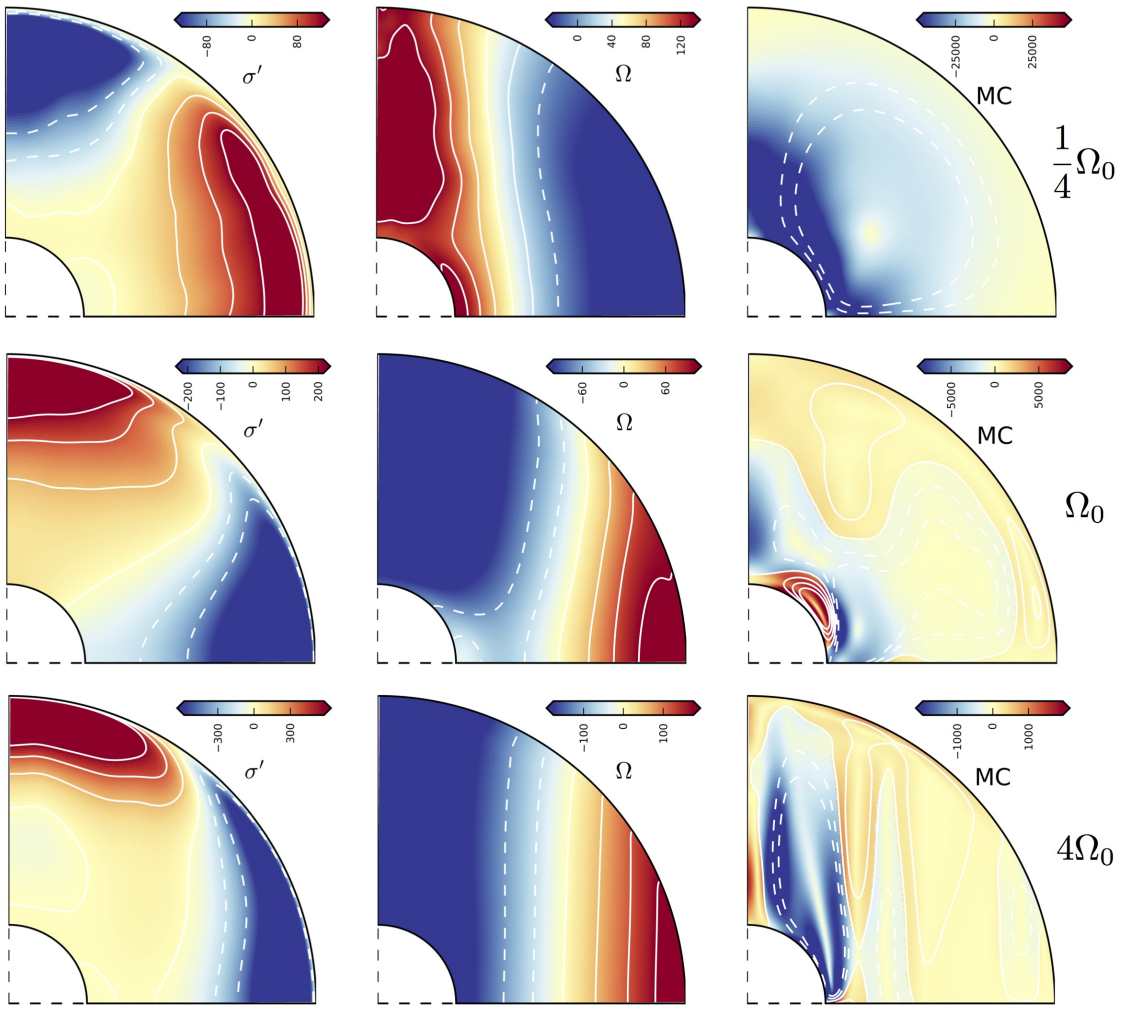

Figure 5.5: Residual entropy (σ'), differential rotation (Ω), and meridional circulation (MC) profiles for three HD simulations spanning the transition from 'anti-solar' (top row) to 'solar' (bottom row) via an increasing rotation rate. The southern Ω and σ' profiles are symmetric whilst the southern MC profile is anti-symmetric. In addition to a clear reversal in the latitudinal entropy and differential rotation gradients, we see a clear shift from a large, dominating MC cell in the 'anti-solar' case to smaller, rotation axis aligned, MC cells in the 'solar' case, just like we would expect to see in a 'sun-like' case. Note that all profiles have been averaged over at least 1000 days worth of equilibrated data.

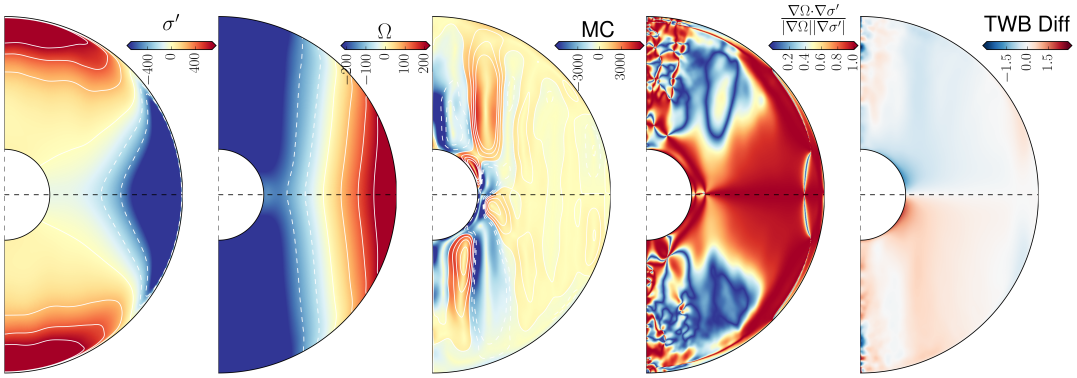

Figure 5.6: Residual entropy (σ'), differential rotation (Ω), meridional circulation (MC), the Alignment factor ($\mathcal{A}$ - the cosine of the angle between contours $\sigma\prime$ and Ω), and TWB agreement (the difference between the LHS and RHS of Equation 5.6, in spherical coordinates) profiles for a 'solar' HD case. At low latitudes, we see good agreement between σ' and Ω contours, but, as we move towards the poles, we find that the two profiles can become almost perpendicular, leading to significant regions in which the link between these quantities is not as strong.

rotation rate. Although not shown here, we also find that the simulation also transitions from 'anti-solar' to 'solar' as we move from low κ/ν to high. In both instances this is can be linked to changes in the Rayleigh, Rossby, and Ekman numbers, as described in more detail below.

At slow rotation rates (top row of Figure 5.5), we find a negative latitudinal residual entropy gradient (σ'), a positive latitudinal differential rotation gradient (Ω), and a single celled, anticlockwise, meridional circulation profile (MC). As we move towards our 'base' rotation rate (middle row), we see evidence of a transition from 'anti-solar' to 'solar' internal flows, with a positive latitudinal entropy gradient, a negative latitudinal differential rotation gradient, and the break up of the previously dominant meridional circulation cell, as smaller 'sun-like' cells starting to form. This trend continues as we increase the rotation rate (bottom row), with a truly 'solar-like' profile forming. Here, as in the SCZ, we see a positive latitudinal entropy gradient, a negative latitudinal differential rotation gradient, and a meridional circulation profile containing axially aligned MC cells, alternating between clockwise and anticlockwise flows.

We now move on to analysing two individual cases in more detail, one 'solar' and one 'anti-solar'. We will focus on these two cases in much of the analysis that follows in subsequent sections, but begin here simply by showcasing the overall flows and entropy contrasts that are ultimately established in both cases. Figure 5.6 shows the residual en-

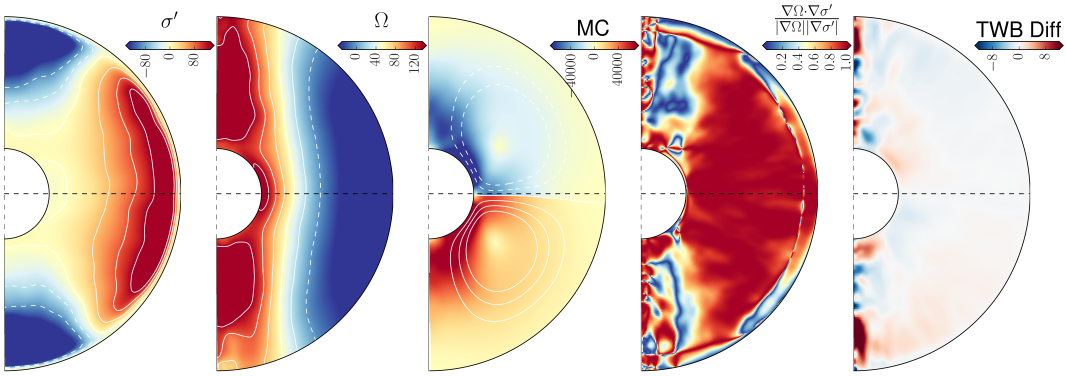

Figure 5.7: Residual entropy (σ'), differential rotation (Ω), meridional circulation (MC), the Alignment factor ($\mathcal{A}$), and TWB agreement profiles for an 'anti-solar' HD case. Here, we see a more general agreement between contours of σ' and Ω, with the majority of the non-boundary regions exhibiting at least some alignment. Yet, as in 'solar' case above, we still find regions of non-alignment near both poles (reduced in scale compared to the 'solar' case).

tropy, differential rotation and meridional circulation (along with the contour alignment and TWB deviation – discussed below) profiles for our first, 'solar', case (rapidly rotating, and at a reduced viscosity). Looking at the meridional circulation profile we see strong rotation axis aligned cells forming, alternating between clockwise and anticlockwise fluid motions. The differential rotation profile consists of a rapidly rotating equator, a slower polar region, and slightly concave differential rotation contours. Finally, the residual entropy reveals a slightly cooler equator, with a correspondingly warmer pole. The detailed origins of each of these features are analysed below; in broad terms, however, the tendency for a rapidly rotating equator and slow pole arises mainly in this case from the Reynolds stresses associated with the "banana cell"-like modes near the equator, which tend to transport angular momentum outwards and equatorwards. They are opposed by viscous diffusion, so a steady state is ultimately reached in which the net angular momentum transport vanishes, resulting in the steady-state profiles here. The detailed thermal pattern achieved is also non-trivial in origin, but is ultimately linked to both the meridional circulations and to the nature of the convection, as indicated in our discussion of the meridional force balance below.

Moving onto our second case, Figure 5.7, we explore the slow rotation regime. Here, we find that the residual entropy, differential rotation, and meridional circulation profiles all fall cleanly into the 'anti-solar' regime. This is evident from the meridional circulation profile, which is dominated by a single large cell in each hemisphere, anticlockwise in the northern hemisphere and clockwise in the southern. Similarly we see a latitudinal de-

crease in residual entropy and increase in differential rotation, leading to a cool, rapidly rotating, pole, and a hot, slowly rotating, equator. As in the more rapidly rotating case, the detailed nature of the flows and thermal patterns achieved is not straightforward to interpret, and is the subject of much of the analysis that follows. However, in broad terms the tendency for a slow equator and faster pole is consistent with fluid parcels that largely conserve angular momentum as they move inwards or outwards, leading to slower rotation in regions that are farther from the axis of rotation.

These results for differential rotation, meridional circulation, and entropy are largely consistent with those found in prior simulations of thinner convection zones intended to represent Solar-like stars (e.g., Miesch et al. (2008), Featherstone and Miesch (2015), and Passos et al. (2016)), with the linear and weakly nonlinear studies that predate these (Gilman). In particular, the tendency for a transition between "solar-like" and "anti-solar" rotation as the rotational influence is varied appears to be quite robust. Here, as in many prior calculations in other geometries and stratifications, this is realised either by explicitly varying the rotation rate or by changing the relative importance of rotation on the flows by modifying the buoyancy driving (e.g., by changing the diffusivity or the heat flux). A link between this "flip" in the differential rotation profile and the meridional flows has also previously been reported in solar-like geometries by Karak et al. (2015), and explored in the context of planetary dynamics by Gastine et al. (2014a). Largely in line with these, we find that solar-like surface differential rotation is generally accompanied by multi-cellular meridional flows that are largely aligned with the rotation axis; by contrast, anti-solar zonal flows are accompanied by a large single cell of meridional circulation in each hemisphere.

5.5.3 Maintenance of the flows - Angular Momentum Transport

We now turn to an analysis of how these zonal flows are established and maintained by both the rotation and the convection. As discussed in subsection 5.4.3, we begin by examining various components of the angular momentum flux in our simulations. Figure 5.8

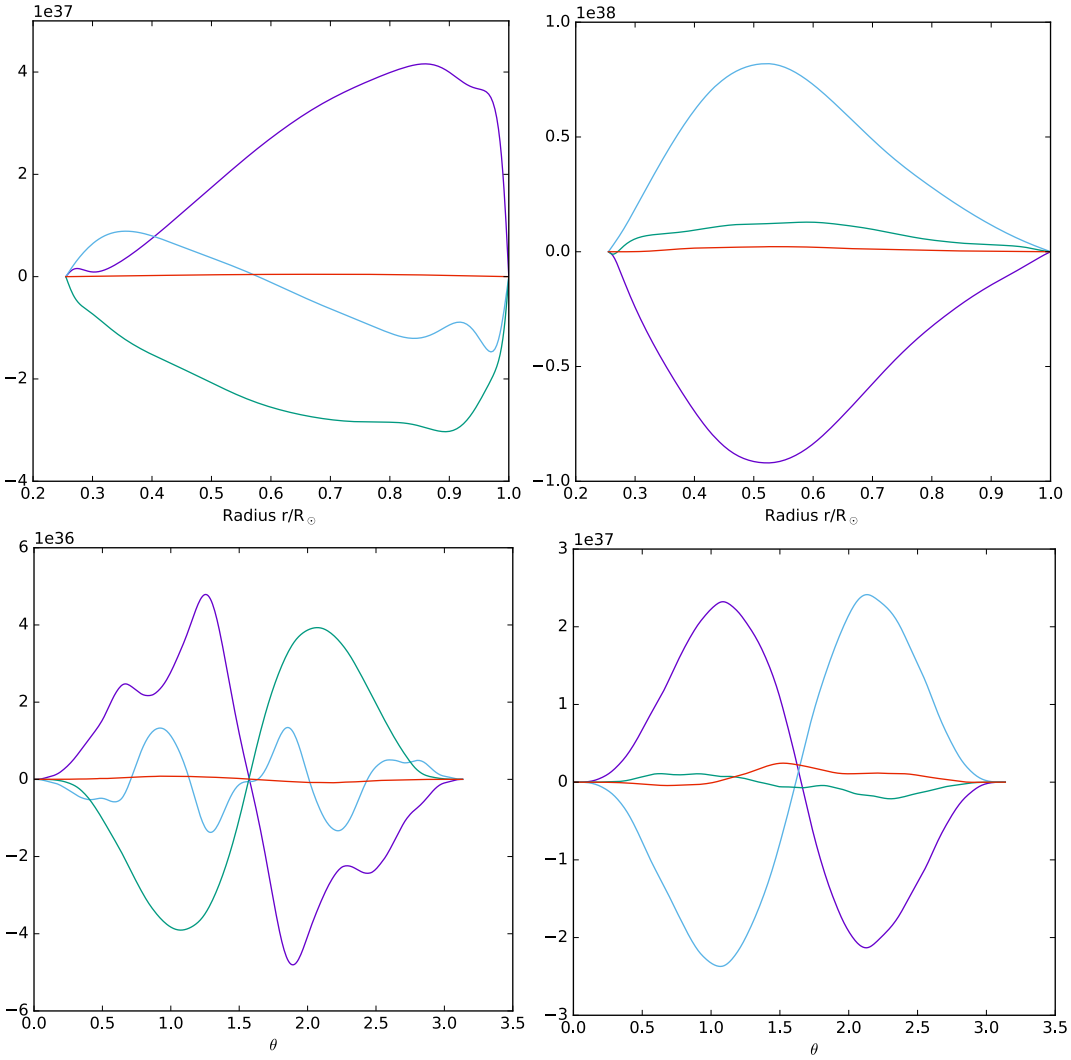

Figure 5.8: Radial and latitudinal angular momentum flux profiles for both 'solar' (left) and 'anti-solar' (right) HD simulations. For each simulation, the *top* row shows the radial profile, whilst the *bottom* shows the latitudinal profile.
The Reynolds stress contribution is in purple, the contribution from meridional circulation is in blue, the contribution from viscous diffusion is in green, and the total angular momentum flux is in red. Positive quantities represent fluxes radially outward or directed latitudinally from north to south. - Solar and Anti-solar plot labels

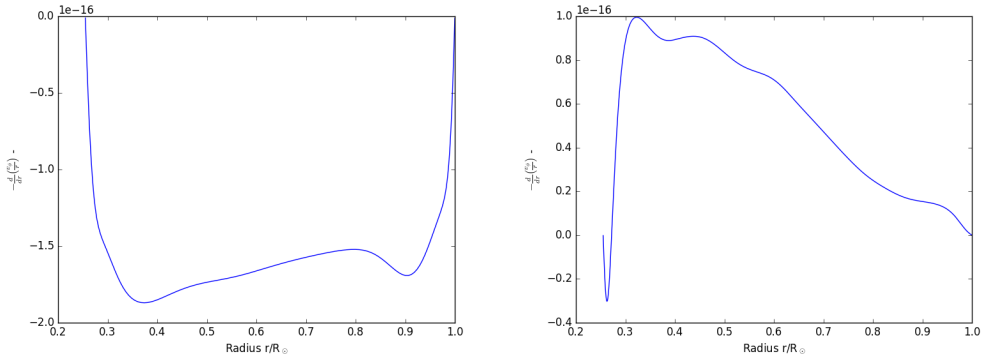

Figure 5.9: Plots of the velocity gradient associated with viscous diffusion ($-\frac{d}{dr}\left(\frac{v_\phi}{r}\right)$ - essentially the gradient of Ω) in both 'solar' (left) and 'anti-solar' (right) HD simulations. Comparing this to the green lines in the top row of Figure 5.8 (which show the contribution from viscous diffusion to the overall, radial, angular momentum balance in our HD simulations), we see that both the direction of the velocity gradient, and its magnitude, agree well with the observed (viscous diffusion driven) angular momentum fluxes: i.e. a strong (weak) negative (positive) velocity gradient is linked with a strong (weak), inwards (outwards), (viscous diffusion driven) angular momentum flux.

shows two example cases, one with a 'solar' differential rotation profile (left), and one with an 'anti-solar' profile (right). There, we examine for each case the angular momentum flux contributions from Reynolds stresses, meridional circulation and viscous diffusion, as well as the total angular momentum flux.

Turning first to our 'solar' case and its radial angular momentum flux profile, we see that the Reynolds stresses act to transport angular momentum towards the surface. This is primarily opposed by viscous diffusion, which acts to transport angular momentum inwardly everywhere. The final contribution, from meridional circulation, plays a far smaller role transporting angular momentum towards middepth ($r \approx 0.55$). Finally the net flux is essentially zero everywhere, confirming that our simulation is well equilibrated.

In this regime, a similar story is told by the latitudinal angular momentum flux profile. Here, Reynolds stresses act to transport angular momentum flux towards the equator (i.e. a positive flux in the northern hemisphere, and a negative in the southern), and are once again opposed by viscous diffusion, which transports flux polewards. The meridional circulation also plays a far more important role here, either acting in concert with the Reynolds stresses (at mid latitudes), or opposing it (near the equator and poles).

Moving onto our 'anti-solar' case, we find significant differences compared to the 'solar' case. To start with, the radial angular momentum flux profile is now dominated by meridional circulation and Reynolds stresses, with viscous diffusion playing a much more minor

role. We find that meridional circulation acts to transport angular momentum towards the surface, with the assistance of a weak viscous diffusion component. This is opposed by the Reynolds stress, which acts to transport angular momentum inwardly. Again we see a small net flux, suggesting that the simulation is near equilibrium.

The latitudinal angular momentum flux profile is different again: whilst it is still dominated by meridional circulation and Reynolds stress contributions (with an almost non-existent viscous diffusion component), they act in much the same way as our 'solar' example. Once again, Reynolds stress act to transport angular momentum towards the equator, but unlike the 'solar' case, it is opposed by an almost equal and opposite meridional circulation flux. Finally the net flux once again suggests an equilibrium has been reached.

Taken together, the above cases show how a difference in the relative contributions of angular momentum flux components can be linked to vastly different differential rotation (and residual entropy) profiles. Whilst the Reynolds stresses associated with turbulent convection play a key role in both cases, the radial transport afforded by these stresses changes sign. In the 'solar' case it acts to transport angular momentum outwardly, whilst in the 'anti-solar' case its role is reversed, transporting angular momentum towards the core. The change in velocity profile between 'solar' and 'anti-solar' also leads to a change in the flux component balancing the Reynolds stress. In the 'solar-like' case, it is opposed by viscous diffusion associated with a strong velocity gradient ($\frac{\partial}{\partial r}\left(\frac{\hat{v}_\phi}{r}\right)$ - which we show explicitly in Figure 5.9: these figures taken together essentially reveal that a strong (weak) negative (positive) velocity gradient is linked with a strong (weak), inwards (outwards), (viscous diffusion driven) angular momentum flux), with smaller contributions from the 'weak' meridional circulation. However, in the 'anti-solar' case, the Reynolds stress contribution is opposed by a strong meridional circulation component, associated with the strong and coherent meridional circulation cell that dominates 'anti-solar' cases (for an example, see Figure 5.5), and almost no contribution from a relatively weak viscous diffusion.

It is striking that in anti-solar cases the Reynolds stresses act both to transport angular momentum radially *inwards*, which would tend to promote "anti-solar" behaviour, but their latitudinal transport is equatorward (which tends to favour solar-like zonal flows). We can partly understand why the anti-solar behaviour "dominates" by considering the entropy

transport afforded by meridional circulations as well. Convective upflows and downflows at low and high latitudes tend to establish an equatorward entropy gradient, giving rise to a baroclinic forcing that enhances the meridional circulation (and its poleward angular momentum transport). Baroclinicity thus provides a positive feedback that amplifies the meridional circulation, leading to the strong single-celled structure observed. This single-celled structure (counter-clockwise in the northern hemisphere) largely acts to isotropise the angular momentum along streamlines, transporting angular momentum of a sense that offsets the convective transport.

Finally we note that whilst the general picture described above appears robust, some of the more detailed features, i.e. the magnitudes of the viscous flux components, have highly non-linear dependencies. For simplicity's sake, and in order to make our analysis clear, we have chosen to show only the time-averaged, and equilibrium, flux profiles. A look at the more transient profiles, generally reveals the same senses and balances described above.

5.5.4 Maintenance of the flows - Gyroscopic Pumping

We now turn to the maintenance of the meridional circulation profile, and its links to the differential rotation. As discussed in subsection 5.2.2, some previous studies have found the concept of gyroscopic pumping useful in understanding how these meridional flows are sustained, and how this is related to the differential rotation. Again, we investigate two cases, one 'solar', and one 'anti-solar', and our results are shown in Figure 5.10 and Figure 5.11. Both figures show the same data with different emphases: the colour maps of Figure 5.10 allow for an in-depth analysis of the data, whilst the contour maps of Figure 5.11 visually emphasise the signs of each quantity. From left to right, these figures show the divergence of the Reynolds stress ($-\boldsymbol{\nabla}\cdot\boldsymbol{F}_{\mathrm{RS}}$), the angular momentum transport by the meridional flow $\left(\bar{\rho}\left\langle v_m\right\rangle\cdot\boldsymbol{\nabla}\mathcal{L}\right)$, and the cylindrical mass flux streamfunction (Ψ). Turning first to the anti-solar case (Figure 5.10), consider the relation between the angular momentum transport and the mass-flux meridional streamfunction. In the northern

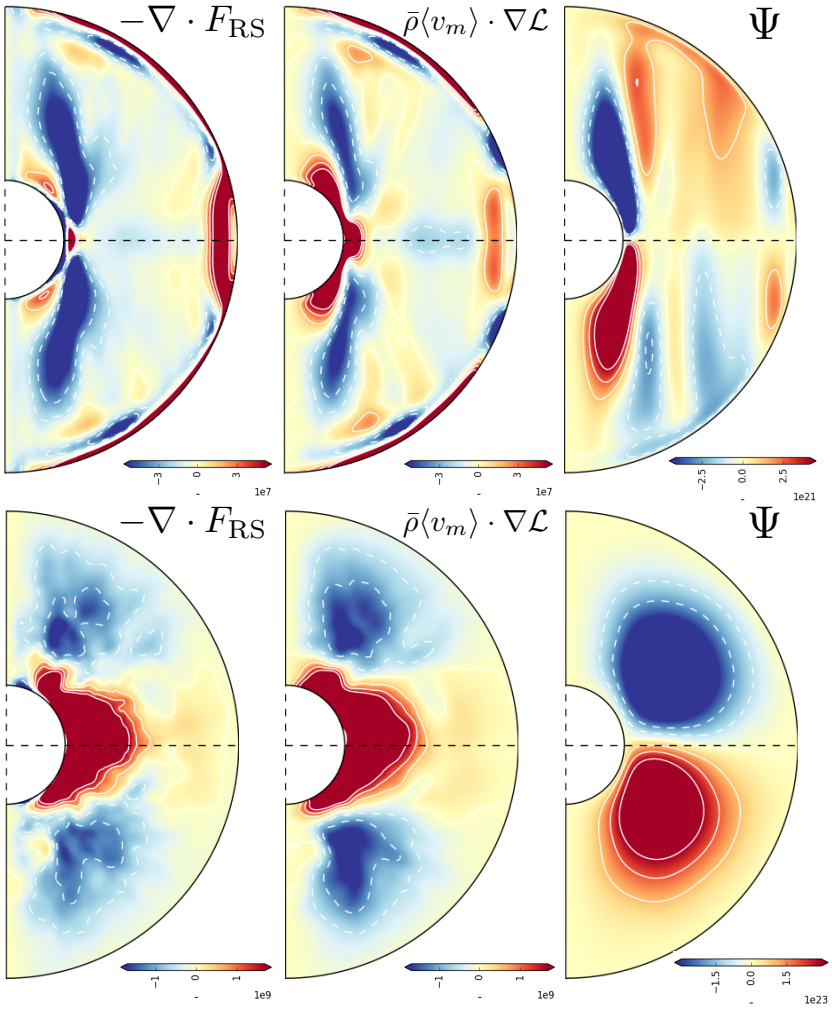

Figure 5.10: Analysis of gyroscopic pumping for two cases; a rapidly rotating 'solar' case ($4\Omega_0$ - top row) and a slowly rotating 'anti-solar' case ($\frac{1}{4}\Omega_0$ - bottom row). The colour maps from left to right are: 1) the divergence of the Reynolds Stress ($-\boldsymbol{\nabla} \cdot \boldsymbol{F}_{\mathrm{RS}}$), 2) the angular momentum transport by the meridional flow $\left(\bar{\rho}\,\langle \boldsymbol{v}_m \rangle \cdot \boldsymbol{\nabla}\mathcal{L}\right)$, 3) the cylindrical mass flux streamfunction (Ψ).

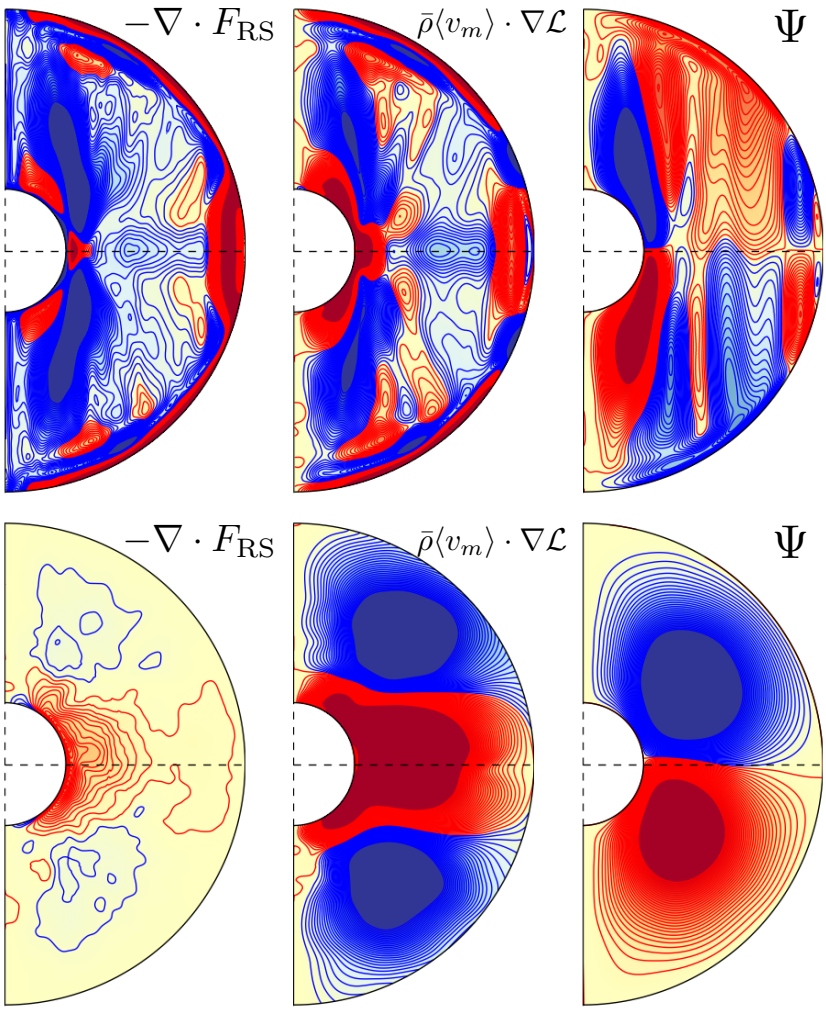

Figure 5.11: Analysis of gyroscopic pumping for two cases; a rapidly rotating 'solar' case ($4\Omega_0$ - top row) and a slowly rotating 'anti-solar' case ($\frac{1}{4}\Omega_0$ - bottom row). The contour maps from left to right are: 1) the divergence of the Reynolds Stress ($-\boldsymbol{\nabla} \cdot \boldsymbol{F}_{\mathrm{RS}}$), 2) the angular momentum transport by the meridional flow ($\bar{\rho}\,\langle v_m \rangle \cdot \boldsymbol{\nabla}\mathcal{L}$), 3) the cylindrical mass flux streamfunction (Ψ).

hemisphere, the meridional flow is counter-clockwise; at this rotation rate, the total angular momentum is nearly constant on cylindrical lines, so that $\nabla\mathcal{L}$ is oriented primarily radially. Thus, near the equator in the northern hemisphere, the radially outward meridional flow is largely aligned with the gradient of $\mathcal{L}$, so that $\left(\bar{\rho}\,\langle v_m\rangle\cdot\nabla\mathcal{L}\right)$ is positive. Near the outer boundary, the flow turns and flows poleward, and is poorly aligned with the gradient of angular momentum, leading to a smaller signal in Figure 5.10; closer to the rotation axis, the return flow becomes more nearly anti-aligned with the angular momentum gradient, implying negative transport of angular momentum (visible in the same figure as a prominent blue region near the rotation axis). In the solar case, the dynamics are more complex, owing to the multi-celled, and disparate, nature of the flows, but similar patterns appear, and the sense of the angular momentum transport is largely consistent with that expected from the mass flux streamfunction coupled to a nearly-cylindrical $\mathcal{L}$ that increases with cylindrical radius.

With the above in place, we can now turn to the mechanism of gyroscopic pumping. Recall that if Reynolds stresses dominate over other effects (including the effects of viscous diffusion), then in a steady state the zonal momentum equation suggests that the convergence of these stresses should largely balance the advection of angular momentum by meridional flows. In both the solar and anti-solar cases considered above (Figure 5.10) we find generally excellent agreement between the convergence of the Reynolds stress and the transport by meridional flows in our simulations. The explanation of this agreement/mechanism is as follows: Since $\nabla\mathcal{L}$ is directed away from the rotation axis, a convergence (divergence) of the Reynolds stresses will induce a meridional flow directed away (towards) from the axis. In essence, in a steady state, the meridional circulation responds to convergences/divergences of angular momentum flux (by, for example, Reynolds stresses) by advecting said angular momentum, leading to continuing meridional circulation. This advection of angular momentum can also be linked to the form of the differential rotation that develops: for more information on this process see, for example, Miesch and Hindman (2011): to summarise, the differential rotation profile is fundamentally linked to the conservation of the angular momentum advected by gyroscopic pumping.

5.5.5 The Meridional Plane Force Balance

We now explore the force balance in the meridional plane, and the applicability of thermal wind balance in our simulations of fully-convective stars. Figure 5.12 shows each term of the meridional plane force balance (as described in Equation 5.1), on the same colour-scale, for a rapidly rotating, low diffusivity, M-star simulation. The first panel (labeled LHS) shows the deviations from the Taylor-Proudman state of cylindrical rotation; the other panels show the remaining terms on the right-hand-side of the same equation, together with their sum (RHS) and the residual arising when this is subtracted from the LHS. This figure shows that almost all of the deviations from the Taylor-Proudman state arise from forces associated with baroclinicity (which occur when surfaces of constant pressure and density do not coincide, giving rise here to a latitudinal entropy gradient); a smaller role is played by viscous stresses in the near-surface regions. The other terms are negligible. (The small residuals that remain when the RHS terms are subtracted appears to arise from non-vanishing temporal variations in the flow; in a steady state, or a long enough time average, this term should vanish. However, we have confirmed that the bulk kinetic energy in the differential rotation and its overall spatial form have achieved a steady state over the intervals we were able to simulate.) The near-equivalence of baroclinic terms and deviations from Taylor-Proudman in turn implies that thermal wind balance (as exemplified in the form represented by Equation 5.4) holds to a good approximation in our models. As this is one of the key factors needed for the theory of Balbus et al. (2009) to hold, we are motivated in the next section to explore whether the link between residual entropy and differential rotation contours – postulated in that theory – also holds.

5.5.6 Linking residual entropy and differential rotation

As discussed in subsection 5.2.1, we now investigate possible links between differential rotation and residual entropy contours, along with the application of this link.
Starting with our 'solar' case, Figure 5.6, a visual inspection would suggest that this alignment of residual entropy and differential rotation may hold true in equatorial regions. This is confirmed by our numerical alignment factor $\mathcal{A}$ (Equation 5.13 – specifically the cosine

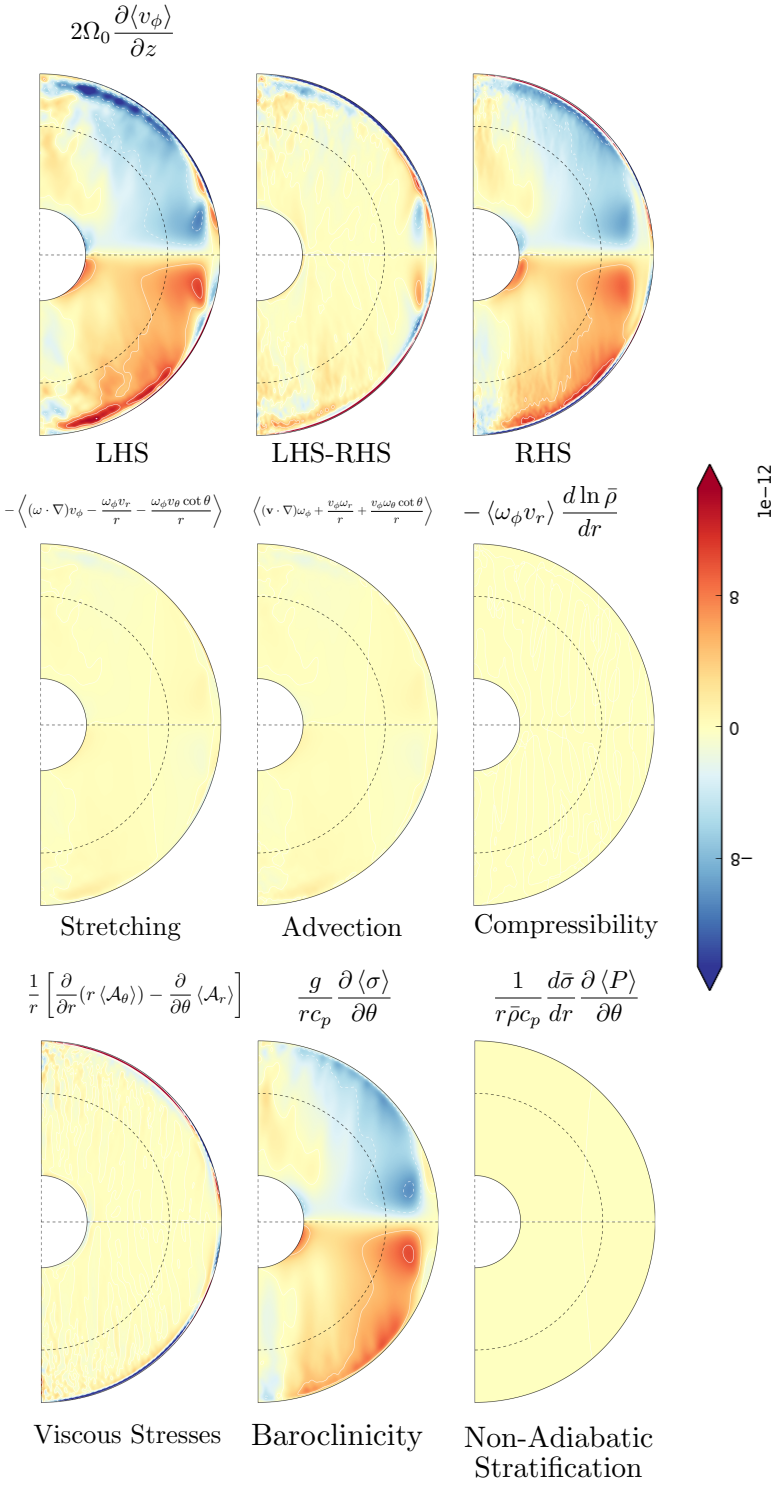

Figure 5.12: The meridional plane force balance for a rapidly rotating, low diffusivity, M-star simulation. The meridional plane force balance is fully defined in Equation 5.1, with the panels of the above figure corresponding to: a) deviations from the Taylor-Proudman constraint (cylindrical rotation), b) the net force in the meridional plane (should be close to zero), c) the sum of terms on the RHS of the meridional plane force balance, d) the stretching term, which describes the stretching and tilting of the vorticity due to velocity gradients, e) the advection term, which describes the advection of vorticity by the flow, f) the compressibility term which describes the change in vorticity due to compressional effects, g) a term encompassing the viscous stresses within the plane, which account for the viscous diffusion of vorticity, g) the baroclinicity term which arises when surfaces of constant pressure and density do not coincide, and finally h) the non-adiabatic stratification term which represents the baroclinic forcing linked with a finite radial entropy profile.

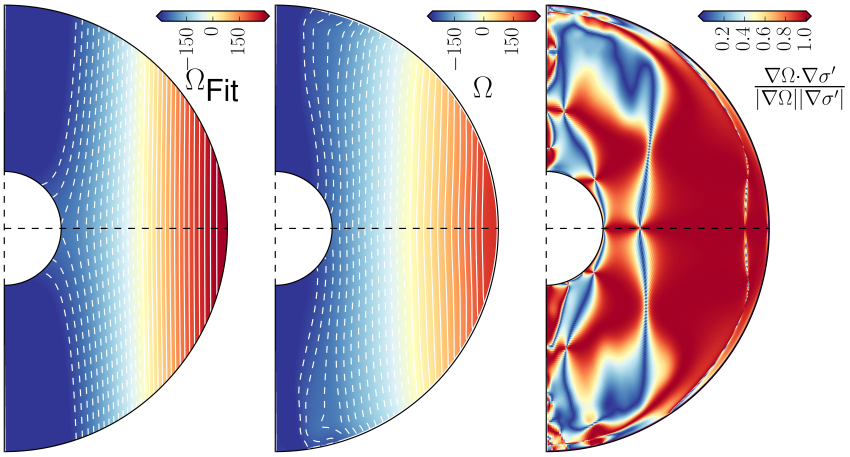

Figure 5.13: TWB differential rotation extrapolation ($\Omega_{\rm Fit}$), Differential rotation (Ω), and Alignment factor ($\mathcal{A}$) for a 'solar' simulation at $4.0\Omega_0$ (i.e. the bottom row of Figure 5.5). Here we show the results of an extrapolation of the differential rotation profile (see Equation 5.11), based upon the surface rotation profile and the assumption that TWB holds throughout the modelled domain. We find good agreement between the extrapolation and our simulation, both in terms of the general contour structure, and the polar and equatorial rotation rates. The regions in which the difference between the two profiles are largest coincide with regions in which differential rotation and residual entropy contours are misaligned.

of the angle between the gradients of σ' and Ω), which exhibits very good agreement between the contours at lower latitudes, and away from the boundaries. The deviations at the boundaries are somewhat to be expected; Balbus et al. (2012) had to pay special attention to, and make adjustments for, both the near surface shear layer and the tachocline in their SCZ calculations, whilst previous studies have shown significant non-physical effects to occur near the boundaries and the central rotation axis (see; Pedlosky 1987). This view is reinforced by the deviation from thermal wind balance, which is dominated by contributions from near the central core and the rotation axis. However this deviation from thermal wind balance does not perfectly track the mis-alignment between residual entropy and angular velocity: at higher latitudes the two sets of contours become almost perpendicular, yet the deviation from thermal wind balance remains relatively small. This behaviour is typical of many of our simulations, which often show significant deviations from contour alignment in the polar regions. The origins of these deviations are not entirely clear to us. However, it is possible that they are linked to the difference in convective flow patterns at high and low latitudes: in the latter, the flow is often reminiscent of "banana cells" that strongly sense the overall rotation of the star, and within these structures the entropy indeed appears to respond to local shear in much the manner suggested by Balbus et al. (2009). At high latitudes, however, the convection is more nearly isotropic and

plume-like, with little evident organisation; in these regions the entropy and the shear are less closely linked. We note that the isorotation contours in our models may well be more cylindrical than those in actual stars; in the Sun, for example, simulations typically find primarily axially-aligned isorotation contours (Featherstone and Miesch 2015), yet global helioseismic inversions (e.g. Howe et al. 2000; Schou et al. 2002; Miesch and Hindman 2011) suggest that these contours should be more radially aligned. If the tendency towards Taylor-Proudman-like states in our simulations is similarly exaggerated, the link between angular velocity and residual entropy in real stars may be even tighter than realised here.

Moving onto our 'anti-solar' case, Figure 5.7, visual inspection once again suggests that the alignment of residual entropy and differential rotation contours may hold true near the equator, and at higher latitudes than our example 'solar' case. This is confirmed by the alignment factor ($\mathcal{A}$), which shows generally good alignment at equatorial and mid latitudes (upto $\sim 60°$), as well as some small regions of alignment near the poles. As expected, we see strong deviations from alignment both near the boundaries and near the central rotation axis, corresponding to the same boundary effects observed in our 'solar' example, and with matching deviations from TWB. We also find significantly reduced, compared to our 'solar-like' case, regions of non-alignment near both poles, without corresponding deviations from TWB.

Of course we are not just interested in the results of our simulations, and the alignment of differential rotation and residual entropy contours, but also in the application of this possible alignment. As such, we also quantitatively investigate the difference between our differential rotation profile, and a differential rotation profile that we extrapolate from the surface rotation. To do this, we follow the prescription of Balbus (2009), as formulated in subsection 5.2.1, but instead of using a sun-like surface profile as they do, we instead use a surface profile generated from an azimuthally, and temporally, averaged simulation. In both the simulations discussed below, we have self consistancly calculated the fitting control parameter B (Equation 5.10) using residual entropy and differentially rotation data from near the outer edge of the simulation domain (more specifically we considered an average of data over the outer $\approx 5\%$, excluding the very top layer that forms part of the

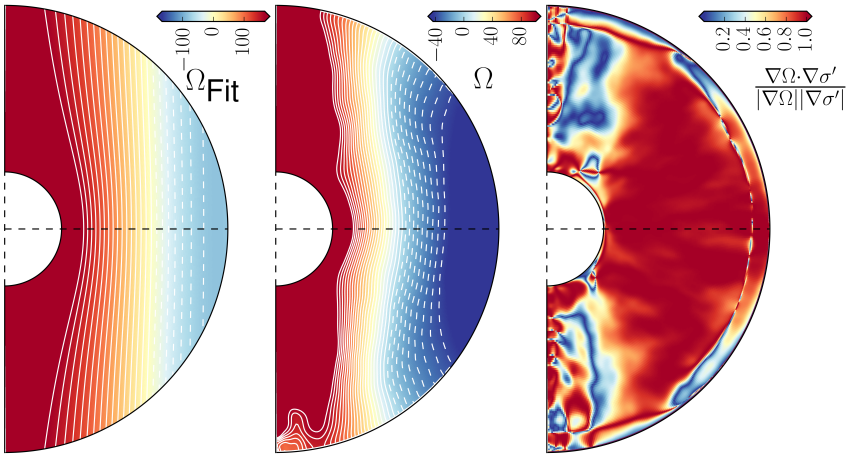

Figure 5.14: TWB differential rotation extrapolation (Ω_{Fit}), Differential rotation (Ω), and Alignment factor ($\mathcal{A}$) for a 'anti-solar' simulation at $\frac{1}{4}\Omega_0$. Here we show the results of an extrapolation of the differential rotation profile (see Equation 5.11), based upon the surface rotation profile and the assumption that TWB holds throughout the modelled domain. We find good agreement between the extrapolation and our simulation, both in terms of the general contour structure, and the polar and equatorial rotation rates. The regions in which the difference between the two profiles are largest coincide with regions in which differential rotation and residual entropy contours are misaligned.

boundary condition).

We start with a relatively simple 'solar' case, shown in Figure 5.13, in which we see good agreement between data from a 'solar' simulation (left panel), and an extrapolation using surface data from the same simulation (central panel), assuming that TWB holds throughout the domain. However, we also find regions in which the two profiles do not agree and, as is to be expected, these regions of disagreement tend to occur in regions in which the differential rotation and residual entropy contours are strongly misaligned (right panel). We also performed this fit for a 'anti-solar' case, shown in Figure 5.14, which, much like our 'solar' case, shows an extrapolation that is a good fit to the simulations differential rotation profile, both in terms of structure and magnitude.

Thus, despite some minor problems, we find, much like Balbus et al. (2009) found for the SCZ, that TWB, and the correspondence of differential rotation and residual entropy contours, provides a reasonably good model for the interior of our fully convective M-star simulations.

5.5.7 Brief Comparison with ASH

As noted in subsection 5.3.2, we also carried out a small number of simulations with ASH, mainly as a consistency check and as a bridge to the parameter regime explored in some prior work. Owing to limitations in our computational resources, we carried out these simulations at only a few values of the relevant non-dimensional parameters; we have chosen in this work to concentrate on the Rayleigh results, since these provide a fuller sampling of the vast parameter space. Here, we provide only a brief guide to how the behaviour in our Rayleigh calculations differs from that realised in somewhat less idealised (ASH) models, while deferring a full analysis to later work.

Broadly, we find the same regimes of behaviour are realised in our ASH calculations as well: at sufficiently slow rotation rates the differential rotation profile is "anti-solar," whilst at higher rotation rates it is "solar-like." These changes are accompanied by changes in the meridional circulation, which again transitions from single-celled to multi-celled as the rotation rate is varied. In the (dimensional) ASH calculations, the absolute values of rotation rate and luminosity at which these transitions occur is different than in our more idealised calculations: essentially, because the ASH calculations include a reference-state "cooling" term intended to mimic radiative losses, they experience greater buoyancy driving at a given value of the luminosity. This implies, among other things, that they convect more readily than our companion Rayleigh calculations: e.g., here we have been forced to adopt luminosities considerably in excess of those typically observed in fully convective stars, because (with the diffusivities adopted here) a simulation with a more realistic luminosity simply wouldn't convect.

We also adopted different boundary conditions in our ASH calculations, mimicking the prior models of Browning (2008): namely, the entropy gradient is fixed at both boundaries. This allows for the possibility of latitudinal entropy variations at the top of the domain, but it also can lead to some unphysical behaviour in the radial entropy profile, as the evolving convection attempts to match on to the pre-defined boundary value of dS/dr. Together, these effects yield somewhat different residual entropy profiles than are found in our standard Rayleigh calculations: in particular, in some regimes the latitudinal variation of the residual entropy is no longer monotonic (as it is in our standard runs). We defer a full

analysis of the differences arising from the varying entropy boundary conditions to later work.

5.6 Introducing the Effects of Magnetism

In this section, we briefly describe the results of a series of simulations including magnetic fields. Here, we have introduced weak seed magnetic fields into progenitor hydrodynamic calculations and followed the growth and evolution of the fields and flows for many convective overturning times. These calculations are significantly more expensive computationally than their hydrodynamic counterparts, so we have sampled the available parameter space somewhat less thoroughly; in that sense the results here must be regarded as somewhat preliminary. Still, they provide a sampling of the intricate dynamics that can occur when convection, rotation, and magnetism interact in fully convective objects. In the discussion below, we first comment on the equilibrated bulk properties of some of these simulations, before turning to an analysis of the zonal flows, meridional circulations, and residual entropy in these models. A summary of the MHD runs is provided in Table 5.4. All the models adopt a magnetic Prandtl number Pm = 2.0, but sample a range of rotation rates, luminosities, and diffusivities. All of the models listed here act as dynamos – i.e., the magnetic Reynolds number in these calculations is sufficiently high that a small seed is amplified by orders of magnitude and sustained against Ohmic decay for as long as we have continued the calculations.

Setting the magnetic Prandtl number to Pm = 2.0 represents a compromise between the low magnetic Prandtl numbers typically required for sustainable dynamo action, and the increase in critical (magnetic) Reynolds number (and hence numerical and computational difficultly) of the fluid as we move to even lower magnetic Prandtl numbers. Note that some studies have managed to investigate magnetic dynamos at lower Pm than considered here (e.g. Schekochihin et al. 2007), but only in simpler geometries - full 3D spherical shells models of low Pm dynamos remain beyond our current numerical capabilities (and CPU time allocations). Studies have also been performed into large Pm dynamos (e.g. Brandenburg 2011), finding that the magnetic energy dissipation is highly linked to the

MHD Runs							
Luminosity	Rotation Rate	Diffusivity	Pr	Pm	Ek	Ro	Raf
0.5	1.0	1.0	$0.3\dot{3}$	2.0	0.00072	0.15	172656
1.0	0.25	1.0	$0.3\dot{3}$	2.0	0.00288	0.76	345313
1.0	0.25	1.5	$0.3\dot{3}$	2.0	0.00433	0.78	102315
1.0	0.25	2.0	$0.3\dot{3}$	2.0	0.00577	0.69	43164
1.0	0.25	3.0	$0.3\dot{3}$	2.0	0.00866	0.67	12789
1.0	0.25	4.0	$0.3\dot{3}$	2.0	0.01155	0.75	5395
1.0	0.25	5.0	$0.3\dot{3}$	2.0	0.01443	0.56	2763
1.0	0.5	1.0	$0.3\dot{3}$	2.0	0.0014	0.37	345313
1.0	0.9	1.0	$0.3\dot{3}$	2.0	0.00080	0.23	345313
1.0	1.0	0.5	$0.3\dot{3}$	2.0	0.00036	0.29	2762505
1.0	1.0	0.9	$0.3\dot{3}$	2.0	0.00065	0.24	473680
1.0	1.0	1.0	$0.3\dot{3}$	2.0	0.00072	0.19	345313
1.0	1.0	1.1	$0.3\dot{3}$	2.0	0.00079	0.19	259438
1.0	1.0	2.0	$0.3\dot{3}$	2.0	0.0014	0.16	43164
1.0	1.1	1.0	$0.3\dot{3}$	2.0	0.00066	0.18	345313
1.0	2.0	1.0	$0.3\dot{3}$	2.0	0.00036	0.066	345313
1.0	4.0	1.0	$0.3\dot{3}$	2.0	0.00018	0.022	345313
1.0	8.0	1.0	$0.3\dot{3}$	2.0	9.0×10^{-5}	0.0040	345313
1.0	10.0	1.0	$0.3\dot{3}$	2.0	7.2×10^{-5}	0.0015	345313
2.0	1.0	1.0	$0.3\dot{3}$	2.0	0.00072	0.26	690626
4.0	1.0	1.0	$0.3\dot{3}$	2.0	0.00072	0.29	1381252
| Fa							

Table 5.4: Dimensional and Non-Dimensional parameters for MHD simulations.

viscosity, thus making high Pm simulations unsuitable for our large-eddy stellar calculations.

We begin by looking at the equilibrium energies of our simulations, specifically looking at the saturation of kinetic and magnetic energies with increasing R_a (via a decreasing diffusivity), and comparing the kinetic saturation energies to those found in purely HD runs. Figure 5.15 shows the equilibrium kinetic energies (and the magnetic energy) for a series of simulations with the same initial parameters as those shown in Figure 5.4, but

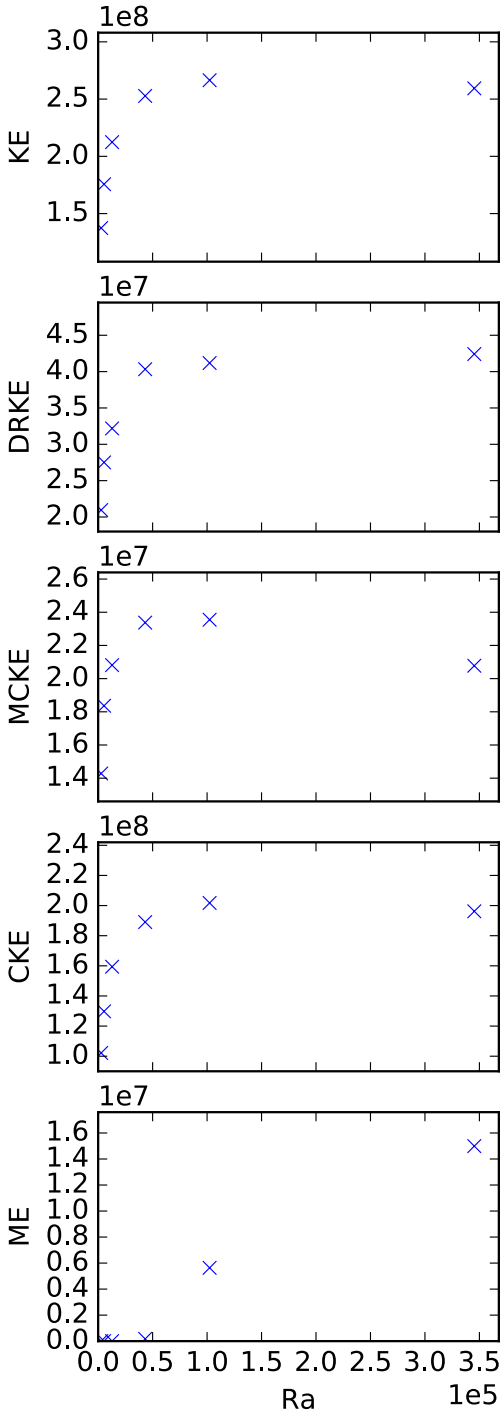

Figure 5.15: Equilibrium magentic and kinetic energies, along with the constituent components of the kinetic energy (Differential rotation (DRKE), meridional circulation (MCKE), and convection (CKE)), for a series of 'anti-solar' simulations at $\frac{1}{4}\Omega_0$, including magnetism, and with varying Rayleigh numbers (Achieved by adjusted the diffusivities $\kappa/\nu/\eta$). In all of the above plots, we see clear evidence that the KE, and the KE components, saturates as we move towards high R_a. However, compared to our HD results, Figure 5.4, we find a slight reduction in said saturation energies, most likely due to the presence of a magnetic energy component in the overall energy balance. As for the magnetic energy, we do not find a corresponding saturation with increasing R_a. Instead, as is to be somewhat expected, we find the dynamo to be highly dependent upon the magnetic diffusivity (and hence magnetic Prandtl number) of the system.

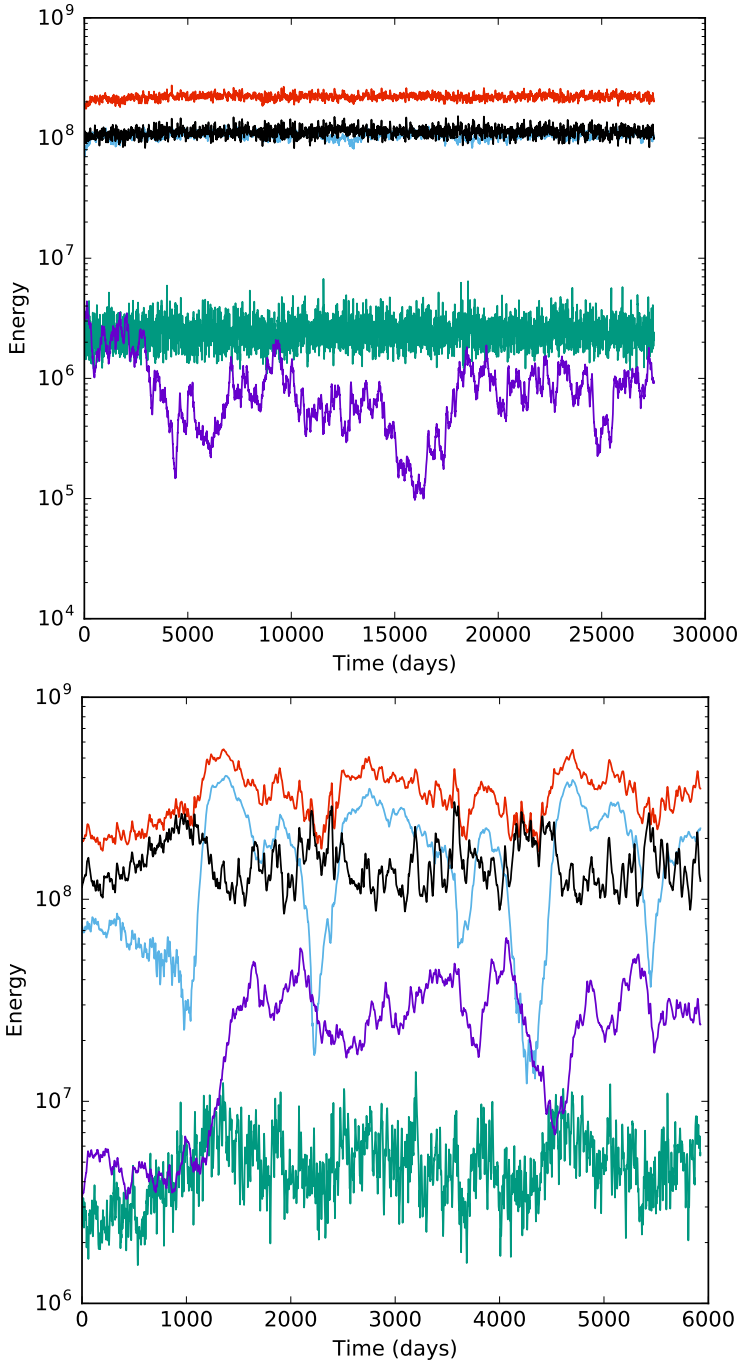

Figure 5.16: Kinetic and magnetic energy evolution for two MHD simulations. In purple is the magnetic energy, blue is the DRKE, black is the CKE, green is the MCKE and red is the total kinetic energy. The upper panel shows our base MHD configuration, which develops a weak magnetic dynamo that does not affect the differential rotation. Whereas the lower panel shows a high luminosity simulation ($L = 2L_0$) in which the magnetic energy component is significant, and spikes in the magnetic energy can be seen to coincide with dips in the differential rotation kinetic energy.

with the addition of a magnetic field. Once again, we find that the kinetic energies saturate as we move to lower diffusivities (higher R_a), with saturation reached at about twice our base diffusivity. If we compare the saturation energies with their HD counterparts, we find saturation values that are noticeably lower than in the HD case. This can be linked to the magnetic dynamo, and its role in converting some of the total kinetic energy to magnetic energy. Note that in the parameter regime considered here, we find a similar (percentage) decrease in all of the saturation kinetic energy components, albeit with a slightly larger decrease in the differential rotation kinetic energy (a 6.1% decrease in DRKE verse a 4.4% decrease in both the MCKE and the CKE), suggesting that the magnetic field (dynamo) is not strong enough to *significantly* suppress the shear associated with differential rotation.

The failure of the magnetic field to suppress differential rotation can be explained by the magnetic energy saturation level, which, even for the strongest dynamo scenario shown here (the lowest diffusivity/highest Ra case), is on the order of the MCKE (i.e. the smallest KE component). As such, in the cases explored here, the effects of Maxwell stress and magnetic tensions never grow to be large enough to significantly affect the shears associated with differential rotation (see, for example, Browning (2008) and Yadav et al. (2015) for more details about how Maxwell stresses (associated with magnetic fields) suppress the generation of differential rotation by suppressing its associated shear).

Note: The magnetic dynamo that forms in our simulations is highly dependent upon both the overall convective structure (and hence rotation rate), and the magnetic diffusivity (η) - as a direct consequence, this result is valid for the particular parameters considered here, but it is not truly robust: to understand the full extent of the MHD kinetic and magnetic energy saturation regime, we must investigate any changes in the the saturation of the magnetic dynamo with either changing magnetic Prandtl number or rotation rate. As such, we defer a further discussion of this until future simulation work is completed.

We now look at two energy evolution profiles in more detail: one case in which the magnetic energy (and hence field) remains weak and so dynamically unimportant, and one in which the magnetic field is significantly stronger, and can be seen to suppress differential rotation. Figure 5.16 shows the volume-averaged magnetic and kinetic energy densities (including kinetic energy components) as a function of time for the aforementioned cases,

which differ only in their imposed luminosity (which is a factor of two larger in the strong-field case). Starting with the weak field case (top) we find a magnetic energy on the order of the weakest kinetic energy component, the meridional circulation. Whilst a dynamo is clearly active (the field is maintained and variable), the field does not affect the differential rotation: that is, fluctuations in the magnetic energy are not reflected in the DRKE. Comparing to the HD simulation with the same parameters (not shown) we find a very similar breakdown between the various kinetic energy components, confirming that the magnetic field has not significantly affected the dynamics. Moving onto our 'strong' field case (bottom), we find that dynamo action has resulted in a significantly stronger magnetic energy, which can be seen to significantly affect the differential rotation kinetic energy. We find significant drops in DRKE which tend to align with spikes in the magnetic energy, and the final energy profile that forms is markedly different from the equivalent HD case. The interplay between the kinetic energy components and the waxing and waning magnetic field is complex; moreover, even the average level at which the field saturates is not yet well understood. Note, for example, that a naive equipartition argument – i.e., the expectation that the magnetic energy might saturate at about the kinetic energy of the convective flows that sustain it (e.g., Roberts 2009) – would suggest similar equilibrated field strengths in these two cases (which differ only by a factor of two in luminosity). Yet their behaviour is markedly different. We defer a more detailed discussion of these issues to future work.

Next, we briefly explore the convective, and associated magnetic, structures that form within our simulations, focusing on the change in convective structure with rotation rate, and the link between the convective structures that form and the radial magnetic field profile. Figure 5.17 shows an instantaneous view of the near surface radial velocity (convective flows - top row) and radial magnetic field (bottom row) for 3 MHD simulations at various rotation rates (increasing from left to right). Upflows, and outwardly directed magnetic fields, are rendered in reddish tones, whilst downflows, and inwardly directed magnetic fields, are blue. Much like our HD simulations, Figure 5.1, we find that at 'slow' rotation rates (leftmost plot) large scale convective cells dominate, with a clear asymmetry between compact and strong downflows, and broader and weaker upflows. As we increase the rotation rate, these convective cells become smaller, and stronger, with significantly smaller,

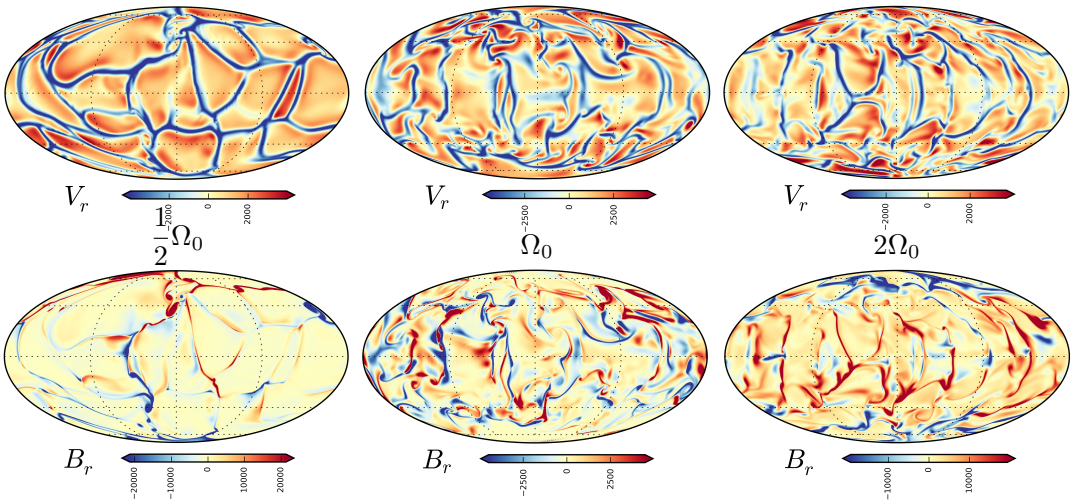

Figure 5.17: Near surface ($R = 0.96R_0$) radial velocity (top) and radial magnetic field (bottom) components for 3 MHD simulations showing how an increasing rotation rate has a significant effect of the convective profile, and how the convective and radial magnetic profiles are intimately linked (with a strong, radial, magnetic field tracing the convective downflows).

and generally uniform, cells forming near the poles, and 'banana-cell-like' structures (i.e. convective rolls parallel to the rotation axis) forming near the equator (rightmost plot) due to the strong Taylor-Proudman constraint. Similar changes in the convective flows with rotation rate have been observed in MHD simulations of both the SCZ (e.g. Miesch et al. 2000) and fully convective shells (e.g. Browning 2008). As for the radial component of the magnetic field, we find that, near the surface, this field primarily traces the convective structures that form: specifically, the field is strongest along the paths traced by the convective downflows. Deeper within the convective region, like the (HD and MHD) convective profiles, the field becomes weaker and more diffuse, operating on significantly broader scales and no longer tightly linked with the convective flows. However, they remain coupled to the magnetic fields at larger radii, with the intricate field structures near the surface emerging from the broader network of deep magnetism.

Finally we introduce, and investigate, the zonal flows at play with our magnetic simulations. We start by looking at the transition from 'anti-solar' to 'solar' differential rotation, meridional circulation and residual entropy, as shown in Figure 5.18, which displays these quantities for three MHD runs at varying rotation rates. We find that the transition between these states occurs in roughly the same parameter regime as in the purely HD case (Figure 5.5): again, the differential rotation is "solar-like" at comparatively rapid rotation rates and "anti-solar" when rotation is sufficiently retarded. There is also an accompany-

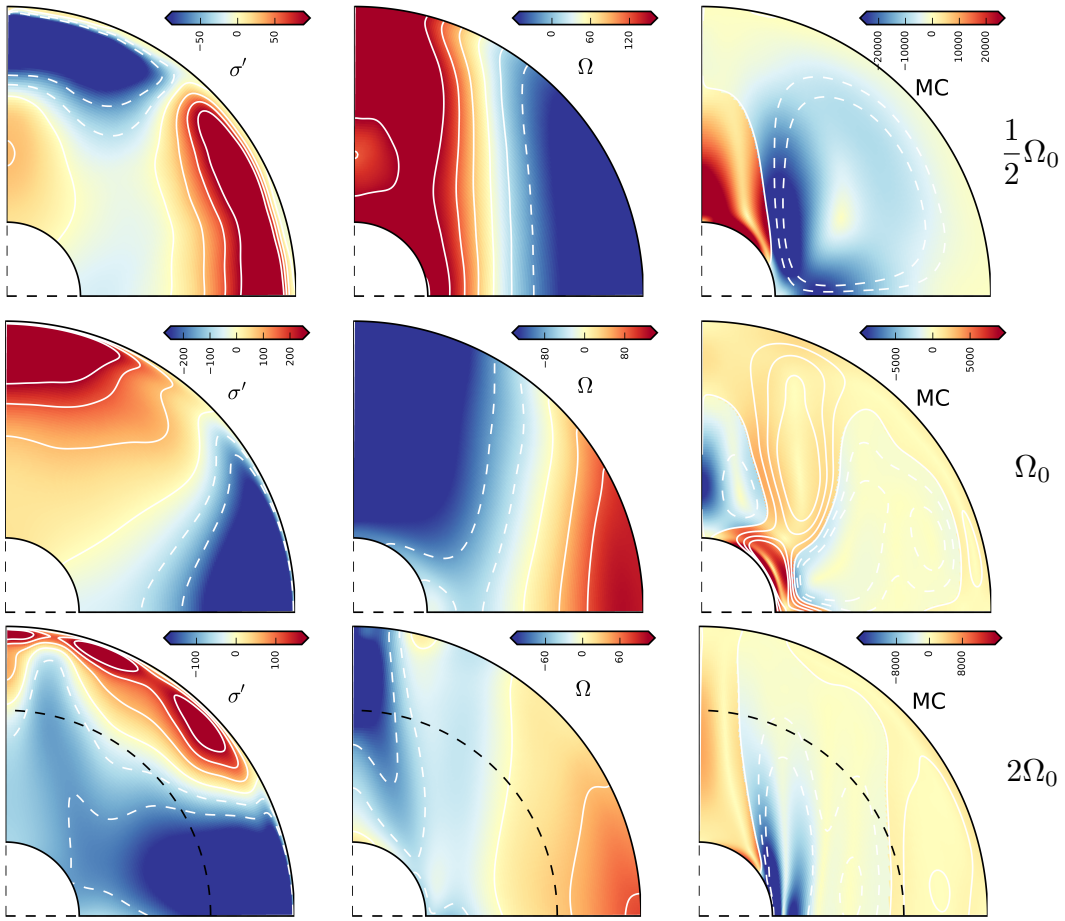

Figure 5.18: Residual entropy (σ'), differential rotation (Ω), and meridional circulation (MC) profiles for three MHD simulations spanning the transition from 'anti-solar' (top row) to 'solar' (bottom row) via an increasing rotation rate. Whilst we see the expected changes in latitudinal entropy and differential rotation gradient, as well as meridional circulation profile, we find that these profiles are more chaotic, with the time dependent oscillations induced by the magnetic dynamo having a significant effect on the structure of the observed profiles. Note that all profiles have been averaged over at least 400 days worth of, equilibrated, data.

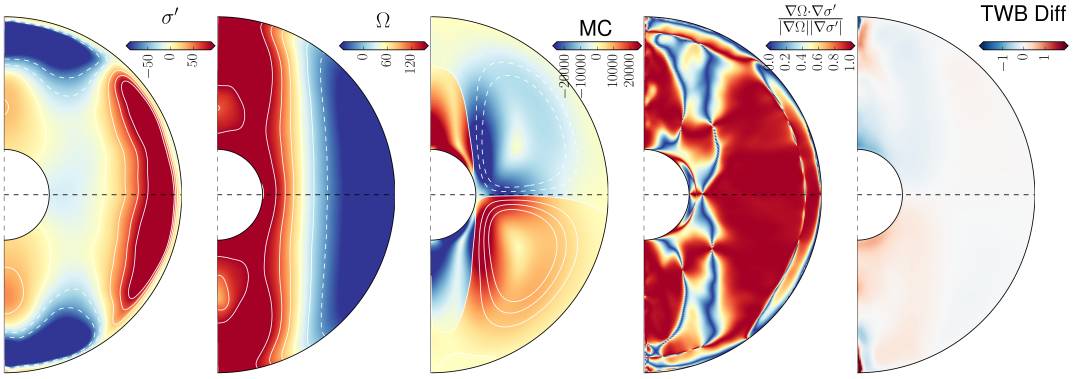

Figure 5.19: Residual entropy (σ'), differential rotation (Ω), meridional circulation (MC), Balbus alignment ($\mathcal{A}$), and TWB agreement profiles for an 'anti-solar' MHD case. Here, we find a structure which is similar to our HD 'anti-solar' case, showing north-south symmetry and a clear, cylindrical, differential rotation profile. This can likely be linked to the relative weakness of the magnetic dynamo in this case (ME ~ MCKE).

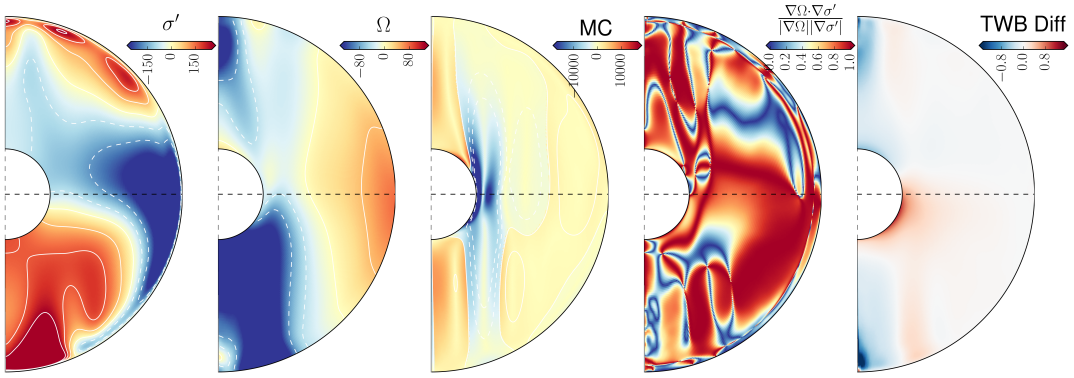

Figure 5.20: Residual entropy (σ'), differential rotation (Ω), meridional circulation (MC), Balbus alignment ($\mathcal{A}$), and TWB agreement profiles for a 'solar' MHD case. Unlike our HD 'solar' case, we do not find symmetric residual entropy, differential rotation, or meridional circulation structures; instead we find a more chaotic structure, which is likely linked to the operation of the magnetic dynamo.

ing clear reversal in residual entropy, and a switch from large-cell to multi-cell meridional circulation. However, the presence of a magnetic dynamo leads to a series of changes in the flows. The differential rotation in our "solar-like" case is visibly reduced in amplitude, with a pole-to-equator contrast of less than 200 nHz (instead of over 300 nHz in the hydrodynamic equivalent). The angular velocity contrasts are also less well-aligned with the rotation axis, possibly reflecting the role that magnetic effects can play in breaking the Taylor-Proudman constraint (see, e.g., Varela et al. 2016). Further, the rich time dependence present in the MHD cases precludes the simulations from reaching a truly steady state. This is likewise evinced in the zonal flows, which reveal more complex spatial structure than their HD equivalents; e.g., in the rapid rotation regime ($\Omega = 2.0\Omega_0$), we find cool "fingers" reaching towards the polar hotspot. This general impression is reinforced by the full azimuthally averaged profiles, shown in Figure 5.19 for the slowly rotating case and Figure 5.20 for the rapidly rotating, which reveal that the zonal flows are on longer symmetric about the equator in the rapidly rotating, 'solar', simulation. As for the alignment of residual entropy and differential entropy, we see agreement of the same order as that seen in the hydrodynamic regime for the slowly rotating, 'anti-solar' case, whereas the rapidly rotating regime exhibits more significant deviation. Broadly, the slowly rotating case shows good alignment between these quantities near the equator (and in smaller regions near the poles), and stronger mis-alignment near the boundaries, the rotation axis, and in some higher latitude (polar) regions. As for the more rapidly rotating regime, the apparent increase in misalignment may be linked to the more non-uniform nature of the

residual entropy and differential rotation contours in strong-field MHD cases. Finally, somewhat stronger deviations from thermal wind balance are present in these cases than in their hydrodynamic counterparts (rightmost panels), but we have not yet analysed this in detail. (As a technical matter, some of these simulations were conducted before we had developed the full suite of diagnostic outputs required to more thoroughly analyse thermal wind balance and gyroscopic pumping. As of this writing, we have not yet "resimulated" all of these cases with this full set of outputs, so our analysis here is still ongoing.) Overall, one of the striking results of our simulations is that in some regimes, strong differential rotation persists even in the presence of dynamo action. Prior simulations of fully convective stars (Browning 2008; Yadav et al. 2015) had found that (in the parameter regimes sampled) the magnetism was strong enough to suppress the zonal flows more completely. Here, despite only modest differences in the numerical approach and parameters adopted, we find many solutions which exhibit only weaker magnetic fields that do not strongly react back on the flows. The origins of these differences are not yet clear: we have no successful, quantitative theory for what sets the equilibrated field strengths achieved in any given dynamo simulation (or in a star), and there is no obvious sense in which the simulations reported here are more (or less) realistic than those conducted previously. There appears, both in our calculations and in these prior works, to be a general correlation between stronger rotational influence and stronger magnetism – but in a dimensional code, this rotational influence is modified not just by the overall rotation rate, but by the numerical diffusivities and the buoyant forcing. (That is, the convective Rossby number is affected both by changes in the Rayleigh number, and by the Taylor or Ekman numbers, and these in turn depend on the boundary conditions and numerical scheme in slightly subtle ways.) Our calculations sample somewhat more turbulent flows than those considered in Browning (2008), for example, so at fixed (dimensional) angular velocity the influence of rotation is then somewhat weaker; this may partially explain why the equilibrated field strengths are then slightly smaller, and the impact on differential rotation commensurately less. The corollary is that still more turbulent flows might reveal further surprises. We are optimistic, though, that given the "saturation" in kinetic energies observed in our simulations as diffusivities are decreased, we may be approaching an asymptotic regime in which the details of the result are less sensitive to some of these

effects. We defer a more detailed analysis of these issues to further work.

5.7 Concluding Remarks

In this chapter, we have investigated the zonal flows, meridional circulations, and the relationships between these in simulations of fully convective stars. This included investigating a possible link between residual entropy and differential rotation contours, which (in conjunction with thermal wind balance, if achieved) would allow us to extrapolate the internal rotation profile of a star just from surface measurements. We were motivated partly by recent studies of the solar convection zone, which used simulations to reveal details about the balances which maintain the zonal flows, and showed good agreement between residual entropy and differential rotation contours, including accurate fits to the differential rotation profile recovered from both simulations and solar observations. We hoped to gain a deeper understanding of fully convective stars and their internal dynamics, which may play a key role in the search for life and exoearths.

Our investigation into the zonal flows within fully convective stars revealed few major surprises. We find clear evidence that both rotation and thermal driving affect the internal dynamics of fully convective stars, with a clear transition between 'solar' and 'anti-solar' flow regimes. This includes reversals in the latitudinal residual entropy and differential rotation, which exhibit a fast equator and slow pole in rapidly rotating cases but the opposite in slower rotators; there is an accompanying switch from single-celled to multi-celled meridional circulation. This transition between 'solar' and 'anti-solar' dynamics is also revealed in the near surface convective profiles, which show a switch from large, asymmetric, convective cells, to axially aligned convective rolls, reminiscent of 'banana-cells'. All of these results are akin to ones previously noted in simulations of solar-like stars (e.g., Gilman and Glatzmaier 1981) and planets (e.g., Gastine et al. 2014a), though our simulations differ from the former in modelling a very deep shell, and from most of the latter in encompassing several density scale heights within the anelastic approximation.

We have also investigated the internal balances and energies which maintain the zonal flows. Starting with the kinetic energy components, we find clear evidence of an energy

saturation as we move towards higher Rayleigh numbers whilst only changing the diffusivity (i.e. at fixed rotation and luminosity). This saturation suggests that our simulations may be approaching an asymptotic regime in which some details of the flow field are relatively independent of the numerical parameter adopted. This is crucial, since it would imply that simulations capturing much of the essential dynamics might be tractable with present-day computational resources, even though stars operate in parameter regimes that are very remote from those considered here. We have also analysed the angular momentum flux balance which acts to maintain, and is itself maintained by, the zonal flows. The results of this analysis are generally in good agreement with previous studies (e.g. Browning 2008, in the solar-like rotation regime), and show a balance between either Reynolds stresses and viscous diffusion in the 'solar' regime, or between meridional circulation and Reynolds stresses in the 'anti-solar' regime. We then took this one step further by investigating gyroscopic pumping and the meridional force plane balance - i.e. linking the angular momentum transport directly to the zonal flows. Our investigation into gyroscopic pumping reveals that the same mechanism which drives the meridional circulation in the SCZ is at play within our fully-convective stars, with meridional velocity motions being driven by (and hence also driving) convergences and divergences of angular momentum flux (specifically Reynolds stresses). As for the force balance in the meridional plane, we find that deviations from the Taylor-Proudman constraint are primarily driven by baroclinic effects, with contributions from viscous stresses near the surface, as would be expected for a convection zone in which the thermal wind approximation is valid (i.e. as in the SCZ).

As mentioned above, we were also interested in the theory of Balbus 2009, who suggested a possible alignment of (residual) entropy and differential rotation contours that could be used to extrapolate, via the TWE, the internal differential rotation profile from surface data. We started by briefly investigating this alignment in both the 'solar' and 'anti-solar' regimes, finding some correlation between the two contours, whilst also finding regions within our simulations that exhibited non correlation. This correlation led us to investigate the extrapolation of the internal rotation profile. Here we found generally excellent agreement between the extrapolated profile and the original simulation profile for both 'solar' and 'anti-solar' cases, suggesting a practical utility for the theory that we did not

initially anticipate. Thus, we confirm that the theory of Balbus (2009) may extend well beyond the solar regime, and in particular at Rossby numbers both greater and smaller than in the Sun, and could prove useful in understanding the internal dynamics of distant stars. However, we still have no thorough quantitative understanding of when, and in what regions, the theory works well; clearly this remains a topic of interest for future work.

We finished by commenting briefly on how our results are affected by the presence of magnetism, drawing on a series of simulations of dynamo action in these objects. We examined both the zonal flows that develop, and the kinetic and magnetic energy balances at play. Whilst we do find evidence that a suitably strong magnetic field can impact, and suppress, the differential rotation (kinetic energy), in line with previous work (e.g., Browning 2008; Yadav et al. 2015), we also find a number of MHD cases in which a fairly strong internal shear can persist. In our models, these weak-field states occur at comparatively lower values of the luminosity (or equivalently, at higher Rossby number). We also find evidence that the presence of a magnetic field reduces the evolved kinetic energies of a system, but it does not prevent the saturation of kinetic energies with decreasing diffusivity. These simulations provide a good basis from which we can launch future studies into the internal dynamics, and balances, of fully-convective stars in the MHD domain.

Overall, perhaps the most striking aspect of our investigation is just how similar the dynamics in these fully convective objects is to that realised in much shallower zones of convection akin to the Sun. This agreement was not pre-ordained: these deep shells of convection possess strong density stratifications, and allow for the possibility of global connectivity between hemispheres that is difficult to achieve in thinner convection zones (where only low latitudes lie outside the tangent cylinder). Yet while the behaviour of fully convective stars is unique, it appears to follow many of the same trends as in solar-like convection zones: namely, there is a clear transition between 'solar' and 'anti-solar' differential rotation; zonal flows both maintain, and are maintained by, angular momentum fluxes; and there is a link between residual entropy and differential rotation which can be used to extrapolate a good approximation for the differential rotation profile from surface data. We direct readers to section 6.2 for details about our plans to extend this work.

Chapter 6

The Conclusion

"When you do things right, people won't be sure you've done anything at all."

— God?, Futurama

6.1 Concluding Remarks

In this work we have investigated flows, instabilities, and magnetic fields within stars and planets via a number of different techniques, ranging from solving tractable (simplified) versions of the MHD equations, to taking a known technique and applying it in a novel manner.

In chapter 2, we discussed the MHD equations that underlie most of our work in some detail, considering two methods by which the equations could be converted into a more tractable form (ideal MHD and anelastic MHD) and a few methods through which these equations could be solved numerically (namely the finite-difference approach, spectral decomposition, and the pseudo-spectral approach) in order to investigate both flows and instabilities within interesting astrophysical environs. This was followed by a look at applications of these techniques, ranging from a 'home-grown' 2D HD code designed to model the seminal thermal (convective) instability, Rayleigh-Bénard convection, to the MHD production codes, ATHENA, *Rayleigh*, and ASH, which we use throughout this

thesis. We finished this section with a quick overview of our data reduction and analysis pipelines, purpose-written to take us from raw data outputs all the way to the plots and analysis shown within this work.

This was followed, in chapter 3, by an in-depth investigation into the Heat-Flux-Driven Buoyancy Instability (HBI), specifically its applicability to stellar and planetary atmospheres. Before this work, the HBI had been investigated within the confines of the interstellar medium, where it was found to both operate and to develop an interesting non-linear effect: a significant restriction of heat transport by anisotropic thermal conduction, leading to thermal isolation and an exasperation of the cooling flow problem (Quataert 2008). This, along with the instability criterion (an outwardly increasing temperature profile), sparked our interest since it suggested that (if operative in these environments) the HBI could provide a mechanism to help explain both the coronal heating problem, and the very hot outer atmospheres of highly irradiated exoplanets.

In order to explore this, we calculated a series of parameter space limitations, on both the magnetic field strength and instability wavelength, that an atmosphere would have to satisfy to be considered HBI unstable. The results of this parameter space exploration revealed only limited applicability in the Sun, requiring magnetic field strengths weaker than typically observed (and even then, the HBI would only develop on global length-scales), and almost no applicability in our example Hot Jupiter (HD209458b).

In order to investigate the HBI in solar environments, as well as to quantify the non-linear effects of the HBI more generally, we turned to 2D finite-difference models calculated using ATHENA. Here we investigated the HBI on both local and global scales, and under different physical conditions, such as simulations in which the thermal conduction was slow relative to the dynamical time, or simulations in which the effects of radiative loss were included. These simulations confirmed that the HBI continues to operate when relatively low levels of radiative loss are included, that the instability is able to grow when the conduction is slow (but this growth is also slow, leaving it vulnerable to external effects), and that the instability can also develop on global-scales (with the same provisos as the local, slow thermal conduction, cases). However the simulations also reinforce the weak field requirements of the instability, suggesting little to no growth at 'low' (i.e. $\beta = 2e3$)

plasma betas.

As such, we ended the chapter on a bit of a mixed note: the HBI may conceivably operate in Solar, stellar and planetary atmospheres, but it is likely to be quite limited in scope. If it occurs at all, it is probably limited to small portions of the atmosphere; it is therefore unlikely to have the same significance or broad applicability as it does in the ICM. However, its dramatic consequences for heat transport in the non-linearly evolved state, and the possibility of unexplored parameter regimes where the instability might develop, suggest that the instability may merit further study (section 6.2).

In chapter 4 we examine a novel approach by which the surface, and maybe even sub-surface, rotation profile of a transiting exoplanet might be observed. This is a modification of the Rossiter-McLaughlin effect (which can be used to measure the surface rotation rate of a transiting planet hosting star), designed to operate on transiting exoplanets near secondary eclipse.

We show that the formalism of the effect, observable only at ingress/egress, is the same as in the original scenario, with just the coordinate system shifted from the perspective of a star being transited by a planet, to a planet transited by a star (a full proof and derivation of this is shown in Appendix B). We then use this analytical description to create a model of the effect (detailed in Appendix C), investigating typical anomalies for a Jupiter-like exoplanet orbiting a Sun-like star. We found anomalies on the 10km/s scale, as well as degeneracies and symmetries between different scenarios.

Finally we investigate the observational implications of the effect, finding that the anomaly is only detectable for planets orbiting the brightest stars, when using upcoming 40m-class telescopes (e.g. E-ELT). We also considered observational limitations, suggesting that either strong stellar activity, or starspots (combined with a sufficiently slowly rotating planet) might influence velocity measurements, or even mask the anomaly completely.

We finish, in chapter 5 with an investigation into the internal dynamics of fully convective stars, specifically the zonal flows and the balances which act to maintain them. This is paired with a brief investigation into a theory suggested by Balbus and Weiss (2010) (or in its original form by Balbus (2009)), which proposes that some form of alignment exists

between residual entropy and differential rotation contours and that, via the thermal wind equation, this could be used to recover the internal differential rotation profile from purely surface data. We investigated this using a series of 3D, anelastic spherical-shell, models calculated using *Rayleigh*, and whose configuration was shaped by preliminary studies using ASH. These simulations were purposefully designed to be easy for the community to reproduce, using a polytropic reference state, and we confirmed that the simulations reach an equilibrium state at relatively high diffusivities, thus minimising the CPU time required to complete a model.

Our investigation into the zonal flows within fully convective stars revealed fairly few surprises. We found clear evidence that both rotation and thermal diffusivity affect the flows, in a similar manner to the effects reported for sun-like stars, with a clear transition between 'solar' and 'anti-solar' dynamics. This included reversals in the latitudinal residual entropy and differential rotation gradients, and a switch from single celled to multi-celled differential rotation.

Moving onto the balances which maintain these flows, we found evidence of the angular momentum flux balance which maintains the zonal flows: a balance between Reynolds stresses and viscous diffusion in the 'solar' regime, or between meridional circulation and Reynolds stresses in the 'anti-solar' regime.

Next, our investigation into the theory of Balbus and Weiss (2010) yielded interesting results, despite the observed deviations from thermal wind balance within our simulations. Starting with the alignment of differential rotation and residual entropy contours, we found generally good agreement, albeit with some regions within our simulation domains showing almost no alignment (perpendicular contours). We also constructed "extrapolated" internal differential rotation profiles, based only on the *surface* differential rotation in the models and *assuming* that the proposed relationship between residual entropy and Ω (and thermal wind balance) holds. The resulting extrapolated profiles were generally in excellent agreement with the result of the full simulated differential rotation profile, albeit with some disagreement in said regions of contour non-alignment. This suggests a robustness in the theory that we did not initially expect, as well as confirming that the theory may have applicability beyond Sun-like stars. This presents the intriguing possibility that differential rotation profiles could be recovered from either asteroseismic or

Rossiter-McLaughlin surface rotation data.
We also introduced some results for simulations including a magnetic field, including an interesting example in which we find that a strong internal shear (differential rotation) can persist, despite the presence of a magnetic field that would normally suppress said shear. Here, we focused mainly on the effects of the magnetic field on the results presented earlier in the chapter (i.e., on differential rotation, meridional circulation, and residual entropy); a fuller exploration of the magnetic field strengths and morphologies is deferred to future investigation (section 6.2).

Taken as a whole, we feel that this thesis provides a valuable insight into an increasingly important area of astrophysics, the internal dynamics of stars and planets. After all, the search for a habitable exoplanet is still ongoing, and without details of both the host star dynamics (which affect the planet externally) and the dynamics of the planet itself, it will remain almost impossible to quantitatively declare a planet habitable. Here we have described different techniques by which this information might be derived, either observationally (chapter 4), though models (chapter 5), or via a combination of the two. These discoveries are being driven by major advances in both the power of computational resources (i.e. Moore's Law - Moore 2006) and the sizes (and hence sensitivities and resolutions) of current (VLT) and next-gen (E-ELT) telescopes. It is an exciting time for astrophysics, one this author looks forward to being part of.

6.2 Further work

As mentioned throughout this thesis, there are a number of different directions in which we can expand this work, either as part of our ongoing investigations, or in the more distant future. Here, we will discuss our ongoing investigations, before concluding with possible extensions, and interesting ideas, reserved for future work.
Our investigation into the zonal flows, and the balances which maintain them, within fully convective stars is ongoing. As mentioned in subsection 5.5.4, we are still working on our analysis of gyroscopic pumping, and its possible links to the meridional circulation. After

publication of the hydrodynamic results, and analysis, shown in chapter 5, we intend to apply these analytical techniques to simulations of fully convective stars with magnetic fields (previewed in section 5.6), investigating the suppression of differential rotation and reconfirming the applicability of the Balbus and Weiss (2010) theory within the magnetic parameter regime.

Other possibilities for future work include investigating the hysteresis effect for the transition between 'solar' and 'anti-solar' differential rotation profiles in M-stars, applying the techniques developed here to giant stars (which are known the exhibit a polar-equator entropy/temperature gradient), and of course investigating both helicity and dynamo action within our magnetic cases in more detail. We also aim to further explore the origins of the "plateau" realised in the simulations' kinetic energies, for example by exploring the detailed balance between buoyant driving and viscous and Ohmic dissipation in our models, in light of recent work that has suggested how the latter varies with stratification and Rayleigh number (Currie & Browning, private communication).

The future of our HBI investigation in stellar and planetary atmospheres is somewhat less clear. It must be admitted that some of our basic results (e.g., the narrow applicability of the HBI to the Sun) might have been predicted without recourse to the detailed analysis here; still, our investigation has revealed a few avenues that may merit future study. In particular, we may use the techniques developed in chapter 3 to investigate the HBI in an extended parameter space survey of stellar and planetary atmospheres, aiming to determine whether there are *any* stars for which the instability might be expected to operate over extended regions, and if so to what effect. Furthermore, within the last 18 months, new HPC facilities have also become available, which will allow us to increase the resolution of our global, and slow thermal conduction, HBI simulations, and investigate the instability over move dynamical times before the breakdown of hydrostatic balance destroys the developing structure (i.e. investigate the global-scale instability in a more idealised environment).

Another possible extension to this work would be to extended our more unusual simulations (e.g. slow thermal conduction, rapid radiative loss, global-scales) from 2.5D to fully 3D simulations a la Kunz et al. (2012) and Avara et al. (2013) . This is motivated by the

fundamentally 3D nature of magnetic field lines, and previous studies (Kunz et al. 2012) which have suggested that the formation, and structure of magnetic filaments can be affected by the dimensionality of the system. Thus we suggest that a series of 3D HBI, global-scale, HBI simulations should be performed in order to investigate the change in the non-linearly evolved state within the mid-beta (β 10^5) parameter regime.

Finally, in the not so distant future, we hope that other authors (and maybe even this author), will be able to use observational data to investigate the Rossiter-Mclauglin effect at secondary eclipse (RMse). As mentioned in chapter 4, the Next Generation of Transit Surveys (NGTS), the Transiting Survey Satellite (TESS) and the Planetary Transits and Oscillations of stars (PLATO) projects are expected to find host stars bright enough to allow for the detection of the RMse. Furthermore, with the upcoming generation of 40m class telescopes (i.e. the E-ELT), the situation only improves. Thus the author remains excited for future studies and investigations, and will eagerly await observational results.

The suggestions above represent only a subset of the many possible extensions to this work. The investigation of flows, instabilities, and magnetism in stars is a never ending bounty of interesting, and valuable, research projects.

6.3 Final Notes

The work presented in this thesis makes extensive use of the *NumPy Python* module (Van Der Walt et al. 2011), and all figures were rendered in *Python* using *Matplotlib* (Hunter 2007).

The author would like to thank the College of Engineering, Maths, and Physical Sciences (CEMPS) at the University of Exeter for funding the PhD position responsible for this work. Additionally, this project has received funding from the European Union's Horizon 2020 research and innovation program under grant agreement no. 337705 (CHASM), allowing the author to share interesting results at workshops and conferences.

The calculations shown in this work used a number of different HPC resources. This included: The DiRAC Blue Gene Q Shared Petaflop system at the University of Edinburgh, operated by the Edinburgh Parallel Computing Centre on behalf of the STFC DiRAC HPC Facility (www.dirac.ac.uk), and funded by BEIS National E-infrastructure capital grant ST/K000411/1, STFC capital grant ST/H008845/1, and STFC DiRAC Operations grants ST/K005804/1 and ST/K005790/1. The DiRAC Complexity system, operated by the University of Leicester IT Services, which forms part of the STFC DiRAC HPC Facility (www.dirac.ac.uk), and is funded by BEIS National E-Infrastructure capital grant ST/K000373/1 and STFC DiRAC Operations grant ST/K0003259/1. DiRAC is part of the National E-Infrastructure. The University of Exeter supercomputer, ZEN, a DiRAC facility jointly funded by the STFC, the large facilities capital fund of BEIS and the University of Exeter. ISCA, the new University of Exeter supercomputer.
Additionally, we acknowledge PRACE for awarding us access to MareNostrum based in Spain at the Barcelona Supercomputing Centre, and both Fermi and Marconi, based in Italy at Cineca.

The Appendices

Appendix A

Rosner Radiative Cooling Profile

"These go to 11"

— Nigel Tufnell, This is Spinal Tap

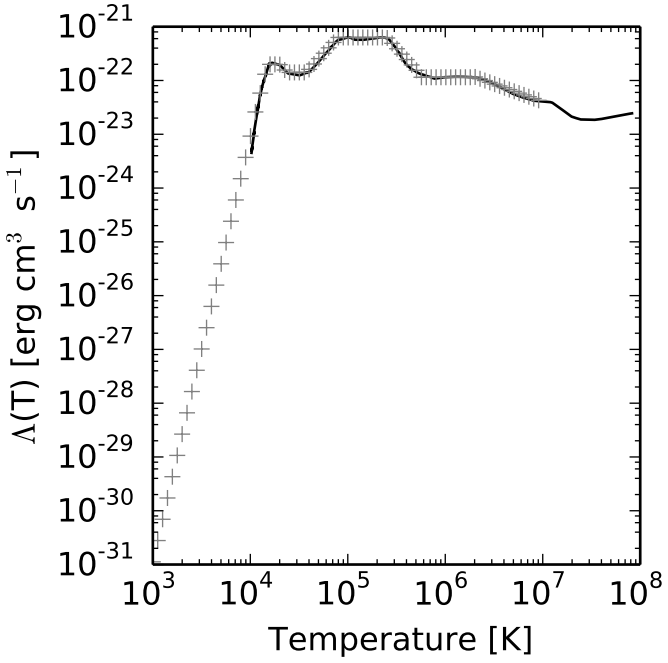

Figure A.1: Figure showing our modified and extended Rosner et al. (1978) radiative loss curve fit (pluses) along with the original radiative loss function (line – In Rosner et al. (1978)), which was calculated using Solar abundances.

In order to calculate radiative cooling times for both the planetary and solar HBI cases, we need to make use of a physical radiative loss function. To that end, we consider the Rosner et al. (1978) fit to a Solar abundance radiative loss function. However,

the original fit is not entirely suited to our purposes, thus we both modify the original fit at lower temperatures (i.e. transition region and corona temperatures) in order to more closely match the original loss function, and then linearly extend this fit to cover even lower temperatures, such as those found in the outer atmospheres of exoplanets. This linear extension of the Rosner radiative loss function is a rough estimate of the radiative loss in exoplanetary atmospheres – it does not affect the solar results – which is useful as a guide whilst we explore possible applications of the HBI.

It is important to note that, the basic nature of this extension not withstanding, using this fit for exoplanetary atmospheres will be fairly approximate since the outer atmospheres of hot Jupiters, whilst sharing a lot in common with the solar corona in terms of composition etc., are also fairly different, thus limiting the radiative loss function to providing only an initial estimate.

This fit is given in Table A.1 and shown with the original radiative loss function in Figure A.1.

$$
\begin{aligned}
P(T) = \quad & \text{nan} && T < 10^{2.001} \\
= \quad & 10^{-54.65} T^{7.9} && 10^{2.001} < T \leq 10^{4.001} \\
= \quad & 10^{-54.65} T^{7.9} && 10^{4.001} < T \leq 10^{4.05} \\
= \quad & 10^{-50.95} T^{7} && 10^{4.05} < T \leq 10^{4.18} \\
= \quad & 10^{-21.7} && 10^{4.18} < T \leq 10^{4.3} \\
= \quad & 10^{-13.1} T^{-2} && 10^{4.3} < T \leq 10^{4.4} \\
= \quad & 10^{-21.85} && 10^{4.4} < T \leq 10^{4.6} \\
= \quad & 10^{-31} T^{2} && 10^{4.6} < T \leq 10^{4.9} \\
= \quad & 10^{-21.2} && 10^{4.9} < T \leq 10^{5.4} \\
= \quad & 10^{-10.4} T^{-2} && 10^{5.4} < T \leq 10^{5.75} \\
= \quad & 10^{-21.94} && 10^{5.75} < T \leq 10^{6.3} \\
= \quad & 10^{-17.73} T^{-2/3} && 10^{6.3} < T \leq 10^{7} \\
= \quad & \text{nan} && T > 10^{7}
\end{aligned}
$$

Table A.1: Modified and extended (Green) version of the Rosner et al. (1978) fit to the radiative loss function. Shown on Figure A.1.

Appendix B

Full Derivation of RMse

"It's still magic even if you know how it's done"

— A Hat Full of Sky, Terry Pratchett

Here, I present a complete derivation of the Rossiter-Mclaughlin effect at secondary eclipse (RMse). This derivation is based upon the work of Ohta et al. (2005), but modified so that the effect is formulated from the planet's perspective (i.e. we use co-ordinate transforms to convert the system to the planet's perspective, with a transiting star). A briefer, publication, version of this method can be found in section 4.2, along with a description of the planetary orbit.

We start, like Ohta et al. (2005), with an initial coordinate system centred at the stars centre, and with its y-axis set to coincide with the observers line of sight (Figure 4.2a). The planet's position is then described by the coordinates (x_p, z_p), corresponding to the orbital plane position and impact parameter respectively. Next, we shift to the planet's reference frame; a coordinate system (x', z') centred on the planet, and which is rotated such that the z'-axis is aligned with the rotation axis of the planet (Ω_p - as shown in Figure 4.2b), and the rotation axis lies within the y'-z' plane.

Ignoring both the differential rotation of the planetary surface, as well as motions associated with atmospheric dynamics, a point on the surface of the rotating planet, with

coordinates (x', z'), will move with a velocity

$$v_p = \Omega_p x' \sin I_p. \tag{B.1}$$

The associated radiation will exhibit a Doppler shift

$$\frac{\Delta\nu}{\nu} = \frac{\Omega_p x' \sin\left(I_p\right)}{c}, \tag{B.2}$$

with respect to the observer along the y'-axis. We now refer the reader to Sec. 3 in Ohta et al. 2005 for a derivation of the radial velocity profile for a star and adopt their expression (20) rewritten for the planet:

$$\Delta v_p = -\Omega_p \sin I_p \frac{\iint x' I(x', z') dx' dz'}{\iint I(x', z') dx' dz'}, \tag{B.3}$$

which relates the radial velocity change Δv_p and the line intensity $I(x', z')$, and, apart from a change in variables, is the same for both stars and planets.
We evaluate this integral assuming a uniform planetary surface intensity,

$$I\left(x', z'\right) = \begin{cases} I_o & \underbrace{x'^2 + z'^2 \leq R_p^2}_{\text{Planet Surface}} \quad \oplus \quad \underbrace{(x' - x'_s)^2 + (z' - z'_s)^2 \geq R_s^2}_{\text{Not The Stars Surface}} \\ 0 & \text{otherwise.} \end{cases} \tag{B.4}$$

ignoring the role of planetary limb-darking and assuming a fully opaque stellar disk.
The RMse occurs during the ingress and egress of the planet behind the star, which occurs when the stellar disk satisfies the relation

$$R_s - R_p < \left(x_s'^2 + z_s'^2\right)^{\frac{1}{2}} < R_s + R_p. \tag{B.5}$$

However, as it stands, solving this is both mathematically and computationally expensive. Therefore, in order to simplify the calculations (Via the power of symmetry), we rotate the coordinate system in a time-dependent manner such that the stellar centre is always

located along the new $\tilde{x}$-axis (see Figure 4.2b) :

$$\begin{pmatrix}\tilde{x}\\ \tilde{z}\end{pmatrix} = \frac{1}{R_p\sqrt{x_s'^2 + z_s'^2}}\begin{pmatrix}x_s' & z_s'\\ -z_s' & x_s'\end{pmatrix}\begin{pmatrix}x'\\ z'\end{pmatrix} \tag{B.6a}$$

$$\therefore \tilde{x} = \frac{1}{R_p\sqrt{x_s'^2 + z_s'^2}}\left[x'x_s' + z'z_s'\right] \tag{B.6b}$$

$$\text{and } \tilde{z} = \frac{1}{R_p\sqrt{x_s'^2 + z_s'^2}}\left[z'x_s' - x'z_s'\right]. \tag{B.6c}$$

In this coordinate system $(x_s', z_s') \rightarrow (\tilde{x}_s, \tilde{z}_s)$, the position of the star is given by:

$$\begin{pmatrix}\tilde{x}_s\\ \tilde{z}_s\end{pmatrix} = \frac{1}{R_p\sqrt{x_s'^2 + z_s'^2}}\begin{pmatrix}x_s' & z_s'\\ -z_s' & x_s'\end{pmatrix}\begin{pmatrix}x_s'\\ z_s'\end{pmatrix} \tag{B.7a}$$

$$= \frac{1}{R_p\sqrt{x_s'^2 + z_s'^2}}\begin{pmatrix}x_s'^2 + z_s'^2\\ x_s'z_s' - x_s'z_s'\end{pmatrix} \tag{B.7b}$$

$$= \frac{\sqrt{x_s'^2 + z_s'^2}}{R_p}\begin{pmatrix}1\\ 0\end{pmatrix} \tag{B.7c}$$

$$= \begin{pmatrix}1+\eta_s\\ 0\end{pmatrix}, \tag{B.7d}$$

where:

$$\eta_s = \frac{\sqrt{x_s'^2 + z_s'^2}}{R_p} - 1. \tag{B.8}$$

The intensity profile is then given by

$$I(\tilde{x}, \tilde{z}) = \begin{cases} I_o & \underbrace{\tilde{x}^2 + \tilde{z}^2 \leq 1}_{\text{Planet Surface}} \quad \oplus \quad \underbrace{\left(\tilde{x} - 1 - \eta_s\right)^2 + \tilde{z}^2 \geq \gamma^2}_{\text{Not The Stars Surface}} \\ 0 & \text{otherwise,} \end{cases} \tag{B.9}$$

where $\gamma = R_s/R_p, R_p = 1$. We confirm the validity of this new intensity profile by investigating the two conditions under-which $I(\tilde{x}, \tilde{z}) = I_o$. Starting with the planetary surface,

we find

$$\tilde{x}^2 + \tilde{z}^2 = \frac{1}{R_p^2\left(x_s'^2 + z_s'^2\right)}\left[(x_s'x' + z_s'z')^2 + (z'x_s' - x'z_s')^2\right] \tag{B.10a}$$

$$= \frac{1}{R_p^2\left(x_s'^2 + z_s'^2\right)}\left[x_s'^2x'^2 + z_s'^2z'^2 + 2x_s'z_s'x'z' - 2x_s'z_s'x'z' + x_s'^2z'^2 + z_s'^2x'^2\right] \tag{B.10b}$$

$$= \frac{1}{R_p^2\left(x_s'^2 + z_s'^2\right)}\left[x'^2\left(x_s'^2 + z_s'^2\right) + z'^2\left(x_s'^2 + z_s'^2\right)\right] \tag{B.10c}$$

$$= \frac{1}{R_p^2\left(x_s'^2 + z_s'^2\right)}\left(x_s'^2 + z_s'^2\right)\left(x'^2 + z'^2\right) \tag{B.10d}$$

$$= \frac{r^2}{R_p^2}. \tag{B.10e}$$

Hence if $\tilde{x}^2 + \tilde{z}^2 \leq 1$ we find $r^2 \leq R_p^2$, thus only the planet's surface is included. Moving onto the second condition, $\left(\tilde{x} - 1 - \eta_s\right)^2 + \tilde{z}^2 \geq \gamma^2$, we find

$$\left(\tilde{x} - 1 - \eta_s\right)^2 + \tilde{z}^2 = \left(\left(\frac{1}{R_p\sqrt{x_s'^2 + z_s'^2}}\left(x_s'x' + z_s'z'\right) - \frac{\sqrt{x_s'^2 + z_s'^2}}{R_p}\right)^2 + \frac{1}{R_p^2\left(x_s'^2 + z_s'^2\right)}\left(x_s'z' - z_s'x'\right)^2\right) \tag{B.11a}$$

$$= \frac{1}{R_p^2\left(x_s'^2 + z_s'^2\right)}\left[\left(\left(x_s'x' + z_s'z'\right) - \left(x_s'^2 + z_s'^2\right)\right)^2 + \left(x_s'z' - z_s'x'\right)^2\right] \tag{B.11b}$$

$$= \frac{1}{R_p^2\left(x_s'^2 + z_s'^2\right)}\left[\left(x_s'^2 + z_s'^2\right)\left((x_s' - x')^2 + (z_s' - z')^2\right)\right] \tag{B.11c}$$

$$= \frac{1}{R_p^2}\left((x_s' - x')^2 + (z_s' - z')^2\right) \geq \left(\frac{R_s}{R_p}\right)^2 \tag{B.11d}$$

$$\therefore R_s \leq (x_s' - x')^2 + (z_s' - z')^2. \tag{B.11e}$$

Thus any points obscured by the stellar disk are not included. Taking these two conditions together confirms that we are only considering regions on the planet's surface not obscured by the stellar disk.

We are now almost ready to start solving for the moments of intensity which contribute

to the radial velocity change (Equation B.3), however we first need to transform them into our new coordinate system. This can be achieved through the Jacobian:

$$\iint F(x', z')\, dx' dz' = \iint f\left(g(\tilde{x}, \tilde{z}), h(\tilde{x}, \tilde{z})\right) \left|\frac{\partial(x', z')}{\partial(\tilde{x}, \tilde{z})}\right| d\tilde{x} d\tilde{z}. \tag{B.12}$$

Which we can solve using the Jacobian matrix, whose determinant is equal to $\frac{\partial(x', z')}{\partial(\tilde{x}, \tilde{z})}$. We solve for this determinant via an inverse transform:

$$\begin{pmatrix} x' \\ z' \end{pmatrix} = \frac{R_s}{\sqrt{x_s'^2 + z_s'^2}} \begin{pmatrix} x_s' & -z_s' \\ z_s' & x_s' \end{pmatrix} \begin{pmatrix} \tilde{x} \\ \tilde{z} \end{pmatrix} \tag{B.13a}$$

$$\therefore x' = \frac{R_s}{\sqrt{x_s'^2 + z_s'^2}} (x_s'\tilde{x} - z_s'\tilde{z}) = A(x_s'\tilde{x} - z_s'\tilde{z}) \tag{B.13b}$$

$$\text{and } z' = A(x_s'\tilde{z} + z_s'\tilde{x}) \tag{B.13c}$$

$$\therefore \frac{\partial x'}{\partial \tilde{x}} = x_s' A \qquad \frac{\partial x'}{\partial \tilde{z}} = -z_s' A \tag{B.13d}$$

$$\frac{\partial z'}{\partial \tilde{x}} = z_s' A \qquad \frac{\partial z'}{\partial \tilde{z}} = x_s' A \tag{B.13e}$$

$$\text{thus: } A^2 \begin{vmatrix} x_s' & -z_s' \\ z_s' & x_s' \end{vmatrix} = A^2 \left(x_s'^2 + z_s'^2\right) = R_p^2. \tag{B.13f}$$

Which reduces the Jacobian transform, and thus our moments of intensity, to

$$\iint I(x', z')\, dx' dz' = R_p^2 \iint I(\tilde{x}, \tilde{z})\, d\tilde{x} d\tilde{z} \tag{B.14a}$$

$$\iint x' I(x', z')\, dx' dz' = R_p^2 \iint x' I(\tilde{x}, \tilde{z})\, d\tilde{x} d\tilde{z}. \tag{B.14b}$$

Now we can start simplifying these moments of intensity by splitting them into separate components for the complete planetary surface, and the stellar disk overlap regions (S -

see Figure 4.2c). We start with Equation B.14a:

$$\iint I(x', z')\, dx' dz' = R_p^2 \iint I(\tilde{x}, \tilde{z})\, d\tilde{x} d\tilde{z} \tag{B.15a}$$

$$= R_p^2 \left[\iint_{\text{All}} I(\tilde{x}, \tilde{z})\, d\tilde{x} d\tilde{z} - \iint_S I(\tilde{x}, \tilde{z})\, d\tilde{x} d\tilde{z} \right] \tag{B.15b}$$

$$= R_p^2 \left[\int_{-1}^{1} \int_{-\sqrt{1-\tilde{x}^2}}^{\sqrt{1-\tilde{x}^2}} I_o d\tilde{x} d\tilde{z} - \iint_S I(\tilde{x}, \tilde{z})\, d\tilde{x} d\tilde{z} \right] \tag{B.15c}$$

$$= R_p^2 \left[2 \int_{-1}^{1} I_o \sqrt{1-\tilde{x}^2}\, d\tilde{x} - \iint_S I(\tilde{x}, \tilde{z})\, d\tilde{x} d\tilde{z} \right] \tag{B.15d}$$

$$= R_p^2 \left[I_o \pi - \iint_S I(\tilde{x}, \tilde{z})\, d\tilde{x} d\tilde{z} \right]. \tag{B.15e}$$

And then moving onto Equation B.14b:

$$\iint x' I(x', z')\, dx' dz' = R_p^2 \iint x' I(\tilde{x}, \tilde{z})\, d\tilde{x} d\tilde{z} \tag{B.16a}$$

$$\text{And: } x = \frac{R_p}{\sqrt{x_s'^2 + z_s'^2}} (x_s' \tilde{x} - z_s' \tilde{z}) \tag{B.16b}$$

$$\therefore \iint x' I(x', z')\, dx' dz' = \frac{R_p^2}{1+\eta_s} \iint (x_s' \tilde{x} - z_s' \tilde{z})\, I(\tilde{x}, \tilde{z})\, d\tilde{x} d\tilde{z} \tag{B.16c}$$

$$= \frac{R_p^2}{1+\eta_s} \left[\iint_{\text{All}} (x_s' \tilde{x} - z_s' \tilde{z})\, I_o d\tilde{x} d\tilde{z} - \iint_S (x_s' \tilde{x} - z_s' \tilde{z})\, I_o d\tilde{x} d\tilde{z} \right]. \tag{B.16d}$$

This can then be simplified, by showing that the 'ALL' component of the integral goes to zero

$$\iint_{\text{All}} (x_s' \tilde{x} - z_s' \tilde{z})\, I_o d\tilde{x} d\tilde{z} = \int_{-1}^{1} \int_{-\sqrt{1-\tilde{x}^2}}^{\sqrt{1-\tilde{x}^2}} (x_s' \tilde{x} - z_s' \tilde{z})\, I_o d\tilde{x} d\tilde{z} \tag{B.17a}$$

$$= I_o \int_{-1}^{1} \left[x_s' \tilde{x} \tilde{z} - \frac{z_s' \tilde{z}^2}{2} \right]_{-\sqrt{1-\tilde{x}^2}}^{\sqrt{1-\tilde{x}^2}} d\tilde{x} \tag{B.17b}$$

$$= I_o \int_{-1}^{1} 2 x_s' \tilde{x} \sqrt{1-\tilde{x}^2} - \frac{z_s' (1-\tilde{x})^2}{2} + \frac{z_s' (1-\tilde{x})^2}{2} d\tilde{x} \tag{B.17c}$$

$$= I_o \int_{-1}^{1} 2 x_s' \tilde{x} \left(1-\tilde{x}^2\right)^{\frac{1}{2}} d\tilde{x} \tag{B.17d}$$

$$= I_o \left[-\frac{2}{3} x_s' \left(1-\tilde{x}^2\right)^{\frac{3}{2}} \right]_{-1}^{1} \tag{B.17e}$$

$$= 0, \tag{B.17f}$$

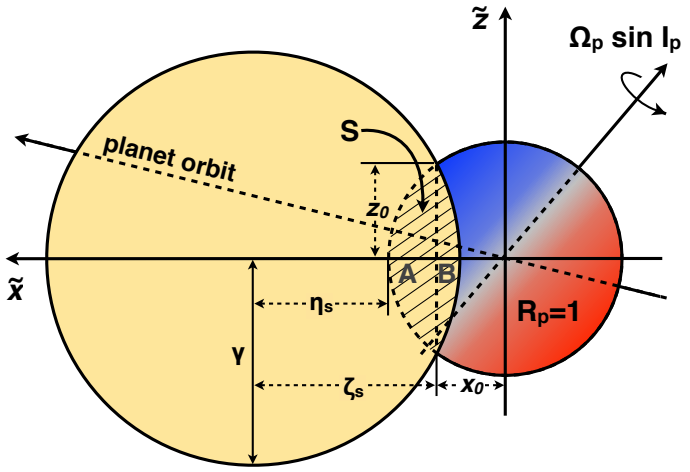

Figure B.1: Schematic illustration of the planetary ingress at secondary eclipse, showing the overlap region (S) and how it is divided into two segments (A and B).

thus giving us our second moment of intensity:

$$\iint x' I\left(x', z'\right) dx' dz' = -\frac{R_p^2}{1+\eta_s} \iint_S \left(x'_s \tilde{x} - z'_s \tilde{z}\right) I_o d\tilde{x} d\tilde{z}. \tag{B.18}$$

Next, we need the range of these overlap integrals. We initially assume this to be the same as Ohta et al. (2005) (but transformed for our system), and then confirm its validity:

$$\iint_S d\tilde{z} d\tilde{x} \rightarrow \underbrace{\int_{x_0}^{1} d\tilde{x} \int_{-\sqrt{1-\tilde{x}^2}}^{\sqrt{1-\tilde{x}^2}} d\tilde{z}}_{\text{A}} + \underbrace{\int_{\tilde{x}_s-\gamma}^{x_0} d\tilde{x} \int_{-\sqrt{\gamma^2-(\tilde{x}-\tilde{x}_s)^2}}^{\sqrt{\gamma^2-(\tilde{x}-\tilde{x}_s)^2}} d\tilde{z}}_{\text{B}}. \tag{B.19}$$

Note that 'A' and 'B' correspond to the two regions of the overlap region, as shown in Figure B.1.

Surface 'A' is relatively easy to put limits on, since it is simply a segment of the planetary circle:

$$S_A = \iint_A d\tilde{x} d\tilde{z} = \int_{x_0}^{1} d\tilde{x} \int_{-\sqrt{1-\tilde{x}^2}}^{\sqrt{1-\tilde{x}^2}} d\tilde{z} \equiv A. \tag{B.20}$$

For surface 'B', we first specify the stellar disks bounding circle (Note: Our rotating coordinate system enforces $z_s = 0$):

$$\tilde{z}^2 + \underbrace{(\tilde{x} - \tilde{x}_s)^2}_{\tilde{x} \text{ coord from star centre}} = \underbrace{\gamma^2}_{R_s^2}, \tag{B.21}$$

which allows us to define the limits for surface 'B':

$$S_B = \iint_B d\tilde{x}d\tilde{z} = \int_{\tilde{x}_s-\gamma}^{x_0} d\tilde{x} \int_{-\sqrt{\gamma^2-(\tilde{x}-\tilde{x}_s)^2}}^{\sqrt{\gamma^2-(\tilde{x}-\tilde{x}_s)^2}} d\tilde{z} \equiv B, \tag{B.22}$$

thus confirming the validity of Equation B.19.

In order to make use of these limits, we must define the intersection point of the planetary and stellar disks $(x_0, \pm z_0)$:

$$x_0 = 1 - \frac{\gamma^2 - \eta_s^2}{2(1+\eta_s)}, \tag{B.23a}$$

$$z_0 = \sqrt{1 - x_0^2} = \frac{\sqrt{(\gamma^2 - \eta_s^2)[(\eta_s+2)^2 - \gamma^2]}}{2(1+\eta_s)}. \tag{B.23b}$$

We now derive these intercepts, starting with x_0, by treating the stellar and planetary circles as simultaneous equations:

$$\tilde{x}^2 + \tilde{z}^2 = 1 \tag{B.24a}$$

$$\tilde{z}^2 + (\tilde{x} - \tilde{x}_s)^2 = \gamma^2 \tag{B.24b}$$

$$\downarrow$$

$$1 - \tilde{x}^2 = \gamma^2 - (\tilde{x} - \tilde{x}_s)^2 \tag{B.24c}$$

$$\tilde{x}^2 + \gamma^2 = 1 + (\tilde{x} - \tilde{x}_s)^2 \tag{B.24d}$$

$$\tilde{x}^2 + \gamma^2 = 1 + \tilde{x}^2 - 2\tilde{x}\tilde{x}_s + \tilde{x}_s^2 \tag{B.24e}$$

$$2\tilde{x}\tilde{x}_s = 1 + \tilde{x}_s^2 - \gamma^2 \tag{B.24f}$$

$$\tilde{x} = \frac{1 + \tilde{x}_s^2 - \gamma^2}{2\tilde{x}_s} \tag{B.24g}$$

$$\tilde{x} = \frac{2\left(1+\eta_s\right) + \eta_s^2 - \gamma^2}{2\left(1+\eta_s\right)} \tag{B.24h}$$

$$x_0 \equiv \tilde{x} = 1 - \frac{\gamma^2 - \eta_s^2}{2\left(1+\eta_s\right)}. \tag{B.24i}$$

From this, we can now derive z_0

$$z_0 = \sqrt{1 - x_0^2} \tag{B.25a}$$

$$= \sqrt{-\frac{\eta_s^2 - \gamma^2}{(1+\eta_s)} - \frac{\left(\eta_s^2 - \gamma^2\right)^2}{4\left(1+\eta_s\right)^2}} \tag{B.25b}$$

$$= \frac{1}{2\left(1+\eta_s\right)}\sqrt{-4\left(1+\eta_s\right)\left(\eta_s^2 - \gamma^2\right) - \left(\eta_s^2 - \gamma^2\right)^2} \tag{B.25c}$$

$$= \frac{1}{2\left(1+\eta_s\right)}\sqrt{\left(\eta_s^2 - \gamma^2\right)\left[\gamma^2 - \eta_s^2 - 4\eta_s - 4\right]} \tag{B.25d}$$

$$= \frac{1}{2\left(1+\eta_s\right)}\sqrt{\left(\gamma^2 - \eta_s^2\right)\left[\left(\eta_s+2\right)^2 - \gamma^2\right]}. \tag{B.25e}$$

Before we finish integrating the moments of intensity, we define a quantity ϵ, which will be used to simplify our final expressions:

$$\epsilon = 1 + \eta_s - x_0 \tag{B.26a}$$

$$= 1 + \eta_s - 1 + \frac{\gamma^2 - \eta_s^2}{2\left(1+\eta_s\right)} \tag{B.26b}$$

$$= \frac{2\eta_s\left(1+\eta_s\right) + \gamma^2 - \eta_s^2}{2\left(1+\eta_s\right)} \tag{B.26c}$$

$$= \frac{\gamma^2 + 2\eta_s + \eta_s^2}{2\left(1+\eta_s\right)}. \tag{B.26d}$$

We are now ready to solve the integrals in our moments of intensity, starting with Equation B.15e, and using the limits from Equation B.19:

$$\iint_S I_0 d\tilde{z} d\tilde{x} \rightarrow \underbrace{I_0 \int_{x_0}^{1} d\tilde{x} \int_{-\sqrt{1-\tilde{x}^2}}^{\sqrt{1-\tilde{x}^2}} d\tilde{z}}_{\text{A}} + \underbrace{I_0 \int_{\tilde{x}_s-\gamma}^{x_0} d\tilde{x} \int_{-\sqrt{\gamma^2-(\tilde{x}-\tilde{x}_s)^2}}^{\sqrt{\gamma^2-(\tilde{x}-\tilde{x}_s)^2}} d\tilde{z}}_{\text{B}}. \tag{B.27}$$

The first component of this integral (A) becomes

$$I_o \int_{x_0}^{1} d\tilde{x} \int_{-\sqrt{1-\tilde{x}^2}}^{\sqrt{1-\tilde{x}^2}} d\tilde{z} = I_o \int_{x_0}^{1} 2\sqrt{1-\tilde{x}^2} d\tilde{x} \tag{B.28a}$$

$$= I_o \left[\tilde{x}\sqrt{1-\tilde{x}^2} + \arcsin\left(\tilde{x}\right)\right]_{x_0}^{1} \tag{B.28b}$$

$$= I_o \left[\frac{\pi}{2} - x_0\sqrt{1-x_0^2} - \arcsin\left(x_0\right)\right]. \tag{B.28c}$$

The second component of the integral (B) is a little more involved, we start by integrating:

$$I_o \int_{\tilde{x}_s-\gamma}^{x_0} d\tilde{x} \int_{-\sqrt{\gamma^2-(\tilde{x}-\tilde{x}_s)^2}}^{\sqrt{\gamma^2-(\tilde{x}-\tilde{x}_s)^2}} d\tilde{z} = I_o \int_{\tilde{x}_s-\gamma}^{x_0} 2\sqrt{\gamma^2-(\tilde{x}-\tilde{x}_s)^2}\, d\tilde{x} \tag{B.29a}$$

$$= I_o \Bigg[-(\tilde{x}_s-\tilde{x})\sqrt{\gamma^2-\tilde{x}_s^2+2\tilde{x}\tilde{x}_s-\tilde{x}^2}$$

$$+\gamma^2 \arctan\left(\frac{\tilde{x}-\tilde{x}_s}{\sqrt{\gamma^2-\tilde{x}_s^2+2\tilde{x}\tilde{x}_s-\tilde{x}^2}}\right)\Bigg]_{\tilde{x}_s-\gamma}^{x_0} \tag{B.29b}$$

$$= I_o \Bigg[-(\tilde{x}_s-x_0)\sqrt{\gamma^2-\tilde{x}_s^2+2\tilde{x}_s x_0-x_0^2}$$

$$+\gamma^2 \arctan\left(\frac{x_0-\tilde{x}_s}{\sqrt{\gamma^2-\tilde{x}_s^2+2\tilde{x}_s x_0-x_0^2}}\right)\Bigg]$$

$$- I_o \Bigg[-\left(\tilde{x}_s-\tilde{x}_s+\gamma\right)\sqrt{\gamma^2-\tilde{x}_s^2+2\tilde{x}_s^2-2\tilde{x}_s\gamma-\tilde{x}_s^2-\gamma^2+2\tilde{x}_s\gamma}$$

$$+\gamma^2 \arctan\left(\frac{\tilde{x}_s-\gamma-\tilde{x}_s}{\sqrt{\gamma^2-\tilde{x}_s^2+2\tilde{x}_s^2-2\tilde{x}_s\gamma-\tilde{x}_s^2-\gamma^2+2\tilde{x}_s\gamma}}\right)\Bigg] \tag{B.29c}$$

$$= I_o \left[-\epsilon\sqrt{\gamma^2-\epsilon^2} + \gamma^2 \arctan\left(\frac{-\epsilon}{\sqrt{\gamma^2-\epsilon^2}}\right) + \frac{\pi\gamma^2}{2} \right], \tag{B.29d}$$

in which we make the following simplification, via the relationship $x_0 = \tilde{x}_s - \epsilon = 1 + \eta_s - \epsilon$:

$$\gamma^2 - \tilde{x}_s^2 + 2\tilde{x}_s x_0 - x_0^2 = \gamma^2 - \tilde{x}_s^2 + 2\tilde{x}_s\left(\tilde{x}_s-\epsilon\right) - \left(\tilde{x}_s-\epsilon\right)^2 \tag{B.30a}$$

$$= \gamma^2 - \epsilon^2. \tag{B.30b}$$

Next, we need to simplify Equation B.29d, which can be achieved via a series of trigono-

metric identities:

$$\arctan(-x) = -\arctan(x) = -\arcsin\left(\frac{x}{\sqrt{x^2+1}}\right) = \arccos\left(\frac{x}{\sqrt{x^2+1}}\right) - \frac{\pi}{2}, \tag{B.31}$$

in which:

$$x = \frac{\epsilon}{\sqrt{\gamma^2-\epsilon^2}} \qquad \text{And} \qquad x^2+1 = \frac{\gamma^2-\epsilon^2+\epsilon^2}{\gamma^2-\epsilon^2} = \frac{\gamma^2}{\gamma^2-\epsilon^2} \tag{B.32a}$$

$$\therefore \frac{x}{\sqrt{x^2+1}} = +\frac{\epsilon}{\sqrt{\gamma^2-\epsilon^2}}\frac{\sqrt{\gamma^2-\epsilon^2}}{\gamma} = +\frac{\epsilon}{\gamma} \tag{B.32b}$$

$$\therefore \arctan\left(-\frac{\epsilon}{\sqrt{\gamma^2-\epsilon^2}}\right) = \arccos\left(\frac{\epsilon}{\gamma}\right) - \frac{\pi}{2}. \tag{B.32c}$$

Thus the second term of the integral (B) becomes:

$$= I_o\left[-\epsilon\sqrt{\gamma^2-\epsilon^2} + \gamma^2\arccos\left(\frac{\epsilon}{\gamma}\right) - \frac{\pi\gamma^2}{2} + \frac{\pi\gamma^2}{2}\right] \tag{B.33a}$$

$$= I_o\left[\gamma^2\arccos\left(\frac{\epsilon}{\gamma}\right) - \epsilon\sqrt{\gamma^2-\epsilon^2}\right]. \tag{B.33b}$$

Putting these terms together (Equation B.28c and Equation B.33b), Equation B.27 becomes

$$\iint_S I_0 d\tilde{z}d\tilde{x} = I_o\left[\frac{\pi}{2} - \arcsin(x_o) - x_o z_o - \epsilon\sqrt{\gamma^2-\epsilon^2} + \gamma^2\arccos\left(\frac{\epsilon}{\gamma}\right)\right] \tag{B.34a}$$

$$= I_o\left[\arcsin\left(\sqrt{1-x_o^2}\right) - z_o(x_o+\epsilon) + \gamma^2\arccos\left(\frac{\epsilon}{\gamma}\right)\right] \tag{B.34b}$$

$$= I_o\left[\arcsin(z_o) - z_o(1+\eta_p) + \gamma^2\arccos\left(\frac{\epsilon}{\gamma}\right)\right]. \tag{B.34c}$$

Which we simplified via the combination of a Pythagorean relationship, $\epsilon^2 + z_0^2 = \gamma^2$, and a trigonometric identity, $\frac{\pi}{2} - \arcsin(x) = \arcsin\left(\sqrt{1-x^2}\right)$. Finally, we substitute this back into Equation B.15e to get the final, first, moment of intensity:

$$\iint I(x',z')\,dx'dz' = I_o R_p^2\left[\pi - \arcsin(z_o) + z_o(1+\eta_p) - \gamma^2\arccos\left(\frac{\epsilon}{\gamma}\right)\right]. \tag{B.35}$$

We now move onto solving the second moment of intensity integral, Equation B.18, once

again using the limits from Equation B.19:

$$\iint_S (\tilde{x}x'_s - \tilde{z}z'_s)\, I_o d\tilde{z} d\tilde{x} = \underbrace{I_o \int_{x_o}^{1} \int_{-\sqrt{1-\tilde{x}^2}}^{\sqrt{1-\tilde{x}^2}} (\tilde{x}x'_s - \tilde{z}z'_s)\, d\tilde{z} d\tilde{x}}_{\text{A}} + \underbrace{I_o \int_{\tilde{x}'_s-\gamma}^{x_o} \int_{-\sqrt{\gamma^2-(\tilde{x}-\tilde{x}'_s)^2}}^{\sqrt{\gamma^2-(\tilde{x}-\tilde{x}'_s)^2}} (\tilde{x}x'_s - \tilde{z}z'_s)\, d\tilde{z} d\tilde{x}}_{\text{B}}. \tag{B.36}$$

We start with the first part of the integral (A):

$$\begin{aligned}
\text{Int}_\text{A} &= I_o x_s \int_{x_o}^{1} \left[\tilde{x}\tilde{z} - \frac{z_s}{2x_s}\tilde{z}^2\right]_{-\sqrt{1-\tilde{x}^2}}^{\sqrt{1-\tilde{x}^2}} d\tilde{x} && \text{(B.37a)}\\
&= I_o x_s \int_{x_o}^{1} 2\tilde{x}\sqrt{1-\tilde{x}^2}\, d\tilde{x} && \text{(B.37b)}\\
&= I_o x_s \left[-\frac{2}{3}\left(1-\tilde{x}^2\right)^{\frac{3}{2}}\right]_{x_o}^{1} && \text{(B.37c)}\\
&= \frac{2}{3} I_o x_s \left(1-x_o^2\right)^{\frac{3}{2}} && \text{(B.37d)}\\
&= \frac{2}{3} I_o x_s z_o^3. && \text{(B.37e)}
\end{aligned}$$

Once again, the second component of the integral (B) is a little more involved:

$$\begin{aligned}
\text{Int}_\text{B} &= I_o x_s \int_{\tilde{x}_s-\gamma}^{x_o} \left[\tilde{x}\tilde{z} - \frac{z_s}{2x_s}\tilde{z}^2\right]_{-\sqrt{\gamma^2-(\tilde{x}-\tilde{x}_s)^2}}^{\sqrt{\gamma^2-(\tilde{x}-\tilde{x}_s)^2}} d\tilde{x} && \text{(B.38a)}\\
&= I_o x_s \int_{\tilde{x}_s-\gamma}^{x_o} 2\tilde{x}\sqrt{\gamma^2-(\tilde{x}-\tilde{x}_s)^2}\, d\tilde{x} && \text{(B.38b)}\\
&= I_o x_s \int_{-\gamma}^{x_o-\tilde{x}_s} 2\left(T+\tilde{x}_s\right)\sqrt{\gamma^2-T^2}\, dT && \text{(B.38c)}\\
&= \underbrace{I_o x_s \int_{-\gamma}^{x_o-\tilde{x}_s} 2T\sqrt{\gamma^2-T^2}\, dT}_{\text{C}} + \underbrace{I_o x_s \tilde{x}_s \int_{-\gamma}^{x_o-\tilde{x}_s} 2\sqrt{\gamma^2-T^2}\, dT}_{\text{D}}, && \text{(B.38d)}\\
& && \text{(B.38e)}
\end{aligned}$$

which required the following substitution:

$$\begin{aligned}
T &= \tilde{x} - \tilde{x}_s \qquad d\tilde{x} = dT && \text{(B.39a)}\\
\therefore \text{If } \tilde{x} &= x_o \qquad T = x_o - \tilde{x}_s && \text{(B.39b)}\\
\therefore \text{If } \tilde{x} &= \tilde{x}_s - \gamma \qquad T = -\gamma. && \text{(B.39c)}
\end{aligned}$$

This now gives us two new integrals to solve, and we start with integral 'C':

$$\text{Int}_\text{C} = I_o x_s \int_{-\gamma}^{x_o-\tilde{x}_s} 2T\sqrt{\gamma^2 - T^2}dT \tag{B.40a}$$

$$= I_o x_s \left[-\frac{2}{3}\left(\gamma^2 - T^2\right)^{\frac{3}{2}}\right]_{-\gamma}^{x_o-\tilde{x}_s} \tag{B.40b}$$

$$= I_o x_s \left[-\frac{2}{3}\left(\gamma^2 - (x_o - \tilde{x}_s)^2\right)^{\frac{3}{2}} + \frac{2}{3}\left(\gamma^2 - \gamma^2\right)^{\frac{3}{2}}\right] \tag{B.40c}$$

$$= I_o x_s \left[-\frac{2}{3}\left(\gamma^2 - \epsilon^2\right)^{\frac{3}{2}}\right] \tag{B.40d}$$

$$= -\frac{2}{3} I_o x_s z_o^3 = -\text{Int}_\text{A}, \tag{B.40e}$$

which cancels out integral 'A'. Moving onto integral 'D', we find that:

$$\text{Int}_\text{D} = I_o x_s \tilde{x}_s \int_{-\gamma}^{x_o-\tilde{x}_s} 2\sqrt{\gamma^2 - T^2}dT \tag{B.41a}$$

$$= I_o x_s \tilde{x}_s \left[T\sqrt{\gamma^2 - T^2} + \gamma^2 \arctan\left(\frac{T}{\sqrt{\gamma^2 - T^2}}\right)\right]_{-\gamma}^{x_o-\tilde{x}_s} \tag{B.41b}$$

$$= I_o x_s \tilde{x}_s \left[(x_o - \tilde{x}_s)\sqrt{\gamma^2 - (x_o - \tilde{x}_s)^2} + \gamma^2 \arctan\left(\frac{x_o - \tilde{x}_s}{\sqrt{\gamma^2 - (x_o - \tilde{x}_s)^2}}\right) + \frac{\pi}{2}\gamma^2\right] \tag{B.41c}$$

$$= I_o x_s \tilde{x}_s \left[-\epsilon\sqrt{\gamma^2 - \epsilon^2} + \frac{\pi}{2}\gamma^2 + \gamma^2 \arctan\left(\frac{-\epsilon}{\sqrt{\gamma^2 - \epsilon^2}}\right)\right]. \tag{B.41d}$$

Which can then be simplified using the relationship in Equation B.32c:

$$\text{Int}_\text{D} = I_o x_s \tilde{x}_s \left[-\epsilon z_o + \frac{\pi}{2}\gamma^2 - \frac{\pi}{2}\gamma^2 + \gamma^2 \arccos\left(\frac{\epsilon}{\gamma}\right)\right] \tag{B.42a}$$

$$= I_o x_s \left(1 + \eta_s\right)\left[-\epsilon z_o + \gamma^2 \arccos\left(\frac{\epsilon}{\gamma}\right)\right]. \tag{B.42b}$$

We now have all the components required to solve for the second moment of intensity

$$\iint_S (\tilde{x}x'_s - \tilde{z}z'_s)\, I_o d\tilde{z} d\tilde{x} = \mathrm{Int_A} + \mathrm{Int_C} + \mathrm{Int_D} \tag{B.43a}$$

$$= \frac{2}{3} I_o x'_s z_o^3 - \frac{2}{3} I_o x'_s z_o^3 + I_o x'_s \left(1 + \eta_s\right) \left[-\epsilon z_o + \gamma^2 \arccos\left(\frac{\epsilon}{\gamma}\right)\right] \tag{B.43b}$$

$$= I_o x'_s \left(1 + \eta_s\right) \left[-\epsilon z_o + \gamma^2 \arccos\left(\frac{\epsilon}{\gamma}\right)\right] \tag{B.43c}$$

$$\therefore \iint x' I\left(x', z'\right) dx' dz' = -I_o x'_s R_p^2 \left[-\epsilon z_o + \gamma^2 \arccos\left(\frac{\epsilon}{\gamma}\right)\right]. \tag{B.43d}$$

With these moments of intensity, we care now ready to find the radial velocity anomaly of the planet (during ingress and egress), as a function of the position of the star (x'_s):

$$\Delta v_p = -\Omega_p \sin\left(I_p\right) \frac{\iint x' I\left(x', z'\right) dx' dz'}{\iint I\left(x', z'\right) dx' dz'} \tag{B.44a}$$

$$= \Omega_p \sin\left(I_p\right) \left[\frac{\frac{R_p^2}{1+\eta_s} \iint_s \left(x'_s \tilde{x} - z'_s \tilde{z}\right) I\left(\tilde{x}, \tilde{z}\right) d\tilde{x} d\tilde{z}}{R_p^2 \left[I_o \pi - \iint I\left(\tilde{x}, \tilde{z}\right) d\tilde{x} d\tilde{z}\right]}\right] \tag{B.44b}$$

$$= \Omega_p \sin\left(I_p\right) \left[\frac{\frac{I_o x'_s \left(1+\eta_s\right)}{\left(1+\eta_s\right)} \left[-\epsilon z_o + \gamma^2 \arccos\left(\frac{\epsilon}{\gamma}\right)\right]}{I_o \pi - I_o \left[\arcsin\left(z_o\right) - \left(1 + \eta_p\right) z_o + \gamma^2 \arccos\left(\frac{\epsilon}{\gamma}\right)\right]}\right] \tag{B.44c}$$

$$= \Omega_p x'_s \sin\left(I_p\right) \left[\frac{-\epsilon z_o + \gamma^2 \arccos\left(\frac{\epsilon}{\gamma}\right)}{\pi - \arcsin\left(z_o\right) + \left(1 + \eta_s\right) z_o - \gamma^2 \arccos\left(\frac{\epsilon}{\gamma}\right)}\right]. \tag{B.44d}$$

This result is equivalent to the result found by Ohta et al. (2005) which is to be expected given the identical overlapping area between the stellar and planetary circles.

Appendix C

Modelling the Rossiter-McLauglin Effect at Secondary Eclipse

"But why male models?"

— Derek Zoolander, Zoolander

As part of the work presented in chapter 4, we created a model, available in both Python and IDL, of the radial velocity curve of a transiting exoplanet. This was built in order to investigate the Rossiter-McLauglin effect during secondary eclipse, specifically during exoplanetary ingress and egress. The model was designed to either work directly with known exoplanets, reading in the required parameters from a file, or in a more idealised mode (used to generate Figure 4.5) in which the user inputs the desired model parameters. What follows is a brief description of the code, from inputs required and calculations performed to the final outputs produced.

We start with the required input parameters:

- $v \sin i$ – The surface rotation velocity multiplied by the sin of the rotation tilt to the observer. This cannot be easily split since the two components are degenerate w.r.t each other.

- θ_Ω – The angle between the rotation axis and the normal of the orbital plane.

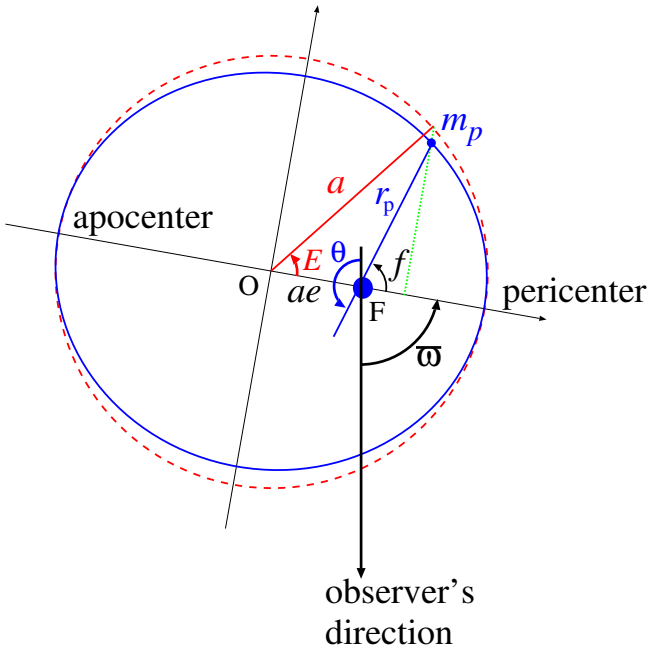

Figure C.1: Schematic top down view of the planetary orbit. The star is located at point F, whilst the barycentre may be found at point O. Reproduced from Ohta et al. (2005).

- γ – The radius of the star, in planetary radii.
- R_{planet} – The radius of the planet, in Jupiter radii.
- $\frac{M_{\text{planet}}}{M_{\text{star}}}$ – The ratio of the planetary and stellar masses.
- P_{orb} – The orbital period in days.
- a – The semi-major axis in AU.
- i – The orbital inclination in degrees.
- $\overline{\omega}$ – The location of the pericentre in degrees.
- e – The eccentricity of the orbit.

Using the parameters, the model first calculates the impact parameter of the secondary eclipse:

$$b = r_p \cos(i)\,, \tag{C.1}$$

where r_p is the star-planet distance at mid transit;

$$r_p = a\frac{1-e^2}{1+e\cos f}, \tag{C.2}$$

in which f is the true anomaly (the angular coordinate of the planet, as measured from the pericentre - see Figure C.1). The true anomaly may then be written in terms of the eccentric anomaly, E (the angular coordinate of the planet, centred on the barycentre, and projected onto a circle):

$$\cos\left(f\right) = \frac{\cos\left(E\right)-e}{1-e\cos\left(E\right)}. \tag{C.3}$$

It is then possible to relate E to the mean anomaly M (the angular position, measured from pericentre, the planet would have if it moved in a circular orbit, with constant speed, and the same orbital period as its true eccentric orbit) through Kepler's equation:

$$M = E - e\sin\left(E\right) = n\left(t-\tau\right), \tag{C.4}$$

where $n = \frac{2\pi}{\mathrm{P_{orb}}}$ is the mean motion, τ is the time of pericentre passage, and t is the time at which M is being measured. Our model starts by calculating values of M for 10000 points throughout two full orbits, and then, using the above formulae (and the Newton-Raphson method where required) solves for the eccentric and true anomalies at each time.
Using these anomalies, the radial velocity of the planet, along the line of sight of the observer, may be calculated (Murray and Dermott 1999):

$$v_{\mathrm{rad},p} \approx \frac{m_s}{m_s+m_p} na\sin i\left[\sin\left(M+\overline{\omega}\right)+e\sin\left(2M+\overline{\omega}\right)\right]. \tag{C.5}$$

We now have the non-eclipse radial velocity curve, as well as a complete model of the planets orbit. As such, it is now relatively simple to calculate the anomalies for which the planet is eclipsed by the star, specifically ingress and egress. We then modify the radial velocity curve with the addition of the Rossiter-McLauglin effect at secondary eclipse:

$$\Delta v_p = \Omega_p x_s' \sin I_p \frac{-\mathrm{z}_0\zeta+\gamma^2\cos^{-1}(\zeta/\gamma)}{\pi-\sin^{-1}\mathrm{z}_0+(1+\eta_s)\mathrm{z}_0-\gamma^2\cos^{-1}(\zeta/\gamma)}. \tag{C.6}$$

For a more detailed description of this equation, and exactly how we come to it, see chap-

ter 4 and Appendix B.

The model finishes by plotting radial velocity curves including the RMse, and deviations from the standard radial velocity profile, i.e. the RMse alone. This model formed a key component of the work shown in chapter 4, allowing us to investigate the RMse in an array of different environments, as well as allowing us to quantitatively analyse the relative contribution of the RMse to the radial velocity curve of known exoplanets (and thus investigate the possibility of observing the effect). Note that, whilst this model was originally written in python, it was ported to IDL for use by a co-author.

Appendix D

Diagnostics and Analytic Routines

"Pay no attention to that man behind the curtain!"

— The Wizard of Oz (1939)

As part of our investigations into both anisotropic buoyancy instabilities (chapter 3) and zonal flows in fully convective stars (chapter 5), we created an extensive series of pipelines in python, designed to ease data analysis. This ranged from manipulation of the raw outputs produced by ATHENA, ASH, and Rayleigh (including modification of how said outputs were generated), to the majority of plots which constitute this work. Here, we give a brief overview of the analysis code developed as part of this work, explaining general details and results, without going too deeply into the internal workings.

D.1 HBI Pipelines

For our HBI analysis, we developed two independent pipelines, one designed to investigate the applicability of the HBI within Solar, stellar, and planetary atmospheres, and one designed to collate and analyse the results of a series of 2.5D HBI simulations, performed using ATHENA. In both cases, the pipelines take raw data as input and produce a series of intermediate analysis outputs, culminating in the plots seen in this work. In terms of accessibility, options (i.e. filenames, gravitational strength, etc) were able to be input by

the user as either command line arguments (thus allowing for the BASH automation) or as responses to prompts upon running the script.

D.1.1 HBI Limits and Growth Rates

We start with the pipeline designed to investigate the parameter space within which the HBI is able to develop and grow. This pipeline works with raw temperature-pressure profiles (using both the ideal gas law and hydrostatic equilibrium to calculate heights relative to the bottom of the profile when required) to calculate, and plot, the limits on HBI development discussed in section 3.4. Using these T-P-H profiles, the pipeline also calculates, and plots, the growth rates of the instability. Our routines can calculate the available parameter space, as well as the growth rates, for scenarios both containing and lacking radiative loss. Examples of the results of this pipeline can be seen throughout section 3.5.

D.1.2 ATHENA Analysis

We now move onto our analysis pipeline for simulations using ATHENA, designed to take as input a series of netCDF files output by ATHENA, and which ultimately produce the plots which make up this work (see section 3.7 and section 3.8).

The pipeline starts by dealing with the outputs of ATHENA, which are initially MPI decomposed. It uses a shell script, and ATHENAs 'join_vtk' executable, to merge the VTK files, and a python script to both merge the decomposed netCDF files, and rearrange the data into individual arrays for each stored variable.

The pipeline then moves onto analysis and visualisation. It calculates the temperature map, the magnetic stream-function, the vertical thermal heat-flux (VHF) through a plane at the centre of the anisotropic region, the Q-value (subsection 3.7.4), the deviation from hydrostatic equilibrium for each cell within the simulation domain, and the averages of the energies, the magnetic field angle in the central region, and the growth rate of the instability. It then plots both these derived variables, and the original outputs, as either 'colour-meshes' or graphs, as appropriate. We also created a script which uses 'avconv'

to convert the outputs of the pipeline into '.mp4' movies for visualisation purposes.

D.2 Rayleigh and ASH pipelines

We finish this chapter with a look at the most developed of our pipelines, which was designed to analyse, and visualise, the results of 3D spherical shell models calculated using both *Rayleigh* and ASH. Note that slightly different versions of the pipeline must be used for *Rayleigh* and ASH simulations due to subtle differences in the format of the simulation outputs. We start by looking at the utility modules and scripts, before discussing the output-type-dependent functionality of the pipeline.

The entire pipeline is based around a core module which provides an interface between python, and *Rayleigh* and ASH. Initially created by our collaborator Nick Featherstone, we extended the interface both to deal with new output parameters, and to read in initial simulation configurations directly from the input files. Modules were also created to calculate the non-dimensional simulation parameters, the stream-function of an arbitrary azimuthally averaged data set, and the latitudinal ratios of both the differential rotation and residual entropy profiles (i.e. the ratio of a parameter at mid-latitude and at the equator).

Both ASH and *Rayleigh* produce a series of diagnostic outputs, ranging from averages over the full domain (Global Averages) to the full 3D, unavenged, spherical data volume. These outputs include Shell Slices, which sample the solution on a series of chosen radial surfaces, and Azimuthal Averages, which do as the name suggests.

Starting with Shell Slices, the pipeline is able to plot a user defined grid of variables (and radii) using either Mollweide projection, or projected onto a sphere using the *geos* library.

As for the Global Averages, the pipeline can plot any output variable as a function of time, either on its own, or with other variables on the same scale. Additionally the Global Averages can themselves be time averaged and used to compare the equilibrium states of multiple simulations. For example, we use these to investigate the saturation of kinetic energy with increasing flux Rayleigh number (e.g.Figure 5.4).

Next, any Shell Averaged variable can be plotted against the normalised radii, either alone

or with other Shell Averages on the same scale. This includes plotting the energy flux components which make up the luminosity profile.

We now come to the most substantial part of our pipeline, the analysis of Azimuthally Averaged data. We use the output Azimuthally Averaged diagnostics to calculate the profiles of residual entropy, differential rotation and meridional circulation (via the mass flux stream-function); the radial and latitudinal angular momentum flux balances (subsection 5.4.3); the two sides of the thermal wind equation (Equation 5.6); the gyroscopic pumping diagnostics (subsection 5.2.2); the differential rotation-residual entropy alignment factor ($\mathcal{A}$ - Equation 5.13); and a fit to the differential rotation profile (following the theory of Balbus (2009), as outlined in subsection 5.2.1). The pipeline can also plot these diagnostics and profiles, either as 'colour-meshes' or graphs, as appropriate. In addition to this, almost all the Azimuthally Averaged diagnostics can be time averaged over a user defined range of time-steps.

Our pipeline also deals with the other diagnostic outputs of *Rayleigh* and ASH: e.g., it can plot the kinetic energy spectrum from the spectral outputs, the equatorial plane from a full 3D spherical output and convert the full 3D spherical outputs into the format required by the VAPOR visualisation suite.

The entire pipeline can be run semi-autonomously via a BASH shell script, allowing for straightforward analysis of 'hot off the press' simulations.

The pipelines discussed above were originally written solely for the author's use, but have since been shared with colleagues at the University of Exeter. We intend to collate and document the scripts which make up the pipeline and make it publicly available via BitBucket.

Appendix E

Stability Boundaries of the HBI Dispersion Relation

"You live and learn. At any rate, you live."

— Douglas Adams

Here, we briefly explore the HBI dispersion relationship in more detail. Specifically, we now solve for the roots of the full, non-radiative, dispersion relationship within a model solar atmosphere (Figure 3.3a). We start we rearranging the, non-radiative, dispersion relation (Equation 3.5):

$$0 = \omega\tilde{\omega}^2 + i\omega_{\text{cond}}\tilde{\omega}^2 - N^2\omega\frac{k_\perp^2}{k^2} - i\omega_{\text{cond}}g\left(\frac{d\ln T}{dz}\right)\frac{\mathcal{K}}{k^2}, \tag{E.1}$$

then substitute in for $\tilde{\omega}$ from Equation 3.6c:

$$0 = \omega(\omega^2 - (\boldsymbol{k}\cdot\boldsymbol{v}_\mathrm{A})^2) + i\omega_\mathrm{cond}(\omega^2 - (\boldsymbol{k}\cdot\boldsymbol{v}_\mathrm{A})^2) - N^2\omega\frac{k_\perp^2}{k^2} - i\omega_\mathrm{cond}g\left(\frac{d\ln T}{dz}\right)\frac{\mathcal{K}}{k^2} \tag{E.2a}$$

$$\downarrow$$

$$0 = \omega^3 - \omega k^2 v_A^2 + i\omega_{cond}\omega^2 - i\omega_{cond}k^2 v_A^2 - N^2\omega\frac{k_\perp^2}{k^2} - i\omega_\mathrm{cond}g\left(\frac{d\ln T}{dz}\right)\frac{\mathcal{K}}{k^2} \tag{E.2b}$$

$$\downarrow$$

$$0 = \omega^3 + \omega^2\left(i\omega_{cond}\right) + \omega\left(-k^2 v_A^2 - N^2\omega\frac{k_\perp^2}{k^2}\right) - i\left(\omega_{cond}k^2 v_A^2 + \omega_\mathrm{cond}g\left(\frac{d\ln T}{dz}\right)\frac{\mathcal{K}}{k^2}\right). \tag{E.2c}$$

We now calculate the coefficients in the above equation (Equation E.2c) using both a range of wavelengths and a model solar atmosphere (Figure 3.3a), before using Python (and NumPy) to solve for the roots of the dispersion relation.

The roots are complex, resulting in both an imaginary, HBI growth, component (see Figure E.1), and a real, exponential decay, component representing the suppression of the instability (see Figure E.2). These two components are generally in good agreement with our more heuristic analysis (section 3.4), with $t_\mathrm{cond} = t_\mathrm{dyn}$ representing a reasonable approximation to the upper stability boundary of the HBI. As such, throughout chapter 3, we stick to our heuristic approach.

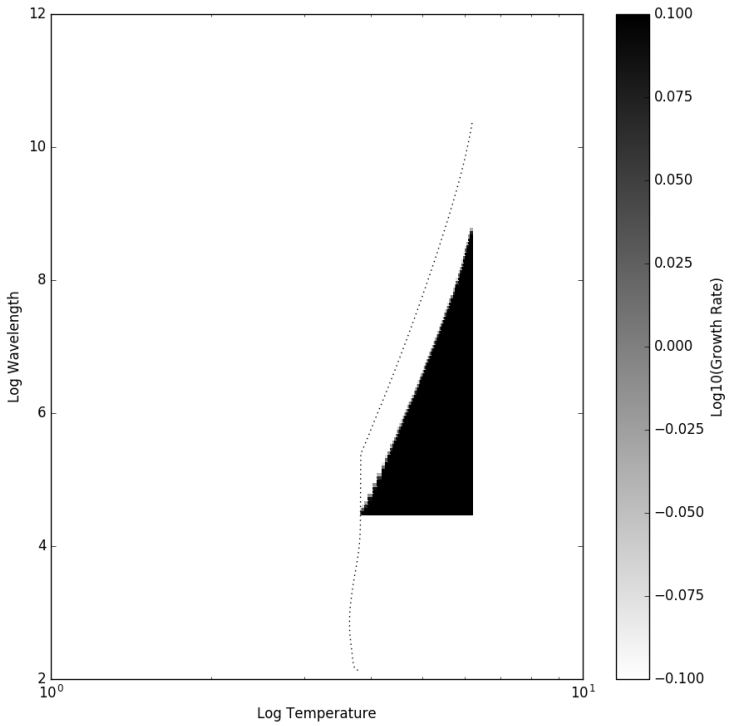

Figure E.1: Imaginary components of the roots of the full, non-radiative, HBI dispersion relation (Equation E.2c). These imaginary components represent HBI growth, and generally agree with the condition that conduction must be rapid relative to the dynamical growth time, with HBI growth dropping off near $t_{\rm cond} = t_{\rm dyn}$ (the dotted line on the above figure).

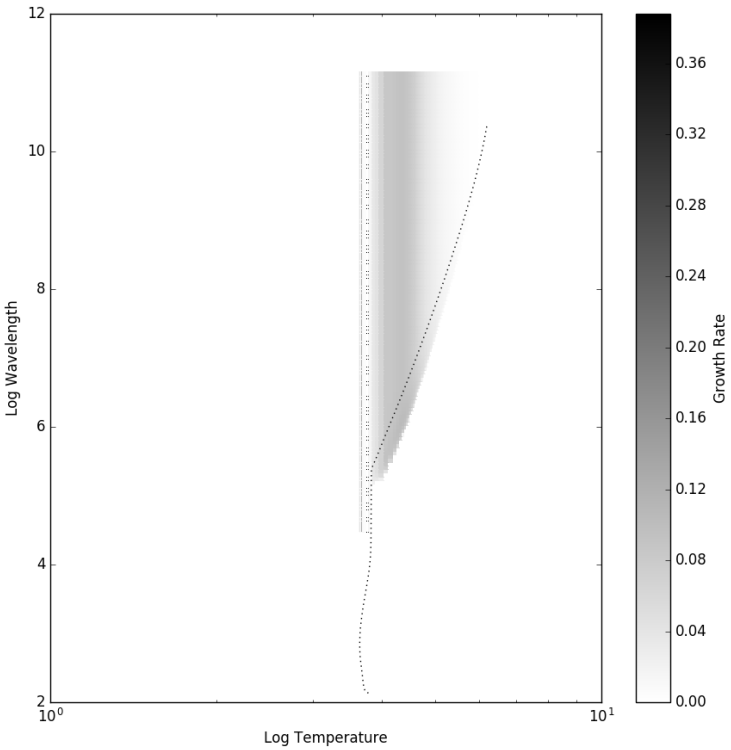

Figure E.2: Real components of the roots of the full, non-radiative, HBI dispersion relation (Equation E.2c). These real components represent exponential decay, and generally agree with the idea that the HBI is suppressed when conduction is slow (i.e. when $t_{\rm cond} > t_{\rm dyn}$ - above the dotted line)..

Bibliography

Aerts, C., J. Christensen-Dalsgaard, and D. W. Kurtz. 2010. *Asteroseismology*.

Agnor, C. B., R. M. Canup, and H. F. Levison. 1999. 'On the Character and Consequences of Large Impacts in the Late Stage of Terrestrial Planet Formation.' *Icarus* 142 (November): 219–237.

Ahlers, G., S. Grossmann, and D. Lohse. 2009. 'Heat transfer and large scale dynamics in turbulent Rayleigh-Bénard convection.' *Reviews of Modern Physics* 81 (April): 503–537.

Alfvén, H. 1942. 'Existence of Electromagnetic-Hydrodynamic Waves.' Nature 150 (October): 405–406.

Arakawa, A. 1966. 'Computational Design for Long-Term Numerical Integration of the Equations of Fluid Motion: Two-Dimensional Incompressible Flow. Part I.' *Journal of Computational Physics* 1 (August): 119–143.

Aschwanden, M.J. 2005. *Physics of the Solar Corona*. Springer Berlin Heidelberg.

Aschwanden, M.J., A. Winebarger, D. Tsiklauri, and H. Peter. 2007. 'The Coronal Heating Paradox.' ApJ 659 (April): 1673–1681.

Augustson, K. C., A. S. Brun, M. Miesch, and J. Toomre. 2015. 'Convective Dynamo Simulation with a Grand Minimum.' In *18th Cambridge Workshop on Cool Stars, Stellar Systems, and the Sun*, edited by G. T. van Belle and H. C. Harris, 18:451–466. Cambridge Workshop on Cool Stars, Stellar Systems, and the Sun. January.

Augustson, K., M. Rast, R. Trampedach, and J. Toomre. 2011. 'Modeling the Near-Surface Shear Layer: Diffusion Schemes Studied With CSS.' In *Journal of Physics Conference Series*, 271:012070. Journal of Physics Conference Series. January.

Avara, Mark J., Christopher S. Reynolds, and Tamara Bogdanović. 2013. 'Role of Magnetic Field Strength and Numerical Resolution in Simulations of the Heat-flux-driven Buoyancy Instability.' ApJ 773 (2): 171.

Avrett, E. H., and R. Loeser. 2008. 'Models of the Solar Chromosphere and Transition Region from SUMER and HRTS Observations: Formation of the Extreme-Ultraviolet Spectrum of Hydrogen, Carbon, and Oxygen.' ApJS 175:229–276.

Ayres, T. R. 2002. 'Does the Sun Have a Full-Time COmosphere?' ApJ 575 (August): 1104–1115.

Ayres, T. R., and J. L. Linsky. 1975. 'Stellar model chromospheres. III - Arcturus /K2 III/.' ApJ 200 (September): 660–674.

Babcock, H. W. 1961. 'The Topology of the Sun's Magnetic Field and the 22-YEAR Cycle.' ApJ 133 (March): 572.

Balbus, S. A. 2000. 'Stability, Instability, and "Backward" Transport in Stratified Fluids.' ApJ 534 (1): 420.

———. 2001. 'Convective and Rotational Stability of a Dilute Plasma.' ApJ 562 (2): 909.

———. 2003. 'Enhanced Angular Momentum Transport in Accretion Disks.' ARA&A 41:555–597.

———. 2009. 'A simple model for solar isorotational contours.' *Monthly Notices of the Royal Astronomical Society* 395, no. 4 (June): 2056–2064.

Balbus, S. A., Julius Bonart, Henrik N. Latter, and Nigel O. Weiss. 2009. 'Differential rotation and convection in the Sun.' *Monthly Notices of the Royal Astronomical Society* 400 (1): 176–182.

Balbus, S. A., and J. F. Hawley. 1991. 'A powerful local shear instability in weakly magnetized disks. I - Linear analysis. II - Nonlinear evolution.' ApJ 376 (July): 214–233.

———. 1992. 'A Powerful Local Shear Instability in Weakly Magnetized Disks. IV. Non-axisymmetric Perturbations.' ApJ 400 (December): 610–621.

Balbus, S. A., and Henrik N. Latter. 2010. 'The tachocline and differential rotation in the Sun.' *Monthly Notices of the Royal Astronomical Society* 407, no. 4 (July): 2565–2574.

Balbus, S. A., Henrik Latter, and Nigel Weiss. 2012. 'Global model of differential rotation in the Sun.' *Monthly Notices of the Royal Astronomical Society* 420 (3): 2457–2466.

Balbus, S. A., and C. S. Reynolds. 2010. 'Radiative and Dynamic Stability of a Dilute Plasma.' ApJL 720 (September): L97–L101.

Balbus, S. A., and Emmanuel Schaan. 2012. 'The stability of stratified, rotating systems and the generation of vorticity in the Sun.' *Monthly Notices of the Royal Astronomical Society* 426, no. 2 (October): 1546–1557.

Balbus, S. A., and Nigel O. Weiss. 2010. 'Differential rotation in fully convective stars.' *Monthly Notices of the Royal Astronomical Society* 404 (3): 1263–1271.

Balbus, Steven A., and John F. Hawley. 1998. 'Instability, turbulence, and enhanced transport in accretion disks.' *Rev. Mod. Phys.* 70 (1): 1–53.

Baraffe, I., D. Homeier, F. Allard, and G. Chabrier. 2015. 'New evolutionary models for pre-main sequence and main sequence low-mass stars down to the hydrogen-burning limit.' A&A 577, A42 (May): A42.

Barker, A. J., A. M. Dempsey, and Y. Lithwick. 2014. 'Theory and Simulations of Rotating Convection.' ApJ 791, 13 (August): 13.

Barnes, J. W., and J. J. Fortney. 2003. 'Measuring the Oblateness and Rotation of Transiting Extrasolar Giant Planets.' ApJ 588 (May): 545–556.

Barnes, R., V. S. Meadows, and N. Evans. 2015. 'Comparative Habitability of Transiting Exoplanets.' ApJ 814, 91 (December): 91.

Basri, G., W. J. Borucki, and D. Koch. 2005. 'The Kepler Mission: A wide-field transit search for terrestrial planets [review article].' *New Astronomy Reviews* 49 (November): 478–485.

Basri, G., L. M. Walkowicz, N. Batalha, et al. 2011. 'Photometric Variability in Kepler Target Stars. II. An Overview of Amplitude, Periodicity, and Rotation in First Quarter Data.' AJ 141, 20 (January): 20.

Bate, M. R., I. A. Bonnell, and N. M. Price. 1995. 'Modelling accretion in protobinary systems.' MNRAS 277 (November): 362–376.

Beck, P. G., J. Montalban, T. Kallinger, et al. 2012. 'Fast core rotation in red-giant stars as revealed by gravity-dominated mixed modes.' Nature 481 (January): 55–57.

Berge, P., and M. Dubois. 1984. 'Rayleigh-Benard convection.' *Contemporary Physics* 25 (December): 535–582.

Birkby, J. L., R. J. de Kok, M. Brogi, et al. 2013. 'Detection of water absorption in the day side atmosphere of HD 189733 b using ground-based high-resolution spectroscopy at 3.2 μm.' MNRAS 436 (November): L35–L39.

Blackman, E. G., and G. B. Field. 2002. 'New Dynamical Mean-Field Dynamo Theory and Closure Approach.' *Physical Review Letters* 89, no. 26, 265007 (December): 265007.

Borrero, Juan M., and Kiyoshi Ichimoto. 2011. 'Magnetic Structure of Sunspots.' *Living Reviews in Solar Physics* 8, no. 1 (September): 4.

Boussinesq, J. 1903. *Théorie analytique de la chaleur.* Gauthier-Villars.

Boyd, John P. 1989. *Chebyshev & Fourier Spectral Methods.* Springer-Verlag Berlin Heidelberg.

Brandenburg, A. 2007. 'Near-surface shear layer dynamics.' In *Convection in Astrophysics*, edited by F. Kupka, I. Roxburgh, and K. L. Chan, 239:457–466. IAU Symposium. May.

———. 2011. 'Dissipation in dynamos at low and high magnetic Prandtl numbers.' *Astronomische Nachrichten* 332 (January): 51.

Brandenburg, A., S. Candelaresi, and P. Chatterjee. 2009. 'Small-scale magnetic helicity losses from a mean-field dynamo.' MNRAS 398 (September): 1414–1422.

Brandenburg, A., and W. Dobler. 2002. 'Hydromagnetic turbulence in computer simulations.' *Computer Physics Communications* 147 (August): 471–475.

Brogi, M., R. J. de Kok, J. L. Birkby, H. Schwarz, and I. A. G. Snellen. 2014. 'Carbon monoxide and water vapor in the atmosphere of the non-transiting exoplanet HD 179949 b.' A&A 565, A124 (May): A124.

Brogi, M., I. A. G. Snellen, R. J. de Kok, et al. 2012. 'The signature of orbital motion from the dayside of the planet τ Boötis b.' Nature 486 (June): 502–504.

Brown, B. P., G. M. Vasil, and E. G. Zweibel. 2012. 'Energy Conservation and Gravity Waves in Sound-proof Treatments of Stellar Interiors. Part I. Anelastic Approximations.' ApJ 756, 109 (September): 109.

Browning, G. L., J. J. Hack, and P. N. Swarztrauber. 1989. 'A Comparison of Three Numerical Methods for Solving Differential Equations on the Sphere.' *Monthly Weather Review* 117:1058.

Browning, M. K. 2008. 'Simulations of Dynamo Action in Fully Convective Stars.' *The Astrophysical Journal* 676 (2): 1262.

Browning, M. K., A. S. Brun, and J. Toomre. 2004. 'Simulations of Core Convection in Rotating A-Type Stars: Differential Rotation and Overshooting.' ApJ 601 (January): 512–529.

Browning, M. K., M. S. Miesch, Allan Sacha Brun, and Juri Toomre. 2006. 'Dynamo Action in the Solar Convection Zone and Tachocline: Pumping and Organization of Toroidal Fields.' *The Astrophysical Journal* 648, no. 2 (September): L157–L160.

Brummell, N. H., T. L. Clune, and J. Toomre. 2002. 'Penetration and Overshooting in Turbulent Compressible Convection.' ApJ 570 (May): 825–854.

Brummell, N. H., N. E. Hurlburt, and J. Toomre. 1996. 'Turbulent Compressible Convection with Rotation. I. Flow Structure and Evolution.' ApJ 473 (December): 494.

Brun, A. S., H. M. Antia, and S. M. Chitre. 2010. 'Is the solar convection zone in strict thermal wind balance?' A&A 510, A33 (February): A33.

Brun, A. S., M. K. Browning, and J. Toomre. 2005. 'Simulations of Core Convection in Rotating A-Type Stars: Magnetic Dynamo Action.' ApJ 629 (August): 461–481.

Brun, A. S., R. A. Garcı a, G. Houdek, D. Nandy, and M. Pinsonneault. 2015. 'The Solar-Stellar Connection.' *Space Science Reviews* 196 (December): 303–356.

Brun, A. S., M. S. Miesch, and J. Toomre. 2004. 'Global-Scale Turbulent Convection and Magnetic Dynamo Action in the Solar Envelope.' ApJ 614 (October): 1073–1098.

———. 2011. 'Modeling the Dynamical Coupling of Solar Convection with the Radiative Interior.' ApJ 742, 79 (December): 79.

Brun, Allan Sacha, and Matthew K. Browning. 2017. 'Magnetism, dynamo action and the solar-stellar connection.' *Living Reviews in Solar Physics* 14, no. 1 (September): 4.

Burke, C. J., S. T. Bryson, F. Mullally, et al. 2014. 'Planetary Candidates Observed by Kepler IV: Planet Sample from Q1-Q8 (22 Months).' ApJS 210, 19 (February): 19.

Burkert, Andreas, Douglas N. C. Lin, Peter H. Bodenheimer, Chris A. Jones, and Harold W. Yorke. 2005. 'On the Surface Heating of Synchronously Spinning Short-Period Jovian Planets.' *The Astrophysical Journal* 618 (1): 512.

Burrows, A. S. 2014. 'Highlights in the study of exoplanet atmospheres.' Nature 513 (September): 345–352.

Busse, F. H. 1970. 'Thermal instabilities in rapidly rotating systems.' *Journal of Fluid Mechanics* 44:441–460.

———. 1973. 'Differential Rotation in Stellar Convection Zones. II.' A&A 28 (October): 27.

———. 1978. 'Non-linear properties of thermal convection.' *Reports on Progress in Physics* 41 (December): 1929–1967.

Busse, F. H., and P. G. Cuong. 1977. 'Convection in rapidly rotating spherical fluid shells.' *Geophysical and Astrophysical Fluid Dynamics* 8:17–41.

Caleo, A., S. A. Balbus, and W. J. Potter. 2015. 'Differential rotation and radiative equilibrium in the Sun: is the tachocline spreading?' *Monthly Notices of the Royal Astronomical Society* 448, no. 3 (February): 2077–2084.

Caleo, A., S. A. Balbus, and E. Tognelli. 2016. 'The Goldreich-Schubert-Fricke instability in stellar radiative zones.' MNRAS 460 (July): 338–344.

Canuto, Claudio, M.Y. Hussaini, and Jr. Zang A.M. Quarteroni T.A. 1988. *Spectral Methods in Fluid Dynamics.* Springer-Verlag Berlin Heidelberg.

Carrington, R.C. 1861. *Observations of the Spots on the Sun from November 9, 1853 to March 24, 1861.* Williams / Norgate, London / Edinburgh.

Chabrier, G. 2003. 'Galactic Stellar and Substellar Initial Mass Function.' PASP 115 (July): 763–795.

Chabrier, G., I. Baraffe, F. Allard, and P. Hauschildt. 2000. 'Evolutionary Models for Very Low-Mass Stars and Brown Dwarfs with Dusty Atmospheres.' ApJ 542 (October): 464–472.

Chandrasekhar, S. 1960. 'The Stability of Non-Dissipative Couette Flow in Hydromagnetics.' *Proceedings of the National Academy of Science* 46 (February): 253–257.

———. 1961. *Hydrodynamic and hydromagnetic stability.*

Charbonneau, D., T. M. Brown, R. W. Noyes, and R. L. Gilliland. 2002. 'Detection of an Extrasolar Planet Atmosphere.' ApJ 568 (March): 377–384.

Charbonneau, Paul. 2010. 'Dynamo Models of the Solar Cycle.' *Living Reviews in Solar Physics* 7 (1): 3.

———. 2013. *Solar and Stellar Dynamos.* Springer-Verlag Berlin Heidelberg.

Christensen, Ulrich R, Volkmar Holzwarth, and Ansgar Reiners. 2009. 'Energy flux determines magnetic field strength of planets and stars.' Nature 457, no. 7226 (January): 167–9.

Christensen-Dalsgaard, J. 2002. 'Helioseismology.' *Reviews of Modern Physics* 74 (November): 1073–1129.

Christensen-Dalsgaard, J., W. Dappen, S. V. Ajukov, et al. 1996. 'The Current State of Solar Modeling.' *Science* 272 (May): 1286–1292.

Christensen-Dalsgaard, J., J. Schou, and M. J. Thompson. 1990. 'A comparison of methods for inverting helioseismic data.' MNRAS 242 (February): 353–369.

Clune, T. C., J. R. Elliott, M. S. Miesch, J. Toomre, and G.A. Glatzmaier. 1999. 'Computational aspects of a code to study rotating turbulent convection in spherical shells.' *Parallel Computing* 25 (4): 361–380.

Correia, A. C. M., and J. Laskar. 2010. 'Tidal Evolution of Exoplanets.' In *Exoplanets,* edited by S. Seager, 239–266. December.

Courant, R., K. Friedrichs, and H. Lewy. 1928. 'Über die partiellen Differenzengleichungen der mathematischen Physik.' *Mathematische Annalen* 100 (1): 32–74.

———. 1967. 'On the Partial Difference Equations of Mathematical Physics.' *IBM Journal of Research and Development* 11 (March): 215–234.

Cowan, N. B., A. Voigt, and D. S. Abbot. 2012. 'Thermal Phases of Earth-like Planets: Estimating Thermal Inertia from Eccentricity, Obliquity, and Diurnal Forcing.' ApJ 757, 80 (September): 80.

Cowling, T. G. 1933. 'The magnetic field of sunspots.' MNRAS 94 (November): 39–48.

Cox, A. N., and C. A. Pilachowski. 2000. 'Allen's Astrophysical Quantities.' *Physics Today* 53, no. 10 (October): 77.

Davies, G. R., W. J. Chaplin, W. M. Farr, et al. 2015. 'Asteroseismic inference on rotation, gyrochronology and planetary system dynamics of 16 Cygni.' MNRAS 446 (January): 2959–2966.

Deheuvels, S., R. A. Garcı a, W. J. Chaplin, et al. 2012. 'Seismic Evidence for a Rapidly Rotating Core in a Lower-giant-branch Star Observed with Kepler.' ApJ 756, 19 (September): 19.

Deubner, F.-L., and D. Gough. 1984. 'Helioseismology: Oscillations as a Diagnostic of the Solar Interior.' ARA&A 22:593–619.

Dikpati, M., and P. Charbonneau. 1999. 'A Babcock-Leighton Flux Transport Dynamo with Solar-like Differential Rotation.' ApJ 518 (June): 508–520.

Dobler, W., M. Stix, and A. Brandenburg. 2006. 'Magnetic Field Generation in Fully Convective Rotating Spheres.' ApJ 638 (February): 336–347.

Domingo, V., B. Fleck, and A. I. Poland. 1995. 'The SOHO Mission: an Overview.' Sol. Phys. 162 (December): 1–37.

Dominguez, Inma, Alessandro Chieffi, Marco Limongi, and Oscar Straniero. 1999. 'Intermediate-Mass Stars: Updated Models.' *The Astrophysical Journal* 524 (1): 226.

Durney, B. R., D. S. De Young, and I. W. Roxburgh. 1993. 'On the generation of the large-scale and turbulent magnetic fields in solar-type stars.' Sol. Phys. 145 (June): 207–225.

Duvall, T. L., Jr. 1979. 'Large-scale solar velocity fields.' Sol. Phys. 63 (August): 3–15.

Eddy, J. A. 1976. 'The Maunder Minimum.' *Science* 192 (June): 1189–1202.

Elliott, J. R., M. S. Miesch, and J. Toomre. 2000. 'Turbulent Solar Convection and Its Coupling with Rotation: The Effect of Prandtl Number and Thermal Boundary Conditions on the Resulting Differential Rotation.' ApJ 533 (April): 546–556.

Elsasser, W. M. 1956. 'Hydromagnetic Dynamo Theory.' *Reviews of Modern Physics* 28 (April): 135–163.

Faggin, F., M. E. Hoff, S. Mazor, and M. Shima. 1996. 'The history of the 4004.' *IEEE Micro* 16, no. 6 (December): 10–20.

Falgarone, Edith, and Thierry Passot. 2003. *Turbulence and Magnetic Fields in Astrophysics.* Springer-Verlag Berlin Heidelberg.

Fan, Y., and F. Fang. 2014. 'A Simulation of Convective Dynamo in the Solar Convective Envelope: Maintenance of the Solar-like Differential Rotation and Emerging Flux.' ApJ 789, 35 (July): 35.

Featherstone, Nicholas A., and B. W. Hindman. 2015. 'The Spectral Amplitude of Stellar Convection and its Scaling in the High-Rayleigh-Number Regime' (November).

Featherstone, Nicholas A., and M. S. Miesch. 2015. 'Meridional Circulation in Solar and Stellar Convection Zones.' *The Astrophysical Journal* 804, no. 1 (May): 67.

Ferziger, Joel H., and Milovan Peric. 2002. *Computational Methods for Fluid Dynamics.* Springer-Verlag Berlin Heidelberg.

Field, G. B. 1965. 'Thermal Instability.' ApJ 142 (August): 531.

Fricke, K. 1969. 'Stability of Rotating Stars II. The Influence of Toroidal and Poloidal Magnetic Fields.' A&A 1 (April): 388.

Fujii, Y., and H. Kawahara. 2012. 'Mapping Earth Analogs from Photometric Variability: Spin-Orbit Tomography for Planets in Inclined Orbits.' ApJ 755, 101 (August): 101.

Galilei, Galileo. 1613. *Istoria e Dimostrazioni intorno alle macchie solari.* Roma, G. Mascadi.

Gardner, Jonathan P., John C. Mather, Mark Clampin, et al. 2006. 'The James Webb Space Telescope.' *Space Science Reviews* 123 (4): 485–606.

Gary, G. Allen. 2001. 'Plasma Beta Above A Solar Active Region: Rethinking the Paradigm.' *Sol. Phys.* 203 (1): 71–86.

Gary, G. Allen, and David Alexander. 1999. 'Constructing the Coronal Magnetic Field By Correlating Parameterized Magnetic Field Lines With Observed Coronal Plasma Structures' [in en]. *Sol. Phys.* 186, nos. 1-2 (May): 123–139.

Gastine, T., M. Heimpel, and J. Wicht. 2014a. 'Zonal flow scaling in rapidly-rotating compressible convection.' *Physics of the Earth and Planetary Interiors* 232 (July): 36–50.

Gastine, T., J. Wicht, and J. M. Aurnou. 2015. 'Turbulent Rayleigh-Bénard convection in spherical shells.' *Journal of Fluid Mechanics* 778 (September): 721–764.

Gastine, T., R. K. Yadav, J. Morin, A. Reiners, and J. Wicht. 2014b. 'From solar-like to antisolar differential rotation in cool stars.' MNRAS 438 (February): L76–L80.

Gilliland, R. L., T. M. Brown, J. Christensen-Dalsgaard, et al. 2010. 'Kepler Asteroseismology Program: Introduction and First Results.' PASP 122 (February): 131–143.

Gillings, Michael R., Martin Hilbert, and Darrell J. Kemp. 2016. 'Information in the Biosphere: Biological and Digital Worlds.' *Trends in Ecology & Evolution* 31 (3): 180–189.

Gilman, P. A. 1972. 'Nonlinear Boussinesq Convective Model for Large Scale Solar Circulations.' Sol. Phys. 27 (November): 3–26.

———. 1975. 'Linear Simulations of Boussinesq Convection in a Deep Rotating Spherical Shell.' *Journal of Atmospheric Sciences* 32 (July): 1331–1352.

———. 1976. 'Theory of Convection in a Deep Rotating Spherical Shell, and its Application to the Sun.' In *Basic Mechanisms of Solar Activity,* edited by V. Bumba and J. Kleczek, 71:207. IAU Symposium.

———. 1977. 'Nonlinear Dynamics of Boussinesq Convection in a Deep Rotating Spherical Shell. I.' *Geophysical and Astrophysical Fluid Dynamics* 8.

———. 1978. 'Nonlinear Dynamics of Boussinesq Convection in a Deep Rotating Spherical Shell. II. Effects of Temperature Boundary Conditions.' *Geophysical and Astrophysical Fluid Dynamics* 11:157–179.

———. 1979. 'Model calculations concerning rotation at high solar latitudes and the depth of the solar convection zone.' ApJ 231 (July): 284–292.

———. 1980. 'Erratum - Model Calculations Concerning Rotation at High Solar Latitudes and the Depth of the Solar Convection Zone.' ApJ 236 (March): 706.

Gilman, P. A., and G. A. Glatzmaier. 1981. 'Compressible convection in a rotating spherical shell. I - Anelastic equations. II - A linear anelastic model. III - Analytic model for compressible vorticity waves.' ApJS 45 (February): 335–388.

Gingold, R. A., and J. J. Monaghan. 1977. 'Smoothed particle hydrodynamics - Theory and application to non-spherical stars.' MNRAS 181 (November): 375–389.

Gizon, L., T. L. Duvall, and J. Schou. 2003. 'Wave-like properties of solar supergranulation.' Nature 421 (January): 43–44.

Glatzmaier, Gary A. 2013. *Introduction to Modeling Convection in Planets and Stars.* Princeton Series in Astrophysics. Princeton University Press.

Goldreich, P., and G. Schubert. 1967. 'Differential Rotation in Stars.' ApJ 150 (November): 571.

Goldreich, P., and S. Soter. 1966. 'Q in the Solar System.' *Icarus* 5:375–389.

Gottlieb, David. 1977. *Numerical analysis of spectral methods: theory and applications.* Philadelphia: Society for Industrial / Applied Mathematics.

Gough, D. 1985. 'Inverting helioseismic data.' Sol. Phys. 100 (October): 65–99.

Gough, D. O. 1969. 'The Anelastic Approximation for Thermal Convection.' *Journal of Atmospheric Sciences* 26 (May): 448–456.

Guillot, T., A. Burrows, W. B. Hubbard, J. I. Lunine, and D. Saumon. 1996. 'Giant Planets at Small Orbital Distances.' ApJL 459 (March): L35.

Guthrie, W. K. C. 1979. *A History of Greek Philosophy: Volume 1, the Earlier Presocratics and the Pythagoreans.* Cambridge University Press.

Hale, G. E., F. Ellerman, S. B. Nicholson, and A. H. Joy. 1919. 'The Magnetic Polarity of Sun-Spots.' ApJ 49 (April): 153.

Hall, Jeffrey C. 2008. 'Stellar Chromospheric Activity.' *Living Reviews in Solar Physics* 5, no. 1 (March): 2.

Hansen, C. J., and S. D. Kawaler. 1994. *Stellar Interiors. Physical Principles, Structure, and Evolution.* 84. Springer-Verlag.

Harvey, J. W., F. Hill, R. P. Hubbard, et al. 1996. 'The Global Oscillation Network Group (GONG) Project.' *Science* 272 (May): 1284–1286.

Hawley, J. F., and S. A. Balbus. 1991. 'A Powerful Local Shear Instability in Weakly Magnetized Disks. II. Nonlinear Evolution.' ApJ 376 (July): 223.

———. 1992. 'A powerful local shear instability in weakly magnetized disks. III - Long-term evolution in a shearing sheet.' ApJ 400 (December): 595–609.

Heller, R., R. Barnes, and J. Leconte. 2011a. 'Habitability of Extrasolar Planets and Tidal Spin Evolution.' *Orig. Life. Evol. Biosph.* 41 (December): 539–543.

Heller, R., J. Leconte, and R. Barnes. 2011b. 'Tidal obliquity evolution of potentially habitable planets.' A&A 528, A27 (April): A27.

Hewitt, J. M., D. P. McKenzie, and N. O. Weiss. 1975. 'Dissipative heating in convective flows.' *Journal of Fluid Mechanics* 68 (April): 721–738.

Hirano, T., Y. Suto, J. N. Winn, et al. 2011. 'Improved Modeling of the Rossiter-McLaughlin Effect for Transiting Exoplanets.' ApJ 742, 69 (December): 69.

Hook, Isobel. 2009. 'The Science Case for the European ELT.' In *Science with the VLT in the ELT Era*, edited by Alan Moorwood, 225–232. Dordrecht: Springer Netherlands.

Howard, R., and B. J. Labonte. 1980. 'The sun is observed to be a torsional oscillator with a period of 11 years.' ApJL 239 (July): L33–L36.

Howe, R. 2009. 'Solar Interior Rotation and its Variation.' *Living Reviews in Solar Physics* 6, 1 (February): 1.

Howe, R., J. Christensen-Dalsgaard, F. Hill, et al. 2000. 'Dynamic Variations at the Base of the Solar Convection Zone.' *Science* 287 (March): 2456–2460.

Hughes, D. W. 2003. 'Planetary spin.' *Planet. Space Sci.* 51 (June): 517–523.

Hui, L., and S. Seager. 2002. 'Atmospheric Lensing and Oblateness Effects during an Extrasolar Planetary Transit.' ApJ 572 (June): 540–555.

Hunter, J. D. 2007. 'Matplotlib: A 2D Graphics Environment.' *Computing in Science Engineering* 9, no. 3 (May): 90–95.

Jackiewicz, J., A. Serebryanskiy, and S. Kholikov. 2015. 'Meridional Flow in the Solar Convection Zone. II. Helioseismic Inversions of GONG Data.' ApJ 805, 133 (June): 133.

Johns, M., P. McCarthy, K. Raybould, et al. 2012. 'Giant Magellan Telescope: overview.' In *Ground-based and Airborne Telescopes IV*, vol. 8444, 84441H. Proceedings of the SPIE. September.

Jones, C. a., P. Boronski, a. S. Brun, et al. 2011. 'Anelastic convection-driven dynamo benchmarks.' *Icarus* 216 (1): 120–135.

Jones, Chris A. 2011. 'Planetary Magnetic Fields and Fluid Dynamos.' *Annual Review of Fluid Mechanics* 43 (1): 583–614.

Jouve, L., and A. S. Brun. 2007. 'On the role of meridional flows in flux transport dynamo models.' *A&A* 474 (October): 239–250.

Julien, K., E. Knobloch, A. M. Rubio, and G. M. Vasil. 2012. 'Heat Transport in Low-Rossby-Number Rayleigh-Bénard Convection.' *Physical Review Letters* 109, no. 25, 254503 (December): 254503.

Karak, B. B., P. J. Käpylä, M. J. Käpylä, et al. 2015. 'Magnetically controlled stellar differential rotation near the transition from solar to anti-solar profiles.' A&A 576, A26 (April): A26.

Kataria, T., A. P. Showman, J. J. Fortney, et al. 2015. 'The Atmospheric Circulation of the Hot Jupiter WASP-43b: Comparing Three-dimensional Models to Spectrophotometric Data.' ApJ 801, 86 (March): 86.

Kataria, Tiffany, David K. Sing, Nikole K. Lewis, et al. 2016. 'The Atmospheric Circulation of a Nine-hot-Jupiter Sample: Probing Circulation and Chemistry over a Wide Phase Space.' *The Astrophysical Journal* 821 (1): 9.

Kawahara, H., and Y. Fujii. 2010. 'Global Mapping of Earth-like Exoplanets From Scattered Light Curves.' ApJ 720 (September): 1333–1350.

Kidder, L. E., and L. S. Finn. 2000. 'Spectral methods for numerical relativity: The initial data problem.' Phys. Rev. D 62, no. 8, 084026 (October): 084026.

Kitchatinov, L. L., and G. Ruediger. 1995. 'Differential rotation in solar-type stars: revisiting the Taylor-number puzzle.' A&A 299 (July): 446.

Kosovichev, A. G. 2011. 'Advances in Global and Local Helioseismology: An Introductory Review.' In *Lecture Notes in Physics, Berlin Springer Verlag*, edited by J.-P. Rozelot and C. Neiner, 832:3. Lecture Notes in Physics, Berlin Springer Verlag.

Krause, F., and K.-H. Raedler. 1980. *Mean-field magnetohydrodynamics and dynamo theory.*

Kroupa, P. 2002. 'The Initial Mass Function of Stars: Evidence for Uniformity in Variable Systems.' *Science* 295 (January): 82–91.

Kulsrud, R. M. 2005. *Plasma physics for astrophysics.*

Kunz, M. W., Tamara Bogdanović, Christopher S. Reynolds, and James M. Stone. 2012. 'Buoyancy Instabilities in a Weakly Collisional Intracluster Medium.' ApJ 754 (2): 122.

Kunz, M. W., J. M. Stone, and E. Quataert. 2016. 'Magnetorotational Turbulence and Dynamo in a Collisionless Plasma.' *Physical Review Letters* 117, no. 23, 235101 (December): 235101.

Lagrange, A.-M., M. Desort, and N. Meunier. 2010. 'Using the Sun to estimate Earth-like planets detection capabilities . I. Impact of cold spots.' A&A 512, A38 (March): A38.

Lantz, S. R., and Y. Fan. 1999. 'Anelastic Magnetohydrodynamic Equations for Modeling Solar and Stellar Convection Zones.' *The Astrophysical Journal Supplement Series* 121 (1): 247.

Larmor, J. 1919a. 'How could a rotating body such as the sun become a magnet?' *Br. Assoc. Adv. Sci. Rep.* 159–160.

———. 1919b. 'Possible rotational origin of magnetic fields of Sun and Earth.' *Elect. Rev.* 85:512.

———. 1919c. 'Possible rotational origin of magnetic fields of Sun and Earth.' *Engineering* 108:461.

Laskar, J., and P. Robutel. 1993. 'The chaotic obliquity of the planets.' Nature 361 (February): 608–612.

Lemen, J. R., A. M. Title, D. J. Akin, et al. 2012. 'The Atmospheric Imaging Assembly (AIA) on the Solar Dynamics Observatory (SDO).' Sol. Phys. 275 (January): 17–40.

Li, G., and J. N. Winn. 2016. 'Are Tidal Effects Responsible for Exoplanetary Spin-Orbit Alignment?' ApJ 818, 5 (February): 5.

Longcope, D.W. 2005. 'Topological Methods for the Analysis of Solar Magnetic Fields.' *Living Reviews in Solar Physics* 2, 7 (November): 7.

Lucy, L. B. 1977. 'A numerical approach to the testing of the fission hypothesis.' AJ 82 (December): 1013–1024.

Lund, M. N., V. Silva Aguirre, G. R. Davies, et al. 2017. 'Standing on the Shoulders of Dwarfs: the Kepler Asteroseismic LEGACY Sample. I. Oscillation Mode Parameters.' ApJ 835, 172 (February): 172.

Mackay, D. H., and A. R. Yeates. 2012. 'The Sun's Global Photospheric and Coronal Magnetic Fields: Observations and Models.' *Living Reviews in Solar Physics* 9, 6 (November): 6.

Mandel, K., and E. Agol. 2002. 'Analytic Light Curves for Planetary Transit Searches.' ApJL 580 (December): L171–L175.

Markakis, C., and L. Barack. 2014. 'High-order difference and pseudospectral methods for discontinuous problems.' *ArXiv e-prints* (June).

Markwardt, C. B. 2009. 'Non-linear Least-squares Fitting in IDL with MPFIT.' In *Astronomical Data Analysis Software and Systems XVIII*, edited by D. A. Bohlender, D. Durand, and P. Dowler, 411:251. Astronomical Society of the Pacific Conference Series. September.

Marsh, T. R., and K. Horne. 1988. 'Images of accretion discs. II - Doppler tomography.' MNRAS 235 (November): 269–286.

Maschke, E.K., and H.J. Perrin. 1984. 'An analytic solution of the stationary MHD equations for a rotating toroidal plasma.' *Physics Letters A* 102 (3): 106–108.

Maunder, E. W., and A. S. D. Maunder. 1905. 'Sun, rotation period of the, from Greenwich sun-spot measures, 1879-1901.' MNRAS 65 (June): 813–825.

Mayne, N. J., I. Baraffe, D. M. Acreman, et al. 2014. 'The unified model, a fully-compressible, non-hydrostatic, deep atmosphere global circulation model, applied to hot Jupiters. ENDGame for a HD 209458b test case.' A&A 561, A1 (January): A1.

Mayne, N. J., F. Debras, I. Baraffe, et al. 2017. 'Results from a set of three-dimensional numerical experiments of a hot Jupiter atmosphere.' *ArXiv e-prints* (April).

McIntyre, M. E. 2001. 'Global effects of gravity waves in the middle atmosphere: a theoretical perspective.' *Advances in Space Research* 27:1723–1736.

McLaughlin, D. B. 1924. 'Some results of a spectrographic study of the Algol system.' ApJ 60 (July): 22–31.

McQuillan, A., S. Aigrain, and T. Mazeh. 2014a. 'VizieR Online Data Catalog: Rotation periods of M-dwarf stars (McQuillan+, 2013).' *VizieR Online Data Catalog* 743 (July).

McQuillan, A., S. Aigrain, and S. Roberts. 2012. 'Statistics of stellar variability from Kepler. I. Revisiting Quarter 1 with an astrophysically robust systematics correction.' A&A 539, A137 (March): A137.

McQuillan, A., T. Mazeh, and S. Aigrain. 2014b. 'Rotation Periods of 34,030 Kepler Main-sequence Stars: The Full Autocorrelation Sample.' ApJS 211, 24 (April): 24.

Miesch, M. S. 2005a. 'Large-Scale Dynamics of the Convection Zone and Tachocline.' *Living Reviews in Solar Physics* 2, 1 (April): 1.

Miesch, M. S., A. S. Brun, M. L. DeRosa, and J. Toomre. 2008. 'Structure and Evolution of Giant Cells in Global Models of Solar Convection.' ApJ 673, 557-575 (January): 557–575.

Miesch, M. S., A. S. Brun, and J. Toomre. 2006a. 'Solar Differential Rotation Influenced by Latitudinal Entropy Variations in the Tachocline.' ApJ 641 (April): 618–625.

Miesch, M. S., Allan Sacha Brun, and Juri Toomre. 2006b. 'Solar Differential Rotation Influenced by Latitudinal Entropy Variations in the Tachocline.' *The Astrophysical Journal* 641 (1): 618.

Miesch, M. S., J. R. Elliott, J. Toomre, et al. 2000. 'Three-dimensional Spherical Simulations of Solar Convection. I. Differential Rotation and Pattern Evolution Achieved with Laminar and Turbulent States.' ApJ 532 (March): 593–615.

Miesch, M. S., and B. W. Hindman. 2011. 'Gyroscopic Pumping in the Solar Near-surface Shear Layer.' ApJ 743, 79 (December): 79.

Miesch, M. S., and J. Toomre. 2009. 'Turbulence, Magnetism, and Shear in Stellar Interiors.' *Annual Review of Fluid Mechanics* 41 (January): 317–345.

Miesch, M. S., and Juri Toomre. 2008. 'Turbulence, Magnetism, and Shear in Stellar Interiors,' *Annu. Rev. Fluid Mech.* 41, no. 1 (October): 317–345.

Miesch, Mark S. 1998. 'Turbulance and Convection in Stellar and Interstellar Environments.' PhD diss., University of Colorado.

———. 2001. 'Numerical Modeling of the Solar Tachocline. I. Freely Evolving Stratified Turbulence in a Thin Rotating Spherical Shell.' *The Astrophysical Journal* 562 (2): 1058.

———. 2003. 'Numerical Modeling of the Solar Tachocline. II. Forced Turbulence with Imposed Shear.' *The Astrophysical Journal* 586 (1): 663.

Miesch, Mark S. 2005b. 'Large-Scale Dynamics of the Convection Zone and Tachocline.' *Living Reviews in Solar Physics* 2, no. 1 (April): 1.

Moffatt, H. K. 1978. *Magnetic field generation in electrically conducting fluids.* Cambridge University Press.

Moore, G. E. 2006. 'Cramming more components onto integrated circuits, Reprinted from Electronics, volume 38, number 8, April 19, 1965, pp.114 ff.' *IEEE Solid-State Circuits Society Newsletter* 11, no. 5 (September): 33–35.

Moses, J. I., C. Visscher, J. J. Fortney, et al. 2011. 'Disequilibrium Carbon, Oxygen, and Nitrogen Chemistry in the Atmospheres of HD 189733b and HD 209458b.' ApJ 737, 15 (August): 15.

Murray, C. D., and S. F. Dermott. 1999. *Solar system dynamics.*

NASA. 2017. 'NASA: The Sunspot Cycle.' Accessed June 2017.

Nelson, N. J., B. P. Brown, A. S. Brun, M. S. Miesch, and J. Toomre. 2013. 'Magnetic Wreaths and Cycles in Convective Dynamos.' ApJ 762, 73 (January): 73.

Newkirk, Gordon, and Martin D. Altschuler. 1970. 'Magnetic fields and the solar corona.' *Solar Physics* 13, no. 1 (July): 131–152.

Nikolov, N., and F. Sainsbury-Martinez. 2015. 'Radial Velocity Eclipse Mapping of Exoplanets.' ApJ 808, 57 (July): 57.

Nordlund, Åke, Robert F. Stein, and Martin Asplund. 2009. 'Solar Surface Convection.' *Living Reviews in Solar Physics* 6 (1): 2.

Ogura, Y., and N. A. Phillips. 1962. 'Scale Analysis of Deep and Shallow Convection in the Atmosphere.' *Journal of Atmospheric Sciences* 19 (March): 173–179.

Ohta, Y., A. Taruya, and Y. Suto. 2005. 'The Rossiter-McLaughlin Effect and Analytic Radial Velocity Curves for Transiting Extrasolar Planetary Systems.' ApJ 622 (April): 1118–1135.

O'Mara, B., M. S. Miesch, N. A. Featherstone, and K. C. Augustson. 2016. 'Velocity amplitudes in global convection simulations: The role of the Prandtl number and near-surface driving.' *Advances in Space Research* 58 (October): 1475–1489.

Orszag, S. A. 1971. 'On the Elimination of Aliasing in Finite-Difference Schemes by Filtering High-Wavenumber Components.' *Journal of Atmospheric Sciences* 28 (September): 1074–1074.

Ossendrijver, Mathieu. 2003. 'The solar dynamo,' 11 (4): 287–367.

Pallé, E., E. B. Ford, S. Seager, P. Montañés-Rodrı guez, and M. Vazquez. 2008. 'Identifying the Rotation Rate and the Presence of Dynamic Weather on Extrasolar Earth-like Planets from Photometric Observations.' ApJ 676 (April): 1319–1329.

Parrish, I. J., M. McCourt, E. Quataert, and Prateek Sharma. 2012. 'The Effects of Anisotropic Viscosity on Turbulence and Heat Transport in the Intracluster Medium.' MNRAS 422, no. 1 (May): 704–718.

Parrish, I. J., and E. Quataert. 2007. 'Nonlinear Simulations of the Heat Flux Driven Buoyancy Instability and its Implications for Galaxy Clusters.' ApJL 677, no. 1 (December): L9.

Passos, D., P. Charbonneau, and M. S. Miesch. 2016. 'New Insights about Meridional Circulation Dynamics from 3D MHD Global Simulations of Solar Convection and Dynamo Action.' In *Coimbra Solar Physics Meeting: Ground-based Solar Observations in the Space Instrumentation Era,* edited by I. Dorotovic, C. E. Fischer, and M. Temmer, 504:179. Astronomical Society of the Pacific Conference Series. April.

Passos, D., M. Miesch, G. Guerrero, and P. Charbonneau. 2017. 'Meridional Circulation Dynamics in a Cyclic Convective Dynamo.' *ArXiv e-prints* (February).

Paz-Chinchón, F., I. C. Leão, J. P. Bravo, et al. 2015. 'The Rotational Behavior of Kepler Stars with Planets.' ApJ 803, 69 (April): 69.

Pedlosky, J. 1987. *Geophysical Fluid Dynamics.* Springer-Verlag New York.

Pesnell, W. D., B. J. Thompson, and P. C. Chamberlin. 2012. 'The Solar Dynamics Observatory (SDO).' Sol. Phys. 275 (January): 3–15.

Plumb, R. A., and A. D. McEwan. 1978. 'The Instability of a Forced Standing Wave in a Viscous Stratified Fluid: A Laboratory Analogue of .the Quasi-Biennial Oscillation.' *Journal of Atmospheric Sciences* 35 (October): 1827–1839.

Price, D. J., J. Wurster, C. Nixon, et al. 2017. 'Phantom: A smoothed particle hydrodynamics and magnetohydrodynamics code for astrophysics.' *ArXiv e-prints* (February).

Proudman, J. 1916. 'On the Motion of Solids in a Liquid Possessing Vorticity.' *Proceedings of the Royal Society of London Series A* 92 (July): 408–424.

Quataert, E. 2008. 'Buoyancy Instabilities in Weakly Magnetized Low-Collisionality Plasmas.' ApJ 673 (February): 758–762.

Rayleigh, Lord. 1916. 'LIX. On convection currents in a horizontal layer of fluid, when the higher temperature is on the under side.' *Philosophical Magazine* 32 (192): 529–546.

Rempel, M. 2005. 'Solar Differential Rotation and Meridional Flow: The Role of a Subadiabatic Tachocline for the Taylor-Proudman Balance.' ApJ 622 (April): 1320–1332.

———. 2006a. 'Flux-Transport Dynamos with Lorentz Force Feedback on Differential Rotation and Meridional Flow: Saturation Mechanism and Torsional Oscillations.' ApJ 647 (August): 662–675.

———. 2006b. 'Transport of Toroidal Magnetic Field by the Meridional Flow at the Base of the Solar Convection Zone.' ApJ 637 (February): 1135–1142.

Ricard, Yanick, Stéphane Labrosse, and Fabien Dubuffet. 2014. 'Lifting the cover of the cauldron: Convection in hot planets.' *Geochemistry, Geophysics, Geosystems* 15 (12): 4617–4630.

Riley, P., J. A. Linker, Z. Mikić, et al. 2006. 'A Comparison between Global Solar Magnetohydrodynamic and Potential Field Source Surface Model Results.' ApJ 653 (December): 1510–1516.

Roberts, P. H., and E. M. King. 2013. 'On the genesis of the Earth's magnetism.' *Reports on Progress in Physics* 76, no. 9, 096801 (September): 096801.

Roettenbacher, R. M., J. D. Monnier, R. O. Harmon, T. Barclay, and M. Still. 2013. 'Imaging Starspot Evolution on Kepler Target KIC 5110407 Using Light-Curve Inversion.' ApJ 767, 60 (April): 60.

Rosén, L., O. Kochukhov, and G. A. Wade. 2015. 'First Zeeman Doppler Imaging of a Cool Star Using all Four Stokes Parameters.' ApJ 805, 169 (June): 169.

Rosner, R., W. H. Tucker, and G. S. Vaiana. 1978. 'Dynamics of the quiescent solar corona.' ApJ 220 (March): 643–645.

Rossi, Elena Maria. 2017. 'Supermassive black hole seeds: updates on the "quasi-star model".' *Journal of Physics: Conference Series* 840 (1): 012027.

Rossiter, R. A. 1924. 'On the detection of an effect of rotation during eclipse in the velocity of the brigher component of beta Lyrae, and on the constancy of velocity of this system.' ApJ 60 (July): 15–21.

Ruediger, G. 1982. 'Reynolds stresses and differential rotation. II - Mean-field models.' *Geophysical and Astrophysical Fluid Dynamics* 21:1–25.

Sakurai, K. 1980. 'The Solar Activity in the Time of Galileo.' *Journal for the History of Astronomy* 11:164.

Salabert, D., and R. A. García. 2009. 'Low-Frequency Solar p Modes as Seen by the GOLF and GONG Instruments.' In *Solar-Stellar Dynamos as Revealed by Helio- and Asteroseismology: GONG 2008/SOHO 21*, edited by M. Dikpati, T. Arentoft, I. González Hernández, C. Lindsey, and F. Hill, 416:329. Astronomical Society of the Pacific Conference Series. December.

Schatten, Kenneth H., John M. Wilcox, and Norman F. Ness. 1969. 'A model of interplanetary and coronal magnetic fields.' *Solar Physics* 6, no. 3 (March): 442.

Scheiner, Christoph. 1630. *Rosa Ursina sive Sol.* Bracciano.

Schekochihin, A. A., A. B. Iskakov, S. C. Cowley, et al. 2007. 'Fluctuation dynamo and turbulent induction at low magnetic Prandtl numbers.' *New Journal of Physics* 9 (August): 300.

Schou, J., H. M. Antia, S. Basu, et al. 1998. 'Helioseismic Studies of Differential Rotation in the Solar Envelope by the Solar Oscillations Investigation Using the Michelson Doppler Imager.' ApJ 505 (September): 390–417.

Schou, J., R. Howe, S. Basu, et al. 2002. 'A Comparison of Solar p-Mode Parameters from the Michelson Doppler Imager and the Global Oscillation Network Group: Splitting Coefficients and Rotation Inversions.' ApJ 567 (March): 1234–1249.

Schou, J., P. H. Scherrer, R. I. Bush, et al. 2012. 'Design and Ground Calibration of the Helioseismic and Magnetic Imager (HMI) Instrument on the Solar Dynamics Observatory (SDO).' Sol. Phys. 275 (January): 229–259.

Schrijver, C. J., A. M. Title, A. R. Yeates, and M. L. DeRosa. 2013. 'Pathways of Large-scale Magnetic Couplings between Solar Coronal Events.' ApJ 773, 93 (August): 93.

Schwarz, H., M. Brogi, R. de Kok, J. Birkby, and I. Snellen. 2015. 'Evidence against a strong thermal inversion in HD 209458b from high-dispersion spectroscopy.' A&A 576, A111 (April): A111.

Schwarzschild, K. 1906. 'Uber das gleichgewicht der sonnenatmosphere.' *Göttingen Nachrichten* 41:1–24.

Seager, S., and L. Hui. 2002. 'Constraining the Rotation Rate of Transiting Extrasolar Planets by Oblateness Measurements.' ApJ 574 (August): 1004–1010.

Seager, S., and D. D. Sasselov. 2000. 'Theoretical Transmission Spectra during Extrasolar Giant Planet Transits.' ApJ 537 (July): 916–921.

Seager, Sara. 2013. 'Exoplanet Habitability.' *Science* 340 (6132): 577–581.

Showman, A. P., K. Menou, and J. Y.-K. Cho. 2008. 'Atmospheric Circulation of Hot Jupiters: A Review of Current Understanding.' In *Extreme Solar Systems*, edited by D. Fischer, F. A. Rasio, S. E. Thorsett, and A. Wolszczan, 398:419. Astronomical Society of the Pacific Conference Series.

Showman, Adam P., Jonathan J. Fortney, Yuan Lian, et al. 2009. 'Atmospheric circulation of hot Jupiters: Coupled radiative-dynamical general circulation model simulations of HD 189733b and HD 209458b' [in en]. ApJ 699, no. 1 (July): 564–584.

Sing, D. K., J. J. Fortney, N. Nikolov, et al. 2016. 'A continuum from clear to cloudy hot-Jupiter exoplanets without primordial water depletion.' Nature 529 (January): 59–62.

Snellen, I. A. G., B. R. Brandl, R. J. de Kok, et al. 2014. 'Fast spin of the young extrasolar planet β Pictoris b.' Nature 509 (May): 63–65.

Snellen, I. A. G., R. J. de Kok, E. J. W. de Mooij, and S. Albrecht. 2010. 'The orbital motion, absolute mass and high-altitude winds of exoplanet HD209458b.' Nature 465 (June): 1049–1051.

Spiegel, E. A. 1971. 'Convection in Stars: I. Basic Boussinesq Convection.' *Annual Review of Astronomy and Astrophysics* 9:323.

Spiegel, E. A., and J.-P. Zahn. 1992. 'The solar tachocline.' A&A 265 (November): 106–114.

Spitzer, L. 1962. *Physics of Fully Ionized Gases.*

Springel, V., S. D. M. White, A. Jenkins, et al. 2005. 'Simulations of the formation, evolution and clustering of galaxies and quasars.' Nature 435 (June): 629–636.

Springel, V., N. Yoshida, and S. D. M. White. 2001. 'GADGET: a code for collisionless and gasdynamical cosmological simulations.' Nature 6 (April): 79–117.

Stello, D., M. Cantiello, J. Fuller, et al. 2016. 'A prevalence of dynamo-generated magnetic fields in the cores of intermediate-mass stars.' Nature 529 (January): 364–367.

Stevenson, D. J. 1979. 'Turbulent thermal convection in the presence of rotation and a magnetic field - A heuristic theory.' *Geophysical and Astrophysical Fluid Dynamics* 12:139–169.

Stone, J. M., T. A. Gardiner, P. Teuben, J. F. Hawley, and J. B. Simon. 2008. 'Athena: A New Code for Astrophysical MHD.' ApJS 178 (September): 137–177.

Strassmeier, K. G. 2009. 'Starspots.' A&A Rev. 17 (September): 251–308.

Taylor, G. I. 1917. 'Motion of Solids in Fluids When the Flow is Not Irrotational.' *Proceedings of the Royal Society of London Series A* 93 (March): 99–113.

Thompson, M. J., J. Christensen-Dalsgaard, M. S. Miesch, and J. Toomre. 2003. 'The Internal Rotation of the Sun.' ARA&A 41:599–643.

Vallis, G. K. 2006. *Atmospheric and Oceanic Fluid Dynamics*, 770. November.

van Ballegooijen, A. A., E. R. Priest, and D. H. Mackay. 2000. 'Mean Field Model for the Formation of Filament Channels on the Sun.' ApJ 539 (August): 983–994.

Van Der Walt, S., S. C. Colbert, and G. Varoquaux. 2011. 'The NumPy array: a structure for efficient numerical computation.' *ArXiv e-prints* (February).

van Saders, J. L., T. Ceillier, T. S. Metcalfe, et al. 2016. 'Weakened magnetic braking as the origin of anomalously rapid rotation in old field stars.' Nature 529 (January): 181–184.

Velikhov, E.P. 1959. 'Stability Of An Ideally Conducting Liquid Flowing Between Rotating Cylinders In A Magnetic Field.' *Zhur. Eksptl'. i Teoret. Fiz.* Vol: 36 (May).

Venot, O., E. Hébrard, M. Agúndez, et al. 2012. 'A chemical model for the atmosphere of hot Jupiters.' A&A 546, A43 (October): A43.

Wiegelmann, Thomas, Julia K. Thalmann, and Sami K. Solanki. 2014. 'The Magnetic Field in the Solar Atmosphere.' A&A Rev. 22 (November): 78.

Williams, D. M., and J. F. Kasting. 1997. 'Habitable Planets with High Obliquities.' *Icarus* 129 (September): 254–267.

Winn, J. N., R. W. Noyes, M. J. Holman, et al. 2005. 'Measurement of Spin-Orbit Alignment in an Extrasolar Planetary System.' ApJ 631 (October): 1215–1226.

Woods, T. N., F. G. Eparvier, R. Hock, et al. 2012. 'Extreme Ultraviolet Variability Experiment (EVE) on the Solar Dynamics Observatory (SDO): Overview of Science Objectives, Instrument Design, Data Products, and Model Developments.' Sol. Phys. 275 (January): 115–143.

Yadav, R. K., U. R. Christensen, J. Morin, et al. 2015. 'Explaining the Coexistence of Large-scale and Small-scale Magnetic Fields in Fully Convective Stars.' ApJL 813, L31 (November): L31.

Zang, Thomas A., Steven E. Krist, and M. Yousuff Hussaini. 1989. 'Resolution requirements for numerical simulations of transition.' *Journal of Scientific Computing* 4 (2): 197–217.

Zeeman, Dr. P. 1897. 'VII. Doublets and triplets in the spectrum produced by external magnetic forces.' *Philosophical Magazine* 44 (266): 55–60.

Zhao, J., R. S. Bogart, A. G. Kosovichev, T. L. Duvall Jr., and T. Hartlep. 2013. 'Detection of Equatorward Meridional Flow and Evidence of Double-cell Meridional Circulation inside the Sun.' ApJL 774, L29 (September): L29.

Index